Microfluidic staining technology and automated image processing for fast and accurate tissue-based diagnostics

THÈSE N^{O} 7422 (2016)

PRÉSENTÉE LE 22 DÉCEMBRE 2016
À LA FACULTÉ DES SCIENCES ET TECHNIQUES DE L'INGÉNIEUR
LABORATOIRE DE MICROSYSTÈMES 2
PROGRAMME DOCTORAL EN MICROSYSTÈMES ET MICROÉLECTRONIQUE

ÉCOLE POLYTECHNIQUE FÉDÉRALE DE LAUSANNE

POUR L'OBTENTION DU GRADE DE DOCTEUR ÈS SCIENCES

PAR

Diego Gabriel DUPOUY

acceptée sur proposition du jury:

Dr A. Schmid, président du jury
Prof. M. Gijs, directeur de thèse
Prof. L. de Leval, rapporteuse
Dr G. Kaigala, rapporteur
Prof. C. Brisken, rapporteuse

EPFL
ÉCOLE POLYTECHNIQUE
FÉDÉRALE DE LAUSANNE
Suisse
2016

I dedicate this thesis to the memory of
my father Raúl Aníbal Dupouy,
my mother Ana María Chicco,
and my brother Juan Ignacio Dupouy.

Acknowledgements

First of all, I would like to express my gratitude to my advisor Prof. Dr. Martin Gijs for giving me the opportunity to conduct my research in his group. Through these years, I learnt from him to keep a calm, simple and focused attitude when it comes to facing problems. I admired him for his multidisciplinary competences and his way of working out scientific problems. With time, I realized that having my PI dedicating so much time to discuss the status of the research and review manuscripts with me was simply a privilege that not every student had. Prof. Gijs has also been a guide from the career point of view, encouraging me to make the necessary decisions and take a turn when it was required, never stopping me from pursuing my interests; for this I am extremely grateful. I would like to thank Prof. Cathrin Brisken, Prof. Laurence de Leval and Dr. Govind Kaigala for accepting to be part of my jury committee and for the interesting discussions during my oral exam. Likewise, I thank Dr. MER Alexandre Schmid for accepting to be the president of the jury. I would also like to acknowledge the National Competence Center for Biomedical Imaging (NCCBI) for the generous financial support of my research.

A special thanks goes to Dr. Ata Tuna Cifltik, for teaching me all about the research he had done before my arrival, involving me in his research activities, being my mentor and co-author and, finally, trusting me to start a company together. I would then like to thank the co-authors of my work: Joan Teixidor, Déborah Heintze, Dr. Maryse Fiche, Dr. Bettina Bisig, Dr. Saska Brajkovic and Alessandro Cavinato. Their contribution was fundamental during these years and I appreciate the efforts they dedicated to push our studies forward. My thesis partially belongs to them. I am also grateful for the help I obtained from the students who worked with me during their semester or master projects: Samuel Spieser, William Courbat and Sahar Ghiasikhou.

I am extremely grateful with my colleagues of LMIS2, particularly to Dr. Matteo Cornaglia and Dr. Rima Padovani. With them, I feel like we grew up together. We went through the phases of excitement and depression of the PhD and stood by each other by all means. I also thank the older PhD students that I looked up to in many aspects: Rana, Jagoda, Hui, Tuna and Chumur, and those who arrived later and gave a new dose of enthusiasm when we had become the “old and experienced”: Cristina, Tuan, Greg and Roger. A big “thank you” to Melis Martin, who meticulously helped me solve everything from my mistakes in the invoices to plane tickets. I somehow always had to ask her something special and she never denied giving me a hand. I would finally like to thank the senior scientists of our laboratory, especially Jalil, who gave me a hand with my laboratory setup in several occasions. Thanks to the CMI team, who helped me through the microfabrication process. My gratitude as well to Lunaphore’s technical team: Pierre, Saska, Giulia and Marco, who helped me run the experiments and discuss. A special thanks to Pierre, for helping me with the abstract in French! Finally, thanks to all the LMIS2&4 lunch “troupe” for sharing so many nice moments together.

Far from home, my friends from Lausanne were key for me to make it to the end of my PhD. I want to thank Matteo (again!): flat-mate, office-mate, volleyball-mate and close friend. To Lucian and Antonio, completing the team of the “Maison des Amis”. We spent 3 years sharing the same apartment and they were key advisors and supporters. Antonio spent hours convincing me not to drop out when I could not see the end. I am really grateful to Chiara, a close friend who listened to me when I needed to decide whether to switch the direction of my research. Thanks to my friends Sergio, Ombretta, Pietro, Mario, Rima and Cristina for the long discussions that in many ways helped me shape the direction to take in my career. Thank you Carla, Ferdinando, Alessandra, Bea, Mariana, Patrizia, Camilla, Andrea, Giulia, Gigi and Aldo, for the countless moments spent together.

Finally, my deepest gratitude to my family in Argentina and Italy. My brother Emanuel and his wife Débora, who supported me from the beginning of my studies, without them I could have not “taken off”. A great “thank you” to my parents-in-law Nicola and Marina, who not only believed in me since the beginning but also had to put up with my stress on several occasions. They even hosted in their house and took care of me so that I could finally write down my thesis.

Last but not least, words cannot express my gratitude to my wife Giovanna. I honestly believe that she owns half of this achievement. Not only did she decide to move to Switzerland because I was pursuing a PhD, but also she accepted to sacrifice countless hours of her time so that I could work during the weekends. She would never stop encouraging me and (almost) never lost patience. She taught me how set priorities, to solve problems one by one and, above all, to never give up. Thank you!!!

Diego G. Dupouy
Lausanne, 28th November 2016

Abstract

The development of microfluidics has led to significant improvements in many areas of *in vitro* diagnostics. This thesis proposes the use of microfluidic device technology in the field of anatomic pathology, leading to faster and more accurate tissue-based diagnosis than was provided by standard diagnostic tools until now.

First, we characterize the fluorescence of the intermediate Parylene C bonding layer used in the fabrication of silicon/Pyrex microfluidic chips. Subsequently, we show how long-term illumination of Parylene C under bonding conditions can deliberately modify the autofluorescence of this material. We then use these programming capabilities to demonstrate several microfluidic applications of interest. In a first study, we show data storage on silicon/Pyrex microfluidic devices, where dynamic programming can be achieved by alternating the exposure of Parylene C to UV and green light. This technique allows data on a microfluidic chip to be read, written and erased using a common fluorescence microscope and could be useful to overcome automation challenges in industrial applications for which communication of information is required. In a second study, we show how modifying the fluorescence of the intermediate Parylene C bonding layer we can create an on-chip reference, which can be used to estimate concentrations and flow-rates of fluorescent molecules in a microfluidic channel. A large number of lab-on-a-chip applications use fluorescence for quantifying biological entities, for which the incorporation of a stable on-chip fluorescent reference source could compensate for instrumental parameter variations, like non-constant illumination intensity over time.

Subsequently, we focus our research on the use of microfluidic technologies to answer clinically relevant questions in the field of anatomic pathology, where microfluidic devices start to be introduced for the immunostaining of tissue sections. We propose a microfluidic precision immunofluorescence method, which accurately quantifies antigen expression levels in a continuous scale based on microfluidic staining of breast carcinoma tissue sections and automated image analysis. We show that the level of human epidermal growth factor receptor 2 (HER2) protein expression, as continuously quantified using microfluidic precision immunofluorescence in 25 breast cancer cases, can predict the number of *HER2* gene copies as assessed by fluorescence *in situ* hybridization. Finally, we demonstrate that the working principle of this technology is not restricted to HER2 but can be extended to other biomarkers. This method has the potential of providing automated, fast and high-quality quantitative *in situ* biomarker data using low-cost immunofluorescence assays, as increasingly required in the era of individually tailored cancer therapy.

Next, we propose two solutions for intraoperative staining using microfluidics: (1) a rapid immunohistochemical (IHC) staining of frozen sections using a polymer microfluidic chip, and (2) an automated fluorescent staining of the surface of thick (> 2 mm) fresh tumoral specimens. Frozen sections of tumor samples play an important role in the microscopic analysis of specimens during surgery. IHC stainings on frozen sections would be of great use during intraoperative consultations, if only the turn-around time was not a limitation. In a first intraoperative application, we show a complete pan-cytokeratin chromogenic staining protocol on frozen sections using a polymer microfluidic chip. We demonstrate an optimized cytokeratin IHC staining protocol that takes less than 12 minutes on several autopsy and tumor biopsy tissues. Breast conservative surgery (BCS), accompanied by adjuvant radiotherapy, has become a standard method for treatment of low grade breast cancers. It has been demonstrated that survival rates after BCS are similar to those achieved after complete mastectomy, though the recurrence rates are generally higher. Accurate assessment of surgical margins is therefore crucial to guarantee the best treatment of breast cancer. In the second intraoperative application, we propose a new microfluidic tool that allows automated staining and imaging of thick (> 2 mm) tissue samples. Sections of breast mastectomies taken from the proximity of the tumor location are inserted in a chamber and fluorescently stained for cytokeratin using the reagent delivery of a microfluidic chip that is custom-fabricated for this application. The dimensions of the microfluidic system used in these studies are compatible with the space constraints of an intraoperative pathology laboratory. We believe that the adoption of microfluidic technologies in the field of surgical pathology can significantly improve intraoperative examination.

Keywords

Microfluidics, Parylene C, fluorescence, microfabrication, microfluidic tissue processor, breast cancer, immunofluorescence, immunohistochemistry, human epidermal growth factor receptor 2 (HER2), quantitative fluorescence, biomarker quantification, image processing analysis, intraoperative examination, frozen sections, surgical margins, surgical pathology, turn-around time, (pan)-cytokeratin, lumpectomy, tumorectomy, mastectomy, tissue-based diagnostics, anatomic pathology.

Résumé

Le développement de la microfluidique a donné lieu à des améliorations importantes dans de nombreux domaines du diagnostic *in vitro*. Ce travail traite de l'utilisation des technologies de microfluidique dans le domaine de la pathologie anatomique qui permettraient un diagnostic basé sur les tissus de cancer plus rapide et plus précis que ceux obtenus en utilisant des outils de diagnostic standard.

Tout d'abord, nous avons caractérisé la fluorescence d'une couche intermédiaire de Parylène C utilisé pour la liaison de tranches dans la fabrication de puces microfluidiques Si/Pyrex. Par la suite, nous avons montré comment une illumination de longuee durée du Parylène C dans des conditions de liaison peut délibérément modifier l'autofluorescence de ce matériau. Nous avons ensuite utilisé ces capacités de programmation pour faire la démonstration de plusieurs applications microfluidiques d'intérêt. Dans une première étude, nous avons démontré le stockage de données sur des dispositifs microfluidiques Si/Pyrex grâce à la programmation dynamique obtenue en alternant l'exposition de Parylène C à lumière UV et verte. Cette technique permet de lire, écrire et effacer des données sur une puce microfluidique en utilisant un microscope à fluorescence standard; elle pourrait être utile pour surmonter les défis d'automatisation dans des applications industrielles pour lesquelles la communication de l'information est nécessaire. Dans une deuxième étude, nous avons révelé comment en modifiant la fluorescence de la couche intermédiaire de Parylène C nous pouvons créer une référence sur la puce qui peut être utilisé pour estimer les concentrations et les débits de molécules fluorescentes dans un canal microfluidique. L'incorporation d'une source stable de référence de fluorescence sur la puce pourrait compenser les variations des paramètres instrumentaux, telles que les intensités d'éclairage variables dans le temps dans un grand nombre d'applications de laboratoire sur puces qui utilisent la fluorescence pour la quantification des entités biologiques.

Par la suite, nous avons focalisé notre recherche sur l'utilisation des technologies microfluidiques pour répondre à des questions cliniquement pertinentes dans le domaine de la pathologie anatomique, où des dispositifs microfluidiques commencent à être introduits pour effectuer de l'immunocoloration des coupes de tissus. Nous avons dévélopé une méthode précise d'immunofluorescence microfluidique, qui permet de quantifier le niveau d'expression des antigènes sur une échelle continue en fonction de la coloration microfluidique des coupes de tissus de carcinome du sein et également de réaliser l'analyse des images automatiquement. Nous montrons que le niveau d'expression de la protéine du récepteur du facteur de croissance épidermique humain 2 (protéine HER2) quantifié en continu par immunofluorescence microfluidique de précision dans 25 cas de cancer du sein permet de prédire le nombre de copies du gène HER2 tel qu'évalué par hybridation *in situ* en fluorescence. Enfin, nous démontrons que le principe de fonctionnement de cette technologie ne se limite pas à HER2 mais peut être étendu à d'autres biomarqueurs. Cette méthode a le potentiel de fournir des données quantitatives de haute qualité liées au biomarqueurs *in situ* de manière rapide et automatisée en utilisant des tests d'immunofluorescence à faible coût, ce qui est de plus en plus requis à l'ère de la thérapie du cancer individualisée.

Enfin, nous proposons deux solutions pour l'immunocoloration péropératoire utilisant la microfluidique: (1) un marquage immunohistochimique (IHC) de coupes congelées à l'aide d'une puce microfluidique en polymère, et (2) un marquage fluorescent automatisé sur la surface de specimen tumoraux frais épais (> 2 mm). Les coupes congelées d'échantillons de tumeur jouent un rôle important dans l'analyse de spécimen durant l'opération. Les marquages IHC de coupes congelées seraient d'un grand intérêt lors d'un examen extemporané si seulement le temps de traitement n'était pas une limitation. Dans une première application péropératoire, nous avons démontré un protocole de marquage chromogénique complet pour les pancytokératines sur des coupes congelées en utilisant une puce microfluidique en polymère. Nous avons démontré un protocole optimisé de marquage IHC pour les cytokératines en moins de 12 minutes sur différents tissus issus d'autopsies et de biopsies de tumeurs. La chirurgie mammaire conservatrice (BCS) accompagnée de radiothérapie adjuvante est devenue une méthode standard de traitement des cancers du sein peu sévères. Il a été démontré que le taux de survie après BCS est similaire à celui obtenu après une mastectomie complète bien que les taux de récurrences soient généralement plus hauts. Un bilan précis des marges chirurgicales est donc crucial pour garantir le meilleur traitement possible. Dans la seconde application péropératoire, nous proposons un nouvel outil microfluidique qui permet le marquage automatique d'échantillons épais de tissus (> 2 mm). Des coupes de mastectomie prises à proximité de la tumeur sont insérées dans une chambre et marquées de manière fluorescente pour les cytokératines en distribuant les réactifs grace à une puce microfluidique fabriquée sur mesure pour cette application. Les dimensions du système microfluidique utilisé dans ces études sont compatibles avec les contraintes d'espace d'un laboratoire d'examen extemporané. Nous croyons que l'adoption des technologies microfluidiques dans le champ de la pathologie chirurgicale peut améliorer de manière signifcative les examens extemporanés.

Mots-clés

Microfluidique, Parylène C, fluorescence, microfabrication, processeur microfluidique de tissus, cancer du sein, immunofluorescence, immunohistochimie, protéine HER2, fluorescence quantitative, quantification de biomarqueurs, traitement d'images, examen extemporané, coupes congelées, marges chirurgicales, pathologie chirurgicale, temps de traitement, (pan)cytokeratines, lumpectomie, tumorectomie, mastectomie, diagnostique histologique, pathologie anatomique.

Contents

Acknowledgements ..... **v**

Abstract ..... **vii**

Résumé ..... **ix**

List of Figures ..... **xv**

List of Tables ..... **xxiii**

List of Equations ..... **xxv**

List of Abbreviations ..... **xxvii**

Chapter 1 Introduction **29**

1.1 Microfluidic chip fabrication: prototyping vs industrial manufacturing 31

1.1.1 Silicon-based devices 32

1.1.2 Hot embossing 33

1.1.3 Micromilling 34

1.1.4 Stereolithography 35

1.1.5 Injection molding 35

1.2 Microfluidic solid-liquid interface reactions: theoretical considerations 36

1.2.1 Antibody-antigen binding at constant bulk concentrations: Langmuir isotherms 38

1.2.2 Adsorption on a semi-infinite planar surface 40

1.2.3 Adsorption from a flow on a surface 41

1.3 Tissue staining methods 43

1.3.1 Tissue preparation 45

1.3.2 Hematoxylin and eosin (H&E) stain 46

1.3.3 Immunohistochemistry (IHC) 46

1.3.4 Immunofluorescence 46

1.3.5 The breast cancer panel 47

1.3.6 Fluorescence *in situ* hybridization (FISH) 48

1.4 Microfluidics for tissue staining: State-of-the-art 48

1.4.1 The « Microfluidic Tissue Processor » 49

Chapter 2 Use of a Parylene C intermediate bonding layer for on-chip micrfofluidic applications **53**

2.1 Charachterization of intermediate bonding layer fluorescence 54

2.1.1 Effect of bonding on Parylene C fluorescence 54

2.1.2 iPBLF under long-term illumination 56

2.1.3 On-chip fluorescent reference printing 59

2.2 Programming of Parylene C bonding layer fluorescence for information storage on microfluidic chips 62

2.2.1 Dynamic programming of iPBLF 63

2.2.2 Example of data storage on-chip 64

2.2.3 Channel recognition 66

2.3 Programming and use of Parylene C fluorescence as a quantitative on-chip reference 66

2.3.1 Experimental setup 68

2.3.2 Concentration sensor 69

2.3.3 Flow rate sensor 70

2.4 Conclusions 71

Chapter 3 Continuous quantification of HER2 expression by microfluidic precision immunofluorescence estimates *HER2* gene amplification in breast cancer 73

3.1 Introduction 74

3.2 Experimental 75

3.2.1 Study design 75

3.2.2 Tissue preparation and reagents 75

3.2.3 Routine analysis 76

3.2.4 Device fabrication and experimental setup 76

3.2.5 MTP staining protocol 76

3.3 Imaging processing protocol 77

3.3.1 Fluorescence image acquisition 77

3.3.2 Determination of the regions of interest for interrogation of the HER2 signal 77

3.4 Results 80

3.4.1 Continuous signal quantification of double IF staining using 80

3.4.2 Scatter plot signatures of HER2 protein expression in 25 breast cancer cases 81

3.4.3 Automated scoring and correlation to routine *HER2* gene copy number 84

3.4.4 MTP IF staining signal proportionality to Ag concentration 86

3.5 Discussion 88

Chapter 4 Microfluidics for rapid cytokeratin detection in multiple frozen section tissues 91

4.1 Introduction 92

4.2 Material and methods 93

4.2.1 Sample preparation 93

4.2.2 Microfluidic setup 94

4.2.3 MTP-based stainings 95

4.2.4 H&E stainings 96

4.2.5 Imaging 96

4.3 Results 96

4.3.1 Pre-staining protocol optimization 96

4.3.2 MTP staining protocol staining protocol optimization 97

4.3.3 Optimized MTP H&E and CK staining results for different tissue types 99

4.4 Discussion 101

4.5 Appendix 101

4.5.1 Quantification of a chromogenic signal 101

4.5.2 Choice of the DAB-based detection system 102

4.5.3 Optimization method 102

Chapter 5 Automated microfluidic cytokeratin staining of thick resections of breast carcinomas 105

5.1 Introduction 106

5.2 Material and methods 107

5.2.1 Sample preparation 107

5.2.2 Working principle 107

5.2.3 Microfluidic setup 108

5.2.4 MTS-based staining 109

5.2.5 Fluorescence image acquisition 110

5.3 Results 110

5.3.1 Characterization 110

5.3.2 CK staining using the MTS 111

5.4 Discussion 112

5.5 Conclusions and outlook 113

Chapter 6 Conclusion 115

6.1 Achieved results 115

6.2 Future development 116

6.2.1 Quantification of Ag expression 117

6.2.2 Multiplexed staining 117

6.2.3 *In situ* sequencing 118

6.2.4 Commercial development at Lunaphore Technologies SA 118

Appendix A. COMSOL simulations of the Microfluidic Tissue Processor 121

A.1. Fluidic behavior of the MTP 122

A.1.1 Parameters 122

A.1.2 Velocity profile 124

A.1.3 Pressure 125

A.1.4 Concentration 126

A.1.5 3D simulation of the velocity field 127

A.2. Reaction Kinetic analysis of the MTP 128

  A.2.1 Loading 128

  A.2.2 Incubation 129

  A.2.3 Washing 132

Curriculum Vitae 133

List of Publications 135

References 137

List of Figures

Figure 1:1 | Gartner Hype Cycle Model. Technology's life cycles can be modelled in five key phases. (1) Technology trigger: a breakthrough takes place which triggers stories in the media that set off publicity, often with no proof of commercial viability. (2) Peak of inflated expectations: a number of success stories emerge accompanied by numerous failures. Some companies enter in the field, many do not. (3) Trough of disillusionment: implementation failure discourages new commercial projects. Investment continues only on surviving products to increase their adoption in the market. (4) Slope of enlightenment: the benefits from the technology start to be widely understood, in combination with second and third-generation products offered by the technology provider. (5) Plateau of productivity: mainstream adoption begins and the criteria for viability are developed. Adapted from [2]. Copyright 2009, Gartner, Inc. 29

Figure 1:2 | Si/Pyrex microfabrication process flow. A bonding technique using Parylene C as an intermediate layer was used [16], [17]. Silicon wafers with 2 µm wet oxide on both sides were chosen. The process started by using photolithography to pattern the backside silicon oxide (1) to define a hard mask (2). The same was subsequently done to the front side of the wafer (3 and 4). Once the hard masks were patterned, a third lithographic step (5) was used to etch around half the depth of the through-holes from the front side (6). The hard mask was then removed by plasma etching and the wafer was thoroughly cleaned (7). In parallel, Parylene C was coated on a Pyrex wafer and a photolithography step (8) was done so as to etch the Parylene on the areas corresponding to microfluidic channels (9). Both wafers were bonded together using a temperature of 280 °C and pressure of 100 kPa (10). Finally, the through-holes were opened by etching the silicon from the backside (11). 33

Figure 1:3 | COC chips microfabrication process flow. (a) Hot embossing: (1) a first master is fabricated using precision tools or Si microfabrication; (2) a second master (stamp) is casted using PDMS from the first master; (3) the stamp is then used to hot emboss the front side of the microfluidic chips made of COC. **(b)** Miromilling: as a post-processing step, (5) the through-holes are micromilled and (6) the backside is patterned. **(c)** Sealing: (7) the microfluidic channels on the front side are finally sealed using PSA. . 34

Figure 1:4 | Comparison between milling, embossing, stereolithography and injection molding as microfabrication methods for plastics. (a) Technical capabilities: material compatibility, feature capability and quality of the results. **(b)** Cost comparison: setup costs and process time and cost. This figure was adapted from [19]. 36

Figure 1:5 | ELISA tests. (a) In sandwich ELISAs, capture antibodies are immobilized on the surface of a well plate. Subsequently, antigens are captured from solution. Finally, an enzyme-based system can be used to generate an amplified fluorescent or colorimetric signal. **(b)** In a direct-capture ELISA test, antigens are immobilized on the surface of well plates. Recognising antibodies are available in solution. Images taken from www.lsbio.com. 37

Figure 1:6 | Antibody binding kinetics. Schematic of the binding curve used to extract the values of the association constant k_{on} and the dissociation constant k_{off}. A solution containing antibodies is flushed on a surface where the corresponding antigens were priorly immobilized. The association curve is observed. Once the equilibrium is reached, an antibody-free solution is flushed on the same surface and the dissociation curve is observed. A fitting algorithm using Eq. (1.6) and Eq. (1.8) is used to determine k_{on} and k_{off}. Figure adapted from [40]. 39

Figure 1:7 | Model system studied. A solution with a bulk concentration c_b is flushed at flow rate Q and velocity profile $u(z)$ through a microfluidic channel of height H and width W_c. The sensing element has a length L and a width W_s, and is functionalized with Γ_{max} receptors per unit area. The association and dissociation constant of the Ab-Ag reaction are given by k_{on} and k_{off}, respectively. The model and figure are adapted from [36]. 42

Figure 1:8 | Mass transport at steady-state conditions. Antibodies are flushed in the microfluidic channel described above. Different steady-state conditions are observed by varying the parameters $\lambda = \mathrm{L}/\mathrm{H}$ and Pe_H, characteristic of the channel geometry and the flow rate Q at which the antibodies are flushed. **(a)** Phase diagram of the model described by Squires *et al.* In phase (ii) a depletion region that is thin compared to the channel height is formed. **(b)**, **(c)** and **(d)** COMSOL simulation results for combinations of λ and Pe_H that fall within the phase (ii) regime. The data and plots were adapted from [36]. 43

Figure 1:9 | Leading immunohistochemistry automats. The most adopted automated immunohistochemistry devices are offered by **(a)** Ventana, a subsidiary from Roche, under the name of Benchmark ULTRA (taken from www.ventana.com), **(b)** DAKO, under the name of Omnis (taken from www.dako.com) and **(c)** Leica Biosystems, under the name of BOND-III (taken from www.leicabiosystems.com). These machines are specialized in liquid handling automation. The providers of these instruments are in essence reagent manufacturers and make use of these companion diagnostics devices to commercialize their immunohistochemical reagents. 44

Figure 1:10 | Routine tissue preparation and staining techniques. (a) Picture of a cryostat used to obtain tissue sections from frozen samples. This machine is normally use for intraoperative diagnosis. **(b)** Tissue blocks embedded in standard paraffin cassettes for appropriate cutting and preservation. **(c)** Adhesion of freshly cut FFPE section on histological glass slides. The latter are functionalized for covalent binding of the tissue to the slide. **(d)** Picture of a H&E-stained slide. 46

Figure 1:11 |Commonly used immunohistochemistry technologies. (a) Labelled polymer technology uses a polymer bone conjugated to secondary Abs and multiple HRP enzyme molecules. When DAB is exposed to HRP, it gets oxidized and deposits in the form of a brown polymer. The enzymatic reaction generates a signal amplification. The observation is done under bright-field microscopy. **(b)** Immunofluorescence makes use of fluorescently-labelled secondary Abs. In enzyme-free configuration, no signal amplification is generated. The observation is done using fluorescence microscopy. The plots were adapted from [48]. 47

Figure 1:12 | Clinical classification of invasive breast cancer based on the expression of ER, PR and HER2. (a) The histology of the specimens is observed using H&E. Representative cases are selected according to the general clinical classifications, where the staining with ER **(b)**, PR **(c)** and HER2 **(d)** are considered. The major classification groups are ER+/PR+/HER-, ER+/PR+/HER+, ER-/PR-/HER+ and triple negative ER-/PR-/HER-. Figure adapted from [49]. Original magnification 40x. 48

Figure 1:13 | Microfluidic devices used to perform IHC stainings of tissue sections. (a) Picture (top) and schematics (bottom) of the MMIHC setup. Parallel microfluidic channels made of PDMS are positioned on top of the tissue sections for multiplexed delivery of the reagents needed for IHC. ER, HER2, PR and Ki-67 stainings results (right) **(b)** Schematics and working principle of the vMFP (left), picture of the vMFP (middle) and staining result (right). A vertical tip is disposed at the vicinity of the tissue section. An injection and an aspiration holes are used to deliver and confine the reagents used during staining on top of the areas of interest for staining. **(a)** and **(b)** were adapted from [62] and [64], respectively. 49

Figure 1:14 | Schematics and working principle of the MTP. (a) Cross-sectional view of the MTP obtained through silicon microfabrication and Si/Pyrex bonding via an intermediate layer of Parylene C. The MTP is interfaced on top of the tissue section forming a microfluidic chamber of reaction. **(b)** Top-view schematic showing the layout of the microfluidic channels that allow rapid and uniform delivery and wash of the reagents over the tissue section. **(c)** COMSOL simulation showing the fast fluidic exchange taking place in the reaction chamber. Figures adapted from [65]. 50

Figure 1:15 | Comparison between standard IHC and MTP-based IF. Sections of the same cases were stained using **(a)** conventional IHC automats and **(b)** MTP-based IF. The stained sections were blindly scored by trained pathologist according to international guidelines [56]. Figure adapted from [65]. 51

Figure 1:16 | Comparison between conventional IHC and MTP-based IF scores. MTP-based IF showed a 90% reduction of the number of ambiguous scores, in concordance with FISH reflex testing. The study was performed on 76 invasive breast carcinoma cases. 51

Figure 2:1 | Characterization of intermediate Parylene C bonding layer fluorescence (iPBLF) before and after bonding. (a) Schematic diagram illustrating the experiments to characterize the effect of bonding of iPBLF. **(b)** Pseudo-coloured fluorescence images (i), (ii), (iii) of 10 μm-thick Parylene C at diced device cross-sections and (iv), (v), (vi) of patterened Parylene C after bonding (images are 200 μm wide), corresponding respectively to the UV/Blue, Blue/Green and Gree/Red filter sets. **(c)** Plot of iPBLF intensity relative to the background, appearing most significant in the UV/Blue and Green/Red channels 55

Figure 2:2 | "Observation" of the induced fluorescence after long-term "llumination". Ω_s sis the illuminated region, Ω_r is a non-illuminated region containing Parylene C, and Ω_b is a background region without Parylene C. The induced fluorescence is calculated considering the pixels within the dashed circles. The image width is 275 μm. 56

Figure 2:3 | Time response of iPBLF under long-term illumination with UV (310-390 nm) and Green (537-562 nm). (a) Fluorescent images showing the iPBLF ''observed'' in the UV/Blue and Green/Red channels. Observation is done initially, just after bonding and before any ''illumination'', and after ''illumination'' with UV and Green light, showing that the UV light can be used to increase fluorescence, whereas Green light can be used to decrease it. Fluorescent images are 275 μm wide. **(b)** Plots of induced fluorescence (F_{ind}) vs. ''illumination'' duration for UV and Green light. The plots show that the iPBLF variation observed in the Green/Red channel has an opposite trend depending on if the spot has been illuminated with UV or Green light, while this is not the case for iPBLF observation in the UV/Blue channel. 58

Figure 2:4 | Induced fluorescence versus the illumination duration under UV illumination using different intensity filters. Grey filters of 100%, 50% and 25% were used. During initial exposure, we observed an exponential decay bleaching behavior in the UV/Blue channel for all intensities. For 100% UV illumination intensity, an increase in the fluorescent signal is observed after a few minutes. On the other hand, with lower UV illumination intensity, bleaching remains dominant and recovery of initial fluorescence cannot be achieved. 58

Figure 2:5 | Fluorescent image observed in the Blue/Green. The figure shows a standard area (Ω_{STD}), an area without Parylene C (Ω_b), an area with non-illuminated Parylene C (Ω_r) and the illuminated reference area (Ω_R). 59

Figure 2:6 | Characterization of the iPBLF in the reference area Ω_R under long-term illumination with UV for a 2 μm, 5 μm and 10 μm thick layer of Parylene C. The $F_{ind}(t)$ curves are obtained from the raw data by using Eq. (2.2) and (2.3). **(a)** Observation in the UV/blue channel, showing a fast increase in the signal, followed by a slower decay. **(b)** Observation in the Blue/Green channel, indicating an increase in the signal followed by a decay, however with a less strong dependence on the dose than the curve of (a). Both UV/Blue and Blue/Green observation channels were fitted according to the formula $I = ax*\exp\text{-}bx + y_0$ representing an initial linear growth of the fluorescence followed by a single exponential decay, though the latter is hardly visible in (**b**). The parameters of the fitted curves $F_{ind}(t)$ for (**a**) and (**b**) were extracted from the model and shown in **Table 2:2** and **Table 2:3**, respectively. 61

Figure 2:7 | Dynamic programming of iPBLF using alternating ''illumination'' by UV and Green light. (a) Time-lapse pictures showing a write–erase cycle of an illuminated region. The decrease in fluorescence upon Green illumination during 5 min is used to ''write'', while subsequent UV illumination of the same spot during 3 min is used to ''erase'' information by reversing the effect. Each time-lapse image is 75 μm wide. **(b)** $F_{ind}(t)$ observed in the Green/Red channel during a sequence of multiple ''write'' and ''erase'' cycles of the same region. 64

Figure 2:8 | Example of data storage on chip. On-chip data writing in the form of a QR-code using induced UV/Blue fluorescence. The obtained fluorescent image is easily recognizable by QR-code reading software. Codes can equivalently be written in the Green/Red channel either by locally inducing or bleaching fluorescence. The width of this fluorescent QR-code is 500 μm. 65

Figure 2:9 | **Stability of the induced fluorescence**. **(a)** Study of the induced fluorescence written by UV illumination and written (bleached) by Green illumination over 7 days. We observe an increase of the induced fluorescence after UV illumination in both UV/Blue and Green/Red channels, when normalized to the one obtained right after the spot writing. For the spots written (by bleaching) using Green illumination and observed in the Green/Red channel, we find that fluorescence has increased about 5% over one week. **(b)** Stability of the QR-code 2 months after writing. After initial code writing, we stored the chip at room temperature without any special protection from atmosphere and humidity for 2 months and later once again acquired the fluorescent image of the code. We have observed no difference in the resulting image and the code was easily recognizable by the software. The width of the fluorescent QR-code is 500 μm 65

Figure 2:10 | Use of iPBLF for detection of geometrical parameters on-chip. (**i**) a single fluorescent image, from which (**ii**) channel positions, (**iii**) actual channel dimensions and (**iv**) marked interrogation zones can be detected. 66

Figure 2:11 | Schematic view of the microfluidic device. **(a)** Top view showing the microfluidic channel with in- and outlets. Several circular structures were etched together with the microfluidic channel in order to more uniformly distribute the pressure during bonding. **(b)** Schematic cross-section of the chip along the A-A' and B-B' profiles of **Figure 2:11a**, showing the position of the Parylene C layer and the backside-etched hole for the inlet. For illumination and observation, the microscope objective is focused on the Parylene C layer. 68

Figure 2:12 | Fluorescent image of the microfluidic channel and the on-chip reference. Image observed in the Blue/Green channel. The fluorescent signal of the solution flowing in the channel is obtained from the pixels in the area Ω_S and is referenced to the pixels of the area Ω_R by using Eq. (2.5). 69

Figure 2:13 | Measurements of the fluorescent signal from a solution of FITC-labelled antibodies flowing in the microfluidic channel. The relative lamp power (P) and the objective magnification (M) are represented as follows: ■ P:100% M: 20x, ● P: 50% M: 20x, ▲ P:25% M:20x, ▼ P:100% M: 10x, ◆ P: 50% M: 10x ◀ P:25% M:10x. (**a**) Values of the average pixel intensity p_S from the area Ω_S plotted against the normalized concentration of the solution flowing in the microfluidic channel. (**b**) Values of F_{rel} calculated using Eq. (2.5) and plotted versus the normalized concentration of the solution in the channel. The curve of this plot is independent on the different hardware configurations used for the experiment. 70

Figure 2:14 | Measurements of the fluorescent signal from a solution of FITC-labelled antibodies flowing in the microfluidic channel under bleaching conditions (slow flow rate) with blue light. (a) Fluorescent image of the microfluidic channel and the on-chip reference, observed in the Blue/Green channel. The fluorescent signal of the solution flowing in the channel is obtained from the pixels along the profile A-A' and is referenced to the area Ω_R by using Eq. (2.5). **(b)** Values of F_{rel} across the profile A-A' for the flow rate Q taking the values of 20, 15, 10, 8, 6, 4, 2 and 1 nl/s, respectively. **(c)** The integrated intensity (area under the curve) across the channel, A, as a function of Q^{-1} for two antibody concentrations (the 1/100 dilution corresponding to a concentration of 123 μg/ml). 71

Figure 3:1 | Experimental setup. (a) Assembled MTP; the microfluidic chamber, formed by clamping the tissue slide to the MTP, is opened to show the different parts and the loading mechanism. **(b)** Overview of the experimental setup. 76

Figure 3:2 | Example of image tile processing for MTP analysis. The image processing algorithm is applied to a case where HER2 is overexpressed **(a)** and not expressed **(b).** The algorithm uses the DAPI channel to mask the locations of the nuclei, as they constitute an area that should not be examined, while the CK channel indicates the location of epithelial cells, i.e. exactly the areas where the HER2 and CK signals should be interrogated. This allows constructing a binary mask by which one can assign a single tile-averaged value for the CK and HER2 signals, obtained from the areas of interest only. Scale bar: 100 μm. 78

Figure 3:3 | Use of CK filter to obtain the HER2 histogram. (a) Example of tissue areas with (top) and without (bottom) epithelial cells and visualized in the raw CK channel (two middle images) and after running the image processing algorithm (two right images). **(b)** Raw histograms of the intensity distribution of the CK (green, first row) and HER2 (red, second row) signals for a HER2 IHC 3+ case (left column) and a HER2 IHC 0 case (right column). The tiles that show a low CK signal intensity are removed from the histogram and the third row shows the HER2 histograms plotted after application of this CK filter. The latter histograms represent the data sets for further analysis. Scale bar: 100 μm. 79

Figure 3:4 | Microfluidic precision immunofluorescence. (a) A breast tumor is surgically resected and is to be prepared in the form of thin histological tissue slides for analysis. **(b)** A slide is clamped with the MTP for IF staining. **(c)** Subsequently the slide is coverslipped with a DAPI-containing mounting solution and imaged using a fluorescent microscope. **(d)** Mosaic images of the stained slide are acquired in 3 fluorescent channels, corresponding to the signals of DAPI, CK, and HER2, respectively, and are automatically and tile-by-tile analyzed. **(e)** 2D scatter plot showing the correlation between the averaged HER2 and CK signal per tile, for three samples with different IHC score obtained from routine analysis: 3+ (green), 2+ (blue) and 0 (red). Scale bars: 10 mm for B and C, 100 µm for D. 81

Figure 3:5 | Scatter plot signatures obtained by MTP IF and the corresponding *HER2* gene copy number for 25 invasive breast carcinoma cases. The listed values for the cell-averaged *HER2* gene copy number (N_{FISH}) were obtained from FISH routine analysis. The HER2 status classification (Class.) by the pathologist is also given, based on N_{FISH} as follows: $N_{FISH} < 4$: Negative; $4 \leq N_{FISH} < 6$: Equivocal; $N_{FISH} \geq 6$: Positive. For the MTP analysis, the 25 cases were grouped into 5 batches and samples were processed sequentially in one run with the MTP, while one positive (IHC 3+ score) and one negative (IHC 0 score) control sample were each time included in the batch. An automated algorithm was used to determine the regions of interest with epithelial cells and remove the background for each tile of the mosaic image of a given sample. This resulted in one average HER2 and CK signal per tile, which is represented by a point in a scatter plot for each patient. The scatter plot shows the correlation between the tile-averaged HER2 and CK signals (blue), compared with the scatter plot data obtained from the IHC 3+ (green) and IHC 0 (red) control samples of the batch. Analysis of the scatter plots, as further illustrated in **Figure 3:6**, provided a MTP score for each patient that clearly correlated with N_{FISH} obtained from routine analysis... 83

Figure 3:6 | **Automated comparison of a scatter plot to those of control cases.** Routine analysis prior resulted in following IHC scores: one 3+ case (green), one 0 case (red), and three borderline cases (blue), the latter having N_{FISH} of 1.9, 4.4, and 9.4, respectively. In our data processing algorithm, the ratio between HER2 and CK signals was obtained on a tile-by-tile basis from the scatter plot data of **Figure 3:5**. The thus obtained population is plotted as a histogram, indicating the frequency of occurrence of a particular ratio; this frequency is normalized by the number of tiles for the given case. A Gaussian fit to the histogram allowed determining the mean HER2/CK value, which was normalized by the mean of the 3+ control sample in the batch, defining the M-score. Similarly, the standard deviation (σ) of the Gaussian fit, normalized by σ of the 3+ control sample, defined the Σ-score. The MTP-score is defined as the product of the M- and Σ -scores.. 84

Figure 3:7 | MTP-Score can estimate N_{FISH} with a high confidence. (a) M-score, **(b)** Σ-score and (**c**) MTP-score vs N_{FISH}. The results of the HER2 status classification according to routine FISH analysis are indicated by the green, orange and red zones, representing negative (Neg), equivocal (Equ) and positive (Pos) cases, respectively. **(d)** M-score, **(e)** Σ -score and **(f)** MTP-score vs *HER2*/CEP17 ratio. The results of the HER2 status classification according to routine FISH analysis are indicated by the green and red zones, representing negative (Neg) and positive (Pos) cases, respectively. ρ and α represent Pearson's coefficients and slopes of the power law fits, respectively. Error bars are obtained from Gaussian fits to the histogram data. 85

Figure 3:8 | **Comparison of the use of short vs long Ab incubation times for accurate IF analysis. (a)** Histograms of the HER2/CK ratio for a few cases, either obtained with (i) the MTP using short incubation times, or (ii) an off-chip protocol using 1 h incubation. We clearly observe that the histograms become broader and shift to higher HER2/CK ratios for the long incubation time. The broadening leads to a less accurate assessment of the HER2 expression level, as evidenced in the plot of the M-score **(b)** and the Σ-score **(c)**, especially for $N_{FISH} < 6$, which is the interval for which equivocal results are encountered. The red points correspond to experiments done with the 1 h incubation time, while blue points were obtained with the MTP using a 2 min incubation time protocol. The green points represent additional control stains done with the MTP using a long incubation time of 1 hour. These results show that the obtained automated scores when using long incubation times have little or no diagnostic value for low N_{FISH}, the interval where quantitative results are most required in practical diagnostics. Using short incubation times with MTP not only solves this problem but also provides a much more proportional score to quantitative results obtained by *in situ* hybridization in all diagnostic range. 86

Figure 3:9 | Effect of the Ab incubation time on the proportionality of Ag and Ab signals. (a) Fluorescent image of AF647 mouse Abs used as Ag and spotted on an epoxy-functionalized glass slide with a concentration ranging from 0 to 1000 $\mu g/ml$ **(b)** Fluorescent image of AF488 anti-mouse Abs, used as Ab delivered and incubated using the MTP. **(c)** and **(d)** show the normalized fluorescent signals of the spotted Ag and its recognizing Ab for 1 hour and 2 minute's incubation time, respectively, versus the Ag spotting concentrations. **(e)** and **(f)** depict the normalized fluorescent signals of the recognizing Ab versus the signals of the spotted Ag for 1 hour and 2 minute's incubation time, respectively. For the short incubation time, the Ab-Ag curve shows a linear-like relation with a regression coefficient of 0.96; this proportionality is in favor of the accuracy of the fast MTP-based staining procedure. 88

Figure 4:1 | Working principle of microfluidic staining of FS. (a) Once the frozen sample preparation is completed, the sample is clamped using a gasket to the MTP to form a reaction chamber, after which the system is ready for fast IHC staining. **(b)** Schematic cross-section of the MTP clamped to the tissue slide. Inside the reaction chamber, reagents are sequentially delivered and washed over the surface of the tissue section. The MTP enables a fast fluidic exchange on a one-second timescale, while keeping reagent exposure times uniform throughout the whole tissue surface. **(c)** Schematics of the laboratory setup used for the experiments: (i) 50 mL reservoirs are used for common reagents, namely PBS, DIW, DAB, and hematoxylin; (ii) 1.5 mL Eppendorf tubes are used to load specific reagents, such as Abs, and blocking solutions; (iii) a computer-operated valve-manifold called RDS allows for the selection of the reagents that are flushed into the chamber of reaction; (iv) MTP/ tissue sample staining chamber. 95

Figure 4:2 | Optimization of the pre-staining protocol on ureteral biopsy sections. Slides show the final CK staining and are compared with CTL samples, obtained by staining without use of the primary Ab, in which case, ideally, only nuclear hematoxylin counterstaining is visible. The immunohistochemical staining of frozen sections described in this work requires a set of common tissue preparation steps (see **Table 4:1**): (1) sectioning, (2) first drying, (3) fixation, (4) second drying, and (5) re-hydration. Step 1 was neither optimized nor counted within the total time of the IHC assay. Steps 2 to 4 were optimized off-chip. **(a)** Comparison of CK staining obtained using fixation by methanol (at 4 °C) and acetone (kept at –20 °C prior to the experiment). In direct acetone fixation, the tissue is immersed in the acetone immediately after sectioning. Indirect means that the tissue is sectioned, dried for 15 min at room temperature, and then immersed in the acetone. Indirect fixation with acetone showed best staining. **(b)** Optimization of the acetone indirect fixation time. Three-minute fixation turned out to be sufficient to obtain a clear staining. Increasing the fixation time resulted in no apparent improvement, while shorter fixation times increased the areas where the staining was not present or was fainter. **(c)** Optimization of the second drying time (step 4 in **Table 4:1**) showed satisfactory results using an air-flow dryer for 2 min. **(d)** One-minute successful re-hydration was achieved by clamping the section to the MTP. The blue frames on each panel represent the 'best conditions' chosen for the final experiments of Figure 5 and are represented in column (iii) of **Table 4:1**. (Scale bars: 50 μm; bottom-left code: identifier of the sample in **Table 4:2** of the Appendix). 97

Figure 4:3 | Optimization of the first part of the MTP staining protocol of Table 4:1 on ureteral biopsy sections. Slides show the final CK staining and are compared with CTL samples, obtained by staining without use of the primary Ab. (**a**) Use of a blocking buffer, standardly done in the manual protocol, did not improve staining in microfluidic IHC, which was the reason to remove the blocking step from the optimized protocol in **Table 4:1**. (**b**) Optimization of the primary Ab incubation time. Incubation during 2 min was sufficient to obtain a high-quality staining. (**c**) Optimization of the secondary Ab incubation time. 4 min was chosen in the initial MTP protocol of column (ii) of **Table 4:1**. The blue frames on each panel represent the 'best conditions' chosen for the final experiments of **Figure 4:5** and are represented in column (iii) of **Table 4:1**. (Scale bars: 50 μm; bottom-left code: identifier of the sample in **Table 4:2**). 98

Figure 4:4 | Optimization of the second part of the MTP staining protocol of Table 4:1 on ureteral biopsy sections. (a) Optimization of the incubation time of DAB obtained from the Novolink kit. Increasing the DAB incubation time between 30 s and 90 s increases the intensity of the signal. However, no difference is perceived between 90 s and 150 s, indicating that incubation longer than 90 s is not necessary. **(b)** DAB reagents from 5 manufacturers were compared under the same experimental conditions. ImmPACT was selected as giving the best staining quality. **(c)** Three hematoxylin suppliers were compared, giving as most suitable choice hematoxylin obtained from Gill3. **(d)** The optimized hematoxylin incubation time was chosen as 15 s. **(e)** Finally, we diluted the hematoxylin solution to 20% of its original concentration using DIW, resulting in lesser viscosity and eosin application without compromising the staining. (Scale bars: 50 μm; bottom-left code: identifier of the sample in **Table 4:2**). 99

Figure 4:5 | Results of the optimized MTP staining protocol for different tissue types for CK in IHC (less than 13 minutes) and H&E (2:30 minutes). Optimized H&E staining (first column), CTL staining (negative control, second column), and CK staining (third column) performed on the following samples: pancreas, ureter, prostate, breast carcinoma, pancreas adenocarcinoma, lung carcinoma (NSCLC), benign lymphoma and Hodgkin lymphoma. The H&E stainings were performed on the MTP in 2:30 minutes. CK staining showed specificity to epithelial cells on non-cancerous tissues and on carcinomas of different origin. At the same time, no false-positive staining was observed on lymphoma cases. Similarly, the negative controls, where the protocols were run without primary anti-CK Abs, showed only nuclear counterstaining, as expected. (Scale bars: 50 μm). 100

Figure 4:6 | IHC quantification algorithm. Starting from a chromogenic CK staining of breast carcinoma samples, the color brightfield image is initially **(a)** converted to grey scale, then **(b)** inverted and finally **(c)** thresholded to represent areas considered as signals distinct from the background, with higher grey values for higher staining intensities. **(d)** Comparison of the average staining intensity obtained from staining of adjacent sections of the same tumor sample, where DAB is flushed at 10 μl/s (blue) and at 25 μl/s (yellow) and primary and secondary Ab incubation times are swept. Error bars are calculated from the standard deviation of the pixel grey values. Plots are normalized to the signal obtained at the maximum Ab incubation time of 16 min. 102

Figure 4:7 | Choice of detection system kit. Comparative test on 4 different commercially available detection kits: Novolink, Quanto, HRP kit TSA and ImmPRESS. ImmPRESS was selected as giving the best results and requiring the fewest protocol steps. The test was realized once the pre-staining steps had been optimized (see **Table 4:1**). Prior to optimization, the Novolink kit was used as the reference (see **Figure 4:2**). (Scale bars: 50 μm) 102

Figure 5:1 | **Microfluidic Tissue Stainer (MTS) working and imaging principle. (a)** Si/Pyrex MTS. **(i)** Schematic cross-section of the Si/Pyrex MTS, which is clamped to the PMMA tissue holder that accommodates the sample, where the gasket assures sealing of the staining chamber. The residual space around the tumor sample is occupied by a custom-made PDMS elastomer to minimize the chamber's dead volume. For staining, spacing between the tissue sample and the lower Pyrex surface is guaranteed by a silicon grid with cross-shaped pillars. **(ii)** Schematic top-view of the Si/Pyrex MTS. The microfluidic channel design allows for equilibrated distribution of staining reagents in the chamber. **(iii)** Schematic of the off-chip petri dish-based imaging setting for tissues after staining using the Si/Pyrex MTS. **(b)** COC/PSA MTS. **(i)** Schematic cross-section of the COC/PSA MTS, which is clamped to the PMMA tissue holder that accommodates the sample. The PSA tapes assure both sealing of the microfluidic channels and formation of the thin (0.1 mm) imaging window that can be deflected during pressure-driven delivery of staining reagents. **(ii)** Schematic top-view of the COC/PSA MTS. **(iii)** Schematic of two options for imaging when staining with the COC/PSA MTS: either off-chip petri dish-based imaging after staining and removal of the tissue from the setup or direct on-chip imaging can be used. 108

Figure 5:2 | Experimental realization of the microfluidic setups. (a) (i) Exploded view of the assembly of the complete manifold, in which the MTS (either Si/Pyrex MTS or COC/PSA MTS) is mechanically clamped with the PMMA tissue holder and surrounding PMMA block. (ii) Schematic of inlet or outlet of the MTS, which is sealed independently from the staining chamber with the PMMA block using an inlet or outlet joint. **(b)** Picture of the (i) Si/Pyrex MTS and (ii) the COC/PSA MTS. (iii) Scanning electron microscope image of a cross-shaped pillar of the Si/Pyrex MTS. Scale bar: 200 μm. **(c)** Picture of the complete manifold assembly with a COC/PSA MTS. **(d)** Pictures of a characterization experiment showing the delivery and washing of food colorants over a breast cancer tumorectomy sample at a flow rate of 100 μl/s: (i) after complete filling during 10 s with red dye, (ii) after washing during 20 s with PBS buffer and (iii) after subsequent filling after 10 s with yellow dye. 109

Figure 5:3 | **Images taken by a widefield fluorescence microscope. (a)** Snapshot off-chip images of CK staining done using the Si/Pyrex MTS. **(b)** Snapshot on-chip images of CK staining performed with a COC/PSA MTS. (CTL: negative control in which a fluorescent secondary antibody (Ab) but no primary anti-CK Ab is applied in the staining protocol; Test: both primary and secondary antibodies are applied in the staining protocol; DAPI: counterstain for highlighting the nuclei; Merge: overlapping DAPI and CK channels. Scale bar: 50 μm) 111

Figure 5:4 | Images taken by a confocal fluorescence microscope. (a) Snapshot off-chip images of CK staining done using the Si/Pyrex MTS. **(b)** Snapshot off-chip images of CK staining performed with a COC/PSA MTS. (CTL: negative control in which a fluorescent secondary Ab but no primary anti-CK Ab is applied in the staining protocol; Test: both primary and secondary antibodies are applied in the staining protocol; DAPI: counterstain for highlighting the nuclei; Merge: overlapping DAPI and CK channels. Scale bar: 50 μm)112

Figure 6:1 | Laboratory Satellite prototype called LABSAT 3. (a) Render view of Lunaphore's staining prototype called LABSAT 3. **(b)** Picture of user inserting a COC MTP chip into the staining area of LABSAT 3. The MTP is clamped automatically against a tissue slide for formation of the reaction chamber and staining. 119

Figure A:2 | MTP 17x17 GDS. Snapshot of the GDS file used for the fabrication of the MTP 17x17 design. Three masks were used on a 4-inch wafer. 123

Figure A:3 | Velocity profile. (a) 17x17 (Linear color scale: Blue 0 m/s, Red 0.04 m/s.); **(b)** 22x22 (Linear color scale: Blue 0 m/s, Red 0.06 m/s.); **(c)** 22x50 (longitudinal) (Linear color scale: Blue 0 m/s, Red 0.1 m/s.); **(d)** 22x50 (transversal). (Linear color scale: Blue 0 m/s, Red 0.06 m/s.) 124

Figure A:4 | Velocity profile without "Shallow Channel Approximation". The third dimension of 2D simulation is considered of the same order of the lateral dimensions when the "Shallow Channel Approximation" is inactive. (Linear color scale: Blue 0 m/s, Red 0.04 m/s.) 125

Figure A:5 | Velocity profile of MTP 17x17 design. (a) Original design. **(b)** Modified design with wider outlet channel. (Linear color scale: Blue 0 m/s, Red 0.3 m/s.) 125

Figure A:6 |Concentration profile at washing. Logarithm of the concentration plot for **(a)** MTP 17x17, **(b)** MTP 22x22, **(c)** MTP 22x50 (longitudinal), **(d)** MTP 22x50 (transversal) devices. For each simulation the image was taken at 0.4 s (left), 0.8 s (middle) and 1.4 s (right) from the beginning of the washing. Red represents initial concentration. Blue represent 10^{-7} times the initial concentration. Washing is considered complete when the concentration in the chamber reaches 10^{-7} of the initial concentration. (Logarithmic color scale, c: concentration, c_0: initial concentration, Blue -10, Red 0.) 126

Figure A:7 | 3D fluidic simulation of MTP 17x17 device. The fluidic simulation with an applied flow rate of 25 μl/s returned a required inlet pressure of 8.8 kPa, which differes of 1.8 kPa from the pressure calculated from the analogous 2D simulation. 127

Figure A:8 | Schematic of reaction kinetic simulation. Lateral view of the reaction chamber of an MTP 17x17 design. Seven reaction points simulating regions containing Ags with an increasing concentration Γ_{max} from left to right. 128

Figure A:9 | Simulation steps. Loading or reagents starts by flushing a solution with a concentration of Abs of 30 μM into a chamber with no Abs until the complete solution is exchanged. Incubation takes place for a minimum of 250 s and a maximum of 2000 s. Subsequently, washing is achieved by flusing a solution with no Abs. Color code: Blue: 0 μM, Red: 30 μM 128

Figure A:10 | Rapid Saturation. Time-dependence of Γ for $\Gamma_{max} \sim 10^{-9}$ mol/m^2 and $k_{on} \sim 10^6$ M^{-1}s^{-1}.130

Figure A:11 | Diffusion limited. Time-dependence of Γ for $\Gamma_{max} \sim 10^{-6}$ mol/m^2 and $k_{on} \sim 10^6$ M^{-1}s^{-1}.131

Figure A:12 | Slow reaction. Time-dependence of Γ for $\Gamma_{max} \sim 10^{-5}$ mol/m^2 and $k_{on} \sim 10^3$ M^{-1}s^{-1}. ... 131

Figure A:13 | Slow saturation. Time-dependence of Γ for $\Gamma_{max} \sim 10^{-10}$ mol/m^2 and $k_{on} \sim 10^4$ M^{-1}s^{-1}.132

List of Tables

Table 1:1 | List of the methods and materials used for the fabrication of our microfluidic devices. The methods used to fabricate the channels, drill the through-holes and seal the channels are described for all the chips types and classified by the material of choice. Si/Pyrex microfluidic chips were fabricated in the EPFL's cleanroom facilities, while PC, COC and GR-1 UV-sensitive resin were externally fabricated by contract manufacturers using the microfluidic designs we provided. RMPD: Rapid Micro Product Development. PSA: Pressure-sensitive adhesive tape. 32

Table 1:2 | Immunohistochemistry automats features. Highlighted features from the technical specifications of the immunohistochemistry automats shown in **Figure 1:1.** The data is adapted from [41]. *Taken from [42], **Taken from www.dako.com and www.leicabiosystems.com, respectively. 44

Table 2:1 |Excitation and emission wavelengths of the filter sets used for the fluorescence experiments and corresponding commercial dyes. BP: bandpass, LP: long pass, DAPI: diamidino-phenylindole, BFP: blue fluorescent protein, GFP: green fluorescent protein, Cy: Cyanine, AF: AlexaFluor (Molecular Probes, Invitrogen) 55

Table 2:2 | Fitting parameters for the UV/Blue channel for 2, 5 and 10 μm thickness of Parylene-C. *RMSE: Root Mean Square Error. 62

Table 2:3 | Fitting parameters for the Blue/Green channel for 2, 5 and 10 μm thickness of Parylene-C. *RMSE: Root Mean Square Error. 62

Table 3:1 | **MTP immunohistochemical staining protocol.** 77

Table 3:2 | Image-processing algorithm. 80

Table 3:3 | Results of the routine IHC and FISH analyses for all cases. Comparison is made between: **i)** IHC scoring following 2013 ASCO/CAP guidelines *(7)*; **ii)** N_{FISH} ; **iii)** *HER2*/CEP17 ratio; **iv)** HER2 status classification based on N_{FISH} ($N_{FISH} < 4$: Negative; $4 \leq N_{FISH} < 6$: Equivocal; $N_{FISH} \geq 6$: Positive) and **v)** HER2 status classification according to 2013 ASCO/CAP guidelines [57]. The aim of this process was to compare MTP results to the results of traditional IHC. Case 13 was removed from the dataset since a control H&E slide showed that only ductal carcinoma *in situ* (DCIS) was left on the sections used for the study. Similarly, case 14 was removed from the dataset because the section presented heterogeneous HER2 status, resulting in two N_{FISH} values. For cases 22 and 25, interpretation of routine IHC on the resected tumor specimen failed due to repeated tissue detachment from the glass slide. The IHC score indicated for these cases is the one found on the initial core biopsy. 82

Table 4:1 | Staining protocols. Details of the complete protocol for (i) manual staining, (ii) prior non-optimized MTP protocol and (iii) optimized MTP protocol. Washing steps, performed in-between the described steps, are not explicitly mentioned. The overall washing time is shown at the end of the table. 94

Table 4:2 | Detailed protocol step times during optimization. The protocol steps and the corresponding time (in minutes) for the optimization experiments are depicted for each test of this study. The sample identifier (ID) corresponds to the bottom-left code present in the figures of the main text. The highlighted rows correspond to the time changes, realized for the parameters of interest. 103

Table 5:1 | Staining protocol using the MTS. Fixation with acetone at -20 °C was performed off-chip. Washing, blocking, primary Ab and secondary Ab steps were performed on-chip. The flow rate during delivery -column (i)- was set to 100 μl/s for buffers and 25 μl/s for Abs. The dispensed volume -column (ii)- was set to 1000 μl/s for all the on-chip steps. Incubation times and number of repetitions are detailed in columns (iii) and (iv), respectively. 109

Table A:1 | MTP device design. Four MTP designs were simulated. The name of each device is given by its reaction chamber lateral dimension and whether the liquid is flown on its longitudinal or transversal axis. The second column shows the volume for each MTP device. The third column shows the flow rate applied at the inlet, which was chosen so as to have a constant average velocity u_{av} in all designs ($u_{av} = Q/V$; Q: flow rate; V: volume) 123

Table A:2 | Inlet pressure. Inlet pressure obtained from fluidic simulations where the inlet flow rate is set as in **Table A:1** for the each MTP design. 125

List of Equations

(1.1) 38
(1.2) 38
(1.3) 38
(1.4) 38
(1.5).......... 39
(1.6) 39
(1.7) 39
(1.8) 39
(1.9) 40
(1.10) 40
(1.11) 40
(1.12) 40
(1.13) 41
(1.14) 41
(1.15) 41
(1.16) 41
(1.17) 42
(1.18) 42
(1.19) 42
(1.20) 43
(2.1) 56
(2.2) 60
(2.3) 60
(2.4) 61
(2.5) 69
(2.6) 71
(A.1) 122
(A.2) 122
(A.3) 122
(A.4) 129
(A.5) 129
(A.6) 129

(A.7) 129

(A.8) 129

List of Abbreviations

c_b	antibody bulk concentration
F_{ind}	induced fluorescence
k_{off}	dissociation constant
k_{on}	association constant
Ab	antibody
Ag	antigen
ALK	anaplastic lymphoma kinase
BIOP	Bioimaging and Optics Platform
CK	cytokeratin(s)
COC	cyclic olefin copolymer
CTL	negative control(s)
$\mathfrak{D}$	Damköhler’s number
D	diffusion coefficient
D	illumination dose
DAB	3,3'-diaminobenzidine
DAPI	4',6-diamidino-2-phenylindole
DCIS	ductal carcinoma *in situ*
DIW	deionized water
DOF	The depth of focus
DRIE	deep reactive ion etching
ELISA	microfluidic enzyme-linked immunoabsorbent assay
ER	estrogen receptor
FCS	fetal bovine serum
FEM	finite element modelling
FFPE	formalin-fixed paraffin-embedded
FISH	fluorescence in situ hybridization
FITC	fluorescein isothiocyanate
FL	fluorescence attenuator
FS	frozen section(s)
GDS	the graphic data system
GFP	green fluorescent protein
H&E	hematoxylin and eosin
HCF	Histology Core Facility
HER2	human epithermal growth factor receptor 2
HRP	horseradish peroxidase
HRP	horseradish peroxidase
IF	immunohistofluorescence
IgGs	immuno-globulins
IHC	immunohistochemistry

iPBLF	intermediate Parylene C bonding layer fluorescence
ISS	*in situ* sequencing
IVD	*in vitro* diagnostics
M	magnification
MEMS	microelectromechanical systems
MMIHC	microfluidic parallel-multiplexed immunohistochemistry platform
MTP	microfluidic tissue processor
MTS	microfluidic tumorectomy stainer
n	refractive index of air
NA	numerical aperture
ND	neutral density
N_{FISH}	*HER2* gene copy numbers
NGS	next generation sequencing
NSCLC	non-small cell lung cancer
PC	polycarbonate
PDMS	polydimethylsiloxane
PEG	polyethylene glycol
PET	polyethylene terephthalate
PMMA	polymethylmethacrylate
PR	progesterone receptor
PS	polystyrene
PSA	pressure sensitive adhesive tape
PVC	polyvinylchloride
Q	flow rate
RDS	reagent delivery system
RMPD	Rapid Micro Product Development
RMSE	root mean square error.
SVR	surface-to-volume ratio
TBS	tris buffered saline
T_g	glass transition temperature
TMA	tissue microarrays
TRITC	tetramethyl rhodamine isothiocyanate
u	flow velocity
vMFP	vertical microfluidic probe
Γ	antibody-antigen surface concentration
δ	depletion region
μTAS	micro total analysis system

Chapter 1 Introduction

The last 25 years have seen an explosive growth of the number of microfluidic-based devices used in academia. Starting in the early nineties with the publication of the micro total analysis system (μTAS) concept [1], key opinion leaders believe that the field of microfluidics is going through a Gartner's Hype Cycle (**Figure 1:1**) [2], consisting of five stages: technology trigger, peak of inflated expectations, trough of disillusionment, slope of enlightenment and plateau of productivity. The peak of inflated expectations took place at the end of the 1990s, when a few success stories were accompanied by a number of failures. The golden success story was the launch of the Agilent Technologies-Caliper Life Sciences Bioanalyzer. In the early 2000s, the field went through a phase of loss of credibility and investors abandoned the field for a while. At this timepoint, experts think that the field saw the trough of disillusionment. Even though the transfer of these technologies into the *in vitro* diagnostics (IVD) world has not been straightforward, we notice since 2010 that the valley has been overcome and see an activity that is running on the slope of enlightenment, with countless microfluidic-based devices reaching the IVD market [3]. How high the plateau of productivity will be is still unanswered. The microfluidics community has now learnt that microfluidics will not be used to merely miniaturize all the routine laboratory tests or to run through all application without major outcomes. Instead, it will serve as a tool to be used in combination with other technologies as an enabler to boost performance [4].

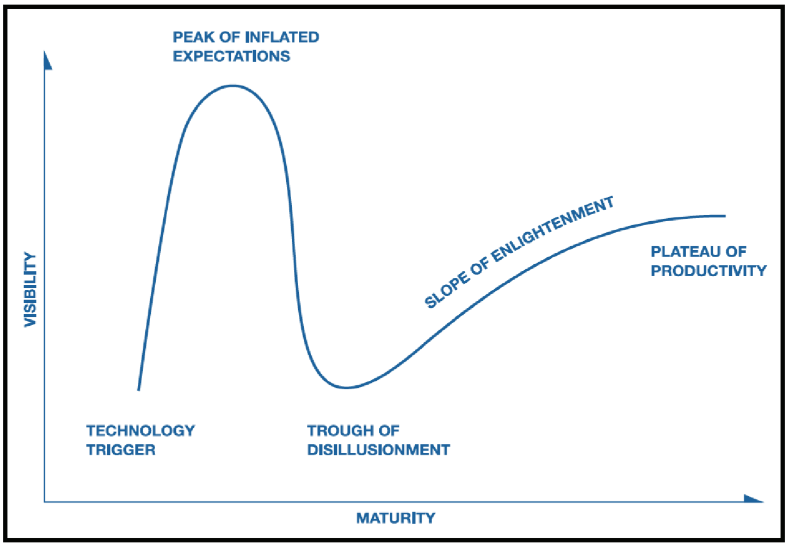

Figure 1:1 | Gartner Hype Cycle Model. Technology's life cycles can be modelled in five key phases. (1) Technology trigger: a breakthrough takes place which triggers stories in the media that set off publicity, often with no proof of commercial viability. (2) Peak of inflated expectations: a number of success stories emerge accompanied by numerous failures. Some companies enter in the field, many do not. (3) Trough of disillusionment: implementation failure discourages new commercial projects. Investment continues only on surviving products to increase their adoption in the market. (4) Slope of enlightenment: the benefits from the technology start to be widely understood, in combination with second and third-generation products offered by the technology provider. (5) Plateau of productivity: mainstream adoption begins and the criteria for viability are developed. Adapted from [2]. Copyright 2009, Gartner, Inc.

Classic macroscopic liquid handling systems, like petri dishes and culture bottles, have been used since more than a century. Moreover, microtiter plates have constituted a platform of common use since 1951. Numerous automation machines, consisting of pipetting robots, have been developed around these tools during the last decades and constitute today a « gold-standard » for sample and reagent processing in pharma and diagnostics [5]. Being able to provide the users with a great flexibility and programmability, these robots offer a potential solution to most applications that require automation, establishing a direct competition to microfluidic systems. Miniaturization of biochemical reaction platforms provides numerous inherent advantages arising from the scaling effects: reduction of assay times due to the reduced diffusion distances, increased efficiency and sensitivity as a consequence of high surface-to-volume ratio (SVR) and significant reduction in the reagents and samples consumption. However, for this miniaturized products to be successful, microfluidic diagnostic systems are also required to overcome some -or all- of the following challenges, depending on the final application: lower cost-per-test, higher throughput, portability/wearability, shorter time-to-answer, less laboratory space intake, as well as a viable consumable-based business model.

In this chapter, I will introduce the techniques and concepts that are at the basis of this thesis. I will first describe all the microfluidic chip fabrication methods that were used, as well as the challenges I met when designing for manufacturing. I will then describe the reactions that take place at the solid-liquid interface between tissue samples and solutions containing reagents. Subsequently, I will introduce the handling protocols of tumor tissue samples, commonly used by pathologists during a diagnosis process. I will continue with a short description of the state-of-the-art microfluidic devices developed in research laboratories with the scope of using microfluidics to stain tissue sections. Finally, I will describe the « Microfluidic Tissue Processor » (MTP), a microfluidic device described by Dr. Ciftlik *et al.*, which constituted the starting point for my research and the venture I co-founded.

1.1 Microfluidic chip fabrication: prototyping vs industrial manufacturing

A number of microfabrication techniques are available for prototyping of microfluidic chips, but these are not always suitable to be transferred to industrial manufacturing. Most of the early work in microfluidics has traditionally used silicon or glass micromachining for early proof-of-principle [6]–[8]. These techniques were developed for the semiconductor industry and were reused amongst the microfluidics community. However, silicon manufacturing costs are driven by the footprint of the devices, which in many applications is hard to scale down [9]. Yet, these fabrication techniques can be used to build the masters from which plastic chips are replicated [10].

Even though not the first in appearance, soft lithography using polydimethylsiloxane (PDMS) [11] became the most widely spread microfluidic chip fabrication technique among research laboratories, most probably due to its flexibility, low cost, and the capability to achieve submicron resolution. However, its elastomeric nature and permeability to gas made this fabrication method unsuitable for most of the applications in immunohistochemistry [12].

Polymer-based microfluidic chips have emerged in recent years as inexpensive and disposable alternatives to micromachined devices, suitable for both prototyping and mass production [13]. Several plastic microfabrication methods are now available, ranging from molding techniques to laser ablation, which turned the fabrication of polymer microchips into a competitive and versatile process. While silicon and glass will remain the material of choice for applications where harsh chemical and physical conditions are present, disposable microchips provide a variety of advantages, like easy functional integration and simple fabrication, allowing for the development of integrated microfluidic systems in an efficient and economical fashion [9].

During the initial phases of prototyping of our microfluidic chips, the choice of the microfabrication technique was determined by the availability of technology and equipment, cost, speed and fabrication capabilities (*i.e.* required feature size). Under these constrains, silicon was the preferred material for the initial microfabrication of our devices. Subsequently, a Parylene C-based bonding technique developed at the Laboratory of Microsystems was used to seal the microfluidic channels. The microfabrication process flow of our Si-based devices is shown in section 1.1.1 below. Moreover, we found that the autofluorescence of Parylene C could be used, as a tool to perform on-chip data storage and is described in chapter 2.

Subsequently, several microfabrication techniques and materials were explored to ultimately achieve microfluidic chip designs that are not only functional, but also scalable and interesting from the industrial manufacturing viewpoint. The first step towards scalability involved the prototyping of our microfluidic designs using polymers. Three different materials were employed: Polycarbonate (PC), Cyclic Olefin Copolymer (COC) and GR-1®, a UV-curable methacrylate-based resin used for stereolithography. The fabrication technique used with each polymer was selected in accordance to the supplier involved in the development. We identified three main fabrication steps, common to all methods: structuring of the channels, drilling of through-holes (or vias) and sealing of the channels. In **Table 1:1** we list the techniques used in each step, as well as whether we hired subcontractors or carried on the fabrication ourselves within EPFL's facilities.

Focusing on the future scalability of the manufacturing process, efforts were also made to adapt the microfluidic design in order to comply to the constrains of injection molding, a mass-production fabrication technique (see further) that would enable industrially feasible polymer chips.

Table 1:1 | List of the methods and materials used for the fabrication of our microfluidic devices. The methods used to fabricate the channels, drill the through-holes and seal the channels are described for all the chips types and classified by the material of choice. Si/Pyrex microfluidic chips were fabricated in the EPFL's cleanroom facilities, while PC, COC and GR-1 UV-sensitive resin were externally fabricated by contract manufacturers using the microfluidic designs we provided. RMPD: Rapid Micro Product Development. PSA: Pressure-sensitive adhesive tape.

Process\Material	*Si/Pyrex*	*PC*	*COC*	*GR-1*
Microchannels structuring	Silicon micromachining	Milling	Hot embossing	RMPD
Through-hole drilling	Silicon micromachining	Milling	Milling	RMPD
Microchannels sealing	Parylene C bonding	Laser bonding	PSA	PSA
Subcontracted	No	Yes	Yes	Yes

1.1.1 Silicon-based devices

Microfabrication on silicon wafers is a combination of technologies used for integrated circuits, also known as « semiconductor device fabrication». In the last two decades, microelectromechanical systems (MEMS), microfluidics, lab-on-a-chips, optical MEMS, RF MEMS, Power MEMS and BioMEMS have re-used, adapted and extended the existing microfabrication methods [5]. The fabrication of a microdevice requires the sequential execution of several processes, often done repeatedly. Typically, these processes consist in depositing a film, patterning it with the desire micro features, and removing (or etching) certain areas of the film. The following silicon-based microfabrication techniques, illustrated in **Figure 1:2**, were used in the fabrication of the microfluidic chips used in chapter 2, chapter 4 and chapter 5:

Photolithography is a process that uses light to transfer a pattern through a mask onto a photo-sensitive resin. The solubility of this photoresist to a specific solvent is modified by its exposure to UV light, which enables the selective coverage of the substrate. Subsequent microfabrication, such as etching or material deposition, can be realized on areas where the photoresist is removed. Photolithography is widely used in microfabrication due to its capability to create extremely small patterns, which can reach a few nanometers in size. The use of the photomask to perform the exposure of the resist allows the patterning of entire wafers, making the technique cost-effective. Possible constraints are that extremely flat substrate surfaces and clean working environments are required.

Etching is used to chemically remove layers from the surface of a wafer during fabrication. Selected areas of the wafer are protected from the etchant by a "masking" material which resists to etching. This material can be simply a photoresist or, in situations where a more resistant mask is required, silicon nitride or silicon oxide can be employed. The etching process can be performed using liquid reagents (wet etch) or a plasma (dry etch). The latter can be configured in a way to allow for anisotropic etching of the substrate, thus obtaining, for example, microfluidic channels with walls that are almost vertical. This process, called deep reactive ion etching (DRIE) was repeatedly used for the microfabrication of our silicon-based devices [14], [15].

Parylene C coating is a physical vapor deposition technique that uses Parylene C, the trade name of a variety of poly(p-xylylene) polymer that is used as a moisture and dielectric barrier. In this work, Parylene C was used to generate an intermediate bonding layer (see further). The deposited Parylene C was also patterned using the techniques described above.

Parylene C-based bonding is a bonding technique developed at the laboratory of Microsystems to seal microfluidic channels [16], [17]. Subsequently, the autofluorescence modification capabilities of this material was studied under bonding conditions and are reported in chapter 2. **Figure 1:2** shows a typical process flow used in EPFL cleanroom facilities to build the microfluidic chips used in this thesis.

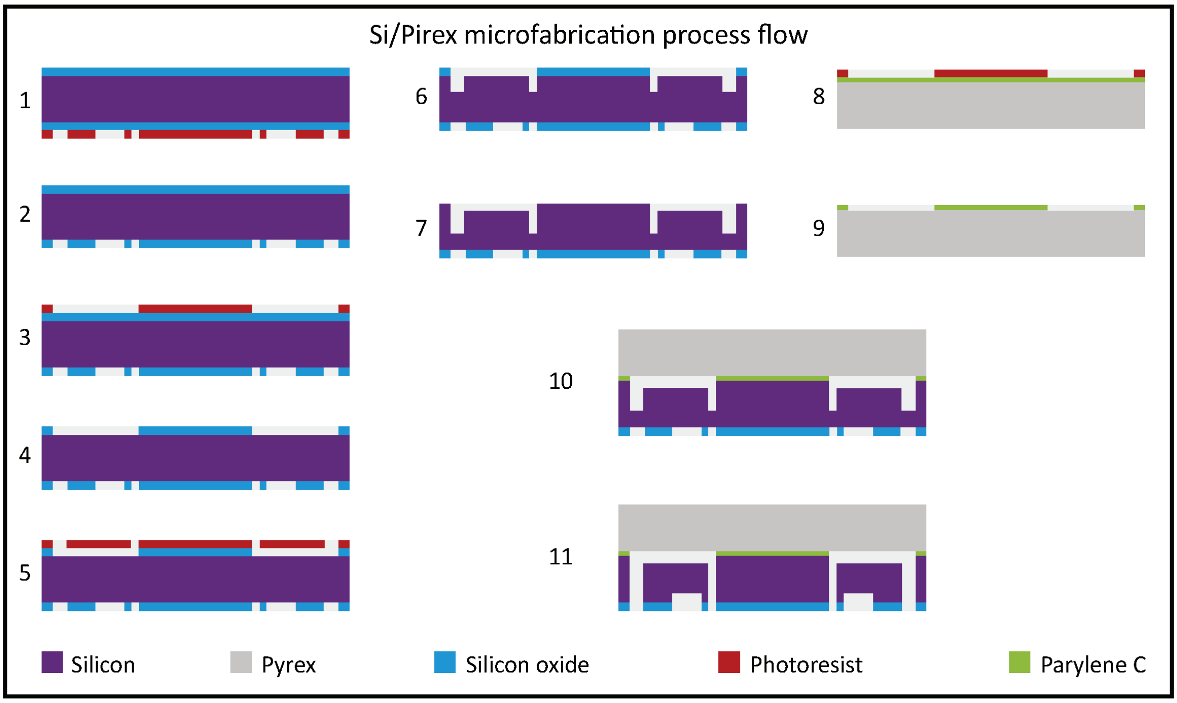

Figure 1:2 | Si/Pyrex microfabrication process flow. A bonding technique using Parylene C as an intermediate layer was used [16], [17]. Silicon wafers with 2 µm wet oxide on both sides were chosen. The process started by using photolithography to pattern the backside silicon oxide (1) to define a hard mask (2). The same was subsequently done to the front side of the wafer (3 and 4). Once the hard masks were patterned, a third lithographic step (5) was used to etch around half the depth of the through-holes from the front side (6). The hard mask was then removed by plasma etching and the wafer was thoroughly cleaned (7). In parallel, Parylene C was coated on a Pyrex wafer and a photolithography step (8) was done so as to etch the Parylene on the areas corresponding to microfluidic channels (9). Both wafers were bonded together using a temperature of 280 °C and pressure of 100 kPa (10). Finally, the through-holes were opened by etching the silicon from the backside (11).

1.1.2 Hot embossing

Hot embossing is a technique to pattern thermoplastic materials, commonly provided in the form of flat sheets, against a master (stamp) using pressure and heat. Thermoplastic materials can be reshaped by heating to the glass transition temperature (T_g). Examples of thermoplastics used in hot embossing include polymethylmethacrylate (PMMA), PC, COC, polystyrene (PS), polyvinylchloride (PVC), and polyethylene terephthalate (PET) [9]. The masters are typically made of silicon or metal using high precision milling or a LIGA-like process (a German acronym for lithography, electroplating and molding). The microfluidic chips used in chapter 3 and chapter 5 were fabricated using a combination of hot embossing for the channels and milling for defining the through-holes (see further). The stamp fabrication was performed in two steps: a primary master realized in PMMA and a secondary master obtained from the PDMS casting of the latter [18]. A schematic of the process flow is represented in **Figure 1:3a**.

1.1.3 Micromilling

Micromilling makes use of cutting tools to remove bulk material from a starting stock piece, and create in this manner microscale features. A milling system consists of a worktable to ensure the correct positioning of the workpiece, a milling tool to cut out the material, and a spindle that secures and rotates the cutting tool [19]. Micromilling for prototyping of microfluidic chips has traditionally been underused because of the presumed high start-up costs and achieved resolution, the large lab space intake and the operating expertise required to handle the tools. However, recent technological advances have significantly tackled these drawbacks, making micromilling a competitive option in microfluidics, at least when it comes to prototyping. Micromilling of the trough-holes and the back-side notch of a microfluidic chip are represented in points (5) and (6) of **Figure 1:3b**, respectively. Finally, channels are typically sealed using a sheet made of polymer that is similar to the one used for the main substrate. In our work, we made use of a pressure sensitive adhesive tape (PSA), which realeases glue that is microencapsulated in a COC sheet when pressure is applied to it, asuring the sealing of the microfluidic channels.

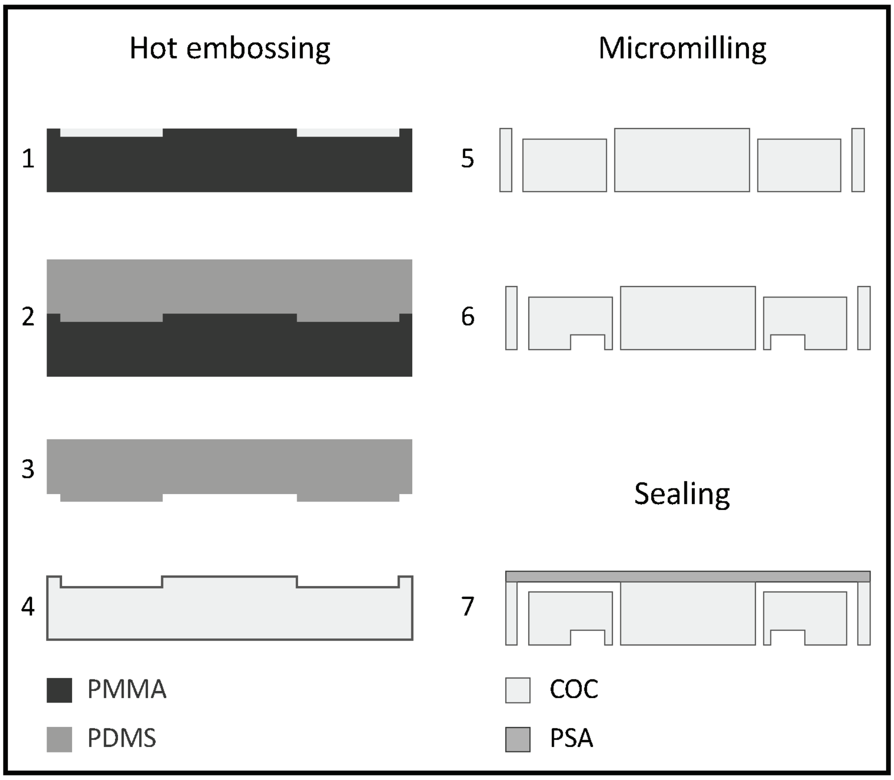

Figure 1:3 | COC chips microfabrication process flow. (a) Hot embossing: (1) a first master is fabricated using precision tools or Si microfabrication; (2) a second master (stamp) is casted using PDMS from the first master; (3) the stamp is then used to hot emboss the front side of the microfluidic chips made of COC. **(b)** Miromilling: as a post-processing step, (5) the through-holes are micromilled and (6) the backside is patterned. **(c)** Sealing: (7) the microfluidic channels on the front side are finally sealed using PSA.

1.1.4 Stereolithography

Stereolithography is an additive fabrication method that uses a laser or other light source to cure photosensitive materials, typically a resin. It is classified as a 3D printing method and has gained significant acceptance for its utility in microfluidic applications and can fill the gap when low-volume microfluidic devices do not justify the investment in injection molding tools [20], [21]. It is worth pointing out that, even though both milling and stereolithography are direct fabrication methods, milling is a subtractive process, while stereolithopgrphy is additive process [19]. In this work, a subtype of stereolithography that can reach micrometric resolutions, called Rapid Micro Product Development (RMPD), was employed in chapter 3 to fabricate the microfluidic chips used for the selection of the reagents to deliver. This technology is commercialized by microTEC Gesellschaft für Mikrotechnologie GmbH, Germany.

1.1.5 Injection molding

Injection molding is a process widely used in the plastic industry to fabricate objects of any shape and dimensions [22]. It is a long established technique, though the tooling costs are extremely high, making prototyping and low-volume production unviable [23]. Pellets of thermoplastic material, (e.g., PC, PMMA, COC) are melted and injected into a mold cavity at high pressure. The cavity, often made of steel, aluminum or brass, contains the template for the features intended to be patterned on the plastic. The contact of the molten polymer with the mold determines the precision of the replication. During the process development, several parameters, such as operating temperature, pressure and cooling time need to be optimized for each production run. The quality of the mold will then determine the long-term quality of the replicas [9]. Due to the complexity of the injection equipment and the fabrication of the master, injection molding is most commonly used for the industrialization of microfluidic devices, rather than for research. When compared to other fabrication techniques, injection molding offers the highest throughput and the lowest cost-per-unit for high-volume production. During this work, microfluidic chips have not been injection molded, mainly due to the extremely high cost of tooling. Nevertheless, several steps were taken to transfer the existing prototypes to injection molding.

A review carried on by *Guckenberg et al.* compares micromilling with other fabrication techniques commonly used in microfluidics [19]. **Figure 1:4** shows a summary of this comparison both from the technical **(Figure 1:4a**) and economic aspects (**Figure 1:4b**). The latter highlights that only injection molding and hot embossing can be viable for mass production.

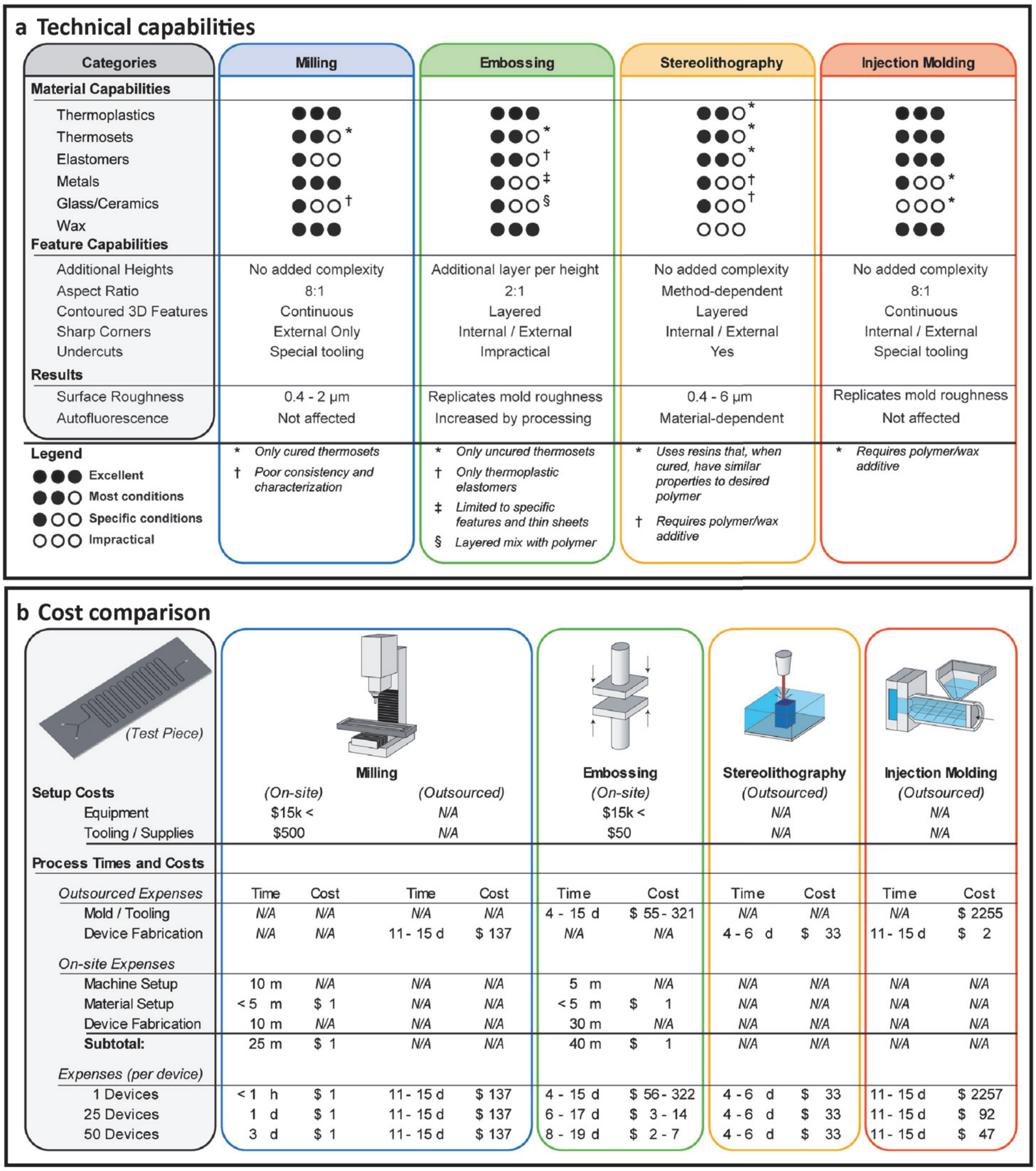

a Technical capabilities

Categories	Milling	Embossing	Stereolithography	Injection Molding
Material Capabilities				
Thermoplastics	●●●	●●●	●●○*	●●●
Thermosets	●●○*	●●○*	●●○*	●●●
Elastomers	●○○	●●○†	●●○*	●●●
Metals	●●●	●○○‡	●○○†	●○○*
Glass/Ceramics	●○○†	●○○§	●○○†	○○○*
Wax	●●●	●●●	○○○	●●●
Feature Capabilities				
Additional Heights	No added complexity	Additional layer per height	No added complexity	No added complexity
Aspect Ratio	8:1	2:1	Method-dependent	8:1
Contoured 3D Features	Continuous	Layered	Layered	Continuous
Sharp Corners	External Only	Internal / External	Internal / External	Internal / External
Undercuts	Special tooling	Impractical	Yes	Special tooling
Results				
Surface Roughness	0.4 - 2 µm	Replicates mold roughness	0.4 - 6 µm	Replicates mold roughness
Autofluorescence	Not affected	Increased by processing	Material-dependent	Not affected
Legend ●●● Excellent ●●○ Most conditions ●○○ Specific conditions ○○○ Impractical	* *Only cured thermosets* † *Poor consistency and characterization*	* *Only uncured thermosets* † *Only thermoplastic elastomers* ‡ *Limited to specific features and thin sheets* § *Layered mix with polymer*	* *Uses resins that, when cured, have similar properties to desired polymer* † *Requires polymer/wax additive*	* *Requires polymer/wax additive*

b Cost comparison

	Milling				Embossing		Stereolithography		Injection Molding	
Setup Costs	*(On-site)*		*(Outsourced)*		*(On-site)*		*(Outsourced)*		*(Outsourced)*	
Equipment	$15k <		*N/A*		$15k <		*N/A*		*N/A*	
Tooling / Supplies	$500		*N/A*		$50		*N/A*		*N/A*	
Process Times and Costs										
Outsourced Expenses	Time	Cost	Time	Cost	Time	Cost	Time	Cost	Time	Cost
Mold / Tooling	*N/A*	*N/A*	*N/A*	*N/A*	4 - 15 d	$ 55 - 321	*N/A*	*N/A*	*N/A*	$ 2255
Device Fabrication	*N/A*	*N/A*	11 - 15 d	$ 137	*N/A*	*N/A*	4 - 6 d	$ 33	11 - 15 d	$ 2
On-site Expenses										
Machine Setup	10 m	*N/A*	*N/A*	*N/A*	5 m	*N/A*	*N/A*	*N/A*	*N/A*	*N/A*
Material Setup	< 5 m	$ 1	*N/A*	*N/A*	< 5 m	$ 1	*N/A*	*N/A*	*N/A*	*N/A*
Device Fabrication	10 m	*N/A*	*N/A*	*N/A*	30 m	*N/A*	*N/A*	*N/A*	*N/A*	*N/A*
Subtotal:	25 m	$ 1	*N/A*	*N/A*	40 m	$ 1	*N/A*	*N/A*	*N/A*	*N/A*
Expenses (per device)										
1 Devices	< 1 h	$ 1	11 - 15 d	$ 137	4 - 15 d	$ 56 - 322	4 - 6 d	$ 33	11 - 15 d	$ 2257
25 Devices	1 d	$ 1	11 - 15 d	$ 137	6 - 17 d	$ 3 - 14	4 - 6 d	$ 33	11 - 15 d	$ 92
50 Devices	3 d	$ 1	11 - 15 d	$ 137	8 - 19 d	$ 2 - 7	4 - 6 d	$ 33	11 - 15 d	$ 47

Figure 1:4 | Comparison between milling, embossing, stereolithography and injection molding as microfabrication methods for plastics. (a) Technical capabilities: material compatibility, feature capability and quality of the results. **(b)** Cost comparison: setup costs and process time and cost. This figure was adapted from [19].

1.2 Microfluidic solid-liquid interface reactions: theoretical considerations

Microfluidic devices have proven a number of advantages originating from two basic characteristics of miniaturized biochemical reaction platforms: increased SVR and reduced diffusion distances. Countless biomedical applications have shown the benefit of increasing the SVR, the most relevant being those in which the immobilization of a target molecule on a surface is required. Examples of these applications are immunoassays [24]–[28], protein microarrays [29], microfluidic enzyme-linked immunoabsorbent assay (ELISA)

[30]–[32], DNA hybridization assays [33], [34] and DNA arrays [35]. Even though fundamentally different, all these applications share the existence of two reagents with certain affinity for each other: the target and the probe. Either the target or the probe is immobilized on a solid surface, while the complementary reagent is brought into contact dissolved in a carrier fluid. The aforementioned affinity results in a reaction between target and probe, which is then measured (or detected) according to the detection technology used in the assay. The role of the increased SVR is simply the maximization of the solid-liquid interface area, which increases the encounter possibilities between target molecules and probes and, in turn, results in higher efficiency and sensitivity of microfluidic assays [36]. **Figure 1:5a** shows a schematic of a sandwich ELISA, where capture antibodies (probes) are immobilized on a well plate, and the antigens (targets) are available in solution. The detection system is finally provided by exposing the surface to a substrate solution. On the contrary, in direct-capture ELISA tests, as shown in **Figure 1:5b**, antigens are immobilized on the plate and their recognizing antibodies are available in solution. Analogously, in immunohistochemical assays, tissue sections (instead of molecules) are immobilized on glass slides (instead of well plates). This method is described in section 1.3.

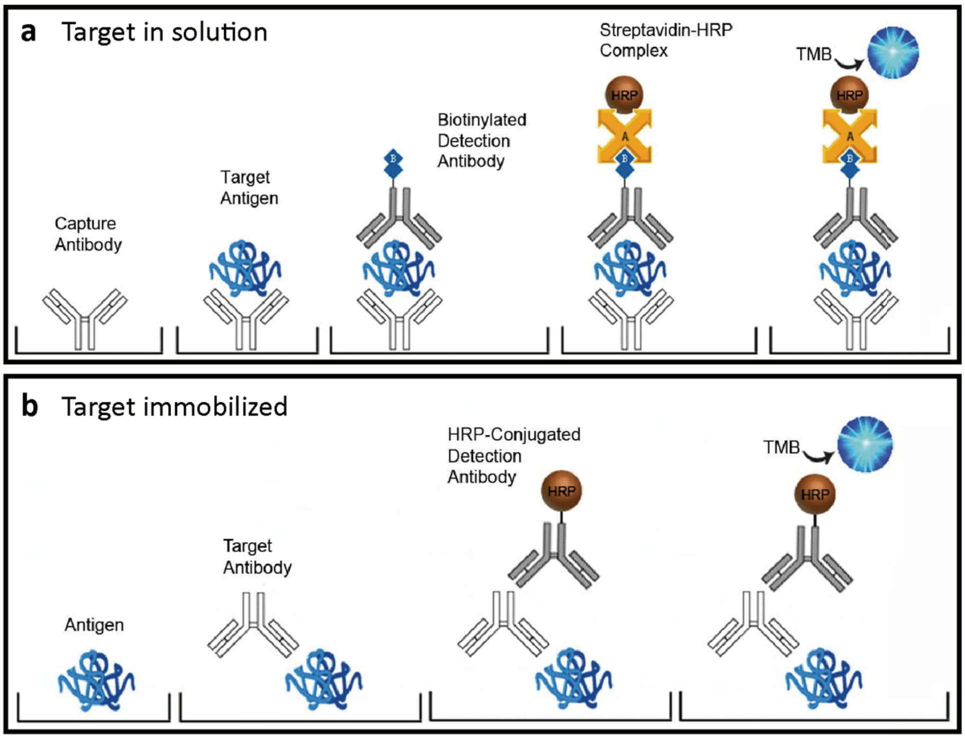

Figure 1:5 | ELISA tests. (a) In sandwich ELISAs, capture antibodies are immobilized on the surface of a well plate. Subsequently, antigens are captured from solution. Finally, an enzyme-based system can be used to generate an amplified fluorescent or colorimetric signal. **(b)** In a direct-capture ELISA test, antigens are immobilized on the surface of well plates. Recognising antibodies are available in solution. Images taken from www.lsbio.com.

The second characteristic of miniaturized assays is the reduction of the diffusion distances. According to Fick's law of diffusion, a quadratic reduction of the diffusion time of the molecules in solution is achieved by scaling down the diffusion distance [37]. In this manuscript, I will revisit some of the main concepts, starting from the most simplified models to finally discuss a model that reflects the microfluidic setup mostly used during my work.

1.2.1 Antibody-antigen binding at constant bulk concentrations: Langmuir isotherms

The specific recognition between an antibody (Ab) and an antigen (Ag) is widely exploited both in research and diagnostics to either detect the presence or measure the concentration of a certain analyte. In most immunoassays, the recognition event occurs between the Ag –the target– in solution and the Ab –the probe– adsorbed on a solid support, which can be a microtiter plate, a microbead or a microarray chip. In our work, we are interested in a configuration that is commonly used in immunohistochemistry (IHC), where the Ab is dissolved in solution and the Ag is a protein that is present immobilized on a tissue section, located on a glass slide (see **Figure 1:11** in section 1.3). This technical difference with respect to other immunoassays adds a level of complexity to the mechanisms behind the Ag-Ab binding, mainly due to the variety of molecules normally present on tissue samples, which can interact non specifically with the Ab. An additional level of complexity is added when considering that Ags may be located at inner layers of the tissue. Nevertheless, for the sake of simplicity, we will model our tissue sections as a uniformly distributed set of Ags immobilized on a glass slide.

In order to understand the binding mechanisms, we will start by the simplest case, in which the recognition process is slow compared to the transport of the Ab at the surface of the slide, and the volume of the solution containing the Ab is sufficiently large (and continuously stirred) to consider the reagent concentration as constant. To characterize the binding process, we define a relation between the Ab-Ag complex surface concentration $\mathit{\Gamma}$ and the Ab bulk concentration c_b. This relation is called the Langmuir isotherm [38] and is based on the following hypotheses:

- The surface is defined by a number of absorption sites $\mathit{\Gamma}_{max}$,
- Equilibrium is reached between absorbed and bulk species,
- There is no lateral interaction between the absorbed target species,

The reaction can be written as

$$Ag + Ab \leftrightarrow AbAg \tag{1.1}$$

For which the rates of absorption and desorption can be respectively written as

$$\frac{d[AbAg]}{dt} = k_{on}[Ag][Ab] \ ; \ -\frac{d[AbAg]}{dt} = k_{off}[AbAg] \tag{1.2}$$

The constants k_{on} and k_{off} are also known as association and dissociation constant, respectively, when they characterize the Ab-Ag binding kinetics. At equilibrium, the rate of absorption is equal to the rate of desorption. This can be written as [39]:

$$K = \frac{k_{on}}{k_{off}} = \frac{[AbAg]}{[Ag][Ab]} = \frac{\Gamma}{(\Gamma_{max} - \Gamma)c_b} \tag{1.3}$$

At equilibrium, the surface coverage is given by

$$\Gamma_{eq} = \Gamma_{max}\frac{\mathrm{K}c_b}{1 + \mathrm{K}c_b} = \Gamma_{max}\frac{\psi}{1 + \psi} \tag{1.4}$$

When the dimensionless parameter $\psi \equiv Kc_b \ll 1$, the binding takes place from a dilute solution and the surface coverage is small and proportional to the bulk concentration c_b. This regime is also known as linearized Langmuir isotherm. On the contrary, when $\psi \gg 1$ the coverage tends to saturate all the available sites and Γ becomes Γ_{max}. The kinetics of the binding reaction can be expressed as the difference between the absorption and the desorption processes, giving

$$\frac{\mathrm{d}\Gamma(\mathrm{t})}{\mathrm{dt}} = k_{on}c_b(\Gamma_{max} - \Gamma(\mathrm{t})) - k_{off}\Gamma(\mathrm{t}) \tag{1.5}$$

The solution of this equation is

$$\Gamma(\mathrm{t}) = \Gamma_{max}\frac{\psi}{1+\psi}[1 - e^{-t/\tau}] \tag{1.6}$$

where τ is the time constant for the adsorption defined as

$$\tau = \frac{1}{k_{on}c_b + k_{off}} = \frac{1}{(1+\psi)k_{off}} \tag{1.7}$$

In order to extract the k_{on} and k_{off} values for each Ab, one can perform a binding experiment where a solution containing the Ab is flushed at $t = 0$. Once the binding density reaches a plateau, a buffer solution is flushed at $t = t_0$. For $0 < t < t_0$ Eq. (1.6) applies, while for $t > t_0$ we have

$$\Gamma(\mathrm{t}) = \Gamma_{max}\frac{\psi}{1+\psi}[1 - e^{-t_0/\tau}]e^{-k_{off}(t-t_0)} \tag{1.8}$$

A fitting algorithm is then applied from the curves using Eq. (1.6) and (1.8), thus extracting the values for k_{on} and k_{off}. **Figure 1:6** shows a schematic of the curve obtained during antibody affinity measurement experiments.

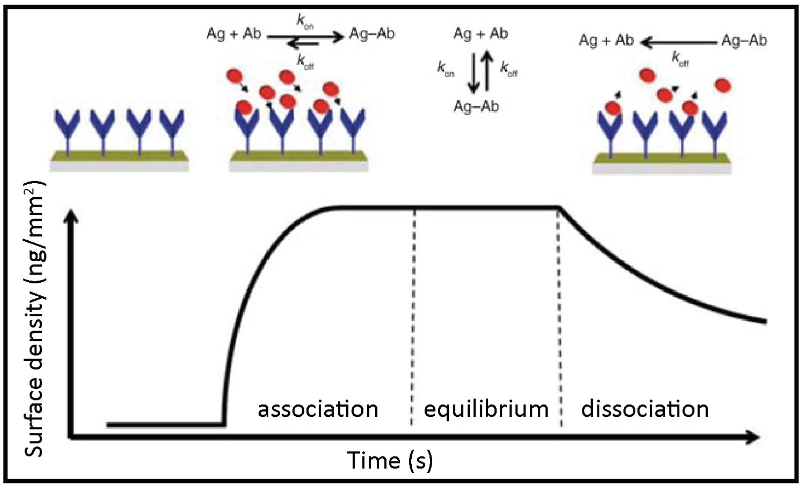

Figure 1:6 | Antibody binding kinetics. Schematic of the binding curve used to extract the values of the association constant k_{on} and the dissociation constant k_{off}. A solution containing antibodies is flushed on a surface where the corresponding antigens were priorly immobilized. The association curve is observed. Once the equilibrium is reached,

an antibody-free solution is flushed on the same surface and the dissociation curve is observed. A fitting algorithm using Eq. (1.6) and Eq. (1.8) is used to determine k_{on} and k_{off}. Figure adapted from [40].

1.2.2 Adsorption on a semi-infinite planar surface

When the rate of adsorption is fast compared to the time scale of diffusion, the kinetics of the Ab-Ag binding may depend on the rate at which Abs reach the surface. To evaluate the regime in which we operate, it is useful to know the diffusion time $t_{diff} = \delta^2/D$, where δ is the thickness of the diffusion layer (or depletion region) and D, the diffusion coefficient of the Ab.

The immunohistochemical assays that are described in this work take place in a reaction chamber where the height is in the microscale (100 μm), while the lateral dimensions of the surface where the Ags are located fall in the mm scale (17x17 mm^2). To understand the reaction kinetics at the surface, we will use a two-layer model, where we define a volumetric Ab concentration c_s in the vicinity of the surface that differs from the bulk concentration c_b. An Ab diffusion flux is then driven by the concentration gradient formed at this interface, which can be simplified as $\nabla c \approx (c_s - c_b)/\delta$.

Rewriting Eq. (1.5) in terms of the Ab-Ag surface concentration $\Gamma(\mathrm{t})$ and the Ab volumetric concentration at the surface c_s we obtain

$$\frac{\mathrm{d}\Gamma(\mathrm{t})}{\mathrm{dt}} = k_{on} c_s (\Gamma_{max} - \Gamma(\mathrm{t})) - k_{off}\Gamma(\mathrm{t}) \tag{1.9}$$

According to Fick’s first law of diffusion, the variation of the Ab concentration at the surface is equal to the flux of arrival and, in turn, to the variation of the Ab-Ag concentration

$$\frac{\mathrm{d}\Gamma(\mathrm{t})}{\mathrm{dt}} = D\left(\frac{\partial c_s(x,t)}{\partial x}\right)_{x=0} = -J(t) \tag{1.10}$$

Even though these equations cannot be solved analytically in the general case, we can find specific solutions for particular conditions. An example of interest for this work is the initial condition in which almost all the Ags are available ($\Gamma \ll \Gamma_{max}$). Under these conditions, we can assume $\Gamma(0) = 0$. Additionally, we can consider that the diffusion layer δ is in steady-state, giving $-J = D(c_s - c_b)/\delta$. Combining these two assumptions, we can simplify Eq. (1.9) and Eq. (1.10) and calculate the Ab volumetric concentration at the surface c_s

$$c_s = \frac{D c_b}{k_{on}\Gamma_{max}\delta + D} \tag{1.11}$$

Therefore, the time change of the Ab-Ag surface concentration can be expressed as

$$\frac{\mathrm{d}\Gamma(\mathrm{t})}{\mathrm{dt}} = \frac{k_{on} c_b \Gamma_{max}}{1 + \frac{k_{on}\Gamma_{max}\delta}{D}} \tag{1.12}$$

Meaning that Γ is a linear function of the time.

$$\Gamma(\mathrm{t}) = \left(\frac{k_{on} c_b \Gamma_{max}}{1 + \mathfrak{D}}\right) t \tag{1.13}$$

The dimensionless number $\mathfrak{D} = k_{on}\Gamma_{max}\delta/D$ is called Damköhler number and represents the ratio between the characteristic adsorption rate and the characteristic diffusion rate. When $\mathfrak{D}$ is large, diffusion is slow compared to adsorption, making diffusion the dominant mechanism. On the other hand, when $\mathfrak{D}$ is small, the diffusion is not limiting the reaction. In other words, for $\mathfrak{D} \ll 1$, we obtain

$$\Gamma(\mathrm{t}) = k_{on} c_b \Gamma_{max} t \tag{1.14}$$

While for $\mathfrak{D} \gg 1$ we obtain a pure diffusion-controlled reaction

$$\Gamma(\mathrm{t}) = \frac{D c_b}{\delta} t \tag{1.15}$$

We can now consider that the diffusion layer δ scales as $\delta = \sqrt{2Dt}$, according to Einstein's equation. Replacing in Eq. (1.15) we obtain

$$\Gamma(\mathrm{t}) = \frac{c_b}{2}\sqrt{2Dt} \tag{1.16}$$

Independently on the importance of the diffusion rate with respect to the reaction rate, we notice from Eq. (1.13) that, at the beginning of the reaction, when the diffusion layer has not yet formed ($\mathfrak{D} \ll 1$), all the regimes turn to be reaction-limited, resulting in a linear dependence of the Ab-Ag surface concentration with time.

In microfluidic systems, the SVR can be very large and the bulk concentration may decrease when the antibodies bind to the targets. The time it takes for this diffusion layer to form and how this depletion will influence the reaction is characteristic of how efficiently the probe binds to the target (k_{on}), how fast it diffuses in solution (D) and how many target sites are available on the tissue surface (Γ_{max}).

1.2.3 Adsorption from a flow on a surface

Before the incubation of the probe molecules is done, we must deliver the reagents in the chamber. While the reagents are being delivered, it is impossible to neglect that the reaction is already starting to take place. Depending on the characteristics of the probe molecules and the flow used, the results can be significantly different. Squires *et al.* have developed a general model that considers a microfluidic channel with a sensing element under flow conditions, as shown in **Figure 1:7** [36]. The model is based on a microchannel with a height H and a width W_c. The sensing layer located on the bottom of the channel has a length L and a width W_s. A solution with a bulk concentration c_b is flown at a flow rate Q, which results in a velocity $u(z)$ that depends on the height parameter z and gives an average velocity $u_{av} = Q/W_cH$.

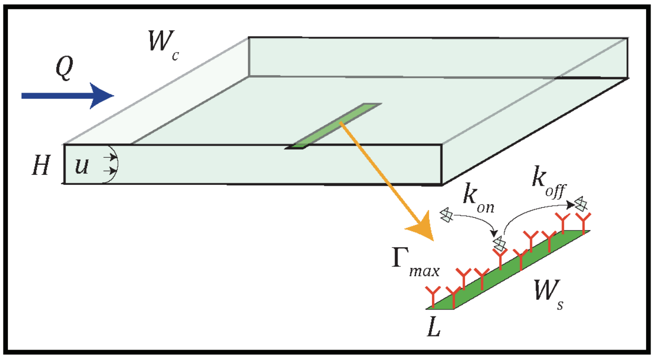

Figure 1:7 | Model system studied. A solution with a bulk concentration c_b is flushed at flow rate Q and velocity profile $u(z)$ through a microfluidic channel of height H and width W_c. The sensing element has a length L and a width W_s, and is functionalized with Γ_{max} receptors per unit area. The association and dissociation constant of the Ab-Ag reaction are given by k_{on} and k_{off}, respectively. The model and figure are adapted from [36].

Diffusion always dominates close to the sensor and advection wins far away. The ratio between the characteristic advection rate and the characteristic diffusion rate is called Péclet number and is defined as $Pe_H = Hu/D$. Notice that we are interested in assessing how fast Abs will diffuse vertically towards the tissue surface, as opposed to how fast the flow will carry them away, when we deliver and wash the reagent chamber. Recall that the purely diffusive depletion region grows into the channel as $\delta = \sqrt{2Dt}$. Under certain flow conditions, δ is eventually stabilized as a steady depletion layer δ_S.

Clearly, in order to focus our experiments on the incubation steps and reduce to the minimum the reaction happening at the dispense of the reagents, we are interested in minimizing δ_S so that $\Gamma(0)$ is as low as possible, where $t = 0$ represents the time in which the incubation starts. But how thick is δ_S at steady conditions? And how long does it take for it to stabilize? According to the model developed by Squires *et al.*, we need to consider the probes in solution that do not « see » the full parabolic profile in the reaction chamber, but only the linear shear flow given by the parabolic profile [36]:

$$u(z) = \frac{6Q}{W_c H^3} z(H - z) \tag{1.17}$$

Considering $\delta_S \ll H$, then we can rewrite Eq. (1.17) as

$$u(z) = \frac{6Q}{W_c H^2} z \tag{1.18}$$

The time τ_C that it takes for δ to reach the steady state δ_S is then calculated as the limit in which the time of flight of molecules above the tissue and the vertical diffusion time are equal [36].

$$\tau_C = \frac{L}{u_{z=\delta_S}} = \frac{\delta_S^2}{D} \tag{1.19}$$

When solving for δ_S, we obtain

$$\delta_s = \left(\frac{DL}{\frac{6Q}{W_c H^2}}\right)^{1/3} = \left(\frac{DLH}{6u_{av}}\right)^{1/3} = \left(\frac{LH^2}{6Pe_H}\right)^{1/3} \tag{1.20}$$

In **Figure 1:8**, several diffusion layer regimes are shown, according to the values of Pe_H and the ratio $\lambda = L/H$ between the the length of the active area where Ags are present and the height of the channel. In region (ii) from plot **Figure 1:8a**, where both L/H and Pe_H are high, the depletion zone is thin compared to both the length L of the active surface and the channel height H. Several regimes are described in Squires's model, while we consider those shown in **Figure 1:8b**, **c** and **d**, the steady state conditions during dispense of reagents that my be relevant during the course of our experiment.

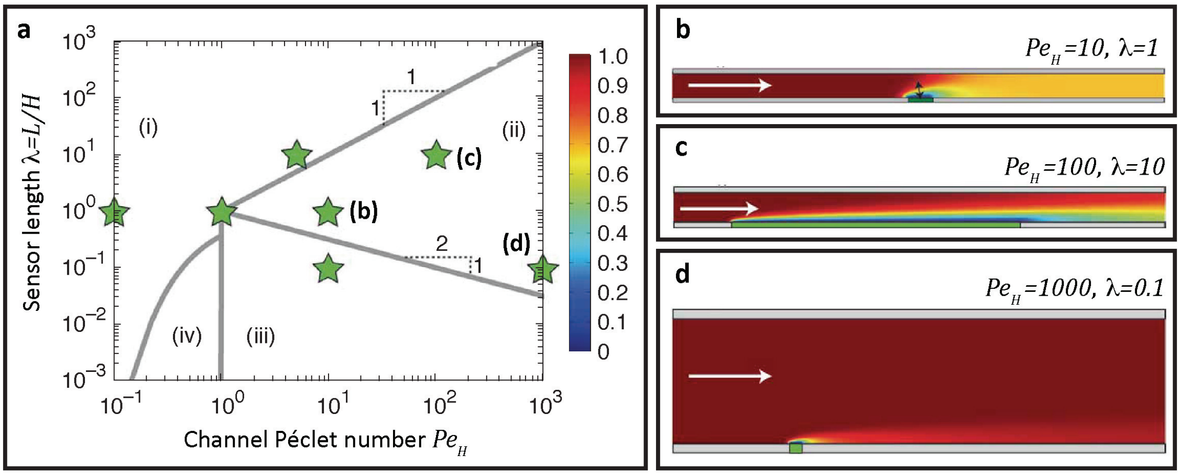

Figure 1:8 | Mass transport at steady-state conditions. Antibodies are flushed in the microfluidic channel described above. Different steady-state conditions are observed by varying the parameters $\lambda = L/H$ and Pe_H, characteristic of the channel geometry and the flow rate *Q* at which the antibodies are flushed. **(a)** Phase diagram of the model described by Squires *et al.* In phase (ii) a depletion region that is thin compared to the channel height is formed. **(b)**, **(c)** and **(d)** COMSOL simulation results for combinations of λ and Pe_H that fall within the phase (ii) regime. The data and plots were adapted from [36].

1.3 Tissue staining methods

This thesis is mostly focused on research related to the market segment of «anatomic pathology». Apart from a few exceptions in research groups, microfluidic devices have not been introduced commercially for the immunohistochemical staining of tissue sections so far. In this field, great level of automation has been accomplished by the market leaders to increase the number of histopathological samples that can be processed in a working day. **Figure 1:9** shows a picture of the three leading tissue staining automats in the market.

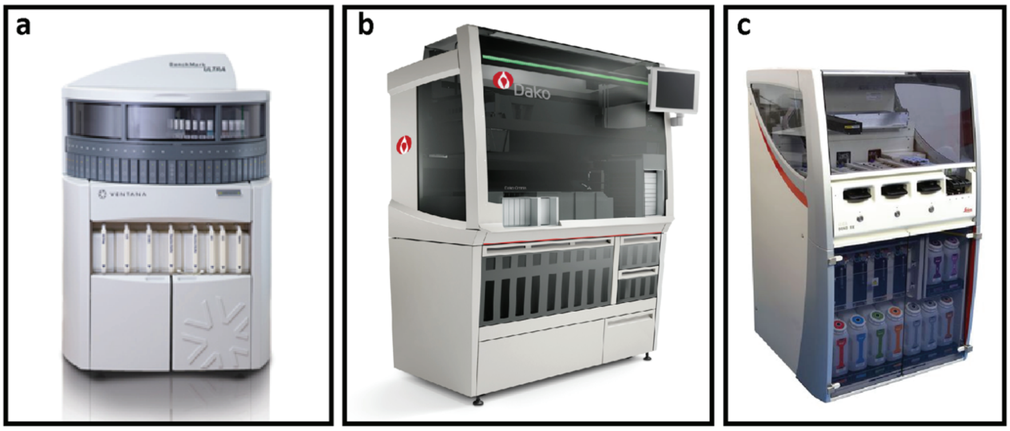

Figure 1:9 | Leading immunohistochemistry automats. The most adopted automated immunohistochemistry devices are offered by **(a)** Ventana, a subsidiary from Roche, under the name of Benchmark ULTRA (taken from www.ventana.com), **(b)** DAKO, under the name of Omnis (taken from www.dako.com) and **(c)** Leica Biosystems, under the name of BOND-III (taken from www.leicabiosystems.com). These machines are specialized in liquid handling automation. The providers of these instruments are in essence reagent manufacturers and make use of these companion diagnostics devices to commercialize their immunohistochemical reagents.

Table 1:2 lists some technical specifications commonly used as selling points, such as the numbers of slides that can be loaded at the same time and the amount of different reagents that can be inserted in the machine. The reagent mixing method, intended as the way reagents are distributed and mixed over the tissue surface, plays an important role as differentiator among the different products, since it constitutes the core of the staining technology. The slide-placement format is fundamental in determining the user workflow in a pathology laboratory: some machines allow for random loading of slides on-demand, while others require the user to gather a batch of slides and run them in parallel. Finally, throughput and turnaround time, although related, are two different value propositions. The first is of interest in estimating how many samples can be process in a working day, while the second determines the fastest result that can be delivered in case of high-priority requests.

These robots are specialized in automating liquid handling and are traditionally designed to mimic manual pipetting and increase the work-flow capabilities in order to process multiple slides in parallel, as opposed to using microfluidics to improve sensitivity and reduce assay times. The core business of these companies lies on supplying the reagents to perform assays needed in the field of anatomic pathology. Efficient and high-quality automation machines and protocols constitute the vehicle for the adoptions of their reagents.

Table 1:2 | Immunohistochemistry automats features. Highlighted features from the technical specifications of the immunohistochemistry automats shown in **Figure 1:1.** The data is adapted from [41]. *Taken from [42], **Taken from www.dako.com and www.leicabiosystems.com, respectively.

Feature	*Ventana Benchmark ULTRA*	*Dako Omnis*	*Leica BOND-III*
Number of slides	30	60	30
Number of reagent containers	35	60	36
Reagent mixing method	Liquid coverslip vortex mix	Dynamic capillary gap	Capillary cover tiles
Slide-placement format	30 random-access slide drawers	12 racks of 5 slides	3 racks of 10 slides

*Average throughput**	56 slides/workday	N/A	29 slides/workday
*Turnaround time***	N/A	2.5 h	4.5 h

1.3.1 Tissue preparation

Tissue biopsies are very delicate as fresh samples, as they can be easily distorted and damaged, thus it is impossible to prepare thin sections from them without an appropriate support. Furthermore, the specimen cannot withstand long ischemia times without jeopardizing the final results [43]. Thus the tissue must be preserved or «fixed» before the sections are prepared. There are mainly two methods routinely employed to provide this support:

Frozen section (FS): The tissue can be immediately frozen after resection, using for example nitrogen vapor, and kept frozen while sectioning with a special kind of cryostatic microtome called cryostat (**Figure 1:10a**). The advantage of FSs is that they can be prepared very quickly and thus used when intraoperative diagnosis is required to guide the surgical procedure. A common example is the examination of sentinel lymph nodes during breast lumpectomy [44].

Formalin-fixed paraffin-embedded (FFPE): The most common histological preparation approach is to fix the tissue specimen using formalin. The cross-linking mechanisms preserve the tissue from degradation without the need of freezing conditions. Subsequently, tissue blocks are infiltrated with liquid paraffin (**Figure 1:10b**), which solidifies at room temperature and provides the appropriate physical conditions to work as a support to cut thin tissue sections (**Figure 1:10c**). This method is commonly preferred due to the higher morphological quality of the sections, as well as the preservations of tissue blocks under room temperature. Nonetheless, the fixing mechanism usually requires overnight incubation in order to assure the formalin penetration. Moreover, methylene bridges formed during fixation can cross-link proteins and can mask antigenic sites, which requires a step called “antigen retrieval” prior to IHC stainings (see further).

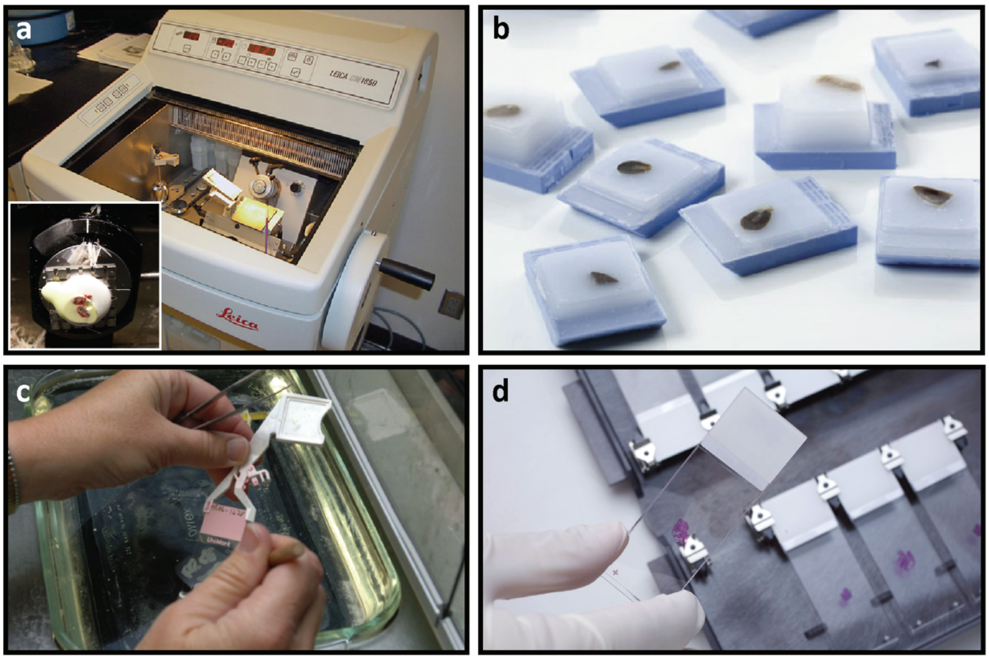

Figure 1:10 | Routine tissue preparation and staining techniques. (a) Picture of a cryostat used to obtain tissue sections from frozen samples. This machine is normally use for intraoperative diagnosis. **(b)** Tissue blocks embedded in standard paraffin cassettes for appropriate cutting and preservation. **(c)** Adhesion of freshly cut FFPE section on histological glass slides. The latter are functionalized for covalent binding of the tissue to the slide. **(d)** Picture of a H&E-stained slide.

1.3.2 Hematoxylin and eosin (H&E) stain

Tissue sections have little or no characteristic contrast when imaged using light microscopy. Staining is employed to increase the contrast and, at the same time, to highlight particular features of interest. H&E stain is routinely used in histopathology laboratories (**Figure 1:10d**) as it provides pathologists and researchers a very detailed view of the tissue. It is achieved by clearly staining cell structures, including cytoplasm, nuclei, organelles and extra-cellular components. The information obtained is often sufficient to allow a disease diagnosis based on the changes in the organization of the cells when compared to normal tissue. Even when advanced staining methods are used, H&E remains the most critical part of the diagnostic picture, as it displays the underlying tissue morphology that allows pathologists to correctly interpret the advanced stain. Indeed, in a clinical histology laboratory, all specimens are initially stained with H&E and advanced stains are only ordered if additional information is needed to provide a more detailed analysis. Zoomed-in examples of H&E stainings of breast carcinomas are shown in **Figure 1:12a** (see further).

1.3.3 Immunohistochemistry (IHC)

IHC is a method used to determine the expression of biomarkers in a tissue. It is based on the specific recognition of Ags within tissue sections by means of specific Abs. Upon the formation of the Ab-Ag complex, a histochemical reaction makes it visible, either in the form of a color for light microscopy or via a fluorophore for fluorescence microscopy observation [45]. In the latter case it is called immunofluorescence or immunohistofluorescence (IF).

In the clinic, IHC is used to diagnose tumors as benign or malignant, determine their stage and grade, and to identify the origin of the primary tumor in case of metastasis. Moreover, IHC is used in drug development to test the efficacy by detecting the activity of disease targets.

The most common IHC method consists on the use of an enzyme, called horseradish peroxidase (HRP), conjugated to a larger polymer molecule to which secondary Abs are bound, as shown in **Figure 1:11a**. Secondary Abs recognize the primary Ab bound to the Ags. Subsequently, 3,3'-diaminobenzidine (DAB) is oxidized in the presence of HRP resulting in the deposition of a brown, alcohol-insoluble precipitate at the site of enzymatic activity. This deposition allows for the visualization of the areas where the specific Ag is expressed. Examples of IHC results are shown in **Figure 1:12** (see further).

1.3.4 Immunofluorescence

IF is a technique widely used in most fields of biology, with samples ranging from cell suspensions to tissue sections, either fresh or fixated. In this thesis, we are interested in its application on tissue sections, especially for the quantitative capabilities it provides with respect to IHC [46], [47].

IF is based on the labeling of antibodies to fluorescent dyes, such as fluorescein isothiocyanate (FITC) or tetramethyl rhodamine isothiocyanate (TRITC). The binding of these labelled Abs to the Ag of interest is then measured with fluorescent techniques, namely array scanner, flow cytometry or automated imaging instruments. The signal can also be simply visualized using epifluorescence or confocal microscopy. Examples of IF stainings are shown in **Figure 1:15b** (see further).

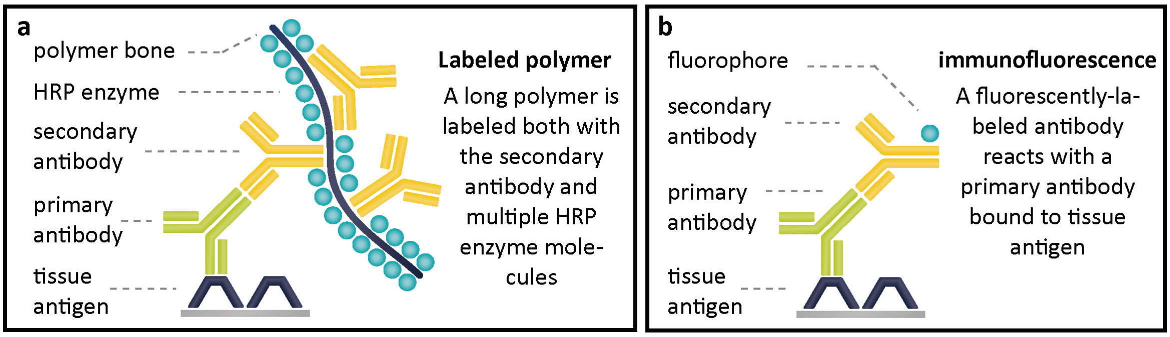
a
polymer bone
HRP enzyme
secondary antibody
primary antibody
tissue antigen
Labeled polymer
A long polymer is labeled both with the secondary antibody and multiple HRP enzyme molecules
b
fluorophore
secondary antibody
primary antibody
tissue antigen
immunofluorescence
A fluorescently-labeled antibody reacts with a primary antibody bound to tissue antigen

Figure 1:11 |Commonly used immunohistochemistry technologies. (a) Labelled polymer technology uses a polymer bone conjugated to secondary Abs and multiple HRP enzyme molecules. When DAB is exposed to HRP, it gets oxidized and deposits in the form of a brown polymer. The enzymatic reaction generates a signal amplification. The observation is done under bright-field microscopy. **(b)** Immunofluorescence makes use of fluorescently-labelled secondary Abs. In enzyme-free configuration, no signal amplification is generated. The observation is done using fluorescence microscopy. The plots were adapted from [48].

1.3.5 The breast cancer panel

Even though the microfluidic technology and IHC assays used during the course of this work can be adapted to any biomarker of interest, we ran our experiments on a set of markers that are commonly used for the diagnosis of breast carcinomas. **Figure 1:12** shows IHC images and classification of breast carcinomas according to the expressions of **(b)** estrogen receptor (ER), **(c)** progesterone receptor (PR) and **(d)** human epithermal growth factor receptor 2 (HER2), respectively [49]. A short description of these markers is presented below.

ER: ER is a protein activated by the hormone estrogen. In breast cancer, the presence of ER in the nuclei is a strong predictive marker for response to hormonal therapy, such us tamoxifen [50].

PR: PR is a protein activated by the steroid protein progesterone. Similarly to ER, PR-positive cancer respond well to endocrine therapy [51].

HER2: HER2/*neu* is a transmembrane tyrosine kinase whose strong expression in breast carcinomas is an indication of adverse prognosis [52], [53]. Additionally, HER2 constitutes a target for trastuzumab, a humanized antibody used in personalized treatments [54], [55]. Recommendation guidelines have been established and updated for pathologists to attribute a score to HER2 stainings, which in turn determines the administration of trastuzumab treatment [56], [57]. The available scores are 0, 1+, 2+ or 3+. When the score is 0 or 1+, the IHC test is considered negative and trastuzumab treatment is not recommended. On the contrary, when the score is 3+, the result is positive and the patient would benefit from the targeted treatment. Finally, 2+ scores are considered equivocal, for which the recommendation is to run a reflex test using *in situ* hybridization (see further).

Keratins or Cytokeratins (CK): CK are filament-forming proteins present in epithelial cells, fundamental for tissue structure and function [58]. Keratins genes are highly differentiation-specific and their mutations are associated with specific tissue-fragility disorders. Thus, the Abs to keratins constitute important markers of differentiation in diagnostic pathology. Another typical application regards the search for cells of epithelial origin on sentinel lymph nodes on breast carcinoma cases, as an indication of a metastatic stage [59].

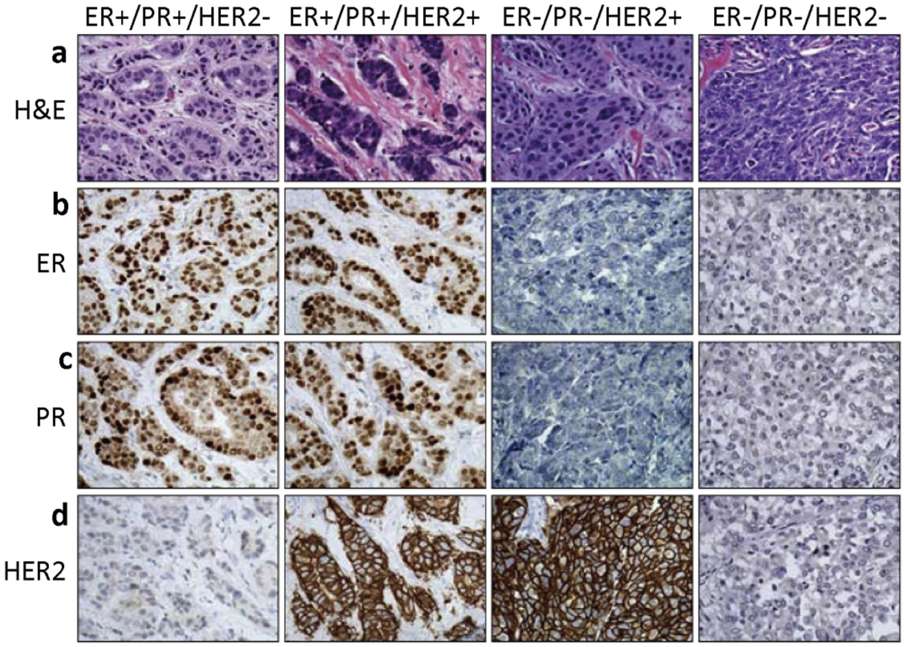

Figure 1:12 | Clinical classification of invasive breast cancer based on the expression of ER, PR and HER2. (a) The histology of the specimens is observed using H&E. Representative cases are selected according to the general clinical classifications, where the staining with ER **(b)**, PR **(c)** and HER2 **(d)** are considered. The major classification groups are ER+/PR+/HER-, ER+/PR+/HER+, ER-/PR-/HER+ and triple negative ER-/PR-/HER-. Figure adapted from [49]. Original magnification 40x.

1.3.6 Fluorescence *in situ* hybridization (FISH)

FISH is a cytogenetic technique that uses fluorescent probes that bind to complementary sequence of the chromosome. Developed in the eighties to map *Drosophila* genes [60], it became a standard tool in the diagnosis of breast cancer by measuring of the ERBB2 (Her-2/*neu*) oncogene [61, p. 2]. Nowadays, FISH is considered part of routine testing on cases that result in HER2 2+ for IHC [56], [57].

1.4 Microfluidics for tissue staining: State-of-the-art

A few research laboratories have been working in applying microfluidics to stain tumor tissue sections, taking advantage of the decreased diffusion distances. A first example concerns the « Microfluidic Parallel-Multiplexed Immunohistochemistry Platform » (MMIHC), a PDMS device consisting on multiple parallel channels that can be interfaced with the tumor tissue section in a reversible fashion [62]. Reagents are sequentially delivered into these channels, independently, allowing for multiplexed staining of the sample. The authors varied the concentration of the primary antibodies and the flow rate used for delivery, showing that, as expected, increased flow rates result in a higher IHC signal. **Figure 1:13a** shows a picture of the microfluidic setup, a schematic of the multichannel multiplexing approach and a staining result of the most common stainings routinely used in the diagnosis of breast cancer: ER, HER2 and Ki-67, a nuclear marker associated cellular proliferation. Finally, the potential use of this technology to stain tissue microarrays (TMAs) is shown.

IBM Research has developed a « Vertical Microfluidic Probe » (vMFP), a silicon-based non-contact microfluidic technology consisting of a tip that is placed vertically on top of the tissue sample. Reagents are delivered from one opening of the tip and aspirated from another one (**Figure 1:13b**), confining picoliters of liquid volumes on the area of interest [63]. With the use of this confinement, micro-IHC was demonstrated [64]. The tip is inserted in a stage that allows scanning of the tissue surface with micron resolution. The authors demonstrated that a clear staining was achieved upon 20 seconds of exposure of the tissue to the reagents, instead of the considerably longer duration of 30 minutes recommended by the reagent supplier for standard IHC.

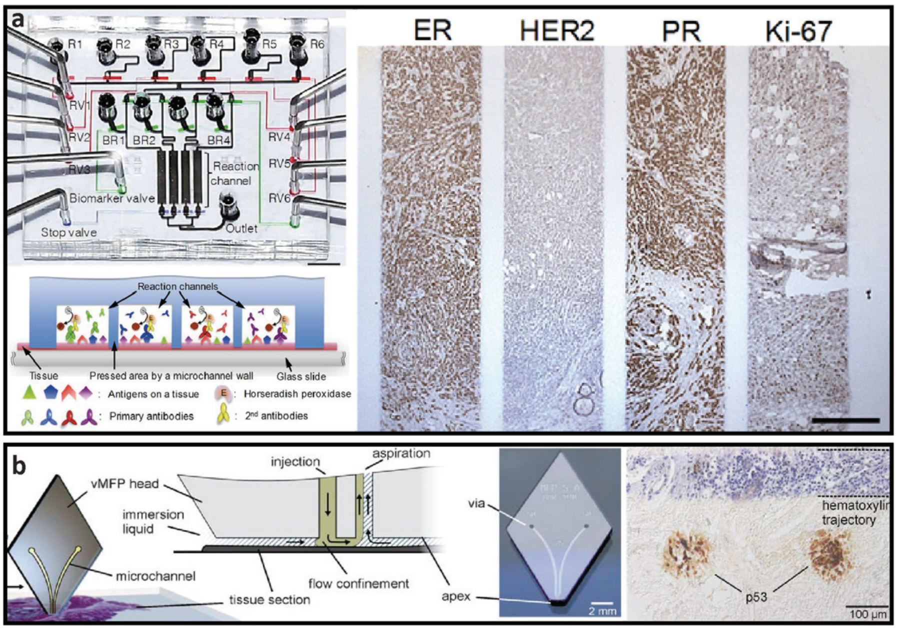
a
R1
R2
R3
R4
R5
R6
RV1
RV2
RV3
RV4
RV5
RV6
BR1
BR2
BR4
Reaction channel
Biomarker valve
Stop valve
Outlet
Reaction channels
Tissue
Pressed area by a microchannel wall
Glass slide
: Antigens on a tissue
E : Horseradish peroxidase
: Primary antibodies
: 2nd antibodies
ER
HER2
PR
Ki-67
b
vMFP head
immersion liquid
microchannel
tissue section
injection
aspiration
flow confinement
via
apex
2 mm
hematoxylin trajectory
p53
100 µm

Figure 1:13 | Microfluidic devices used to perform IHC stainings of tissue sections. (a) Picture (top) and schematics (bottom) of the MMIHC setup. Parallel microfluidic channels made of PDMS are positioned on top of the tissue sections for multiplexed delivery of the reagents needed for IHC. ER, HER2, PR and Ki-67 stainings results (right) **(b)** Schematics and working principle of the vMFP (left), picture of the vMFP (middle) and staining result (right). A vertical tip is disposed at the vicinity of the tissue section. An injection and an aspiration holes are used to deliver and confine the reagents used during staining on top of the areas of interest for staining. **(a)** and **(b)** were adapted from [62] and [64], respectively.

1.4.1 The « Microfluidic Tissue Processor »

Ciftlik *et al* have introduced the use of a microfluidic device, called «Microfluidic Tissue Processor» to perform IHC reactions on large areas (17x17 mm^2) of tissue samples for the first time, showing that not only could these assays be realized in a fraction of the time normally employed by the automated stainers commercially available, but also a greater level of signal accuracy could be obtained [65].

Microfluidic design: A glass/silicon micromachined structured was built using the process flow depicted in **Figure 1:2**. **Figure 1:14a** shows the schematic cross-section. The device is composed of inlet and outlet vertical access holes, and an o-ring (or gasket) for sealing of the reaction chamber. The height of the chamber, of around 100 $\mu\mathrm{m}$, was design to present microfluidic characteristics and, at the same time, be high enough compared to a tissue section, which can vary from 4 to 10 $\mu\mathrm{m}$ in thickness. Several other considerations were taken to design this chamber, such as the fluidic resistance and, thus, the pressure needed for liquid dispensing. **Figure 1:14b** shows a top view schematic of the device architecture. Bifurcated microfluidic channels were implemented to uniformly distribute the reagents in the reaction chamber, as opposed to the parabolic profile that would normally develop upon a single chamber entry. **Figure 1:14c** describes a simulation of a washing step, where the reaction chamber is initially filled with a reagent. In this picture we can appreciate the influence of the lateral channels at the outlet, which decrease the fluidic resistance at the edges in order to prevent the parabolic profile to develop at the second half of the chamber. It is also shown how the fluidic exchange profile is almost a uniform front and how the concentration of the initial reagent decreases in 1 s. According to Ciftlik *et al.*, simulations suggested that, after applying a washing buffer, the concentration in the chamber gets reduced to 10^{-7} times the initial concentration in only 2.5 s [65]. When applied to real examples and measured using fluorescent dyes, the authors found out that the filling and washing performance was 0.38 $\mathrm{dec/s}$, indicating that 5 s of flushing was enough to decrease the existing concentration in the chamber by 99%, thus it can be considered as an almost complete fluidic exchange.

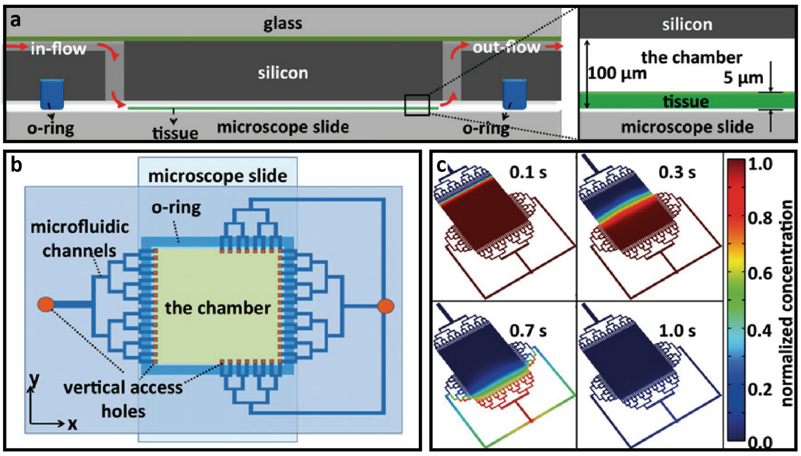
a
glass
in-flow
silicon
out-flow
o-ring
tissue
microscope slide
o-ring
silicon
the chamber
100 µm
5 µm
tissue
microscope slide
b
microscope slide
o-ring
microfluidic channels
the chamber
vertical access holes
y
x
c
0.1 s
0.3 s
0.7 s
1.0 s
1.0
0.8
0.6
0.4
0.2
0.0
normalized concentration

Figure 1:14 | Schematics and working principle of the MTP. (a) Cross-sectional view of the MTP obtained through silicon microfabrication and Si/Pyrex bonding via an intermediate layer of Parylene C. The MTP is interfaced on top of the tissue section forming a microfluidic chamber of reaction. **(b)** Top-view schematic showing the layout of the microfluidic channels that allow rapid and uniform delivery and wash of the reagents over the tissue section. **(c)** COMSOL simulation showing the fast fluidic exchange taking place in the reaction chamber. Figures adapted from [65].

Staining of tissue sections: The MTP was successfully used to perform IHC assays on breast carcinoma samples. **Figure 1:15** shows a comparison of the images obtained from a HER2 staining using a gold standard automated stainer (top row) with respect to the fluorescence stainings obtained using the MTP. Ciftlik *et al.* showed that high-quality stainings can be obtained in a fraction of the time when compared to standard techniques. The reproducibility and uniformity of the stainings were also addressed [65].

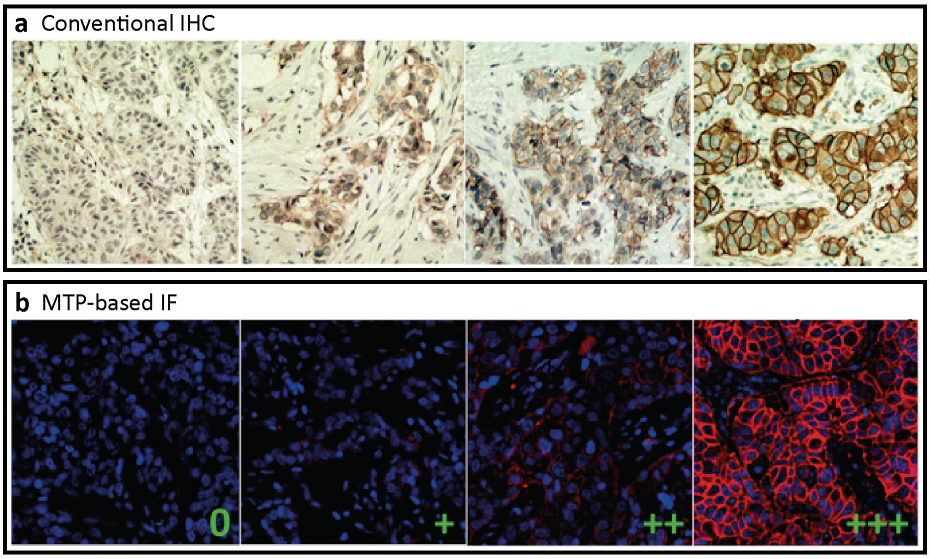

Figure 1:15 | Comparison between standard IHC and MTP-based IF. Sections of the same cases were stained using **(a)** conventional IHC automats and **(b)** MTP-based IF. The stained sections were blindly scored by trained pathologist according to international guidelines [56]. Figure adapted from [65].

Clinical results: The optimized protocol was subsequently run in a cohort of 76 invasive ductal breast carcinoma cases. The choice of the number of cases for each HER2 grade was done in way that the number of ++ cases, as assessed from standard staining methods, was incremented with respect to the real statistical distribution. The reasoning behind this choice was investigate the accuracy of the MTP-staining especially for the cases that are normally considered as giving an ambiguous outcome. The results of this clinical study showed no false-positives or false-negatives and, even more interestingly, the number of cases that obtained ++ scores was reduced from the original 27 to 3. Furthermore, the FISH results done to all the ++ cases were in concordance with the score obtained upon MTP-based staining. The details of these results are shown in **Figure 1:16**.

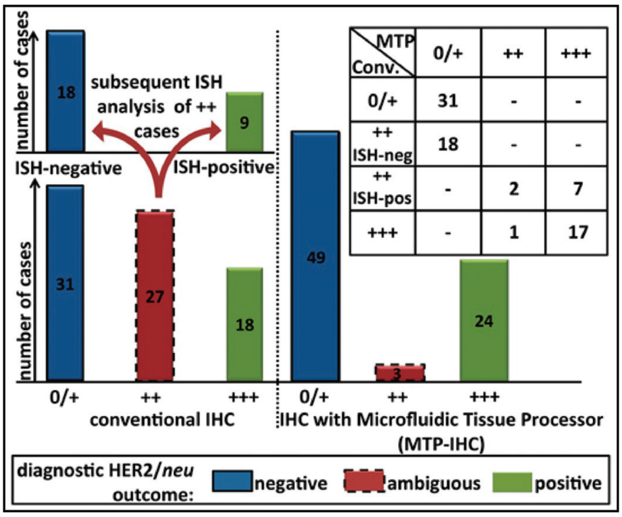

MTP / Conv.	0/+	++	+++
0/+	31	-	-
++ ISH-neg	18	-	-
++ ISH-pos	-	2	7
+++	-	1	17

Figure 1:16 | Comparison between conventional IHC and MTP-based IF scores. MTP-based IF showed a 90% reduction of the number of ambiguous scores, in concordance with FISH reflex testing. The study was performed on 76 invasive breast carcinoma cases.

Chapter 2 Use of a Parylene C intermediate bonding layer for on-chip micrfofluidic applications

In this chapter, we first characterize the intermediate Parylene C bonding layer fluorescence (iPBLF) used in the microfabrication of Si/Pyrex chips, as introduced in chapter 1, as well as the effect of the bonding process on the autofluorescence of this material. Subsequently, we show how long-term illumination of Parylene C, under bonding conditions, can deliberately modify the autofluorescence of this material. The programming capabilities of iPBLF were used then to demonstrate several applications of interest in the microfluidics field.

In a first study, we demonstrate data storage on Si/Pyrex microfluidic devices. Dynamic programming was achieved by alternating the exposure of Parylene C to UV and green light. This technique allows data on a microfluidic chip to be read, written and erased using a common fluorescent microscope. Until now, no studies had focused on storing data like expiry date, protocol or operational parameters on a chip. However, this could be useful to overcome certain automation challenges in industrial applications for which communication of information is required. We also demonstrate the application of iPBLF for detecting channel dimensions and positions, and for marking on-chip zones of particular interest.

A large number of lab-on-a-chip applications use fluorescence for quantifying biological entities. In such applications, incorporation of a stable on-chip fluorescent reference source would be highly desirable in order to compensate for instrumental parameter variations, like non-constant illumination intensity over time. In a second study, we show how using iPBLF to program an on-chip reference with which we can perform a concentration measurement of a fluorescently labelled analyte in solution, and a measurement of the flow-rate in a microfluidic channel. Thanks to the on-chip reference, this measurments are consistant, even under changing experimental conditions of illumination intensity and taking different microscope objectives.

This chapter is an adapted version of the following publications:

- A. T. Ciftlik, **D. G. Dupouy**, and M. A. M. Gijs, “Programmable parylene-C bonding layer fluorescence for storing information on microfluidic chips,” *Lab on a Chip*, vol. 13, no. 8, p. 1482, 2013.
- **D. G. Dupouy**, A. T. Ciftlik, J. Teixidor, and M. A. M. Gijs, “Programming and use of Parylene C fluorescence as a quantitative on-chip reference,” *RSC Adv.*, vol. 4, no. 90, pp. 49367–49373, Sep. 2014.

2.1 Charachterization of intermediate bonding layer fluorescence

Fluorescence of common polymer materials used in lab-on-a-chip devices has been studied, however, such fluorescence was generally seen as a negative effect, and most studies focused on trying to eliminate it. Hawkins *et al.* characterized thin films of polymers, including PET, PMMA and PS, by exposing using a mercury arc lamp the films to blue and green light, respectively [66]. They reported that continuous exposure to these wavelengths resulted in a bleaching of the fluorescence, which can be best characterized by an exponential decay of the fluorescent signal with increasing illumination time. A similar study was done by Piruska *et al.,* using lasers at specific wavelengths rather than a mercury lamp with fluorescent filters, and they reported that similar exponential decay characteristics under continuous illumination was observed for PMMA, PC, PDMS and COC [67]. In another study, Lu *et al.* showed that, when as-deposited Parylene C and Parylene D films were exposed to UV (mercury lamp with 340-380 nm filter), the observed fluorescence had an initial increase during the first 5-10 minutes, which was followed by a subsequent exponential like decrease [68].

Although fluorescence of as-deposited Parylene C films under UV light has been studied previously [68], [69], iPBLF can behave significantly different. This is related to changes in the polymeric structure, as induced by specific temperature processing during the bonding operation, and vacuum-like conditions in the bonding stack preventing direct exposure of Parylene C layers to atmosphere.

2.1.1 Effect of bonding on Parylene C fluorescence

In order to determine the effect of the bonding process on iPBLF, we first experimentally quantified the fluorescence in patterned Parylene C structures before and after bonding, as well as at the cross-section of the bonding stack, as illustrated in **Figure 2:1a**. An upright fluorescent microscope (Axio Imager M2m, Zeiss GmbH, Germany) with a monochrome charge coupled device (CCD) camera (AxioCam MRm, Zeiss GmbH, Germany) was used for the fluorescence experiments. Coverslip thickness-corrected 20x and 40x objectives (LD Plan-Neofluar Ph2 Korr, Zeiss GmbH, Germany) were used in order to illuminate and observe channels through the 550 µm thick Pyrex. Fluorescence experiments were done by short exposure time (< 1 s) using excitation and emission wavelengths corresponding to the 6 different filter sets (Zeiss GmbH, Germany) of **Table 2:1**, corresponding to common commercial dyes. The relative fluorescence originating from the Parylene C layer was obtained by dividing the average measured intensity by the signal from a background region as obtained during planar observation. For normalizing images taken with different filter sets, we adjusted the intensity filters and camera exposure duration in a way that the intensity in a background region is just higher than the noise level of the camera.

Table 2:1 | Excitation and emission wavelengths of the filter sets used for the fluorescence experiments and corresponding commercial dyes. BP: bandpass, LP: long pass, DAPI: diamidino-phenylindole, BFP: blue fluorescent protein, GFP: green fluorescent protein, Cy: Cyanine, AF: AlexaFluor (Molecular Probes, Invitrogen)

Filter set (Excitation/ Emission color)	*Excitation wavelength (nm)*	*Emission wavelength (nm)*	*Common dyes*
UV / Blue	BP 310-390	LP 420	DAPI, BFP, AF 350
Blue / Green	BP 450-490	BP 515-565	Fluorescein, AF 488, GFP
Green / Red	BP 537-562	BP 570-640	Cy3, AF 546, Rhodamine
Yellow / Deep Red	BP 575-600	BP 612-682	Cy 3.5, AF 594, Texas red
Red / Near IR	BP 625-655	BP 665-715	Cy 5.5, AF 647
Deep red / IR	BP 670-700	BP 715-745	AF 700

Figure 2:1b shows fluorescent images for emission wavelengths in the visible range. The UV/Blue fluorescent image of **Figure 2:1b.iv** shows that the Parylene C defining the channel walls is perfectly visible. Although such fluorescence is mostly perceived as a negative effect, compromising detection limits, it can be an advantage here, as the Parylene C never appears as a background layer of a microfluidic channel. Indeed, this can be useful in many applications requiring optical detection of channel positions, displacement analysis and other automated microscopy applications (see following sections). **Figure 2:1c** shows the experimental results using 6 different fluorescent filters corresponding to common dyes. Although the fluorescence intensity is increased in all cases after the bonding process, the results suggest that patterned Parylene C fluorescence is only significant when excited by UV and Green light, and stays very close to 1 for the other wavelengths. While the fluorescence is expected for the UV/Blue case [68], the intensity in the Green/Red case can possibly be attributed to modifications in the crystalline structure during thermo-compression of the polymer.

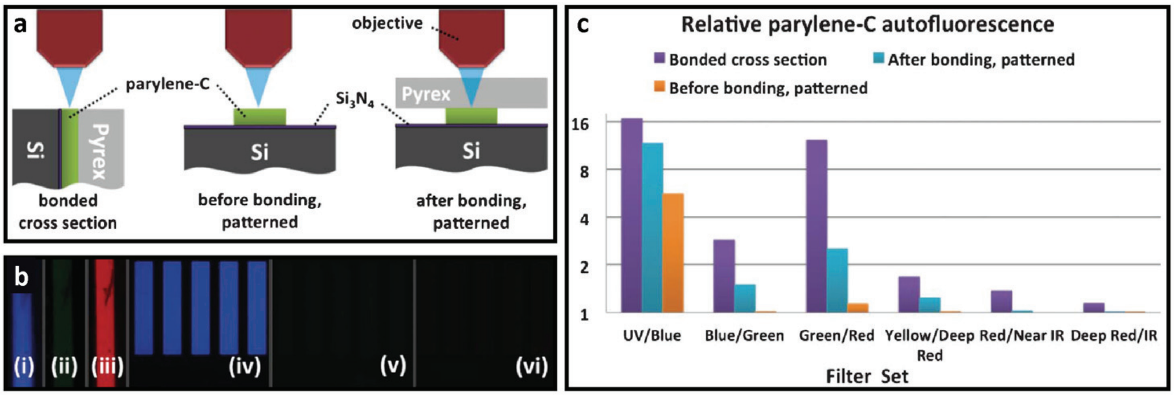

Figure 2:1 | Characterization of intermediate Parylene C bonding layer fluorescence (iPBLF) before and after bonding. (a) Schematic diagram illustrating the experiments to characterize the effect of bonding of iPBLF. **(b)** Pseudo-coloured fluorescence images (i), (ii), (iii) of 10 µm-thick Parylene C at diced device cross-sections and (iv), (v), (vi) of patterened Parylene C after bonding (images are 200 µm wide), corresponding respectively to the UV/Blue, Blue/Green and Gree/Red filter sets. **(c)** Plot of iPBLF intensity relative to the background, appearing most significant in the UV/Blue and Green/Red channels

2.1.2 iPBLF under long-term illumination

Above results suggest that iPBLF is only significant when observed in the UV/Blue and Green/Red channels. Therefore, we focused our study on analysing the dynamic behaviour of iPBLF, by exposing the Parylene C to the excitation wavelengths of these channels. First, we characterized the time response of iPBLF under long-term illumination with UV and Green light, which is shown in **Figure 2:2**. Here, “illumination” corresponds to a long exposure (> 1 min) to a given wavelength in order to induce fluorescence (or bleach it). Illumination was done with a 50 W mercury short-arc light source (HBO 50W/AC). In contrast, “observation” corresponds to taking an instantaneous (< 1 s) image in a fluorescence channel. In order to visualize the effect, illumination was done by adjusting the microscope’s diaphragm opening to expose only a local region, while the observation was done under a full diaphragm opening. This resulted in an image similar to the one shown in **Figure 2:2**; the induced fluorescence F_{ind}, that is read at an instant $t = t_a$, is calculated as follows based on such image. First we take the mean value over the image pixel values p_n in the different domains as follows:

1. $p_n \in \Omega_s$, where Ω_s is the “illuminated” region, giving a mean signal pixel value $p_s(t_a)$.
2. $p_n \in \Omega_r$, where Ω_r is a non-illuminated region containing a Parylene C bonding layer, giving a mean pixel reference value $p_r(t_a)$
3. $p_n \in \Omega_b$, where Ω_b is a background region without any Parylene C, giving a mean pixel background $p_b(t_a)$
4. Later, the induced fluorescence is calculated as follows:

$$F_{ind}(t_a) = \frac{p_s(t_a) - p_b(t_a)}{p_r(t_a) - p_b(t_a)} \tag{2.1}$$

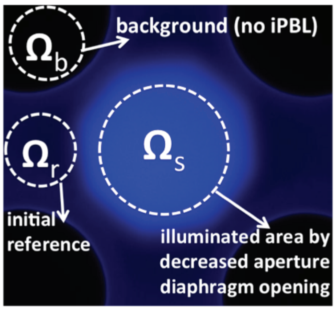

Figure 2:2 | “Observation” of the induced fluorescence after long-term “llumination”. Ω_s sis the illuminated region, Ω_r is a non-illuminated region containing Parylene C, and Ω_b is a background region without Parylene C. The induced fluorescence is calculated considering the pixels within the dashed circles. The image width is 275 µm.

Such calculation of the dimensionless induced fluorescence allows us to compensate changes due to used intensity filters, camera exposure time, binning, noise and used gain levels as well as fluctuations in the fluorescent light intensity and ambient light. In order to see the effect of long-term exposure, we programmed the microscope to first illuminate the central region for a predefined period of Δt (1-5 min), and then observe the same spot in the UV/Blue and Green/Red channels. By repeating this operation for the same spot, we performed the study of the time-dependence of iPBLF. Here, note that, although observation also requires a short light exposure of the sample, this affects minimally the calculated F_{ind}, since (i) the observation duration is much less than Δt, and (ii) the required light intensity for observation is much less than that during illumination.

Figure 2:3 shows response of iPBLF long-term illumination with UV and Green light. In **Figure 2:3a**, fluorescent images obtained using two observation channels are shown, both initially before any illumination, and after long-term exposure to UV and Green light. We see that illumination with UV light induced fluorescence in both observation channels. In contrast, Green illumination did not have any effect on the fluorescence observed in the UV/Blue channel. However, Green light exposure has a bleaching effect of iPBLF, when observed in the Green/Red channel.

Figure 2:3b (first panel) shows the plots of induced fluorescence F_{ind} versus the illumination duration for UV light. The F_{ind} observed in the UV/Blue channel presented a saturating trend, unlike earlier reports for as-deposited Parylene C films [68]. Indeed, Lu et al. reported that F_{ind} of as-deposited Parylene C has a decreasing trend under UV illumination, after an initial increase. The decrease of fluorescence was attributed to oxidation of the Parylene C at the film surface; however, no data were given in a non-oxygenated environment.

We think that the different behaviour between the here-observed iPBLF and the results for as-deposited Parylene C may be explained by the vacuum-like condition at the bonding interface, preventing the Parylene C surface from oxidation. Bera *et al.* studied the photolysis of Parylene C under vacuum and its photo-oxidation in presence of oxygen, and found major differences in the two cases [70]. When UV-exposed under vacuum, they reported that Parylene C can form fluorene-type structures through hydrogen abstraction and subsequent chlorine radical formation, a process which introduces additional C=C double bonds. Under oxygen atmosphere, these double bonds are attacked and mostly converted to C=O and C-O bonds. Presence of the highly-excitable C=C bonds may contribute to the increased fluorescence [68]. Therefore, we think that the observed trend of iPBLF in the UV/Blue channel after UV illumination can indeed be attributed to vacuum-like conditions at the bonding interface.

In addition to this, in an independent study, Remington *et al.* reported that increasing the number of double bonds in a chromophore correlates with longer absorbance and emission wavelengths in a fluorescent protein, and that the number of these bonds plays a key role in determining the excitation and emission colour [71]. Therefore, we can expect that a Parylene C film with an increased number of C=C bonds, as explained above, should generate an increased fluorescence intensity (i.e. F_{ind}) at longer wavelengths. Consistent with this, Lu *et al.* found a red shift in the fluorescence emission spectra of Parylene C film during the first 5 minutes, before oxygenation becomes dominant [68]. Therefore, the iPBLF intensity increase in the Green/Red channel upon UV illumination is not unexpected and is correlated with an increased number of C=C bonds.

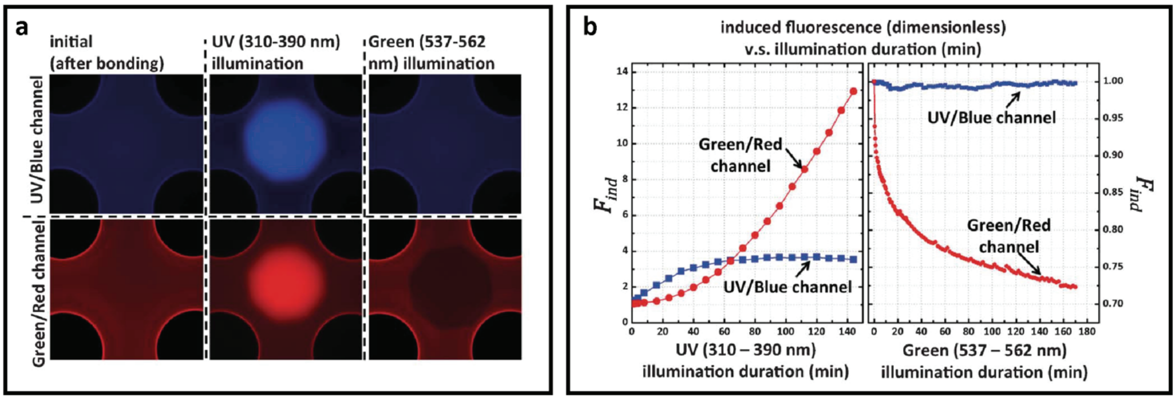

Figure 2:3 | Time response of iPBLF under long-term illumination with UV (310-390 nm) and Green (537-562 nm). (a) Fluorescent images showing the iPBLF ‘‘observed’’ in the UV/Blue and Green/Red channels. Observation is done initially, just after bonding and before any ‘‘illumination’’, and after ‘‘illumination’’ with UV and Green light, showing that the UV light can be used to increase fluorescence, whereas Green light can be used to decrease it. Fluorescent images are 275 μm wide. **(b)** Plots of induced fluorescence (F_{ind}) vs. ‘‘illumination’’ duration for UV and Green light. The plots show that the iPBLF variation observed in the Green/Red channel has an opposite trend depending on if the spot has been illuminated with UV or Green light, while this is not the case for iPBLF observation in the UV/Blue channel.

Figure 2:3b (second panel) shows the plots of induced fluorescence F_{ind} versus the illumination duration for Green light. In this case, F_{ind} observed in the UV/Blue channel does not change, at least for the 170 minutes of illumination. However, the same Green light illumination resulted in a decrease in iPBLF intensity when observed in the Green/Red channel. Such bleaching behaviour was previously observed in the form of a multi-parameter exponential decay, when characterizing fluorescence of other polymers. Such exponential decay with 2-3 exponential terms is generally correlated with simple bleaching of 2-3 fluorophore species in the polymer. Note that we have observed a similar exponential bleaching behaviour also in the UV/Blue channel under low intensity UV illumination conditions (see **Figure 2:4**). Hence, the observed bleaching of the Parylene C fluorescence is consistent with the previously reported studies on fluorescence of polymers. To adjust the light intensity, we used neutral density (ND) and fluorecence attenuator (FL) filters included in the microscope.

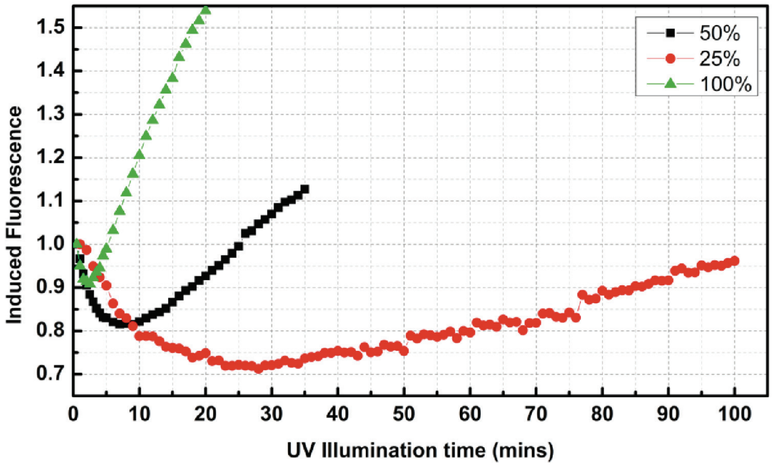

Figure 2:4 | Induced fluorescence versus the illumination duration under UV illumination using different intensity filters. Grey filters of 100%, 50% and 25% were used. During initial exposure, we observed an exponential decay bleaching behavior in the UV/Blue channel for all intensities. For 100% UV illumination intensity, an increase in the

fluorescent signal is observed after a few minutes. On the other hand, with lower UV illumination intensity, bleaching remains dominant and recovery of initial fluorescence cannot be achieved.

2.1.3 On-chip fluorescent reference printing

In the attempt to further characterize iPBLF, we ran a second experiment in which (i) the Parylene C used for bonding of the microfluidic chips was deposited with a thickness of 2 μm, 5 μm and 10 μm, and (ii) F_{ind} was studied with respect to the illumination dose (instead of the time). For this reason, we designed the printing of a quantitative fluorescence "reference" Ω_R, as depicted in **Figure 2:5**. We first printed a fluorescent pattern, which we call an on-chip fluorescent "standard" Ω_{STD}, and was realized by illuminating through the microscope objective (20x) with UV light during 1 hour through the Pyrex wafer using the method explained above. A 120 W mercury vapour short arc lamp (X-Cite 120 PC Q Microscope Illumination System, Lumen Dynamics, Canada) was used. The goal of the standard is to provide an on-chip source of fluorescent signal, which would never be exposed again to additional illumination doses. Later, we observed this fluorescence and used it to correct for time-dependent variations in intensity of the fluorescent excitation source, as noted during long-term illuminations.

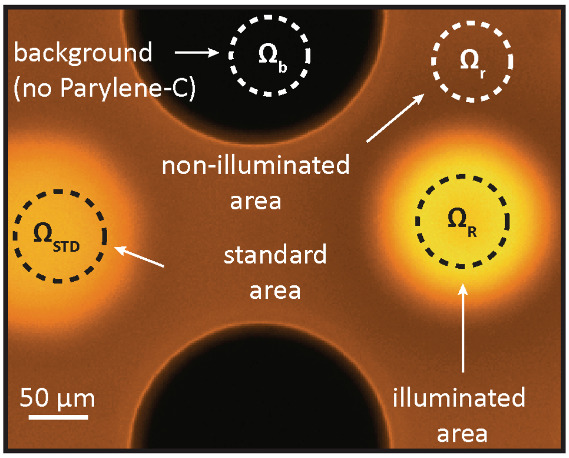

Figure 2:5 | Fluorescent image observed in the Blue/Green. The figure shows a standard area (Ω_{STD}), an area without Parylene C (Ω_b), an area with non-illuminated Parylene C (Ω_r) and the illuminated reference area (Ω_R).

In order to characterize the fluorescence reference printing process in detail, we performed several cycles of 60 s illumination steps nearby a previously printed standard and observed them in the UV/Blue and the Blue/Green channels. The intensity of the light and the exposure time used for observation were chosen such as to provide a significantly lower observation dose, compared to the illumination dose to avoid any alteration of the fluorescence of the standard and reference during observation. The printing experiments resulted in images as the one shown in **Figure 2:5**. The induced fluorescence, F_{ind}, read at any instant t, is calculated using the mean value of the pixel intensity from the different regions of interest from the obtained images, as described below.

First, we extract the mean pixel values of the pixels p_i in each domain:

- $p_i \in \Omega_R$, where Ω_R is the reference region, from which the extracted mean signal is $p_R(t)$.
- $p_i \in \Omega_{STD}$, where Ω_{STD} is the standard region, from which the extracted mean signal is $p_{STD}(t)$.

- $p_i \in \Omega_b$, where Ω_b is the background region without any Parylene C, from which the extracted mean signal is $p_b(t)$.
- $p_i \in \Omega_r$, where Ω_r is the non-illuminated region of Parylene C, from which the extracted mean signal is $p_r(t)$.

The corrected induced fluorescence of the reference region is then calculated as

$$F_{ind}(t) = \frac{p_R(t) - p_b(t)}{p_r(t) - p_b(t)} \tag{2.2}$$

This method employed to calculate F_{ind} allows us to compare the induced fluorescence in the region Ω_R with respect to the autofluorescence of the non-illuminated Parylene C area Ω_r. If only autofluorescence would be present (no printing is done), Eq. (2.2) is equal to one. To obtain the exact instantaneous illumination dose for a given time t, correcting for eventual fluctuations in time of the lamp intensity, we use the expression

$$D(t) = D(t_0) \cdot \frac{p_{STD}(t)}{p_{STD}(t_0)} \tag{2.3}$$

The second factor of Eq.(2.3) corrects for the time variations in the lamp intensity by comparing the signal in the standard area Ω_{STD} at every moment in time with the one at the beginning of the experiment. In this manner, by measuring the power of the lamp at $t = t_0$, we could deduce the dose across the whole experiment. If the excitation intensity does not change over the time of duration of the experiment, the second factor simply becomes 1. The total dose is simply obtained by integrating the instantaneous doses over the duration of the experiment. The UV irradiance power received by the sample was measured with a power meter (Model 306, Optical Associates Inc., CA, USA) calibrated for a wavelength of 365 nm at the beginning of each experiment.

In order to see the effect of a long-term illumination and to extract data from different exposures, we programmed the microscope to illuminate the sample for fixed periods Δt of 60 s and to acquire the images in the different excitation/emission channels at every interval. We also set a mosaic acquisition experiment to perform the same illumination-observation sequence in six different positions of the chip, so as to reproduce the characterization several times. The same steps were repeated for 2, 5 and 10 μm thicknesses of the Parylene C intermediate bonding layer. The resulting induced fluorescence values, as calculated using Eq. (2.2) and Eq. (2.3), are shown separately for the UV/Blue (**Figure 2:6a**) and for the Blue/Green (**Figure 2:6b**) channels.

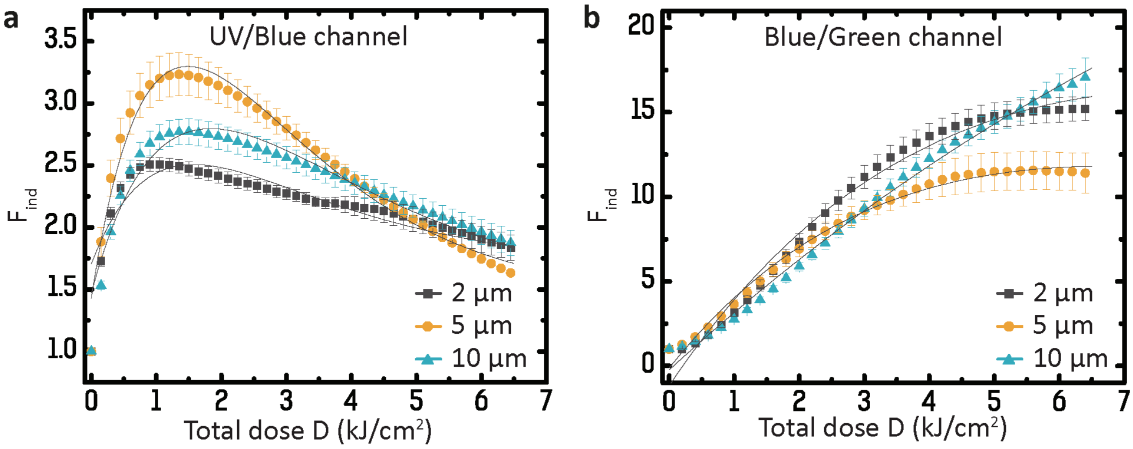

Figure 2:6 | Characterization of the iPBLF in the reference area Ω_R under long-term illumination with UV for a 2 µm, 5 µm and 10 µm thick layer of Parylene C. The $F_{ind}(t)$ curves are obtained from the raw data by using Eq. (2.2) and (2.3). **(a)** Observation in the UV/blue channel, showing a fast increase in the signal, followed by a slower decay. **(b)** Observation in the Blue/Green channel, indicating an increase in the signal followed by a decay, however with a less strong dependence on the dose than the curve of (a). Both UV/Blue and Blue/Green observation channels were fitted according to the formula $I = ax * \exp(-bx) + y_0$ representing an initial linear growth of the fluorescence followed by a single exponential decay, though the latter is hardly visible in (**b**). The parameters of the fitted curves $F_{ind}(t)$ for (**a**) and (**b**) were extracted from the model and shown in **Table 2:2** and **Table 2:3**, respectively.

Concerning the UV/Blue channel, the general observed trend consists of a fast increase of the induced fluorescence followed by a peak and a slower decay. In the case of 2 μm thickness, a maximum is reached at a total dose of 1050 J/cm^2, earlier than for the thicknesses of 5 and 10 μm, which show peak values at 1350 and 1450 J/cm^2, respectively. Considering that for a thicker layer, more fluorescent material is available, this result is expected. On the contrary, the value of the intensity of the peaks does not follow the same order: the maximum value of F_{ind} for 2, 5 and 10 μm are 2.51, 3.23 and 2.77, respectively. We believe that the reason for this relies on the depth of focus of the objective we used to illuminate the Parylene C. The depth of focus (DOF) of the objective determines the volume where the light is focused and, thus, where the intensity is at the maximum. The DOF can be calculated as

$$DOF = \frac{\lambda_0 n}{NA^2} + \frac{n}{M \cdot NA} e \tag{2.4}$$

where λ_0 is the wavelength of the light (365 nm), n is the refractive index of air (1), NA is the numerical aperture of the objective (0.4) and e is the smallest feature that can be resolved by a detector that is placed in the image plane of the microscope objective (6.45 μm). The DOF of the 20x objective used for this experiment is then equal to 3.0 μm. When the Parylene C layer is thinner than the DOF, the whole material is exposed to the maximum intensity. On the contrary, when the thickness of the Parylene C is greater than the DOF, not all the Parylene C is exposed in the same way, resulting in a partial exposure of the material.

Table 2:2 | Fitting parameters for the UV/Blue channel for 2, 5 and 10 µm thickness of Parylene-C. *RMSE: Root Mean Square Error.

Thickness	a	b	y_0	*RMSE
2 µm	1.38E-3	6.35E-4	1.71	1.07E-2
5 µm	3.42E-3	6.74E-4	1.43	5.64E-3
10 µm	1.96E-3	5.44E-4	1.47	7.83E-3

Table 2:3 | Fitting parameters for the Blue/Green channel for 2, 5 and 10 µm thickness of Parylene-C. *RMSE: Root Mean Square Error.

Parameters	a	b	y_0	*RMSE
2 µm	4.81E-3	1.48E-4	-0.11	7.13E-2
5 µm	5.72E-3	1.20E-4	-1.16	3.33E-1
10 µm	3.52E-3	3.81E-5	-0.23	1.32E-1

2.2 Programming of Parylene C bonding layer fluorescence for information storage on microfluidic chips

Industrial applications of microfluidic devices will bring additional automation challenges where the functionality, layout and protocol parameters will need to be stored and adjusted with changing versions of microfluidic chips. Therefore, information required for successful operation of each individual microfluidic chip, like the expiry date, optimized protocol for the specific layout and external hardware should be communicated to automated platforms that microfluidic devices operate with. In addition to these, due to fabrication and integration tolerances, the dimensions of the microchannels may vary as well as the absolute positions of the functional regions, like on-chip detection and interrogation zones, may change. In order to increase the reproducibility of the outcome, which is vital for most biomedical applications, automated platforms should optimize the applied protocols to compensate for these changes for each individual chip. For example, volumetric flow rate or pressure applied to the channel inlet should be adjusted to achieve a required fixed fluid flow speed, despite a varying channel width due to lithography and etching variations. Moreover, actualized protocol information, like the number of utilisation cycles or the last reagents used may need to be stored for each individual chip.

Despite the apparent need, a technique that allows the manufacturer and, in particular, the user to dynamically and locally store data on a microfluidic chip was not presented. In certain cases, electronic components can be integrated to microfluidic systems; however, integration of additional electronic memory elements and their programming increases complexity and cost of both the microfluidic chip itself and the peripheral equipment. Fluorescently recognizable polymer microtaggants were also demonstrated recently by lithographically shaping codes on a polyethylene glycol (PEG) polymer layer and conjugating it with a fluorescent polymer [72]. However, if used for data storage on microfluidic chips, such a technique would occupy valuable chip area, be impossible to modify *a posteriori,* not be scalable, introduce additional materials like fluorescent acrylic monomers and photo initiators, which might also interfere with the established fabrication process of the microfluidic device. Therefore, for fulfilling above requirements, ideally, on-chip data storage should introduce no additional steps or materials in microfabrication, be easily programmable and readable by standard equipment, both during production and utilization.

Exploiting fluorescence of certain polymer materials used during fabrication of the microfluidic devices would be an ideal case for data storage, since one could profit from existing fluorescent imaging systems required for operation of these devices. Modification of the fluorescent parameters of these materials would allow information to be optically written within the material itself, while reading and writing operations can be conducted with a fluorescent microscope, as well as using common mask-based lithographic techniques.

In this section, we exploit iPBLF to store and rewrite data on Si/Pyrex microfluidic devices that were fabricated with this bonding technology by using the fluorescent microscope used for observation and characterization in the previous section. Subsequently, we demonstrate that iPBLF can also be used to determine channel dimensions, channel positions and regions of interest.

2.2.1 Dynamic programming of iPBLF

Above analysis revealed that F_{ind} observed in the Green/Red channel has an opposite trend depending on if the spot is illuminated with UV or Green light, while F_{ind} observed in the UV/Blue channel cannot be reversed. This implies that alternating illumination of a single region to these different wavelengths may be exploited for re-writable data storage on-chip. **Figure 2:7** shows dynamic programming of iPBLF with this technique. We used the intensity decrease upon Green illumination during 5 minutes to “write” while subsequent UV illumination of the same region during 3 minutes is used to “erase” information by reversing the effect. **Figure 2:7** shows a timing diagram of 5 concatenated “write” and “erase” cycles with 8 min period of the same region. This directly demonstrates how iPBLF can be used to program a fluorescent memory bit. We anticipate that an increase of the intensity of illumination light can help reducing the data cycle period, either by using a higher numerical aperture objective, or a more powerful light source like a laser.

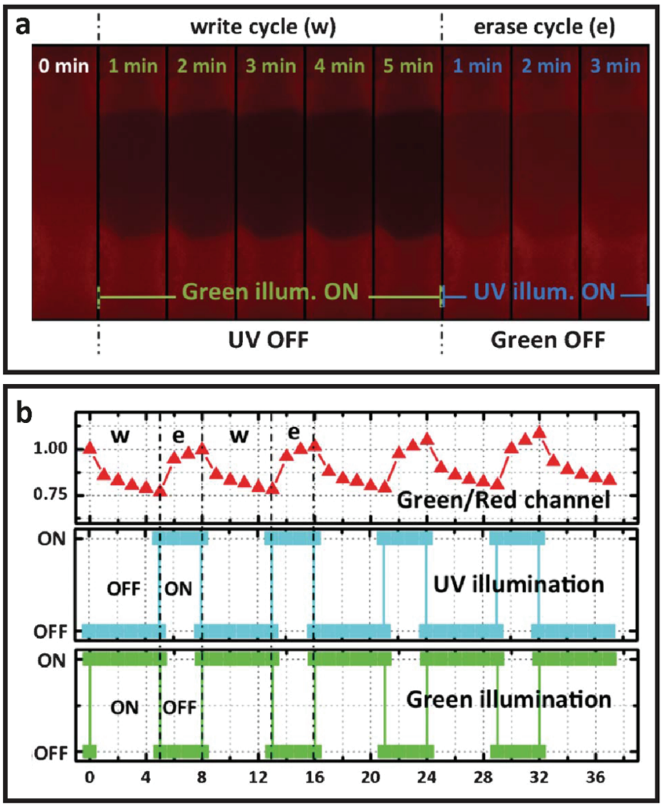

Figure 2:7 | Dynamic programming of iPBLF using alternating ‘‘illumination’’ by UV and Green light. (a) Time-lapse pictures showing a write–erase cycle of an illuminated region. The decrease in fluorescence upon Green illumination during 5 min is used to ‘‘write’’, while subsequent UV illumination of the same spot during 3 min is used to ‘‘erase’’ information by reversing the effect. Each time-lapse image is 75 μm wide. **(b)** $F_{ind}(t)$ observed in the Green/Red channel during a sequence of multiple ‘‘write’’ and ‘‘erase’’ cycles of the same region.

2.2.2 Example of data storage on-chip

iPBLF can be used for diverse applications related to automated operation of a microfluidic chip. For data storage, q-codes with different data volumes can easily be engraved and modified, as shown in **Figure 2:8.** Q-codes can be used to store any kind of data, their use is free of any licence, and recognition software exists on many platforms, free of charge. In this example, we UV-exposed microfluidic devices via a standard lithography mask, which marked each device with a q-code. Later we have acquired the image with a fluorescent microscope, and found that a single fluorescent image was sufficient for recognition of the q-code with a smart-phone. The irreversible nature of the induced UV/Blue channel fluorescence also provides an opportunity for read-only data storage, since the code will always be visible in this channel. However, the code observed in the Green/Red channel is modifiable by illuminating with Green light, and this allows modification *a posteriori* by the user.

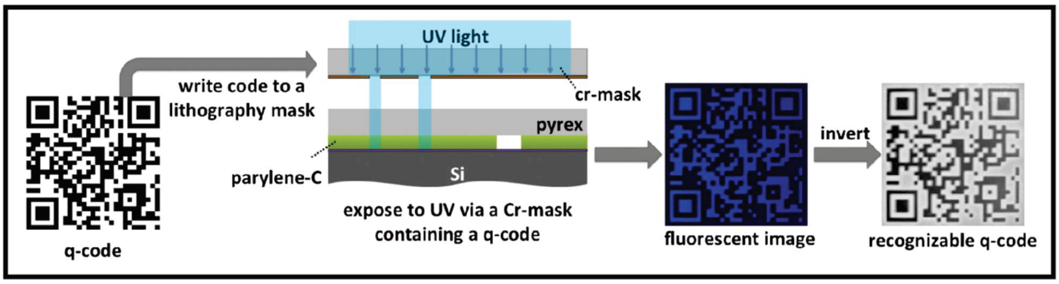

Figure 2:8 | Example of data storage on chip. On-chip data writing in the form of a QR-code using induced UV/Blue fluorescence. The obtained fluorescent image is easily recognizable by QR-code reading software. Codes can equivalently be written in the Green/Red channel either by locally inducing or bleaching fluorescence. The width of this fluorescent QR-code is 500 μm.

The time stability of a printed dot data was studied over a short term of 7 days (**Figure 2:9a**), showing that the induced fluorescence was not lost in time, both for the UV illuminated and the Green illuminated spots. We observed an increase of the induced fluorescence after UV illumination in both UV/Blue and Green/Red channels, when normalized to obtained right after the spot writing. For the spots written (by bleaching) using Green illumination and observed in the Green/Red channel, we find that it has increased about 5% over one week. This incremented fluorescence could also be attributed to setup settings, since the on-chip reference was not implemented for this experiment. In order to assess the stability of the data in the longer term, we also imaged a QRcode 2 months after writing, which was successfully recognized by the QRcode reader software. After initial code writing, we stored the chip at room temperature without any special protection from atmosphere and humidity for 2 months and later once again acquired the fluorescent image of the code. We have observed no difference in the resulting image and the code was easily recognizable by the software, as can be observed from **Figure 2:9b**.

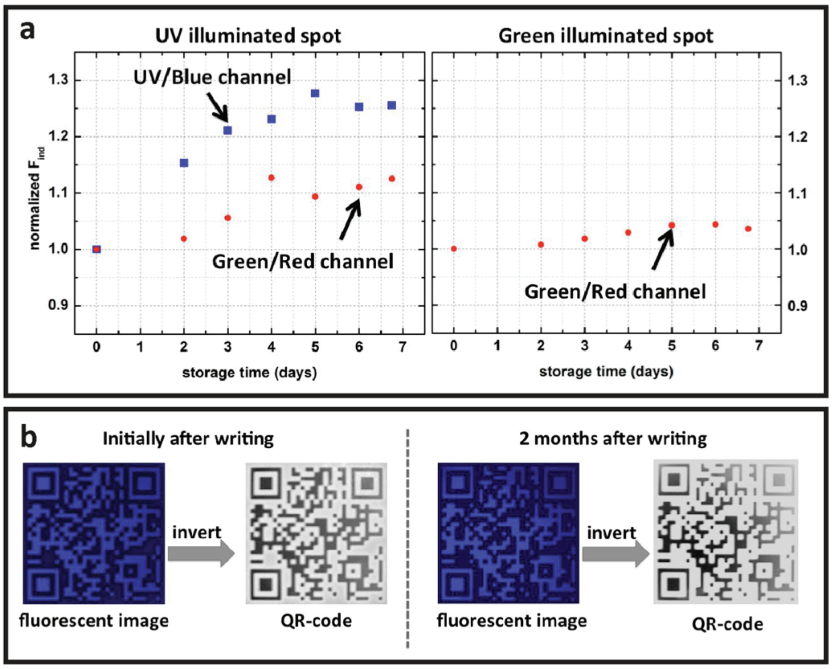

Figure 2:9 | Stability of the induced fluorescence. (a) Study of the induced fluorescence written by UV illumination and written (bleached) by Green illumination over 7 days. We observe an increase of the induced fluorescence after

UV illumination in both UV/Blue and Green/Red channels, when normalized to the one obtained right after the spot writing. For the spots written (by bleaching) using Green illumination and observed in the Green/Red channel, we find that fluorescence has increased about 5% over one week. **(b)** Stability of the QR-code 2 months after writing. After initial code writing, we stored the chip at room temperature without any special protection from atmosphere and humidity for 2 months and later once again acquired the fluorescent image of the code. We have observed no difference in the resulting image and the code was easily recognizable by the software. The width of the fluorescent QR-code is 500 µm

2.2.3 Channel recognition

iPBLF enables not only data storage, but also detection of channel dimensions and positions, marking and determination of regions of interest like on-chip interrogation zones, as shown in **Figure 2:10**. The fluorescence along the channel wall edges always appears higher and we used this to estimate the actual width of a microfluidic channel, by using the edge detection feature of open-source software Fiji (ImageJ). In another setting, we marked zones of interest with custom-made codes. These can be used, for example, to give feedback to the motorized stage of a microscope for automatic alignment of objectives to the microfluidic interrogation zones, followed by subsequent experimental data acquisition.

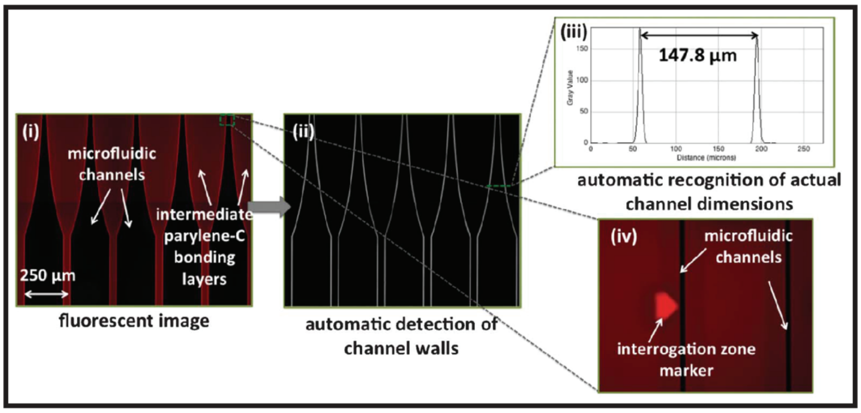
(i)
microfluidic channels
intermediate parylene-C bonding layers
250 µm
fluorescent image
(ii)
automatic detection of channel walls
(iii)
147.8 µm
Gray Value
150
100
50
0
0
50
100
150
200
250
Distance (microns)
automatic recognition of actual channel dimensions
(iv)
microfluidic channels
interrogation zone marker

Figure 2:10 | Use of iPBLF for detection of geometrical parameters on-chip. (**i**) a single fluorescent image, from which (**ii**) channel positions, (**iii**) actual channel dimensions and (**iv**) marked interrogation zones can be detected.

2.3 Programming and use of Parylene C fluorescence as a quantitative on-chip reference

Fluorescence microscopy is widely used as a signal readout method in microfluidic platforms [5]. In many applications, the intensity of the fluorescence signal is used to quantify the extent or concentrations of the biological entities on-chip. One popular application is that of on-chip immunoassays [73], where the obtained fluorescent intensity is used to quantify the target antigen concentration. In addition, the fluorescent intensity obtained from solutions of fluorescently labelled molecules within microchannels can be used to estimate their surface concentration [74]. Other applications include protein expression quantification using green fluorescent protein (GFP)-tagged molecules or immunocytochemical signals [75]. Despite its widespread use, achieving a reliable quantification of the fluorescent signal is not straightforward in practice. The measured fluorescent signal intensity depends on a large number of parameters that are difficult to standardize universally. These parameters can be listed as: (i) variations in the intensity of the light source over time, (ii) magnification, numerical aperture, depth-of-focus and transmission spectra of the objectives, (iii) absorption in the light path of the microscope, (iv) efficiency and transmission spectrum of the fluorescent filters, and (v) pixel size, binning, spectral sensitivity, dark noise and frame rate of the imaging sensor. In order to be independent of these variations, several calibration steps and a meticulous treatment of the data are required, even when using the same microscope hardware [76]–[80]. A typical approach to build such reference involves the use of fluorescent dyes embedded in a polymer layer [81]–[85], a standard technique that implicates difficult preparation steps. Alternatively, a method concerning gelatine-based probes used as phantoms was proposed [86], but this approach is too specific for the intended purpose of being a generally usable method. Commercially available solutions are also proposed, for example, kits of fluorescent compounds that can be added to the sample. Fluorescent microspheres custom-mounted on glass slides are also proposed as a commercial solution. Although very reliable, most of these techniques require a trained person, long preparation steps to add external compounds, or the exchange of the sample under the microscope. Such kind of calibration is particularly problematic when it comes to microfluidic systems that claim robust mobile or point-of-care applications, and for which the user has less possibilities to calibrate the instrument. Besides the clear advantage of an *in situ* reference for portable applications, we have shown recently that a more quantitative fluorescent signal is also at the basis of a more accurate read-out of biomarker expression on tissue slices obtained from breast cancer tumour samples, as evidenced by a fluorescent immunohistochemical assay [65].

Therefore, if incorporation of a fluorescent on-chip reference next to the measurement point could be realized, this would be an ideal solution for fluorescent lab-on-a-chip applications. Firstly, this would not only prevent removing the sample to acquire the reference image but also would enable numerous analyses where the comparison to the reference is required in real time. Next, read-out of such reference could also immediately correct for temporal variations, like blinking in the intensity of the light, and hence can render each data point comparable, both during the course of a single experiment and when studying multiple samples. Finally, such mobile diagnostic applications could be run on any image reader without relying on the user for the calibration.

A number of methods that integrate an on-chip fluorescent reference by making use of external materials and additional fabrication steps have been presented in the literature. For example, in one study, Hoi *et al.* incorporated colloidal crystals inside a microchannel system and used them as a reference wavelength calibration line for online optical analysis [87]. However, this approach increases the cost and complexity of devices, by introducing non-standard materials and additional steps in the fabrication protocol. Moreover, placement of the reference to a pre-defined position on the chip constitutes another challenge.

A reliable on-chip reference should (i) be located in close proximity to the sample so that both are exposed to the same experimental conditions, (ii) be deterministically written prior to the assay and (iii) show both time and illumination stability under the experimental conditions chosen for the fluorescent assay.

In this section, we printed on-chip references nearby a microfluidic channel containing fluorescent molecules, and demonstrated that, using the reference, we can correct for externally induced fluctuations of the fluorescent signal, as originating from variations in the intensity of the lamp, or the magnification and numerical aperture of the objective. Importantly, the reference is realized by printing a fluorescent pattern using high power UV light. The low power light used subsequently to read out the fluorescent signal from our analyte will not impact on the fluorescence of the pattern, so that the latter is a true on-chip reference allowing quantitative analysis. Moreover, we show that this technique can also be used to determine the flow rate in a microfluidic channel, in which a fluorescent dye is transported.

2.3.1 Experimental setup

Figure 2:11a shows the layout of the microfluidic chip we have used in our experiments: it contains a microfluidic channel with a width of 50 µm, a height of 60 µm and connected to an inlet and an outlet. The white areas represent the parts of the chip, which have been etched and are without Parylene C coverage, i. e. the microfluidic channel and circular structures, which are used to homogenize the pressure distribution during bonding. **Figure 2:11b** is a schematic cross-section of the chip along the A-A’ and B-B’ profiles of **Figure 2:11a**, also showing that the inlet and outlet are etched from the backside of the wafer. A PMMA holder was used as interface with the microfluidic chip via o-rings. Commercial fluidic connectors (IDEX Health & Science, WA, USA) were used to connect the system to a neMESYS low-pressure syringe pump (Cetoni GmbH, Germany) for flowing the liquids through the microfluidic channel.

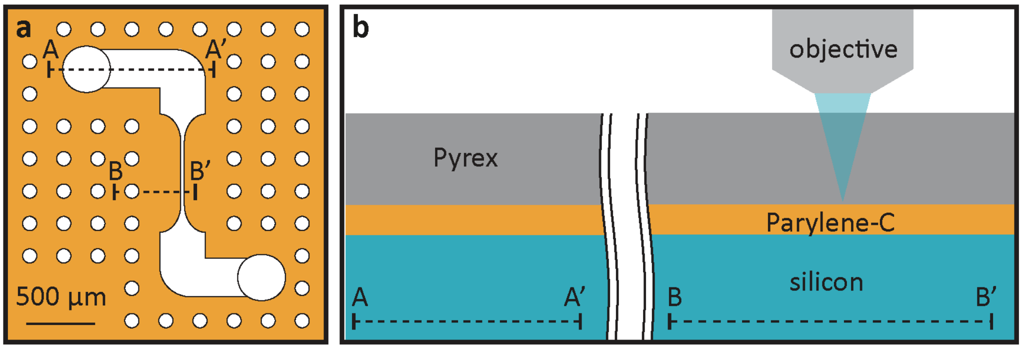

Figure 2:11 | Schematic view of the microfluidic device. **(a)** Top view showing the microfluidic channel with in- and outlets. Several circular structures were etched together with the microfluidic channel in order to more uniformly distribute the pressure during bonding. **(b)** Schematic cross-section of the chip along the A-A’ and B-B’ profiles of **Figure 2:11a**, showing the position of the Parylene C layer and the backside-etched hole for the inlet. For illumination and observation, the microscope objective is focused on the Parylene C layer.

The iPBLF can be used for several applications where the presence of a reference is required to interprete quantitatively fluorescent experiments and compare the results of different samples. For our quantitative sensing experiments, we printed a fluorescent reference dot nearby a microfluidic channel with the goal of having it on the same field of view as the fluorescent sample liquid flowing through the channel. In this manner, the fluorescence of the sample can be automatically compared to that of the fluorescent reference and, thus, to other experiments. In **Figure 2:12**, we define the areas of interest for calculating in a quantitative way the fluorescence signal of the liquid.

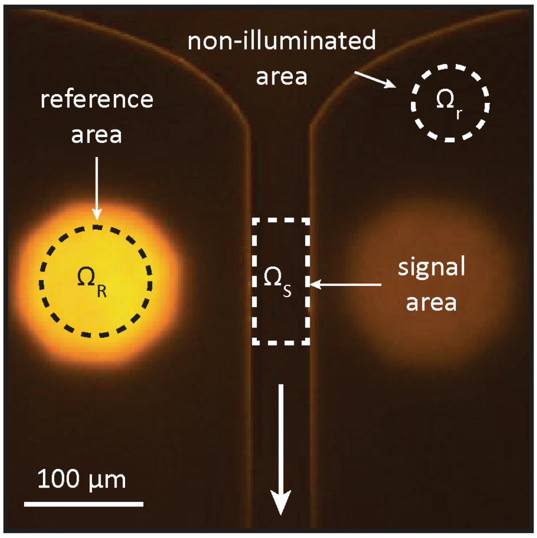

Figure 2:12 | Fluorescent image of the microfluidic channel and the on-chip reference. Image observed in the Blue/Green channel. The fluorescent signal of the solution flowing in the channel is obtained from the pixels in the area Ω_S and is referenced to the pixels of the area Ω_R by using Eq. (2.5).

Similarly, to the assessment of the dot printing and iPBLF characterization above, we defined the different regions of interest as

- $p_i \in \Omega_S$, where Ω_S is the sample region from which the extracted mean signal is p_S. This region is where the liquid sample to be analysed is located.
- $p_i \in \Omega_R$, where Ω_R is the reference region, from which the extracted mean signal is p_R.
- $p_i \in \Omega_r$, where Ω_r is the non-illuminated region of Parylene C from which the extracted mean signal is p_r. This region is used to evaluate the autofluorescence of the background.
- The relative fluorescence is then calculated as

$$F_{rel} = \frac{p_S - p_r}{p_R - p_r} \tag{2.5}$$

With Eq. (2.5) we calculate the intensity of the sample under analysis with respect to the intensity of the reference dot. Note that, in this experiment, there is only 'observation' of the fluorescence and no UV 'illumination'. The latter was needed only for printing of the on-chip reference. Moreover, as we performed the fluorescent observation experiments in the stationary flow regime, we do not consider the time depence of Eq. (2.5).

2.3.2 Concentration sensor

In this experiment, we applied a stationary flow of different concentrations of FITC-labelled IgGs (F9137, Sigma Aldrich, USA) at 0.5 $\mu l/s$, corresponding to an average flow velocity of 170 mm/s, i.e. a fluorophore in the liquid stream on the average passes through the microchannel in 1.5 ms. Under these conditions, the fluorescent signal originating from the channel is uniform across its width and the flow rate was high enough to refresh the molecules in the channel so that the bleaching effect was insignificant, even though the lamp was continuously on. The antibodies (12.3 $\mathrm{mg/ml}$) were diluted in a solution of 0.05% V/V Tween in PBS and were delivered in the microfluidic channel using the syringe pump.

Once the stationary flow conditions achieved (we start the experimental observation for safety at least 2 minutes after starting the flow), we acquired an image like the one shown in **Figure 2:12** in the Blue/Green channel. We repeated the same experiments at different dilutions, the highest antibody concentration being 123 $\mu\mathrm{g/ml}$. In order to compare the results obtained from the experiment under different external conditions, we ran the same set of experiments varying the excitation intensity (100, 50 and 25%) and the objectives used to acquire the images (20x and 10x). We then compared the intensity of the signal in the region Ω_S with and without making use of the reference dot. In the case in which no referencing was performed, the values of p_S were directly plotted against the normalized concentration (normalized by the highest value) of the antibodies (**Figure 2:13a**). However, when the signal obtained from the identical sample set was processed with Eq. (2.5), correcting the values with respect to the reference dot, a single linear plot (**Figure 2:13b**) was obtained, independent of the imaging parameters. This clearly demonstrates the efficiency of the on-chip programmed quantitative iPBLF reference in calibrating fluorescence intensity measurements.

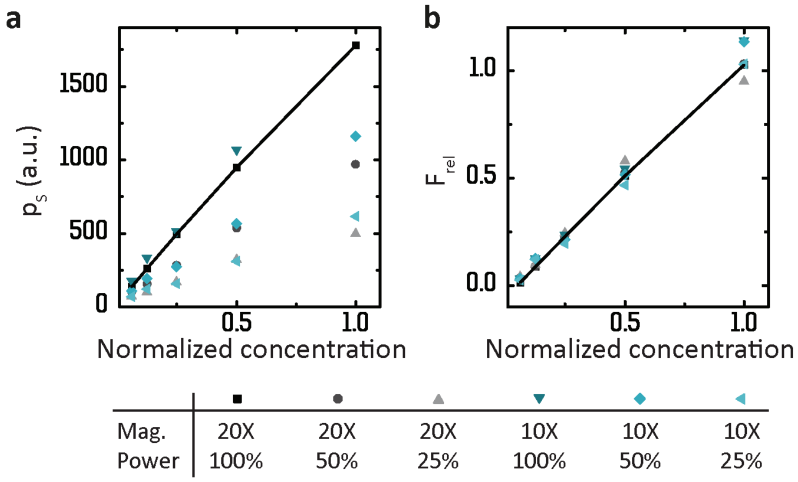

Figure 2:13 | Measurements of the fluorescent signal from a solution of FITC-labelled antibodies flowing in the microfluidic channel. The relative lamp power (P) and the objective magnification (M) are represented as follows: ■ P:100% M: 20x, ● P: 50% M: 20x, ▲ P:25% M:20x, ▼ P:100% M: 10x, ◆ P: 50% M: 10x ◀ P:25% M:10x. (**a**) Values of the average pixel intensity p_S from the area Ω_S plotted against the normalized concentration of the solution flowing in the microfluidic channel. (**b**) Values of F_{rel} calculated using Eq. (2.5) and plotted versus the normalized concentration of the solution in the channel. The curve of this plot is independent on the different hardware configurations used for the experiment.

2.3.3 Flow rate sensor

In this experiment, we lower the flow rate, at which we deliver the antibodies through the microfluidic channel until the bleaching rate and the molecules refreshment rate become comparable. Due to the parabolic profile, characteristic of liquid flowing in a channel driven by pressure, the rate of molecule refreshment in the centre of the channel is higher than the one closer to the edges. We consider a parabolic flow velocity in the channel as

$$v(x) = k \cdot (w - x)x \tag{2.6}$$

with v the velocity in the channel, y the direction along the channel, x the direction across the channel and w its width. The middle of the channel, where $x = w/2$, corresponds to the maximum velocity of the flow and, thus, to the point where the refreshment rate is the highest. In order to visualize the parabolic flow profile, we plotted the fluorescent signal across the line A-A' of **Figure 2:14a**, which measures both the reference and the fluorescent signal of the liquid. **Figure 2:14b** shows the parabolic-like profiles of the signal for a dilution of 1/100. We again use Eq. (2.5) to calculate F_{rel}, with p_S taken now as the value of the average pixel intensity for a given value of x along the line A-A'. The average values p_R and p_r are again used as the reference and background, respectively. The same profile was plotted for flow rates of 20, 15, 10, 8, 6, 4, 2 and 1 $\mathrm{nl/s}$.

In order to find a relationship between the fluorescent intensity observed in the channel and the flow rate applied, we integrated F_{rel} across the width of the channel: $A(y) = \int_{-w/2}^{w/2} F_{rel}(x, y)dx$. The area $A(y)$ under the curve obtained with this calculation represents the overall fluorescent intensity that results from the molecules that were still unbleached with blue light at a given *y*-position. In **Figure 2:14c**, we plotted the integrated signals A against the inverse of the flow rate Q^{-1}. The reason for this choice is that Q^{-1} gives a 'mean' time that the antibodies have spent under illumination, during which bleaching can occur. We also plotted the experimental results obtained when flowing the antibodies with a dilution of 1/200. We can clearly observe that there is a linear dependence of A with respect to Q^{-1}. Hence the measured value of A can be used to determine the flow rate, once calibration of the curve is done by applying a known flow rate for a given fluorescent molecule concentration.

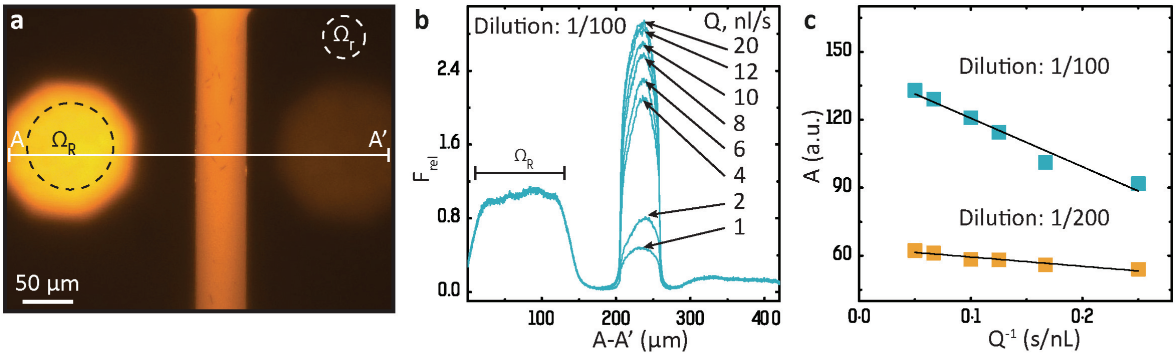

Figure 2:14 | Measurements of the fluorescent signal from a solution of FITC-labelled antibodies flowing in the microfluidic channel under bleaching conditions (slow flow rate) with blue light. (a) Fluorescent image of the microfluidic channel and the on-chip reference, observed in the Blue/Green channel. The fluorescent signal of the solution flowing in the channel is obtained from the pixels along the profile A-A' and is referenced to the area Ω_R by using Eq. (2.5). **(b)** Values of F_{rel} across the profile A-A' for the flow rate Q taking the values of 20, 15, 10, 8, 6, 4, 2 and 1 $\mathrm{nl/s}$, respectively. **(c)** The integrated intensity (area under the curve) across the channel, A, as a function of Q^{-1} for two antibody concentrations (the 1/100 dilution corresponding to a concentration of 123 $\mu\mathrm{g/ml}$).

2.4 Conclusions

We showed programming of iPBLF and its characterization as a function of the ultraviolet (UV) dose and Parylene C thickness. This technique requires no additional steps in the fabrication of the microfluidic chip and the fluorescence reference zones can simply be incorporated by local exposure to UV light after fabrication.

We presented the use of iPBLF for data storage on a microfluidic chip by using a fluorescent microscope and filters corresponding to common commercial dyes. This was a result of the complementary behaviour of iPBLF intensity under illumination to UV and green light. The possibility to induce or erase fluorescence was then exploited to program dynamically a memory region for many cycles. Finally, we demonstrated use of dynamically programmable iPBLF to store data on a microfluidic chip and to detect actual layout, channel dimensions, and regions of interest. If coupled with motorized stages, or miniaturized optical systems, like those that can be found in commercial data storage systems like DVDs, it may easily be possible to realize a fully automated protocol application optimized for each microfluidic chip using simultaneous optical information writing and experimental data collection. In fact, this is likely to be a must for industrial exploitation of microfluidics in biomedical applications, which requires a very high level of reproducibility and operational control of device parameters. The major advantage of this method relies on the possibility to modify the fluorescence of an existing structural layer just by illuminating with UV light after fabrication, with no additional materials or steps. In addition, a standard mask aligner is sufficient to assure printing of fluorescent references on all devices of a wafer. The demonstrated programming technique showed how to program the fluorescence to define a high and low intensity level, as required by digital information storage.

Quantitative programming of iPBLF proved to be very useful as an on-chip fluorescent reference, and opens ways to calibrate fluorescent intensity measurements using protocols of low complexity. The presented method eliminates the need for modifying fabrication flows and materials associated with the accommodation of the on-chip reference, and it can easily be scaled up to the wafer level by applying UV light with a mask aligner. Moreover, low-complexity processing algorithms allow multiple measurements, including but not limited to the demonstrated analyte concentration and the flow rate determination in a channel. We anticipate that point-of-care and mobile diagnostic applications that require the measurement of a fluorescent signal can benefit from the presented method in reducing the dependence of the outcome of the test on the skills of the operator and in simplifying the procedures required for calibration. Calibration of microfluidic chip protocols for enabling quantitative fluorescent measurements, in which inter- and intra-experiment variations are ruled out, is still lengthy and time-consuming, even in the laboratory. Quantitative programming of iPBLF can simplify and shorten these procedures, and is particularly of use for automatized biological experiments, where data collection with large image stacks is required.

Chapter 3 Continuous quantification of HER2 expression by microfluidic precision immunofluorescence estimates *HER2* gene amplification in breast cancer

Chromogenic IHC is omnipresent in cancer diagnosis, but has also been criticized for its technical limit in quantifying the level of protein expression on tissue sections, thus potentially masking clinically relevant data. Shifting from qualitative to quantitative, IF has recently gained attention, yet the question of how precisely IF can quantify antigen expression remains unanswered, regarding in particular its technical limitations and applicability to multiple markers. Here we introduce microfluidic precision IF, which accurately quantifies the target expression level in a continuous scale based on microfluidic IF staining of standard tissue sections and low-complexity automated image analysis. We show that the level of HER2 protein expression, as continuously quantified using microfluidic precision IF in 25 breast cancer cases, including several cases with equivocal IHC result, can predict the number of *HER2* gene copies as assessed by fluorescence *in situ* hybridization. Finally, we demonstrate that the working principle of this technology is not restricted to HER2 but can be extended to other biomarkers. We anticipate that our method has the potential of providing automated, fast and high-quality quantitative *in situ* biomarker data using low-cost IF assays, as increasingly required in the era of individually tailored cancer therapy.

This chapter is adapted from the following publication:

- **D. G. Dupouy**, A. T. Ciftlik, M. Fiche, D. Heintze, B. Bisig, L. de Leval, and M. A. M. Gijs, “Continuous quantification of HER2 expression by microfluidic precision immunofluorescence estimates HER2 gene amplification in breast cancer,” *Scientific Reports*, vol. 6, p. 20277, Feb. 2016

3.1 Introduction

With the advancement of personalized cancer medicine, precise molecular profiling of tumors is gaining significant importance in routine diagnostic pathology [88], [89]. With the evolution towards personalized treatments tailored to the molecular features of malignant tumors, the last decade has witnessed an increasing use of molecular analysis approaches, including but not limited to FISH, mRNA expression profiling techniques and next generation sequencing (NGS). IHC, however, remains by far the most used method in the routine diagnostic evaluation of tumor tissues, with the advantages of wide availability, low cost, and preservation of the information-rich morphological context. While ELISA and Western blotting are also useful protein quantification techniques and eventually can be used for testing large amounts of cells of controlled HER2 status, they require fairly large lysed samples [90] and therefore are less suitable for assessing protein expression levels in the morphological context of the tissue slide.

Continuous quantification of protein expression in tumor sections has long been the missing link between methods analyzing nucleic acids and conventional IHC. The majority of IHC tests currently used in clinical diagnosis cannot quantify the Ag expression but rather perform a binary or semi-quantitative assessment as interpreted by the pathologist [91]. An example of such semi-quantitative tests is the assessment of the HER2 protein expression level in breast cancer, for which the scoring can have four different levels: 0, 1+, 2+ or 3+ [57]. This non-continuous assessment results in a loss of information regarding the Ag expression level [46], [47]. Comparison studies between IHC and FISH methods for HER2 have been widely performed in clinical research [92], [93]. Yet, if a routine method that precisely quantifies Ag expression in tissues while preserving the morphology could be established, not only would this reduce the requirement for expensive complementary gene analysis but also increase the precision of diagnosis, prognosis and the success of targeted therapies, in clinical trials and routine patient care.

In this context, as clinical pathology moves from qualitative to quantitative, IF is gaining relevance in the research settings and laboratory-developed tests, mainly due to its increased capacity to measure the signal intensity of one or more biomarkers as compared to traditional chromogenic techniques [47], [94]. Several image processing techniques that quantify the extent of IF signal have already been reported in the literature [95], [96]. However, there is little or no evidence suggesting that the IF signal *per se* can be used to precisely quantify Ag expression amount on tissue sections. Indeed, due to the kinetics of Ab-Ag binding, a 2-step IF assay does not result in a signal that is linearly proportional to the Ag expression [36], [74], which potentially ends up in a misleading quantification and, hence, obscures the potential of IF in providing precise biomarker data. There is therefore a need to find out how precise IF can be in continuously quantifying tissue biomarkers. IF has a high potential to quickly replace routine chromogenic stain-based diagnostic IHC, since it would use the same primary Abs, established sample preparation techniques and, hence, involve the less significant change from current laboratory practice. Therefore if a proportional relationship between signal intensity and Ag expression could be established, this could eventually allow IF to precisely quantify the Ag expression level, and evolve as a routine diagnostic tool that establishes the missing link.

We have recently introduced a microfluidic tool, called MTP that increased the accuracy of semi-quantitative IF biomarker scoring in histopathological tissue sections [65]. However, it just provided a better semi-quantitative scoring, and the use of this technology still did not show the quantification of the biomarker expression. Yet, this technology has a high potential to be a starting point in reaching continuous quantitative IF. Here, we introduce microfluidic precision IF, a method that precisely quantifies the target

Ag expression in a continuous scale based on double staining of standard tissue sections with MTP and low-complexity automated image analysis. In the following, we selected 25 invasive breast carcinoma cases whose HER2 biomarker expression ranged across a large range of values known by routine diagnostics, as assessed by the two conventional methods used (*i.e.* IHC and FISH), and for which several cases presented equivocal results. With these cases we show that, using continuous quantification of the HER2 protein expression by microfluidic precision IF, one can estimate the number of copies of the coding gene, as assessed by FISH. Later, in a proof-of-concept experiment, we prove that the MTP fine-tunes immunoreactions on the tissue surface in a way that allows an IF staining to establish a linearly proportional relationship between the IF signal intensity and its Ag expression level. Therefore, we hypothesize that the working principle is not restricted to the above cases, and in principle, can be extended to other biomarkers. We anticipate that this method has the potential to provide automated and precise continuous quantitative *in situ* biomarker data using low-cost immunofluorescence assays, as increasingly required for personalized cancer therapy.

3.2 Experimental

3.2.1 Study design

This pilot study tested the ability to quantitatively score the level of overexpression of the HER2 protein in breast carcinoma samples using the MTP and compare it with the *HER2* gene copy numbers (N_{FISH}) value and the *HER2*/CEP17 ratio provided by routine diagnostic. Patient samples were obtained from the Institute of Pathology, Centre Hospitalier Universitaire Vaudois (CHUV), Université de Lausanne (UNIL), Lausanne, Switzerland. Twenty-five samples from patients were carefully selected to span across a wide range of N_{FISH} values, assessed at the Institute of Pathology according to 2013 ASCO recommendations [57]. For the MTP analysis, the 25 cases were grouped into 5 batches that were processed sequentially. One positive (IHC 3+ score) and one negative (IHC 0 score) control sample was each time included in the batch.

3.2.2 Tissue preparation and reagents

Breast carcinoma samples were obtained from the bio-bank of the Institute of Pathology and provided as 4 μm FFPE sections mounted on Super Frost Plus slides (Menzel-Glaser, Germany). Tissue samples were first dehydrated for 10 min at 65 °C, then dewaxed using Histo-clear (National Diagnostics, GA, USA) for 10 min and rapidly rehydrated using ethanol solutions in decreasing concentrations (100%, 95%, 70% and 40% vol/vol) (Sigma-Aldrich, MO, USA). Subsequently, heat-induced Ag retrieval was done using sodium citrate buffer pH 6 (code: S1699 Dako, Denmark) for 10 min at 95 °C in a hot bath. The samples were then cooled down to room temperature for 20 min and immersed in phosphate buffered saline pH 7.4 (PBS) (Sigma Aldrich, MO, USA). The histological slides were inserted into the device to run the MTP staining assay. PBS was used as a buffer for cleaning and priming of the fluidic path. Double-staining was performed using rabbit anti-human c-erbB-2 oncoprotein (code: A0485, Dako, Denmark) and mouse anti-human cytokeratin, clone AE1/AE3 (code M3515, Dako, Denmark), as primary antibodies, with a concentration of 1.28 $\mu\mathrm{g/ml}$ and 1.02 $\mu\mathrm{g/ml}$, respectively. For fluorescent detection, Alexa Fluor 594 goat anti-rabbit IgG (H+L) (code: A-11037, Life Technologies, CA, USA) and Alexa Fluor 647 goat anti-mouse IgG (H+L) (code: A-21236, Life Technologies, CA, USA) secondary antibodies, at a concentration of 50 $\mu\mathrm{g/ml}$, were employed. Nuclear counterstaining was realized using 4',6-diamidino-2-phenylindole (DAPI), included in Fluoroshield (code: F6057, Sigma Aldrich, MO, USA) mounting solution. All the antibodies were dissolved in a 0.05% V/V solution of Tween 20 (code: P137-9, Sigma Aldrich, MO, USA) in PBS.

3.2.3 Routine analysis

For routine determination of HER2 status of breast cancer cases at the Institute of Pathology, IHC was performed on 4 µm FFPE sections on the Ventana Benchmark automat (Ventana Medical Systems, AZ, USA). The samples were stained using Ventana anti-HER2/*neu* Ab (clone: 4B5) and scored according to current ASCO/CAP guidelines [57]. FISH was done manually on 4 µm FFPE sections using the PathVysion HER-2 DNA probe kit (Abbott Molecular, IL, USA). Signal analysis was performed on a minimum of 40 nuclei per case after screening of the whole section.

3.2.4 Device fabrication and experimental setup

The MTP was designed using Virtuoso (Cadence, CA, USA) and then fabricated via DRIE of microfluidic channels on a silicon substrate, followed by bonding of a Parylene C-coated Pyrex wafer as described in chapter 1, thereby forming 100-µm high and 250-µm wide microfluidic channels. The details of this fabrication technique can be found elsewhere [16], [17], [65].

The MTP formed a fluidic halve-chamber that was reversibly clamped with a tissue slide using the force provided by a permanent magnet **Figure 3:1a**. When forming the MTP-glass slide fluidic chamber, the histological glass slide was clamped against the MTP via a polydimethylsiloxane gasket, both to fix the height of the reaction chamber to 100 µm and to prevent leakage. For interfacing the MTP with external fluidic control systems, a polymethylmetacrylate holder is assembled with the MTP. Fluid manipulation was realized using five syringe pumps (Cetoni, Germany) that were filled with the required reagents and connected to the inlet of the MTP via the holder **Figure 3:1b**.

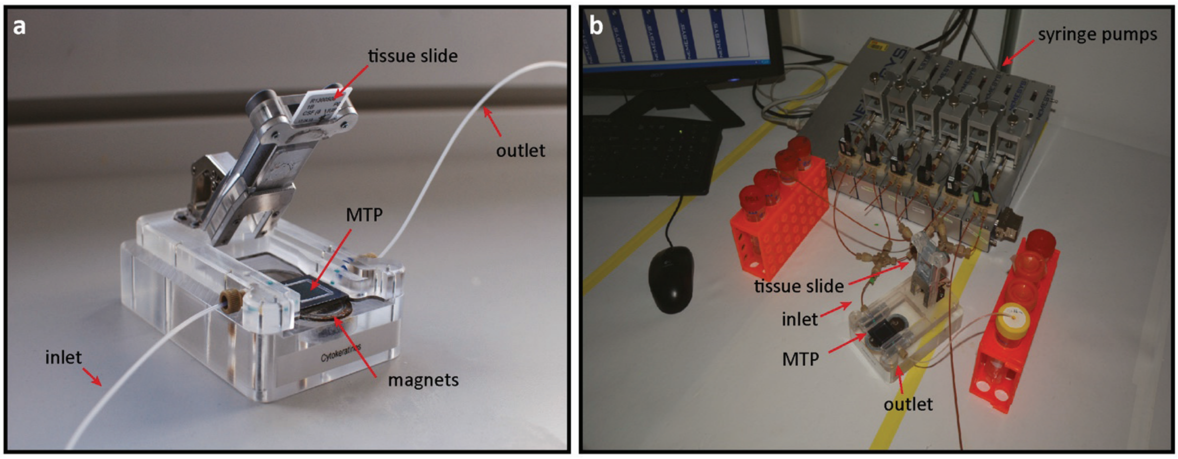

Figure 3:1 | Experimental setup. (a) Assembled MTP; the microfluidic chamber, formed by clamping the tissue slide to the MTP, is opened to show the different parts and the loading mechanism. **(b)** Overview of the experimental setup.

3.2.5 MTP staining protocol

After clamping the MTP with the glass slide, the staining protocol lasted 10 minutes and detailed in **Table 3:1**. PBS, used to wash the chamber in between steps, was delivered at 25 µl/s for 10 seconds. Ab solutions were delivered at 10 µl/s for 12 seconds, and incubated for 2 minutes with a slow flow of 20 nl/s. Upon finalization of the staining protocol, the tissue samples were washed off-chip with deionized water for ten seconds and mounted using 170-µm coverslip using a DAPI-containing solution. For our experimental design related to the incubation time, we considered the typical values of IgG Ag-Ab binding constants k_{on}

(~10^6 M^{-1}) and k_{off} (~10^{-3} s^{-1}) [97], [98]. The bulk Ab concentration c_b (~10^{-8} M) was chosen large enough so that it is not a limiting factor for the Ab surface coverage and the IF signal in a Langmuir isotherm hypothesis. The binding constants allow to calculate the desorption time $t_d = 1/k_{off} \sim 10^3$ s, while the time constant of the recognition reaction is $t_d = 1/(k_{on}\, c_b + k_{off}) \sim 10^2$ s. This forms the basis for our choice of a few minute incubation times.

Table 3:1 │ MTP immunohistochemical staining protocol.

Reagent	*Flow duration (s)*	*Incubation time (min)*	*Total time (s)*
PBS buffer	10	-	10
Anti-human c-erbB-2 oncoprotein	12	2	132
PBS buffer	10	-	10
Anti-human cytokeratin, clone AE1/AE3	12	2	132
PBS buffer	10	-	10
AF 594 goat anti-rabbit IgG (H+L)	12	2	132
PBS buffer	10	-	10
AF 647 goat anti-mouse IgG (H+L)	12	2	132
PBS buffer	10	-	10
Total	98	8	578

3.3 Imaging processing protocol

3.3.1 Fluorescence image acquisition

Slides were inserted in an automated epi-fluorescent microscope (Axio Imager M2m, Zeiss, Germany) and mosaic images were obtained using a CCD camera. Images in three fluorescent channels, corresponding to the signals of DAPI, CK and HER2, respectively, were automatically obtained. Autofocusing, acquisition, scanning and stitching were done automatically. Prior to analysis, all images were checked if they contained artifacts that could influence the analysis. The average image acquisition varies from 10 to 40 minutes, depending on the size of the sample.

3.3.2 Determination of the regions of interest for interrogation of the HER2 signal

HER2 protein is situated on epithelial cell membranes. We performed double-staining IF assays using CK as a second marker in addition to the HER2 analysis, due to its expression in all epithelial cells, so that the information on the CK channel could be used to define the areas where the expression of HER2 should be interrogated. ImageJ macros were applied tile-by-tile (n=40482). To do this, we built an auto-thresholding algorithm that determines where CK is expressed to define the region of interest. Similarly, the information in the DAPI channel was used to identify the nuclei as areas that should not be interrogated, as HER2 does not constitute a nuclear marker. In HER2-overexpressing samples **Figure 3:2a**, the use of HER2 signal alone would be clearly sufficient to determine the regions of interest; for tumors that do not strongly overexpress HER2 **Figure 3:2b**, it would be difficult to distinguish epithelial cells from surrounding parts in the tissue. Especially in these cases, employing the signal in the CK channel allowed us to assure that the regions of interest for interrogation of the HER2 signal corresponded to epithelial cells, independent from the intensity of the HER2 signal.

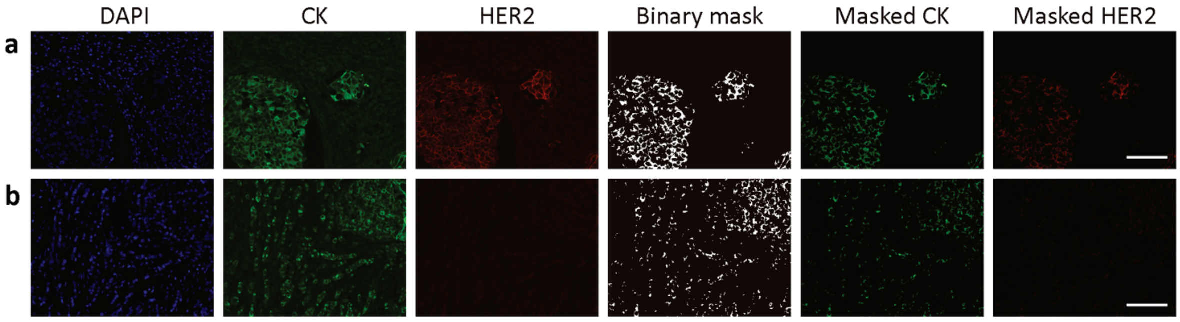

Figure 3:2 | Example of image tile processing for MTP analysis. The image processing algorithm is applied to a case where HER2 is overexpressed **(a)** and not expressed **(b).** The algorithm uses the DAPI channel to mask the locations of the nuclei, as they constitute an area that should not be examined, while the CK channel indicates the location of epithelial cells, i.e. exactly the areas where the HER2 and CK signals should be interrogated. This allows constructing a binary mask by which one can assign a single tile-averaged value for the CK and HER2 signals, obtained from the areas of interest only. Scale bar: 100 μm.

As a result of this procedure, every tile was assigned an average signal value both for CK and HER2. The thus obtained CK signal intensities were analyzed and filtered, in a case-by-case fashion, in order to remove from further analysis, the tiles that had none or a few epithelial cells. In particular, these tiles showed a CK average that felt below a given threshold and were automatically filtered out from the dataset (**Figure 3:3**). Finally, *de facto* establishing an upper threshold of the CK signal, we removed the 5% brightest tiles for each case, to account for possible artifacts like small agglomerates of fluorophores that eventually result in saturation of the fluorescent signal intensity. All tiles that showed a CK value above the lower and below the upper thresholds were kept for further analysis.

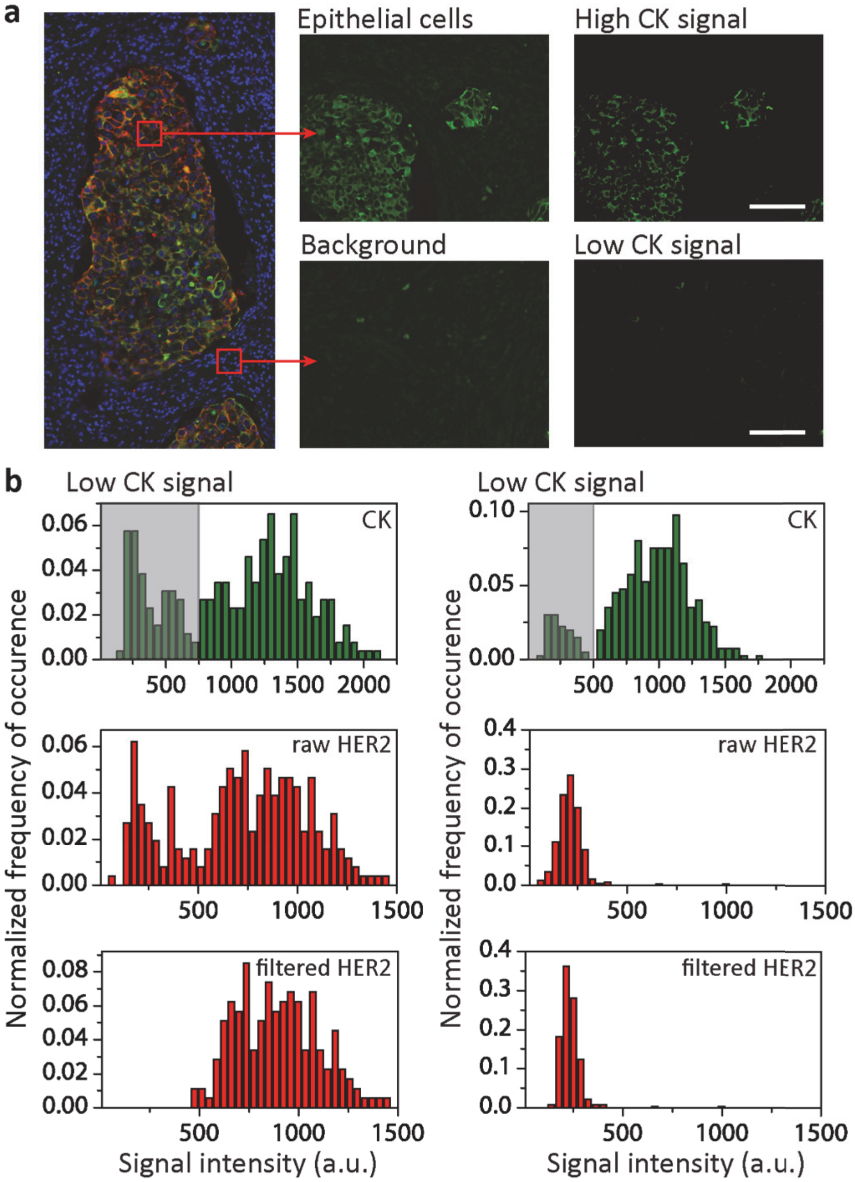

Figure 3:3 | Use of CK filter to obtain the HER2 histogram. (a) Example of tissue areas with (top) and without (bottom) epithelial cells and visualized in the raw CK channel (two middle images) and after running the image processing algorithm (two right images). **(b)** Raw histograms of the intensity distribution of the CK (green, first row) and HER2 (red, second row) signals for a HER2 IHC 3+ case (left column) and a HER2 IHC 0 case (right column). The tiles that show a low CK signal intensity are removed from the histogram and the third row shows the HER2 histograms plotted after application of this CK filter. The latter histograms represent the data sets for further analysis. Scale bar: 100 μm.

The detailed steps of the image-processing algorithm can be found in **Table 3:2**. OriginLab software (OriginLab Corporation, MA, USA) was used to obtain scatter plots, histograms and statistical values. The image-processing algorithm takes approximately 20 minutes per batch, giving an average of 3 minutes per sample.

Table 3:2 | Image-processing algorithm.

inputs		operation	output
Tile-by-tile processing			
Raw CK tile	-	autothresholding	CK mask
Raw DAPI tile	-	autothresholding	DAPI mask
CK mask	DAPI mask	Binary product	Epithelial cells mask
Raw CK tile	Epithelial cells mask	Signal extraction of relevant regions only	Average CK signal
Raw HER tile	Epithelial cells mask	Signal extraction of relevant regions only	Average HER2 signal
Average CK signal	-	FOR loop (all tiles)	CK data matrix
Average HER2 signal	-	FOR loop (all tiles)	HER2 data matrix
Data matrix processing			
CK data matrix	-	autothresholding	Filtered CK matrix
HER2 data matrix	-	autothresholding	Filtered HER2 matrix
Data analysis			
Filtered CK matrix	-	binning	CK histogram
Filtered HER2 matrix	-	binning	HER2 histogram
CK histogram	HER2 histogram	x-y plot	HER2-CK scatter plot
CK histogram	HER2 histogram	Ratio calculation	HER2-CK ratio histogram
HER2-CK histogram		Gaussian fit	Mean and sigma

3.4 Results

3.4.1 Continuous signal quantification of double IF staining using

For this proof-of-concept study, we used the MTP to perform IF staining assays on FFPE sections of surgically resected human invasive breast carcinoma samples (**Figure 3:4a**). By clamping the MTP half-chamber with the tissue slide (**Figure 3:4b**), a shallow flow chamber with a height of 100 µm is formed, which constitutes a critical parameter of the working principle of the device [65], allowing fast and uniform delivery and washing of the reagents over a large surface (17 ×17 mm^2) of a tissue section, as explained above. The chosen microfluidic architecture allows distributing the bioreagents uniformly within the chamber. To minimize variations in the exposure time of tissue sections to the bioreagents, the transport of the latter should rely minimally on diffusion within in-plane directions. To address this problem, we designed a distributed microfluidic channel network that permitted homogeneous flow throughout the entire chamber and assured that convection was the dominant mechanism for the in-plane bioreagent transport.

This resulted in an IF signal that was more proportional to the Ag concentration than what could be obtained by traditional IHC methods. The samples were first incubated with primary Abs for HER2 and CK, in a sequential manner [99]–[101]. CK constitutes a marker for epithelial cells and it has been widely used in carcinomas to distinguish epithelia from stroma [102]–[104]. Furthermore, CK-based normalization has proven to be a useful technique to increase accuracy in the quantification of HER2, by compensating for variations in the staining quality of the samples [105]. In a second step, two fluorescently labeled secondary Abs were sequentially delivered into the chamber, first for HER2 and then for CK detection. Finally the slides were washed with deionized water and cover-slipped using a solution containing DAPI for nuclear counterstaining. After the staining process, the slides were automatically tile-by-tile scanned to obtain a mosaic image in three fluorescent channels, corresponding to the signals of DAPI, CK and HER2, respectively (**Figure 3:4c**,**d**). Each tile from the resulting mosaic images was then analyzed by running a custom-made image-processing algorithm that identified locations of CK expression and created a region of interest to limit the interrogation of the HER2 signal to epithelial areas only. Similarly, the information from the DAPI channel was used to remove the nuclei from the interrogation zones, as the HER2 and CK markers of interest are not expressed in the nuclei.

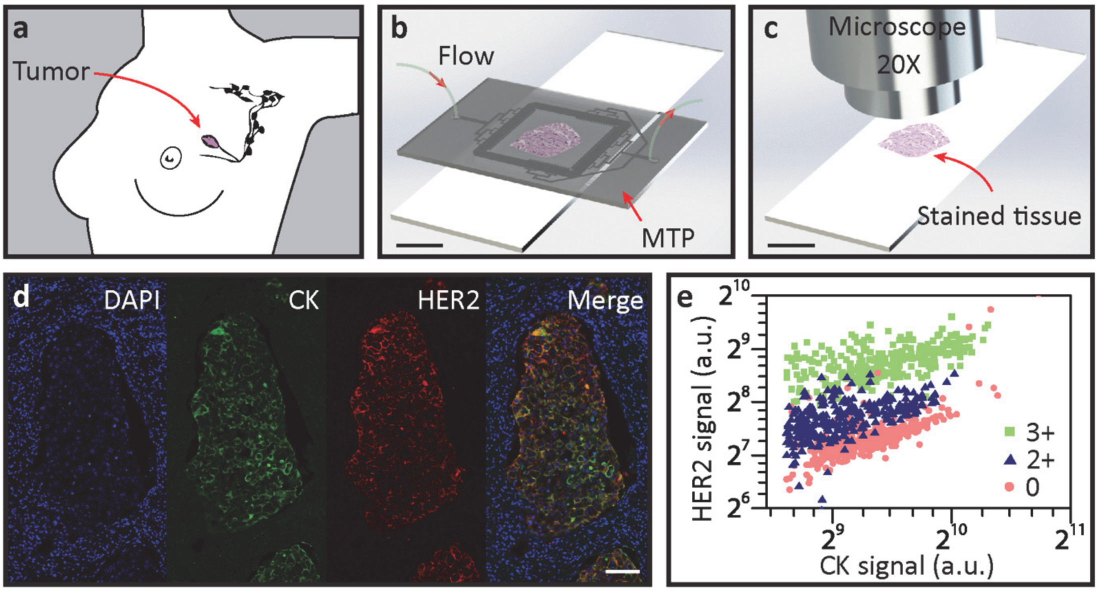

Figure 3:4 | Microfluidic precision immunofluorescence. (a) A breast tumor is surgically resected and is to be prepared in the form of thin histological tissue slides for analysis. **(b)** A slide is clamped with the MTP for IF staining. **(c)** Subsequently the slide is coverslipped with a DAPI-containing mounting solution and imaged using a fluorescent microscope. **(d)** Mosaic images of the stained slide are acquired in 3 fluorescent channels, corresponding to the signals of DAPI, CK, and HER2, respectively, and are automatically and tile-by-tile analyzed. **(e)** 2D scatter plot showing the correlation between the averaged HER2 and CK signal per tile, for three samples with different IHC score obtained from routine analysis: 3+ (green), 2+ (blue) and 0 (red). Scale bars: 10 mm for B and C, 100 µm for D.

3.4.2 Scatter plot signatures of HER2 protein expression in 25 breast cancer cases

As a result of the image-processing algorithm, 2D scatter plots were obtained, in which the averaged HER2 and CK signals per tile were represented as points. **Figure 3:4e** is an example of such scatter plot, in which an IHC HER2 2+ (equivocal) case is compared to a 3+ and a 0 case, the latter two being used as positive and negative controls, respectively. The data from each scatter plot were subsequently processed to provide statistical indicators of HER2 expression, which finally resulted in the 'MTP-score' of our analysis (see further).

We selected 25 invasive breast carcinoma cases, for which routine FISH analysis gave a wide range of N_{FISH} ranging from 1.9 to 15 (see **Table 3:3**). IHC results were equivocal in several cases out of this series. **Table 3:3** shows the classification of IHC results for these 25 cases following the 2013 ASCO/CAP interpretation guidelines [57] by two blinded experienced pathologists. By routine *HER2* FISH analysis, based on the N_{FISH} values, 10 cases out of the 25 were classified as negative ($N_{FISH} < 4$), 9 cases as positive ($N_{FISH} \geq 6$), and 6 cases as equivocal ($4 \leq N_{FISH} < 6$) (Neg, Pos, and Equ, respectively, in **Figure 3:5**). Although the 2013 ASCO/CAP guidelines for HER2 status classification also takes into account the *HER2*/CEP17 ratio, we decided for the purpose of this study to focus on the correlation between HER2 protein expression and N_{FISH}.

Table 3:3 | Results of the routine IHC and FISH analyses for all cases. Comparison is made between: **i)** IHC scoring following 2013 ASCO/CAP guidelines *(7)*; **ii)** N_{FISH} ; **iii)** *HER2*/CEP17 ratio; **iv)** HER2 status classification based on N_{FISH} ($N_{FISH} < 4$: Negative; $4 \leq N_{FISH} < 6$: Equivocal; $N_{FISH} \geq 6$: Positive) and **v)** HER2 status classification according to 2013 ASCO/CAP guidelines [57]. The aim of this process was to compare MTP results to the results of traditional IHC. Case 13 was removed from the dataset since a control H&E slide showed that only ductal carcinoma *in situ* (DCIS) was left on the sections used for the study. Similarly, case 14 was removed from the dataset because the section presented heterogeneous HER2 status, resulting in two N_{FISH} values. For cases 22 and 25, interpretation of routine IHC on the resected tumor specimen failed due to repeated tissue detachment from the glass slide. The IHC score indicated for these cases is the one found on the initial core biopsy.

Case	**i) IHC scoring**	**ii) N_{FISH}**	**iii) *HER2*/CEP17 ratio**	**iv) HER2 status based on N_{FISH}**	**v) HER2 status classification**
1	2+	1.9	0.76	negative	negative
2	2+	2.25	1.06	negative	negative
3	1+	2.30	1.01	negative	negative
4	1+	2.38	1.29	negative	negative
5	1+	2.54	1.20	negative	negative
6	0	2.70	1.19	negative	negative
7	0	2.80	1.22	negative	negative
8	2+	2.90	1.12	negative	negative
9	2+	3.10	1.60	negative	negative
10	1+	3.30	1.38	negative	negative
11	2+	4.38	1.80	equivocal	equivocal
12	3+	4.64	1.48	equivocal	positive
13	2+ (only DCIS left)	4.85	2.09	equivocal	positive
14	2+	4.90/2.50	2.7/1.3	equivocal (heterogeneous)	positive (heterogeneous)
15	1+	4.90	2.30	equivocal	positive
16	1+	5.80	2.80	equivocal	positive
17	2+	6.13	2.08	positive	positive
18	2+	6.80	1.80	positive	positive
19	3+	7.60	3.30	positive	positive
20	3+	9.35	5.30	positive	positive
21	3+	9.40	2.60	positive	positive
22	3+	10.70	4.90	positive	positive
23	3+	13.00	3.40	positive	positive
24	3+	15.00	3.00	positive	positive
25	3+ (core biopsy)	15.00	7.50	positive	positive

For the MTP analysis, we grouped the 25 cases into 5 batches and processed all samples in a batch sequentially in one experimental run. We used an automated algorithm to define the areas that had epithelial cells and were to be interrogated for the presence of a HER2 signal, from which we obtained the average CK and HER2 signal for each tile of the mosaic image, resulting in the scatter plots of **Figure 3:5**. From a statistical analysis of the latter, we calculated an MTP-score for each sample that clearly correlated with the N_{FISH} values obtained from routine analysis (see further). At first sight already, the scatter plots of **Figure 3:5** show that the samples assigned a low N_{FISH} value (< ~3) have a linear correlation of HER2 with CK, while for N_{FISH} > ~5, HER2 values get systematically higher and more dispersed.

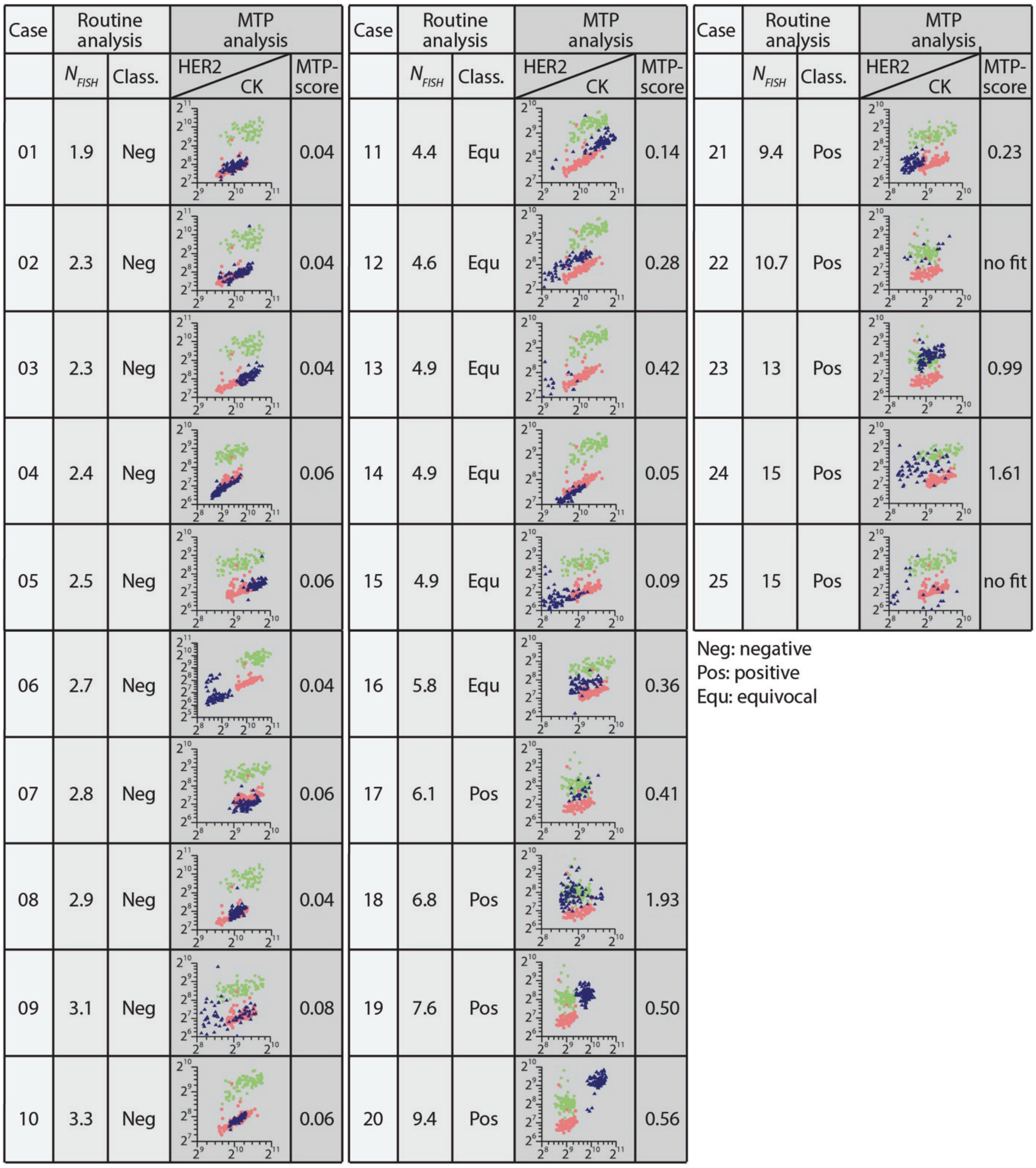

Case	Routine analysis		MTP analysis
	N_{FISH}	Class.	MTP-score
01	1.9	Neg	0.04
02	2.3	Neg	0.04
03	2.3	Neg	0.04
04	2.4	Neg	0.06
05	2.5	Neg	0.06
06	2.7	Neg	0.04
07	2.8	Neg	0.06
08	2.9	Neg	0.04
09	3.1	Neg	0.08
10	3.3	Neg	0.06
11	4.4	Equ	0.14
12	4.6	Equ	0.28
13	4.9	Equ	0.42
14	4.9	Equ	0.05
15	4.9	Equ	0.09
16	5.8	Equ	0.36
17	6.1	Pos	0.41
18	6.8	Pos	1.93
19	7.6	Pos	0.50
20	9.4	Pos	0.56
21	9.4	Pos	0.23
22	10.7	Pos	no fit
23	13	Pos	0.99
24	15	Pos	1.61
25	15	Pos	no fit

Neg: negative
Pos: positive
Equ: equivocal

Figure 3:5 | Scatter plot signatures obtained by MTP IF and the corresponding *HER2* gene copy number for 25 invasive breast carcinoma cases. The listed values for the cell-averaged *HER2* gene copy number (N_{FISH}) were obtained from FISH routine analysis. The HER2 status classification (Class.) by the pathologist is also given, based on N_{FISH} as follows: $N_{FISH} < 4$: Negative; $4 \leq N_{FISH} < 6$: Equivocal; $N_{FISH} \geq 6$: Positive. For the MTP analysis, the 25 cases were grouped into 5 batches and samples were processed sequentially in one run with the MTP, while one positive (IHC 3+ score) and one negative (IHC 0 score) control sample were each time included in the batch. An automated algorithm was used to determine the regions of interest with epithelial cells and remove the background for each tile of the mosaic image of a given sample. This resulted in one average HER2 and CK signal per tile, which is represented by a point in a scatter plot for each patient. The scatter plot shows the correlation between the tile-averaged HER2 and CK signals (blue), compared with the scatter plot data obtained from the IHC 3+ (green) and IHC 0 (red) control samples of the

batch. Analysis of the scatter plots, as further illustrated in **Figure 3:6**, provided a MTP score for each patient that clearly correlated with N_{FISH} obtained from routine analysis.

3.4.3 Automated scoring and correlation to routine *HER2* gene copy number

To exploit the scatter plot data of **Figure 3:5**, we implemented a data processing algorithm that compares the scatter plot of a case under interrogation to those obtained from absolute negative and positive control cases. This algorithm starts by calculating the ratio between HER2 and CK signals on a tile-by-tile basis. The thus obtained data array is then plotted as a histogram, representing the frequency of occurrence of a given HER2/CK ratio normalized to the number of tiles. **Figure 3:6** shows as examples the histograms obtained for five patients, to whom prior routine analysis attributed the following IHC scores: 3+ (green), 0 (red), and three cases (blue) from which two scored as 2+ and one as 3+ and had N_{FISH} values of 1.9, 4.4, and 9.4, respectively. The positive and negative controls were used as references of the expected HER2 signal intensities for each sample. For the three samples represented in blue, the histograms shifted more towards the right as the N_{FISH} increased, indicating an average increment in the acquired HER2 signal with respect to CK, when the number of *HER2* gene copies was higher. Moreover, the widening of the histogram for high N_{FISH} cases showed that the overexpression of HER2 also corresponded to a larger dispersion of the HER2 signal.

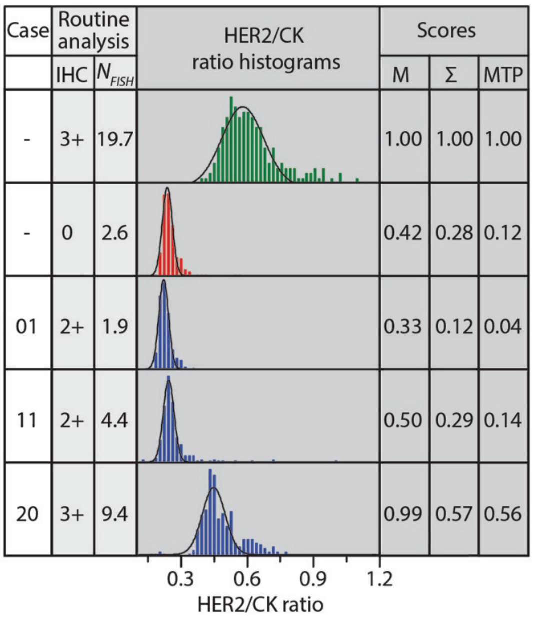

Figure 3:6 │ Automated comparison of a scatter plot to those of control cases. Routine analysis prior resulted in following IHC scores: one 3+ case (green), one 0 case (red), and three borderline cases (blue), the latter having N_{FISH} of 1.9, 4.4, and 9.4, respectively. In our data processing algorithm, the ratio between HER2 and CK signals was obtained on a tile-by-tile basis from the scatter plot data of **Figure 3:5**. The thus obtained population is plotted as a histogram, indicating the frequency of occurrence of a particular ratio; this frequency is normalized by the number of tiles for the given case. A Gaussian fit to the histogram allowed determining the mean HER2/CK value, which was normalized by the mean of the 3+ control sample in the batch, defining the M-score. Similarly, the standard deviation (σ) of the Gaussian fit, normalized by σ of the 3+ control sample, defined the Σ-score. The MTP-score is defined as the product of the M- and Σ -scores.

A Gaussian fit of a histogram allowed determining the mean HER2/CK value and normalizing this by the mean obtained for the IHC 3+ control sample in the batch defined the M-score. Similarly, we extracted the standard deviation (σ) from the Gaussian fit of a histogram and normalized it by the σ value of the positive control of the batch to define the Σ -score. We finally defined an MTP-score for each sample as the product of the M- and Σ-scores. **Figure 3:7a**, **b** and **c** show the M-, Σ-, and MTP-scores values against N_{FISH}, respectively, obtained using our algorithm over the full set of cases used in this study. The M-, Σ-, and MTP-scores obtained a Pearson coefficient ρ of 0.90, 0.90, and 0.93, respectively, and an increasing exponent α of the power law fit ($y \sim x^{\alpha}$). This correlation demonstrates that MTP-based IF assays can indeed deliver quantitative information on the overexpression of HER2, which can be as precise as gene copy number obtained by FISH. Similarly, the correlation of the M-, Σ-, and MTP-scores with the *HER2*/CEP17 ratio is depicted in **Figure 3:7d**, **e** and **f**. The correlation in this case is, nevertheless, less performing than in the case of N_{FISH}, giving a Pearson coefficient of 0.84, 0.82 and 0.85, respectively. Cases 22 and 25 were removed from the dataset due to the lack of epithelial cells in the stained slide that resulted in a Gaussian fit with a low adjusted R^2 value of 0.4837 and 0.4806, respectively. This is already evident from the scatter plot in **Figure 3:5** that indicated a lack of tiles for that case.

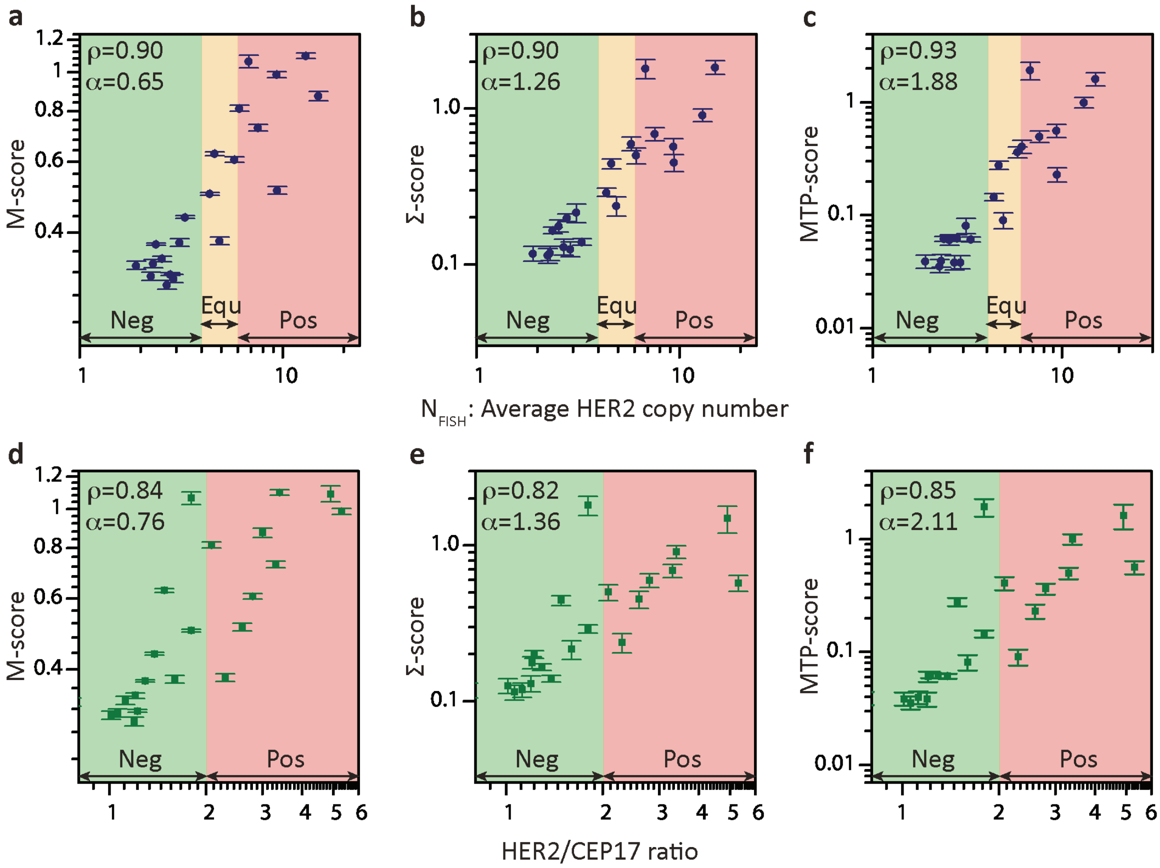

Figure 3:7 | MTP-Score can estimate N_{FISH} with a high confidence. (a) M-score, **(b)** Σ-score and (**c**) MTP-score vs N_{FISH}. The results of the HER2 status classification according to routine FISH analysis are indicated by the green, orange and red zones, representing negative (Neg), equivocal (Equ) and positive (Pos) cases, respectively. **(d)** M-score, **(e)** Σ -score and **(f)** MTP-score vs *HER2*/CEP17 ratio. The results of the HER2 status classification according to routine FISH analysis are indicated by the green and red zones, representing negative (Neg) and positive (Pos) cases, respectively. ρ and α represent Pearson's coefficients and slopes of the power law fits, respectively. Error bars are obtained from Gaussian fits to the histogram data.

Moreover, in an effort to explore the advantages of short incubation times for accurate IHC independent of the image analysis protocol, we have done additional experiments on tissue samples, in which we specifically used an off-chip protocol with long incubation times (typically 1 hour) for the staining, after which IF was assessed using the same automatic image analysis protocol. **Figure 3:8a** shows the histograms of the HER2/CK ratio for a few cases, either obtained with (i) the MTP using short incubation times, or (ii) the off-chip protocol using 1 hour incubation. We clearly observe that the histograms become broader and shift to higher HER2/CK ratios for the long incubation time, rendering a less accurate assessment of the HER2 expression level, as evidenced in the plot of the M-score (**Figure 3:8b**) and the Σ-score (**Figure 3:8c**), especially for $N_{FISH} < 6$, which is the interval for which equivocal results are encountered.

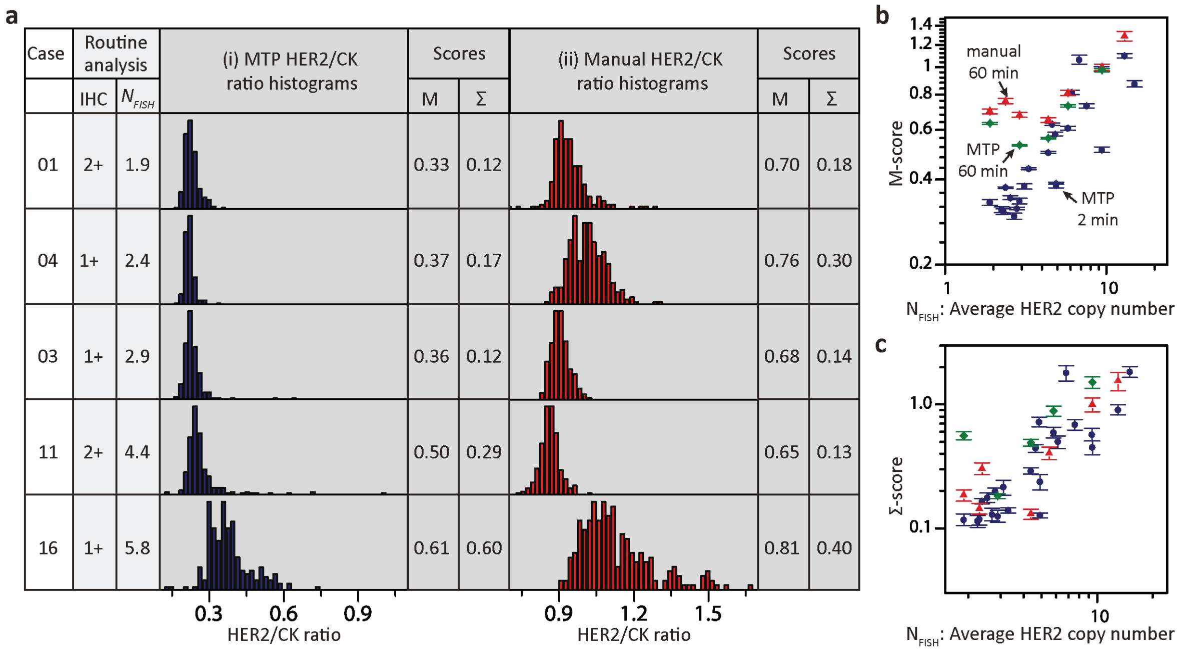

Case	Routine analysis IHC	Routine analysis N_{FISH}	(i) MTP HER2/CK ratio histograms	Scores M	Scores Σ	(ii) Manual HER2/CK ratio histograms	Scores M	Scores Σ
01	2+	1.9		0.33	0.12		0.70	0.18
04	1+	2.4		0.37	0.17		0.76	0.30
03	1+	2.9		0.36	0.12		0.68	0.14
11	2+	4.4		0.50	0.29		0.65	0.13
16	1+	5.8		0.61	0.60		0.81	0.40

Figure 3:8 | **Comparison of the use of short vs long Ab incubation times for accurate IF analysis. (a)** Histograms of the HER2/CK ratio for a few cases, either obtained with (i) the MTP using short incubation times, or (ii) an off-chip protocol using 1 h incubation. We clearly observe that the histograms become broader and shift to higher HER2/CK ratios for the long incubation time. The broadening leads to a less accurate assessment of the HER2 expression level, as evidenced in the plot of the M-score **(b)** and the Σ-score **(c)**, especially for $N_{FISH} < 6$, which is the interval for which equivocal results are encountered. The red points correspond to experiments done with the 1 h incubation time, while blue points were obtained with the MTP using a 2 min incubation time protocol. The green points represent additional control stains done with the MTP using a long incubation time of 1 hour. These results show that the obtained automated scores when using long incubation times have little or no diagnostic value for low N_{FISH}, the interval where quantitative results are most required in practical diagnostics. Using short incubation times with MTP not only solves this problem but also provides a much more proportional score to quantitative results obtained by *in situ* hybridization in all diagnostic range.

3.4.4 MTP IF staining signal proportionality to Ag concentration

In order to better understand the origins of the precision in the obtained IF staining that can even be used to estimate the gene copy number, we performed a proof-of-concept experiment by immobilizing fluorescently labeled Ags on the surface with various volume concentrations, which ranged from 0 to 1000 μg/ml. Fluorescently labeled AF647 mouse Abs (code: A-21239, Life Technologies, CA, USA) were spotted on epoxy-functionalized glass slide (Super Epoxy slides, Arrayit, CA, USA) with a concentration ranging from 0 to 1000 μg/ml using a commercially available contact spotter (QArray Mini, Genetix, MA, USA). The MTP-based incubation of recognizing antibodies was done using AF488 anti-mouse Abs (code: A-11034, Life

Technologies, CA, USA), with a concentration of 50 μg/ml. ImageJ macros were used to segment the spot areas and obtain the average fluorescent signal. OriginLab software (OriginLab Corporation, MA, USA) was used to plots the results.

As depicted in **Figure 3:9**, long incubation times of one hour for manual assays resulted in a non-linear relationship between the Ab fluorescent signal and its Ag, showing sudden Ab signal saturation with respect to its Ag concentration. On the contrary, when the incubation time for the Ab-Ag reaction was limited to 2 minutes and the MTP was used for the staining, we observed a signal from the antibodies that was more proportional to that of the Ags. The linear fit of the Ab-Ag signal plotted in **Figure 3:9f** resulted in a regression coefficient of 0.96. This experiment was performed using a fluorescently labeled IgG as Ab and showed the advantage of using precise microfluidic IF to significantly reduce the incubation times when compared to current standard protocols that use incubation times from 30 minutes to a few hours. Even though the characteristics of the IgG spotting experiments do not fully correspond to those of the tissue, the recognition process is also based on an Ag-Ab interaction at a surface, like on a tissue slide. The implementation of a spotting microarray allowed us to obtain a direct fluorescence signal from the Ags and compare it to the signal from the recognizing Abs in an analytical fashion. On top of this, this assay allowed us to create a controlled gradient of Ag concentrations on the same slide, which is not possible with tissue sections. Finally, we performed a second incubation with antibodies that recognized the previously incubated IgGs. The results (not shown in this plot) also manifested that a short incubation time of 2 minutes gave a signal that is more proportional to the Ag concentration than an incubation of one hour.

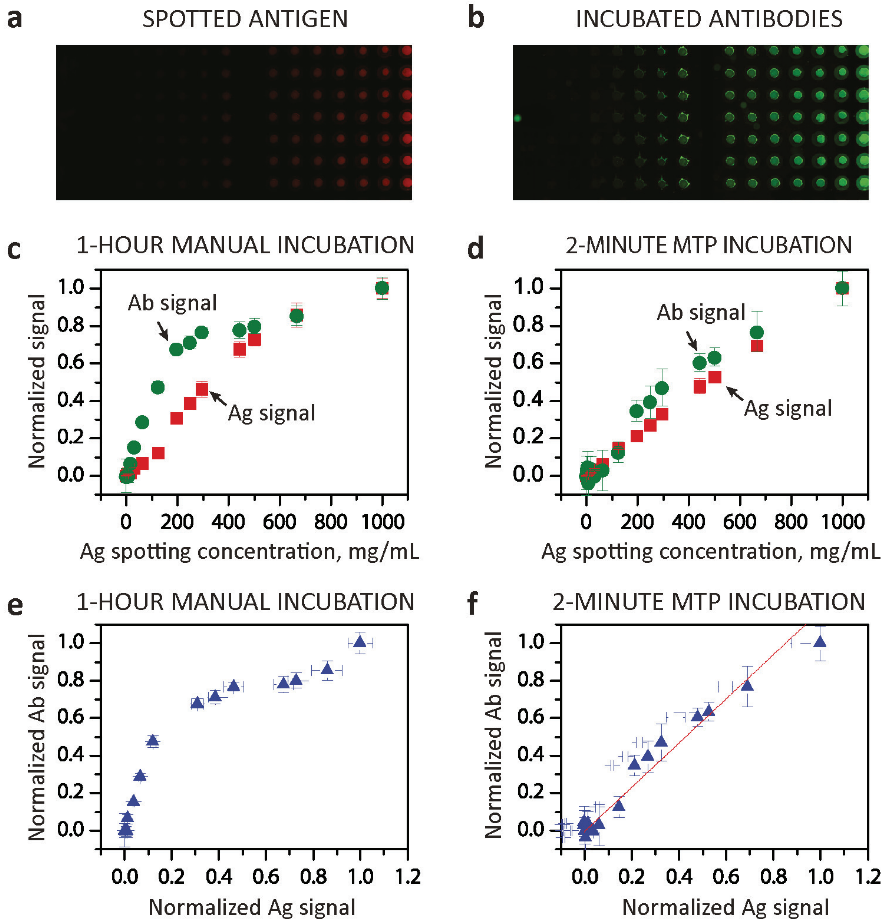

Figure 3:9 | Effect of the Ab incubation time on the proportionality of Ag and Ab signals. **(a)** Fluorescent image of AF647 mouse Abs used as Ag and spotted on an epoxy-functionalized glass slide with a concentration ranging from 0 to 1000 µg/ml **(b)** Fluorescent image of AF488 anti-mouse Abs, used as Ab delivered and incubated using the MTP. **(c)** and **(d)** show the normalized fluorescent signals of the spotted Ag and its recognizing Ab for 1 hour and 2 minute's incubation time, respectively, versus the Ag spotting concentrations. **(e)** and **(f)** depict the normalized fluorescent signals of the recognizing Ab versus the signals of the spotted Ag for 1 hour and 2 minute's incubation time, respectively. For the short incubation time, the Ab-Ag curve shows a linear-like relation with a regression coefficient of 0.96; this proportionality is in favor of the accuracy of the fast MTP-based staining procedure.

3.5 Discussion

Microfluidic precision IF proved to be very powerful in terms of quantifying Ag expression in histopathological tissue sections, significantly increasing the precision of the information that can be obtained by an immunoassay. Experiments showed that HER2 biomarker quantification, as obtained by the presented method, can provide molecular information that is as precise as data obtained by FISH tests, while keeping the cost and time advantage of an IF assay. We showed that the low incubation times (< 8 minutes) allowed by microfluidic staining resulted in a proportional relationship between the IF signal and the corresponding Ag concentration, and that this feature was lost when using higher incubation times, which basically explained the basis of the precision in the results. The linearity of the staining, combined with low-complexity image analysis, allowed us to establish a continuous scoring that linearly followed the gene copy number as assessed by *in situ* hybridization.

Today, ISH is used as a gold standard for *HER2* gene amplification assessment in breast cancer and for other diagnostic applications, and is replaced to some extent by conventional IHC as a surrogate marker of the genetic status. While this first proof-of-concept comparison of the presented method against FISH results is already promising, showing that the same results can be obtained much faster and at a lower cost, the microfluidic precision IF method used to obtain the scatter plots hereby presented has potentially a higher degree of clinical relevance.

FISH assessment is done by averaging the *HER2* gene copy number and the *HER2*/CEP17 ratio of 20 to over 100 nuclei of invasive cancer cells, though intra-tumoral genetic heterogeneity is a well-known phenomenon and a challenge for HER2 evaluation in some breast cancer cases [106]. 2013 ASCO/CAP guidelines have partially clarified this point and stressed the importance of screening the whole section to detect heterogeneous, (partially) amplified cases [57].

Interestingly, for cases 6, 9 and 14 in this study, heterogeneity was detected by both technical approaches. Routine IHC followed by FISH analysis demonstrated two areas of the tissue expressing/amplifying HER2 at different levels. On the other hand the scatter plots obtained (see **Figure 3:5**) using our method showed that there are 2 distinct populations with different levels of HER2 expression, in comparison to a negative N_{FISH}.

What is more, we do know that gene copy number gain is not always sufficient for protein overexpression. The scatter plot of case 15, having an N_{FISH} value of 4.9, correlates more with the HER2-negative control signature with MTP-scores less than 0.1, suggesting that although there is a moderate copy number gain, there is no significant protein overexpression. Indeed, case 15 was considered equivocal/positive by FISH analysis, even though the IHC score was +1 (see **Table 3:3**).

Further clinical studies comparing the MTP score to clinical outcomes (such as survival and response to anti-HER2 targeted therapies) are required to show if the MTP score can be used to more precisely predict the treatment success in clinical assessment of HER2. In addition to the HER2 biomarker case presented here, another example is anaplastic lymphoma kinase (ALK) biomarker searched in non-small cell lung cancer (NSCLC), where *ALK* gene rearrangements assessed by FISH is used to define a positive ALK status [107]. However, the response rate to targeted therapy (Crizotinib) remains around 58% for ALK-positive patients diagnosed this way [108]. While ALK protein expression as detected by IHC is progressively being introduced as a surrogate marker for *ALK* gene rearrangement [109], [110], one immediate further validation of our approach could involve the quantitative evaluation of ALK expression in NSCLC. Finally, the scatter signature and MTP score obtained by precision microfluidic IF can increase the correlation between the biomarker assessment and treatment response, by establishing the missing link between gene status assessment by FISH and protein expression evaluation by IHC.

To conclude, we anticipate that the clinical implication of the presented results is potentially more significant than a mere application of the presented method in eliminating complementary ISH assessment in HER2 expression or other biomarkers. The experiments showing a more linearly proportional IF staining with respect to the Ag expression level, combined with the obtained scatter plots, imply that standard IHC is potentially masking some clinically relevant protein biomarker information. The expansion of this technique and the integration of the obtained information to routine diagnostic workflows may imply a major leap towards the concretization of precision medicine. Microfluidic precision IF uses standard sample preparation techniques and clinically validated primary antibodies. As digital pathology slide scanners are becoming more and more common, a switch to IF scanning would be easier, and does not imply high testing costs as opposed to complementary genetic testing practices like ISH. A low-complexity algorithm, as presented here, can easily generate scatter plots and a score without requiring too much computational power. Such quantitative data can be used as a scoring aid to pathologists, to increase success of treatment response prediction and prognosis. In the future, larger clinical studies for several markers will be required to further validate and prove the impact of microfluidic precision IF technology in cancer diagnosis.

Chapter 4 Microfluidics for rapid cytokeratin detection in multiple frozen section tissues

FS of tumor samples represent a cornerstone of pathological intraoperative consultation and play an important role in the microscopic analysis of specimens during surgery. IHC stainings on FS would be of great use during intraoperative consultations, if only the turn-around time was not a limitation. Microfluidic technologies have proven to bring substantial improvement in many fields of diagnostics, though only a few microfluidic devices have been designed to improve the performance of IHC assays. In this work, we show optimization of a complete pan-cytokeratin chromogenic immunostaining protocol on FS using a microfluidic tissue processor, into a protocol taking less than 12 minutes. Our results showed specificity and low levels of background. The dimensions of the microfluidic prototype device are compatible with the space constraints of an intraoperative pathology laboratory. We therefore anticipate that the adoption of microfluidic technologies in the field of surgical pathology can significantly improve the way FSs influence surgical procedures.

This chapter is an adapted version of the following submitted manuscript:

- S. Brajkovic, **D. G. Dupouy**, L. de Leval, and M. A. M. Gijs, "Microfluidics for rapid cytokeratin detection in multiple frozen section tissues immunohistochemistry", Laboratory Investigations, submitted.

4.1 Introduction

FS play an important role in the microscopic analysis of specimens during surgery. Surgeons may require an intraoperative consultation from pathologists for different purposes, ranging from the assessment of a resection margin in a tissue-conserving procedure, to the determination of a metastatic condition or the identification of the possible cause of the symptoms in exploratory surgeries [111]. In the vast majority of the FS consultations, H&E is used by pathologists to seek whether the tumoral dissection presents a clear margin. Although the cost-benefit of the exhaustive use of FS is under discussion for some procedures [112], [113], the clinical advantage is clear in most cases. Even for breast carcinomas, where cryosectioning is troublesome due to the high fat content [114], studies showed that intraoperative assessment via gross examination and H&E of the margins can significantly decrease the re-operative rates [115], [116]. Intraoperative methods based on H&E alone, even though very specific, often lack sensitivity [117], which can be attributed to the absence of cancer cell-specific staining. Under these conditions, interpretation mostly relies on the experience of the pathologist, and a small number of infiltrating cancer cells into healthy tissue may not be easily recognizable. Studies show that false negative cases can reach values of 50% when the tumor size is smaller than 2 mm in breast cancer surgery, and that this rate can be significantly reduced using CK staining for intraoperative consultation of sentinel lymph nodes [113]. Numerous additional immunohistochemical markers would be interesting to test during intraoperative consultations, if only the turn-around time was not a limitation. Only for a few particular intraoperative consultations, IHC tests are available today. An example is the rapid IHC test for sentinel lymph nodes, which helps pathologists assess whether the lesions have metastized and surgeons determine what is the extent of the dissection [117]–[121]. Another example is Mohs surgery of melanomas, where real-time margin analysis is required in order to ensure the lesion was fully dissected, while a maximum tissue preservation is guaranteed [122]–[125]. A rapid (10 min) IHC test for the proliferation marker Ki-67 was also proposed to diagnose gliomas intraoperatively [126]. All these methods were based on the use of rapid IHC kits, expressly developed for a particular marker and tissue type, hindering more general use of the technique on other specimens and/or other markers of interest.

Technological improvements have significantly increased the throughput of IHC assays on FFPE samples run by automated machines, both by reducing the staining time and parallelizing the number of assays. The first automats mimicked manual stainings by dropping reagents on top of horizontally disposed slides [127]. Nowadays, Ventana Medical Systems makes use of an inert liquid to avoid evaporation, and airstreams to increase reagent mixing [127]. The latest technology from Dako uses capillary forces to drive reagents by opening and closing the gap between the slide and a movable coverslip, and claims a turn-around time of 2.5 h for IHC [127], [128], showing the importance of boosting the reagent transport over the tissue section. Increased reagent transport has also been achieved in research settings by making use of an alternating electrical field on top of the tissue, leading to faster IHC staining [129], [130]. We have recently demonstrated that, making use of microfluidics to deliver the reagents, fast immunostaining (< 10 min) on FFPE sections can be achieved using kits that would normally require a minimum of 2 hours upon manual or automat-based process [65], [131]. So far, the capabilities of this technology have only been demonstrated for immunofluorescence staining of HER2 and CK, where a few Ab and washing steps were required.

In this work, we show the development of a complete pan-CK chromogenic staining protocol on FS using the MTP as the core technology of our stainer. Starting from an existing 43-min microfluidic protocol working in our laboratory, we optimized each step and achieved a working protocol in less than 20 min, which included tissue preparation after cryosectioning (8 min) and immunohistochemical staining (< 12 min). We show the results of the optimized protocol on 3 different autopsy and 4 tumor biopsy tissues. The increased time performance of our assays relies on the microfluidic handling and not on the reagents themselves. Therefore, our technique has the potential to provide pathologists with a versatile tool for fast IHC stainings on frozen sections of any type. Moreover, the microfluidic characteristics allowed us to develop an experimental prototype that matches the space constraints often found in FS laboratories. We believe that many more questions could be answered intraoperatively with the use of our new technology to reduce the turnaround time of IHC assays.

4.2 Material and methods

4.2.1 Sample preparation

Anonymized frozen samples were obtained from the Institute of Pathology at the Centre Hospitalier Universitaire Vaudois (CHUV). Ethical approval was obtained from the “Commission cantonale d'éthique de la recherche sur l'être humain” (CER-VD) under the protocol number 511/12. The samples included ureter, pancreas, prostate, breast carcinoma, pancreas adenocarcinoma, lung adenocarcinoma (NSCLC) and Hodgkin lymphoma. The details of the protocol steps are shown in **Table 4:1**. Frozen tissue blocks were cut with a cryostat (Leica, CM1850) and mounted on standard histopathology slides (step 1) at the Histology Core Facility (HCF) of EPFL. In the optimized MTP protocol (**Table 4:1iii**), sections were dehydrated (step 2) using cold air of an air-flow dryer for 2 min. Fixation (step 3) was then performed by incubating the slides for 3 min in cold acetone (kept at -20 °C prior to the experiment, Fischer Chemicals, A/0600/15) and subsequently dried for a second time (step 4) with the air-flow dryer using cold air for 2 min. All the subsequent steps of the staining were performed on the MTP-device (referred to as “On chip” in **Table 4:1**). Several reagents were tested during optimization of the pre-staining steps: fixation with methanol during 10 min (-20 °C, Fischer Chemicals, M/4000/15) immediately after sectioning; fixation with acetone for 10 min (on ice, Fischer Chemicals, A/0600/15) immediately after sectioning; and tissue dehydration at temperature for 15 min or using air flow for 2 min.

Table 4:1 | Staining protocols. Details of the complete protocol for (i) manual staining, (ii) prior non-optimized MTP protocol and (iii) optimized MTP protocol. Washing steps, performed in-between the described steps, are not explicitly mentioned. The overall washing time is shown at the end of the table.

Step number	Group	Step	**(i) Manual protocol** Time (min)		**(ii) Prior MTP protocol** Time (min)		**(iii) Optimized MTP protocol** Time (min)	
1	PRE – STAINING	Sectioning	0.0	Off chip	0.0	Off chip	0.0	Off chip
2		First drying	15.0		15.0		2.0	
3		Fixation	10.0		10.0		3.0	
4		Second drying	15.0		15.0		2.0	
5		Re-hydration	15.0		15.0		1.0	On chip
PRE-STAINING subtotal			**55.0**		**55.0**		**8.0**	
6	STAINING PART I	Peroxidase block	5.0		2.0	On chip	0.0	
7		Protein block	5.0		2.0		0.0	
8		Primary Ab	30.0		4.0		2.0	
9		Post primary	30.0		4.0		0.0	
10		Secondary Ab	30.0		4.0		4.0	
11	STAINING PART II	DAB	5.0		2.5	Off chip	1.5	
12		Counterstaining	5.0		4.0		0.3	
STAINING subtotal (no washing)			110.0		22.5		7.8	
Washing			105.0		5.8		3.3	
STAINING subtotal			**215.0**		**28.3**		**11.1**	
TOTAL			**270.0**		**83.3**		**19.1**	

4.2.2 Microfluidic setup

Once the frozen sample preparation is completed, the tissue section is clamped using a gasket to the MTP to form a reaction chamber, after which the system is ready for fast IHC staining (**Figure 4:1**). Inside the reaction chamber, reagents are sequentially delivered and washed over the surface of the tissue section (**Figure 4:1b**). The MTP enables a fast fluidic exchange on a one-second timescale. Additional details about the MTP working principle can be found elsewhere [65]. **Figure 4:1c** shows a schematic of the automated pressure-driven laboratory setup that was used for the experiments. The setup consisted of: (i) 50 mL reservoirs used for common reagents, namely PBS, deionized water (DIW), DAB, and ethanol; (ii) 1.5 mL Eppendorf tubes for specific reagents, such as Abs, blocking solutions and hematoxylin; (iii) a computer-operated valve-manifold called Reagent Delivery System (RDS) used to select among the reagents to be flushed into the reaction chamber; (iv) the MTP/tissue sample staining chamber.

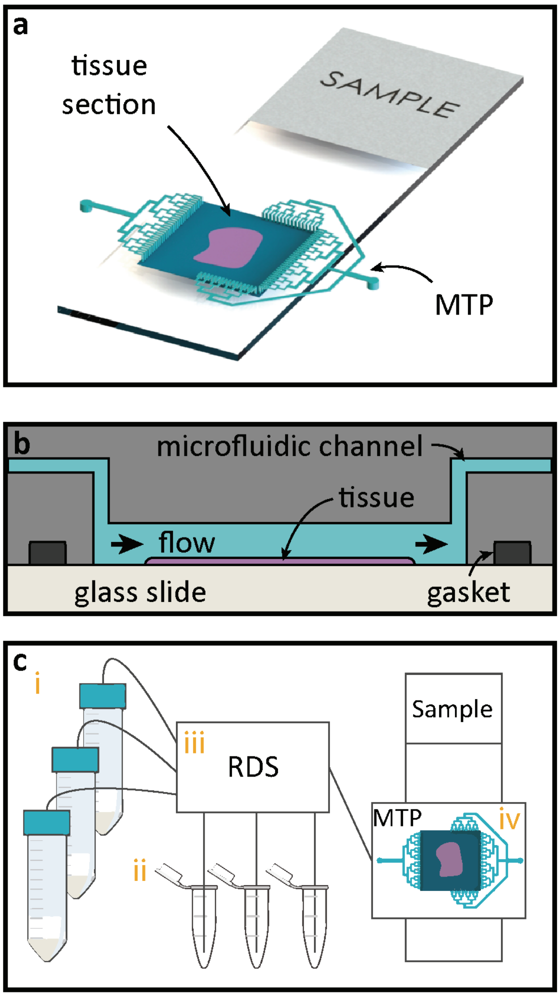

Figure 4:1 | Working principle of microfluidic staining of FS. (a) Once the frozen sample preparation is completed, the sample is clamped using a gasket to the MTP to form a reaction chamber, after which the system is ready for fast IHC staining. **(b)** Schematic cross-section of the MTP clamped to the tissue slide. Inside the reaction chamber, reagents are sequentially delivered and washed over the surface of the tissue section. The MTP enables a fast fluidic exchange on a one-second timescale, while keeping reagent exposure times uniform throughout the whole tissue surface. **(c)** Schematics of the laboratory setup used for the experiments: (i) 50 mL reservoirs are used for common reagents, namely PBS, DIW, DAB, and hematoxylin; (ii) 1.5 mL Eppendorf tubes are used to load specific reagents, such as Abs, and blocking solutions; (iii) a computer-operated valve-manifold called RDS allows for the selection of the reagents that are flushed into the chamber of reaction; (iv) MTP/ tissue sample staining chamber.

4.2.3 MTP-based stainings

After the tissue was dried and clamped to the MTP, the “On chip” steps in columns (ii) and (iii) from **Table 4:1** were performed. The protocol was defined on a graphical user interface and executed entirely by the automated laboratory setup. Tissue rehydration (step 5) and all the washing steps were realized using Tris Buffered Saline solution (TBS, Sigma Life Science, T5912-1L). Blocking solutions (step 6 and 7) were not used in the optimized MTP protocol. Primary Ab incubation (step 8) was done using mouse anti-human CK (Dako, M3515), diluted 1/100 in TBS Tween 0.05% (Tween 20, Fischer Scientific, BP337-100). Incubation with post-primary Ab (step 9) used in column (ii) but removed from the optimized protocol of column (iii). After primary Ab application, tissue sections were directly incubated with ImmPRESS (Vector Laboratories, MP-

7402), a micro-polymer conjugated with anti-mouse secondary Ab and horseradish peroxidase (HRP) enzyme molecules (step 10). The reaction was revealed (step 11) using the DAB chromogen (ImmPACT, Vector SK-4105) and the nuclei counterstaining (step 12) was achieved using hematoxylin Gill3 20% (Thermo Scientific, 72604). Finally, slides were washed, unclamped from the MTP and coverslipped (mounting solution from Sigma, F6182-20). All negative controls (CTL) were obtained by performing a parallel staining by replacing the primary Ab by a solution of TBS Tween 0.05%.

During optimization, alternative detection kits were tested: ImmPRESS Excel (Vector, MP-7602), Novolink (Novocastra, Biosystems, RE7290), and Quanto (Thermo Scientific, TL-060-QHD). Each of these kits provided its own peroxidase block (step 6), protein block (step 7), amplifier or post-primary Ab (step 9), polymer (step 10) and DAB buffer (step 11). Additional DAB chromogens were tested: DAB EqV (Vector, MP-7602), DAB Reveal (Spring, DABC-001/15), DAB Novolink (Novocastra, Biosystems, RE7105/06), DAB Metal enhanced (Thermo Scientific 34065/1855910). Counterstaining tests were also done with hematoxylin from Novolink (Novocastra, Biosystems, RE7107) and hematoxylin QS (Vector H-34004).

4.2.4 H&E stainings

The total time needed for the optimized H&E protocol execution was 2:30 min. Slides were stained with hematoxylin QS (Vector, H-34004) for 15 s and then rinsed with tap water. A second rinsing was then applied using ethanol 100% (Fischer Chemical, E/0650DF/15). Subsequently, tissue sections were stained using eosin Y 1% (Sigma, E4382) in 70% ethanol with 1% phloxine (Fluka, 28550) for 15 s, rinsed again with ethanol 100% and then tap water. Finally, specimens were unclamped from the MTP and coverslipped using DPX mounting media for histology (Sigma, 06522-100ML).

4.2.5 Imaging

Images of stained slides were taken using a slide scanner (VS-ASW FL, Olympus) with a 20x 0.75 NA objective. A color depth of 24-bit and a resolution of 346 nm/pixel was achieved and saved in .vsi format. The extracted images were exported as TIFF images using Fiji Image J and a plugin provided by the Bioimaging and Optics Platform (BIOP) of EPFL.

4.3 Results

4.3.1 Pre-staining protocol optimization

The common tissue preparation steps, referred to as “pre-staining” in **Table 4:1**, were optimized on ureter autopsy specimens, from an initial total time of 55 min to a final time of 8 min. The five pre-staining steps were (1) sectioning, (2) first drying, (3) fixation, (4) second drying, and (5) re-hydration. Step 1 was not optimized, as being part of a service from HCF. Steps 2 to 4 were optimized off-chip, while step 5 was first performed off-chip, then included on-chip. **Figure 4:2a** shows a comparison of CK staining obtained using fixation by methanol (at 4 °C) and acetone (kept at –20 °C prior to the experiment). In direct acetone fixation, the tissue is immersed in acetone immediately after sectioning, while for the indirect mode, the tissue is sectioned, dried for 15 min at room temperature, and then immersed in acetone. Indirect fixation with acetone showed the best staining. In **Figure 4:2b**, the optimization of the acetone indirect fixation time is shown, where fixation times between 10 min to 1 min were tested. Three-minute fixation turned out to be sufficient to obtain a clear staining. Increasing the fixation time above three minutes resulted in no apparent improvement, while shorter fixation times increased the areas where the staining was not present or was fainter. **Figure 4:2c** depicts the results of the optimization of the second drying time (step 4 in **Table 4:1**), showing satisfactory results using cold air of an air-flow dryer for 2 min, instead of passive drying over 15 min. The same drying procedure was applied for first drying in step 2. **Figure 4:2d** shows how the rehydration step, prior to staining, could be successfully achieved in 1 min, once the slide was clamped to the MTP.

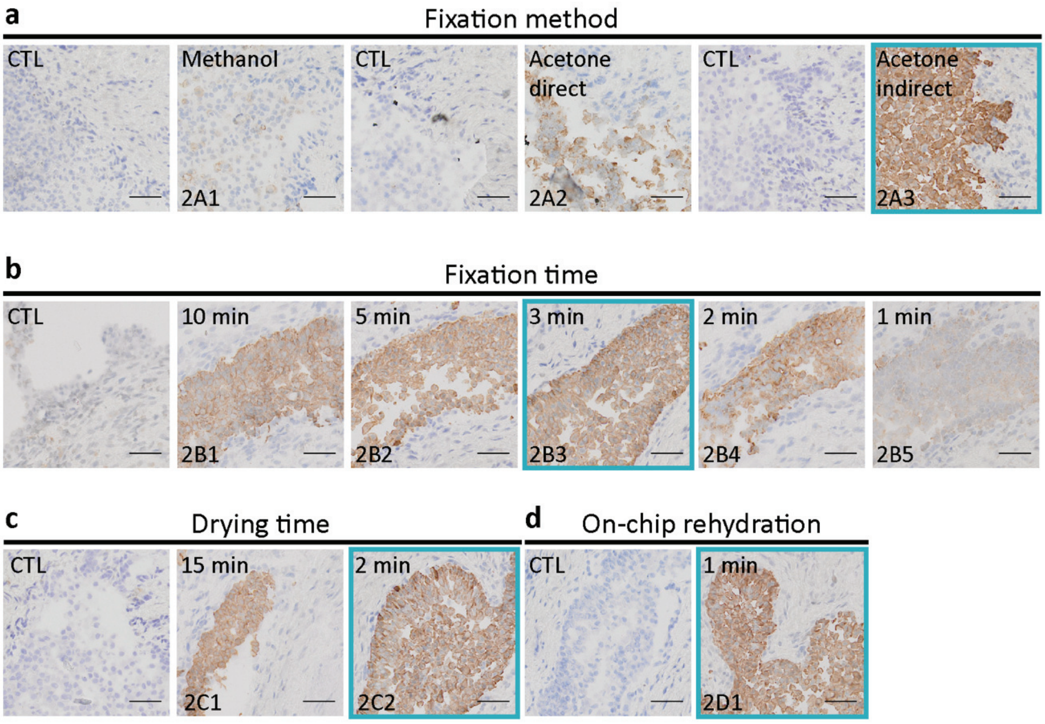

Figure 4:2 | Optimization of the pre-staining protocol on ureteral biopsy sections. Slides show the final CK staining and are compared with CTL samples, obtained by staining without use of the primary Ab, in which case, ideally, only nuclear hematoxylin counterstaining is visible. The immunohistochemical staining of frozen sections described in this work requires a set of common tissue preparation steps (see **Table 4:1**): (1) sectioning, (2) first drying, (3) fixation, (4) second drying, and (5) re-hydration. Step 1 was neither optimized nor counted within the total time of the IHC assay. Steps 2 to 4 were optimized off-chip. **(a)** Comparison of CK staining obtained using fixation by methanol (at 4 °C) and acetone (kept at –20 °C prior to the experiment). In direct acetone fixation, the tissue is immersed in the acetone immediately after sectioning. Indirect means that the tissue is sectioned, dried for 15 min at room temperature, and then immersed in the acetone. Indirect fixation with acetone showed best staining. **(b)** Optimization of the acetone indirect fixation time. Three-minute fixation turned out to be sufficient to obtain a clear staining. Increasing the fixation time resulted in no apparent improvement, while shorter fixation times increased the areas where the staining was not present or was fainter. **(c)** Optimization of the second drying time (step 4 in **Table 4:1**) showed satisfactory results using an air-flow dryer for 2 min. **(d)** One-minute successful re-hydration was achieved by clamping the section to the MTP. The blue frames on each panel represent the ‘best conditions’ chosen for the final experiments of Figure 5 and are represented in column (iii) of **Table 4:1**. (Scale bars: 50 μm; bottom-left code: identifier of the sample in **Table 4:2** of the Appendix).

4.3.2 MTP staining protocol staining protocol optimization

Once the optimum times for the pre-staining steps were found, the choice of ImmPRESS as our detection system was done based on a direct comparison test that can be found in the Supplementary Information (**Figure 4:7**). Subsequently, the steps corresponding to “staining part I” of **Table 4:1** were optimized. **Figure 4:3a** shows that the use of a blocking buffer, standardly done in the manual protocol, did not improve the quality of the staining in microfluidic IHC, which was the reason why it was removed from from the optimized protocol in column (iii) of **Table 4:1**. **Figure 4:3b** and . **Figure 4:3c** show the optimization of the primary Ab and the secondary Ab incubation times, respectively. Incubation during 2 min for the primary Ab and 4 min for the secondary Ab were sufficient to obtain a high-quality staining. Such Ab incubation times using the MTP technology had already been demonstrated before for immunohistofluorescence assays in in our laboratory [65], [131].

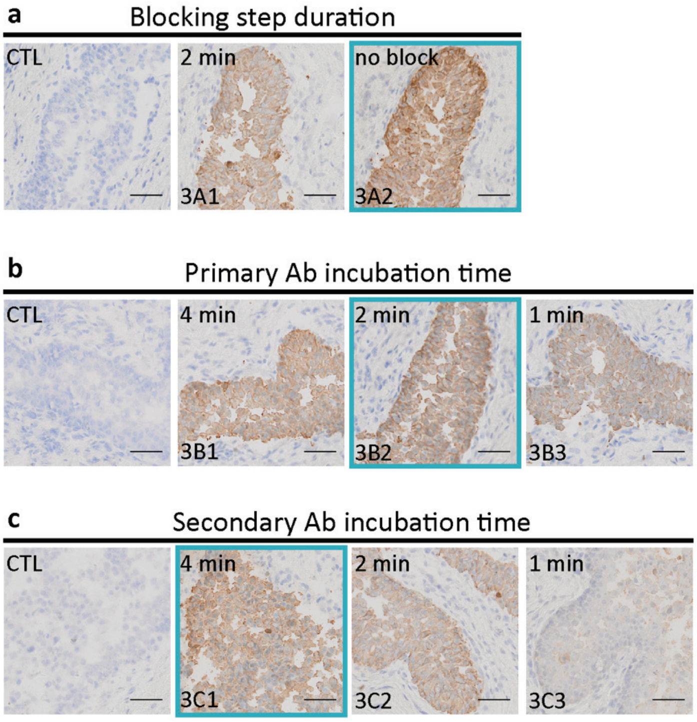

Figure 4:3 | Optimization of the first part of the MTP staining protocol of Table 4:1 on ureteral biopsy sections. Slides show the final CK staining and are compared with CTL samples, obtained by staining without use of the primary Ab. (**a**) Use of a blocking buffer, standardly done in the manual protocol, did not improve staining in microfluidic IHC, which was the reason to remove the blocking step from the optimized protocol in **Table 4:1**. (**b**) Optimization of the primary Ab incubation time. Incubation during 2 min was sufficient to obtain a high-quality staining. (**c**) Optimization of the secondary Ab incubation time. 4 min was chosen in the initial MTP protocol of column (ii) of **Table 4:1**. The blue frames on each panel represent the 'best conditions' chosen for the final experiments of **Figure 4:5** and are represented in column (iii) of **Table 4:1**. (Scale bars: 50 μm; bottom-left code: identifier of the sample in **Table 4:2**).

"Staining part II" steps from **Table 4:1** were optimized by both the choice of the reagents that gave the best imaging result and the shortest incubation times. Figure 4a shows the incubation time optimization of the DAB obtained from the kit Novolink, which was used as our reference standard during the experiments described above. Increasing the DAB incubation time between 30 s and 90 s showed an increment in the intensity of staining. However, no difference was perceived between 90 s and 150 s, indicating that incubation longer than 90 s was not necessary. Subsequently, DAB reagents from five different providers were compared under the same experimental conditions and shown in **Figure 4:4b**. ImmPACT was selected as giving the best staining results in the IHC MTP settings. Similarly, in **Figure 4:4c**, three hematoxylin suppliers were compared, giving Gill3 as the most suitable choice of hematoxylin for our experiments. The incubation time of Gill 3 hematoxylin was optimized down to 15 s (**Figure 4:5d**). Finally, the hematoxylin solution was diluted to 20% of its original concentration using DIW, resulting in lesser viscosity without compromising staining (**Figure 4:4e**).

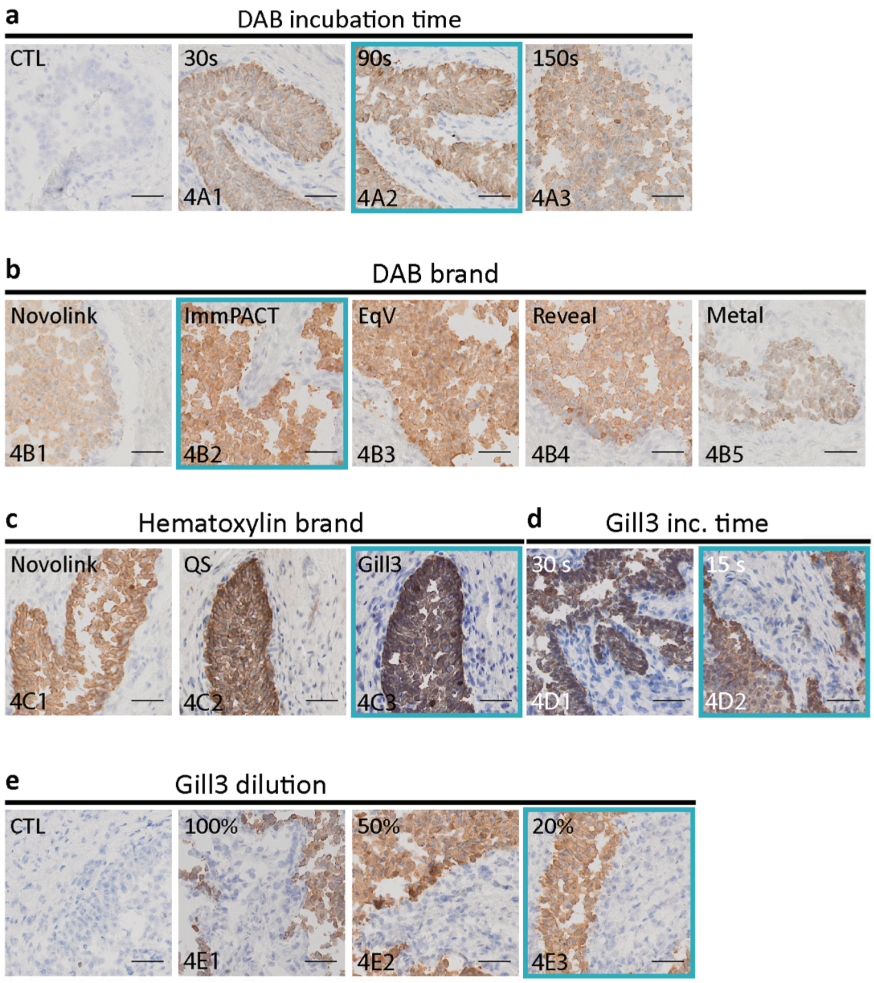
a
DAB incubation time
CTL
30s
90s
150s
4A1
4A2
4A3
b
DAB brand
Novolink
ImmPACT
EqV
Reveal
Metal
4B1
4B2
4B3
4B4
4B5
c
Hematoxylin brand
Novolink
QS
Gill3
4C1
4C2
4C3
d
Gill3 inc. time
30 s
15 s
4D1
4D2
e
Gill3 dilution
CTL
100%
50%
20%
4E1
4E2
4E3

Figure 4:4 | Optimization of the second part of the MTP staining protocol of Table 4:1 on ureteral biopsy sections. (a) Optimization of the incubation time of DAB obtained from the Novolink kit. Increasing the DAB incubation time between 30 s and 90 s increases the intensity of the signal. However, no difference is perceived between 90 s and 150 s, indicating that incubation longer than 90 s is not necessary. **(b)** DAB reagents from 5 manufacturers were compared under the same experimental conditions. ImmPACT was selected as giving the best staining quality. **(c)** Three hematoxylin suppliers were compared, giving as most suitable choice hematoxylin obtained from Gill3. **(d)** The optimized hematoxylin incubation time was chosen as 15 s. **(e)** Finally, we diluted the hematoxylin solution to 20% of its original concentration using DIW, resulting in lesser viscosity and eosin application without compromising the staining. (Scale bars: 50 µm; bottom-left code: identifier of the sample in **Table 4:2**).

4.3.3 Optimized MTP H&E and CK staining results for different tissue types

Figure 4:5 shows images of the H&E (first column), CTL (negative control, second column) and CK (third column) stains using the MTP optimized protocols, performed on the following samples: pancreas, ureter, prostate, breast carcinoma, pancreas adenocarcinoma, lung adenocarcinoma (NSCLC) and Hodgkin lymphoma. Successful H&E stains were achieved for all the tissue types used in our study and the turn-around time was 2 minutes and 30 seconds. CK staining showed specificity to epithelial cells on non-cancerous tissues and on carcinomas of different origin. At the same time, no false-positive staining was observed on

lymphoma cases. Similarly, the negative controls, where the protocols were run without primary anti-CK Abs, showed only nuclear counterstaining, as expected.

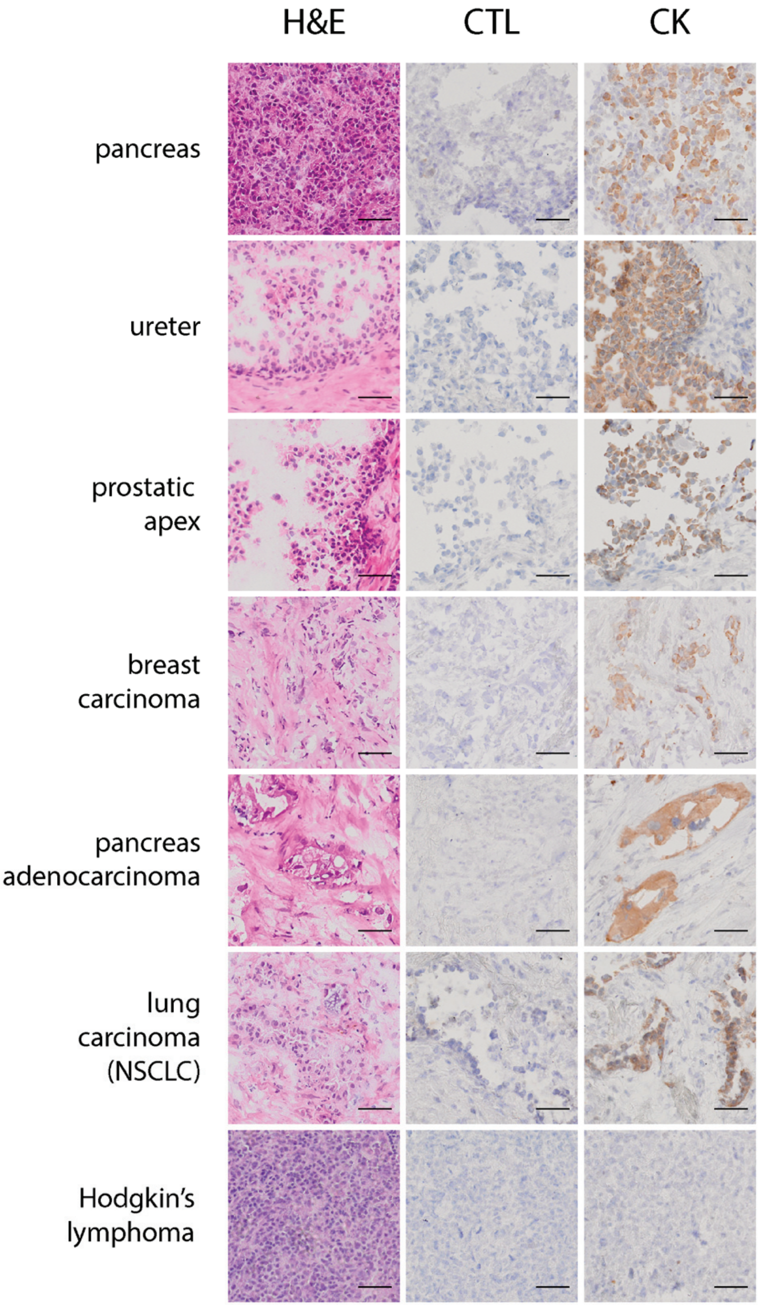
H&E
CTL
CK
pancreas
ureter
prostatic apex
breast carcinoma
pancreas adenocarcinoma
lung carcinoma (NSCLC)
Hodgkin's lymphoma

Figure 4:5 | Results of the optimized MTP staining protocol for different tissue types for CK in IHC (less than 13 minutes) and H&E (2:30 minutes). Optimized H&E staining (first column), CTL staining (negative control, second column), and CK staining (third column) performed on the following samples: pancreas, ureter, prostate, breast carcinoma, pancreas adenocarcinoma, lung carcinoma (NSCLC), benign lymphoma and Hodgkin lymphoma. The H&E stainings were performed on the MTP in 2:30 minutes. CK staining showed specificity to epithelial cells on non-cancerous tissues and on carcinomas of different origin. At the same time, no false-positive staining was observed on lymphoma cases. Similarly, the negative controls, where the protocols were run without primary anti-CK Abs, showed only nuclear counterstaining, as expected. (Scale bars: 50 μm).

4.4 Discussion

Microfluidics has already proven to bring substantial improvement in many fields of diagnostics, with point-of-care applications being the most popular [3]. Seemingly, laboratory-based microfluidics enabled improvements in genomics, sequencing, high-throughput screening, and separations. The higher surface-to-volume ratio achieved by handling reagents in the micrometer scale allows for higher sensitivity and assay turn-around-time. Surprisingly enough, only a few microfluidic devices have been designed to improve the performance of IHC assays used in the field of tissue diagnostics [62], [64]. While these devices confine the staining on a small portion of the tissue section, the MTP is designed to deliver and wash reagents over the entire tissue surface in a time scale of one second.

We demonstrated that our microfluidic technology can deliver fast (< 12 min) and automated IHC stains using conventional anti-CK Abs on multiple frozen tissue types, as opposed to the rapid kits that could be found in literature. Results showed specificity to cells of epithelial origin and low levels of background in the negative controls. The dimension of the prototype used for the staining experiments is compatible with the space constraints typically observed in intraoperative laboratories. The need for fast pathological examination during surgery makes FSs one of the most stressful tasks that the pathologist performs in practice. As of today, except for a few dedicated fast IHC kits [117]–[126], [129], intraoperative diagnosis is based on H&E alone and confronted post-operatively to the corresponding permanent sections. Rapid and automated IHC tests made available at the intraoperative laboratory would significantly add to the accuracy of the diagnosis for the most complicated cases.

More is to be done in order to offer pathologists a tool for IHC diagnosis on FS, namely the availability of a broad spectrum of markers pathologists can choose for the staining. We anticipate that the adoption of microfluidic technologies in the field of surgical pathology can significantly improve the way FS analysis influence surgical procedures.

4.5 Appendix

4.5.1 Quantification of a chromogenic signal

Small molecules that have large diffusion coefficients, tend to be consumed from the reaction chamber more rapidly than large molecules like Abs. We observed that the delivery of DAB at the same flow rates as the ones used for the Abs (10 μl/s) was giving an nonuniform staining with a clear gradient in the direction of the flow. We compared a staining for which DAB was delivered at 10 μl/s against the same experiment deliverying DAB at 25 μl/s. Indeed, we could observe more uniform staining. To quantify the extent of this difference, we developed a simple ImageJ algorithm that allowed us to extract an average signal value from a chromogenic image. **Figure 4:6** shows intermediate images used in the quantification algorithm: **(a)** RGB images were taken by brightfield microscopy and converted into grey scale (8-bit); **(b)** in order to represent the signal on the higher grey values, the 8-bit image was subsequently inverted; **(c)** an auto-threshold algorithm, included in the ImageJ database, was applied to determine the limiting grey value over which the pixel are considered to be part of the signal. Finally an average value and a standard deviation of the thresholded pixels' grey value was automatically calculated. **Figure 4:6d** shows a comparison of the average signal obtained when flushing DAB at 10 μl/s (blue) and at 25 μl/s (yellow), where the increased uniformity at higher flow rate is clear from teh error bars of the plot.

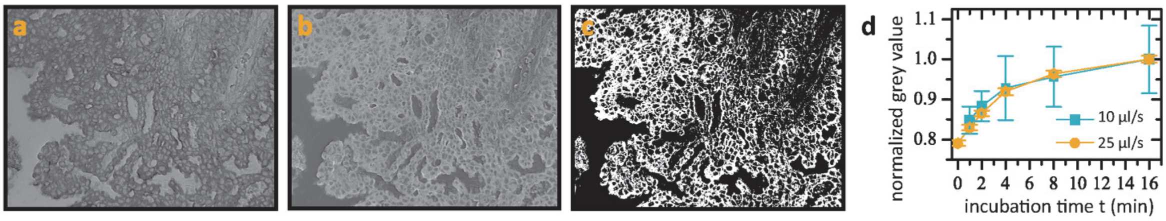

Figure 4:6 | IHC quantification algorithm. Starting from a chromogenic CK staining of breast carcinoma samples, the color brightfield image is initially **(a)** converted to grey scale, then **(b)** inverted and finally **(c)** thresholded to represent areas considered as signals distinct from the background, with higher grey values for higher staining intensities. **(d)** Comparison of the average staining intensity obtained from staining of adjacent sections of the same tumor sample, where DAB is flushed at 10 µl/s (blue) and at 25 µl/s (yellow) and primary and secondary Ab incubation times are sweeped. Error bars are calculated from the standard deviation of the pixel grey values. Plots are normalized to the signal obtained at the maximum Ab incubation time of 16 min.

4.5.2 Choice of the DAB-based detection system

Several detection systems were tested under the same experimental conditions, with the scope of finding the one giving the best quality staining when applied on our microfluidic system. Staining results were satisfactory for three detection systems, as depicted in **Figure 4:7**: Novolink, Quanto and ImPRESS. We chose to continue our experiments using Impress because, on top of the satisfactory staining, fewer protocol steps were required, by avoiding blocking steps and post-primary Ab incubation.

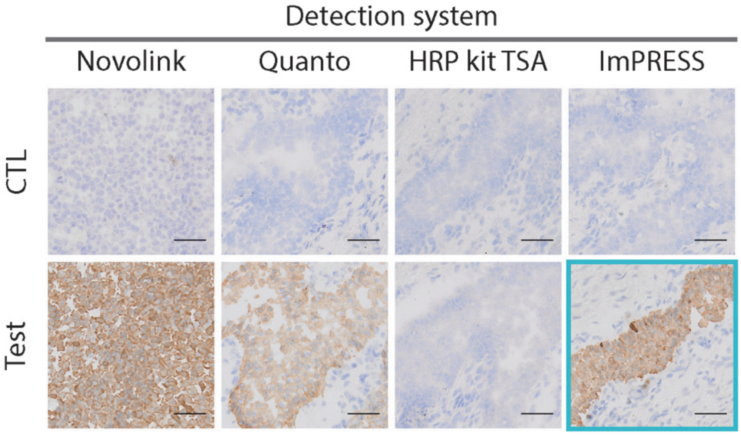

Figure 4:7 | Choice of detection system kit. Comparative test on 4 different commercially available detection kits: Novolink, Quanto, HRP kit TSA and ImmPRESS. ImmPRESS was selected as giving the best results and requiring the fewest protocol steps. The test was realized once the pre-staining steps had been optimized (see **Table 4:1**). Prior to optimization, the Novolink kit was used as the reference (see **Figure 4:2**). (Scale bars: 50 µm)

4.5.3 Optimization method

In order to optimize for each step and reagent, staining tests and their controls were done varying one parameter at a time. In each test, the conditions giving the best staining quality were selected to be used in the final optimized protocol of **Table 4:1**. The details of the optimization are shown in **Table 4:2**, for which times are expressed in minutes. The sample ID corresponds to the bottom-left codes present in the pictures of **Figure 4:2**, **Figure 4:3** and **Figure 4:4**. The parameter optimize for each test is highlighted in grey.

Table 4:2 | Detailed protocol step times during optimization. The protocol steps and the corresponding time (in minutes) for the optimization experiments are depicted for each test of this study. The sample identifier (ID) corresponds to the bottom-left code present in the figures of the main text. The highlighted rows correspond to the time changes, realized for the parameters of interest.

	Slide number	6	3	8	22	25	27	26	23	22	17	19	59	61	30	36	37	39	40	41
	Sample ID	2A1	2A2	2A3	2B1	2B2	2B3	2B4	2B5	2C1	2C2	2D1	3A1	3A2	3B1	3B2	3B3	3C1	3C2	3C3
1	Sectioning	0.0	0.0	0.0	0.0	0.0	0.0	0.0	0.0	0.0	0.0	0.0	0.0	0.0	0.0	0.0	0.0	0.0	0.0	0.0
2	Tissue drying	0.0	0.0	15.0	15.0	15.0	15.0	15.0	15.0	15.0	2.0	15.0	15.0	15.0	15.0	15.0	15.0	15.0	15.0	15.0
3	Fixation	10.0	10.0	10.0	10.0	5.0	3.0	2.0	1.0	10.0	10.0	10.0	10.0	10.0	10.0	10.0	10.0	10.0	10.0	10.0
4	Drying	15.0	15.0	15.0	15.0	15.0	15.0	15.0	15.0	15.0	2.0	15.0	15.0	15.0	15.0	15.0	15.0	15.0	15.0	15.0
5	Rehydration	15.0	15.0	15.0	15.0	15.0	15.0	15.0	15.0	15.0	15.0	1.0	15.0	15.0	15.0	15.0	15.0	15.0	15.0	15.0
6	Peroxidase block	2.0	2.0	2.0	2.0	2.0	2.0	2.0	2.0	2.0	2.0	2.0	0.0	0.0	0.0	0.0	0.0	0.0	0.0	0.0
7	Washing	0.5	0.5	0.5	0.5	0.5	0.5	0.5	0.5	0.5	0.5	0.5	0.0	0.0	0.0	0.0	0.0	0.0	0.0	0.0
8	Protein block	2.0	2.0	2.0	2.0	2.0	2.0	2.0	2.0	2.0	2.0	2.0	2.0	0.0	2.0	2.0	2.0	0.0	0.0	0.0
9	Washing	0.5	0.5	0.5	0.5	0.5	0.5	0.5	0.5	0.5	0.5	0.5	0.5	0.0	0.5	0.5	0.5	0.0	0.0	0.0
10	Ab I	4.0	4.0	4.0	4.0	4.0	4.0	4.0	4.0	4.0	4.0	4.0	2.0	2.0	4.0	2.0	1.0	4.0	4.0	4.0
11	Washing	0.5	0.5	0.5	0.5	0.5	0.5	0.5	0.5	0.5	0.5	0.5	0.5	0.5	0.5	0.5	0.5	0.5	0.5	0.5
12	Post I	4.0	4.0	4.0	4.0	4.0	4.0	4.0	4.0	4.0	4.0	4.0	0.0	0.0	0.0	0.0	0.0	0.0	0.0	0.0
13	Washing	0.5	0.5	0.5	0.5	0.5	0.5	0.5	0.5	0.5	0.5	0.5	0.0	0.0	0.0	0.0	0.0	0.0	0.0	0.0
14	Ab II	4.0	4.0	4.0	4.0	4.0	4.0	4.0	4.0	4.0	4.0	4.0	4.0	4.0	4.0	4.0	4.0	4.0	2.0	1.0
15	Washing	0.5	0.5	0.5	0.5	0.5	0.5	0.5	0.5	0.5	0.5	0.5	0.5	0.5	0.5	0.5	0.5	0.5	0.5	0.5
16	DAB	2.4	2.4	2.4	2.4	2.4	2.4	2.4	2.4	2.4	2.4	2.4	2.0	2.0	5.0	5.0	5.0	2.4	2.4	2.4
17	Washing	0.5	0.5	0.5	0.5	0.5	0.5	0.5	0.5	0.5	0.5	0.5	0.5	0.5	5.0	5.0	5.0	0.5	0.5	0.5
18	Counterstaining	4.0	4.0	4.0	4.0	4.0	4.0	4.0	4.0	4.0	4.0	4.0	2.0	2.0	5.0	5.0	5.0	4.0	4.0	4.0
19	Washing	0.5	0.5	0.5	0.5	0.5	0.5	0.5	0.5	0.5	0.5	0.5	0.5	0.5	5.0	5.0	5.0	5.0	5.0	5.0
	Total	**65.9**	**65.9**	**80.9**	**80.9**	**75.9**	**73.9**	**72.9**	**71.9**	**80.9**	**59.9**	**66.9**	**69.5**	**67.0**	**86.5**	**84.5**	**83.5**	**80.4**	**78.4**	**77.4**

	Slide number	45	43	39	91	90	92	93	94	62	62	65	68	72	89	80	79
	Sample ID	4A1	4A2	4A3	4B1	4B2	4B3	4B4	4B5	4C1	4C1	4C3	4D1	4D2	4E1	4E2	4E3
1	Sectioning	0.0	0.0	0.0	0.0	0.0	0.0	0.0	0.0	0.0	0.0	0.0	0.0	0.0	0.0	0.0	0.0
2	Tissue drying	15.0	15.0	15.0	15.0	15.0	15.0	15.0	15.0	15.0	15.0	15.0	15.0	15.0	15.0	15.0	15.0
3	Fixation	10.0	10.0	10.0	3.0	3.0	3.0	3.0	3.0	10.0	10.0	10.0	3.0	3.0	3.0	3.0	3.0
4	Drying	15.0	15.0	15.0	15.0	15.0	15.0	15.0	15.0	15.0	15.0	15.0	2.0	2.0	15.0	15.0	15.0
5	Rehydration	15.0	15.0	15.0	15.0	15.0	15.0	15.0	15.0	15.0	15.0	15.0	1.0	15.0	15.0	15.0	15.0
6	Peroxidase block	0.0	0.0	0.0	0.0	0.0	0.0	0.0	0.0	0.0	0.0	0.0	0.0	0.0	0.0	0.0	0.0
7	Washing	0.0	0.0	0.0	0.0	0.0	0.0	0.0	0.0	0.0	0.0	0.0	0.0	0.0	0.0	0.0	0.0
8	Protein block	0.0	0.0	0.0	0.0	0.0	0.0	0.0	0.0	2.0	2.0	2.0	0.0	0.0	0.0	0.0	0.0
9	Washing	0.0	0.0	0.0	0.0	0.0	0.0	0.0	0.0	0.5	0.5	0.5	0.0	0.0	0.0	0.0	0.0
10	Ab I	4.0	4.0	4.0	2.0	2.0	2.0	2.0	2.0	2.0	2.0	2.0	2.0	2.0	2.0	2.0	2.0
11	Washing	0.5	0.5	0.5	0.8	0.8	0.8	0.8	0.8	0.5	0.5	0.5	0.5	0.5	0.8	0.8	0.8
12	Post I	0.0	0.0	0.0	0.0	0.0	0.0	0.0	0.0	0.0	0.0	0.0	0.0	0.0	0.0	0.0	0.0
13	Washing	0.0	0.0	0.0	0.0	0.0	0.0	0.0	0.0	0.0	0.0	0.0	0.0	0.0	0.0	0.0	0.0
14	Ab II	4.0	4.0	4.0	4.0	4.0	4.0	4.0	4.0	4.0	4.0	4.0	4.0	4.0	4.0	4.0	4.0
15	Washing	0.5	0.5	0.5	0.8	0.8	0.8	0.8	0.8	0.5	0.5	0.5	0.5	0.5	0.8	0.8	0.8
16	DAB	0.5	1.5	2.5	1.5	1.5	1.5	1.5	1.5	2.0	2.0	2.0	1.5	1.5	1.5	1.5	1.5
17	Washing	5.0	0.5	0.5	0.8	0.8	0.8	0.8	0.8	0.5	0.5	0.5	0.5	0.5	0.8	0.8	0.8
18	Counterstaining	4.0	4.0	4.0	0.3	0.3	0.3	0.3	0.3	2.0	2.0	2.0	0.5	0.3	0.3	0.3	0.3
19	Washing	5.0	0.5	0.5	1.0	1.0	1.0	1.0	1.0	0.5	0.5	0.5	1.0	1.0	1.0	1.0	1.0
	Total	**69.4**	**70.5**	**70.5**	**59.0**	**59.0**	**59.0**	**59.0**	**59.0**	**69.5**	**69.5**	**69.5**	**31.5**	**45.3**	**59.0**	**59.2**	**59.2**

Chapter 5 Automated microfluidic cytokeratin staining of thick resections of breast carcinomas

Positive surgical margins during breast conservative surgery are associated with breast tumor recurrence. Therefore, accurate assessment of surgical margins has become crucial to guarantee the best treatment of breast cancer. A tool that could aid surgeons assess the margin of the surgical cut intraoperatively would decrease the intraoperative analysis time without sacrificing important features such as margin width assessment and morphological information. In this study, we show the development of a microfluidic tool that allows automated staining and imaging of thick tissue samples. Tranches of breast mastectomies taken from the proximity of the tumor location are inserted in a chamber and stained for presence of cytokeratins using microfluidic chips fabricated for this application. We anticipate that the microfluidic chip and method presented in this work have the potential to translate fast immunostaining capabilities to their application in the intraoperative assessment of lumpectomy margins.

This chapter is an adapted version of the following manuscript in preparation:

- **D. G. Dupouy**, A. Cavinato, M. Fiche, L. de Leval, and M. A. M. Gijs, “Automated microfluidic cytokeratin staining of thick resections of breast carcinomas”, Lab on a Chip, in preparation.

5.1 Introduction

Breast conservative surgery (BCS), accompanied by adjuvant radiotherapy, has become a standard method for treatment of low-grade breast cancers. It has been demonstrated that survival rates after BCS are similar to those achieved after complete mastectomy, though the recurrence rates are generally higher [132]. Studies have shown that positive surgical margins are associated with breast tumor recurrence [133], but, even though this could be prevented by augmenting the resected volume around the tumor, the cosmetic and psychological impact for the patient are significantly increased [134]. Therefore, accurate assessment of surgical margins has become crucial to guarantee the best treatment of breast cancer.

Currently, the standard procedure consists of a first gross examination with or without a radiologic image of the resection, depending on whether the tumoral mass is palpable or not [135]. If the resection margin is close or positive (< 1cm), the pathologist performs a frozen section analysis on the suspicious areas and evaluate the margin's width. There is not enough evidence to state that a wide margin presents advantages over a narrow margin, as long as the latter remains negative. [136]. However, frozen section analysis can only measure the margin width on a few chosen areas due to time constrains, and thereby does not discard the possibility of positive margins on adjacent areas. Moreover, the absence of a tumor-specific staining implies risks of low detection sensitivity of invasive cancer cells. A proposed alternative to frozen section analysis is the cytologic "touch prep" analysis of the lumpectomy margins, which consists in gently pressing freshly cut surfaces of the specimen against a glass slide and subsequently staining them with hematoxylin and eosin [137]. This method is accurate, rapid and cost-efficient in determining whether the margin is positive or not. Furthermore, it allows for testing the complete surface of the lumpectomy, which is impossible with frozen sections [138]. However, the intrinsic insensitivity of this technique to visualize cells below the surface of the cut prevents pathologists from estimating how close the margin is to the tumor, which increases the risk of false negativity. Combining gross examination of the main resection to shaved margin analysis of the lumpectomy cavity has been proposed as significantly reducing the re-excision rates [139]. The main disadvantages of this method are the increased intraoperative time and the loss of information regarding the margin width. Several alternative intraoperative margin assessment techniques have been described in literature, which make use of magnetic resonance [140], ultrasound [141] or impedance spectroscopy [142] to create an image or detect a signal due to the presence of cancer cells. The major common drawback these techniques is the lack of microscopic examination capabilities, preventing the pathologist to spot a small number of infiltrating tumor cells and eventually resulting in positive margins. For formalin-fixed paraffin-embedded tissue sections, we have already demonstrated that the use of microfluidic techniques can significantly decrease the required Ab incubation time of immunofluorescence stainings [65], [131], leading to rapid morphological characterization of the tissue samples and accurate diagnosis.

There is a clear need for a tool that can aid surgeons and pathologists assess the margin of the surgical cut intraoperatively, reducing the use of frozen sections. This would decrease the intraoperative analysis time without sacrificing important features such as margin width assessment and morphological information. In this work, we show the development of a microfluidic tool that allows automated staining and imaging of thick tissue samples. Tranches of breast mastectomies taken from the proximity of the tumor location are inserted in a chamber and stained for presence of CK using two types of microfluidic chips fabricated for this application, called Microfluidic Tumorectomy Stainers (MTS). A first type consists of a Si/Pyrex MTS that is clamped to a PMMA tissue holder that accommodates the sample; in this case imaging of the stained sample is done after removal of the tissue from the Si/Pyrex MTS. A second type consists of a COC/PSA MTS; in this case imaging of the stained sample can be either directly done on-chip, as the chip incorporates a thin imaging window, or after removal from the COC/PSA MTS. Fluorescence images of the stained tissue specimens and their negative controls were taken both in widefield and confocal settings. We anticipate that the microfluidic chip and method presented in this work have the potential to translate fast immunostaining capabilities to their application in the intraoperative assessment of lumpectomy margins.

5.2 Material and methods

5.2.1 Sample preparation

Anonymized resections from two mastectomy samples were obtained from the Institute of Pathology at the Centre Hospitalier Universitaire Vaudois (CHUV). Ethical approval was obtained from the “Commission cantonale d'éthique de la recherche sur l'être humain” (CER-VD) under the protocol number 81/13. The specimens were cut by a specialized pathologist from the surroundings of the primary tumor using a scalpel, immediately frozen using liquid nitrogen vapor and kept at -25 °C until the beginning of the staining experiment. Prior to the microfluidic staining, samples were removed from the freezer and immersed in cold acetone (-20 °C) for fixation.

5.2.2 Working principle

Once the sample preparation was finalized, the tissue specimen was inserted into the cavity of a custom-designed PMMA tissue holder and then clamped with the MTS via two inlet/outlet joints and a gasket. The residual space around the tumor sample was occupied by a custom-cut PDMS elastomer block to minimize the chamber’s dead volume. Two different MTS designs and fabrication methods were tested during our experiments. The first approach, illustrated in **Figure 5:1a**, is based on Si/Pyrex microfabrication [16], [17], which consists in the patterning of microchannels in Si using deep reactive ion etching, followed by bonding of a Pyrex wafer using an intermediate Parylene C bonding layer. Details of the microfabrication process flow were shown in chapter 1. Spacing between the tissue sample and the lower Pyrex surface is guaranteed by a silicon grid with cross-shaped pillars (see **Figure 5:2b.iii**). The second MTS design, shown in **Figure 5:1b**, was implemented using first hot-embossing and milling of COC by a subcontractor, followed by the addition of PSA to assure both sealing of the microfluidic channels and formation of the thin (0.1 mm) imaging window.

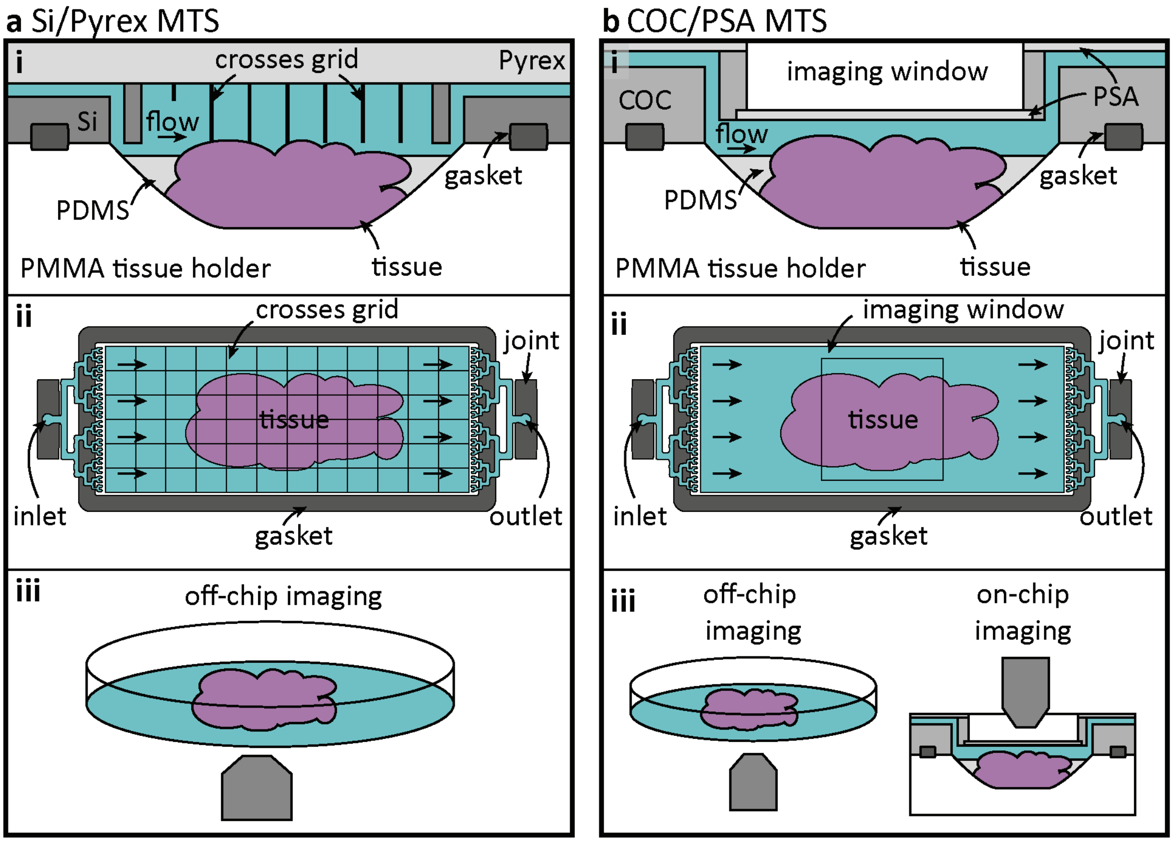
a Si/Pyrex MTS
i
crosses grid
Pyrex
Si
flow
gasket
PDMS
PMMA tissue holder
tissue
ii
crosses grid
joint
tissue
inlet
outlet
gasket
iii
off-chip imaging
b COC/PSA MTS
i
imaging window
COC
PSA
flow
gasket
PDMS
PMMA tissue holder
tissue
ii
imaging window
joint
tissue
inlet
outlet
gasket
iii
off-chip imaging
on-chip imaging

Figure 5:1 │ Microfluidic Tissue Stainer (MTS) working and imaging principle. (a) Si/Pyrex MTS. **(i)** Schematic cross-section of the Si/Pyrex MTS, which is clamped to the PMMA tissue holder that accommodates the sample, where the gasket assures sealing of the staining chamber. The residual space around the tumor sample is occupied by a custom-made PDMS elastomer to minimize the chamber's dead volume. For staining, spacing between the tissue sample and the lower Pyrex surface is guaranteed by a silicon grid with cross-shaped pillars. **(ii)** Schematic top-view of the Si/Pyrex MTS. The microfluidic channel design allows for equilibrated distribution of staining reagents in the chamber. **(iii)** Schematic of the off-chip petri dish-based imaging setting for tissues after staining using the Si/Pyrex MTS. **(b)** COC/PSA MTS. **(i)** Schematic cross-section of the COC/PSA MTS, which is clamped to the PMMA tissue holder that accommodates the sample. The PSA tapes assure both sealing of the microfluidic channels and formation of the thin (0.1 mm) imaging window that can be deflected during pressure-driven delivery of staining reagents. **(ii)** Schematic top-view of the COC/PSA MTS. **(iii)** Schematic of two options for imaging when staining with the COC/PSA MTS: either off-chip petri dish-based imaging after staining and removal of the tissue from the setup or direct on-chip imaging can be used.

5.2.3 Microfluidic setup

An exploded view of the assembly of the complete manifold is shown in **Figure 5:2a.i**. The MTS (either Si/Pyrex MTS or COC/PSA MTS) is mechanically clamped with the PMMA tissue holder and the surrounding PMMA block. Two separate sets of screws are used to seal the inlet/outlet joints independently from the chamber gasket. **Figure 5:2a.ii** illustrates how the MTS is interfaced with the inlet and outlet tubes of the PMMA block.

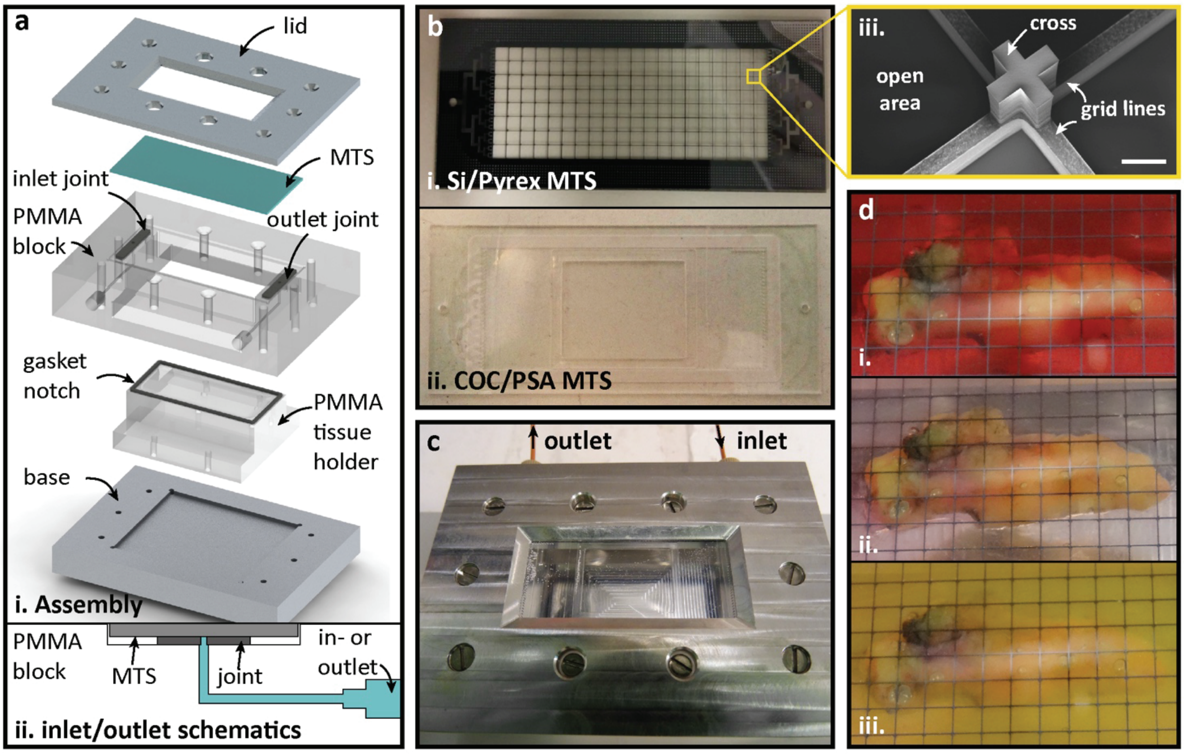

Figure 5:2 | Experimental realization of the microfluidic setups. (a) (i) Exploded view of the assembly of the complete manifold, in which the MTS (either Si/Pyrex MTS or COC/PSA MTS) is mechanically clamped with the PMMA tissue holder and surrounding PMMA block. (ii) Schematic of inlet or outlet of the MTS, which is sealed independently from the staining chamber with the PMMA block using an inlet or outlet joint. **(b)** Picture of the (i) Si/Pyrex MTS and (ii) the COC/PSA MTS. (iii) Scanning electron microscope image of a cross-shaped pillar of the Si/Pyrex MTS. Scale bar: 200 µm. **(c)** Picture of the complete manifold assembly with a COC/PSA MTS. **(d)** Pictures of a characterization experiment showing the delivery and washing of food colorants over a breast cancer tumorectomy sample at a flow rate of 100 µl/s: (i) after complete filling during 10 s with red dye, (ii) after washing during 20 s with PBS buffer and (iii) after subsequent filling after 10 s with yellow dye.

5.2.4 MTS-based staining

After the tissue was inserted into the PMMA tissue holder and clamped to the MTS, the “on-chip” steps in **Table 5:1** were performed. The protocol was defined using the graphical user interface of a fluidic manipulation setup realized with four syringe pumps (Cetoni, Germany). Staining was done with mouse anti-human CK, clone AE1/AE3, diluted 1/100 times (code M3515, Dako) followed by Alexa Fluor 594 goat anti-mouse diluted 1/140 (code: A-11032, Thermo Fisher). Washing A (steps 2, 7 and 9) was done using 1% Triton-X (code: T8787, Sigma Aldrich) in PBS pH 7.4 (code: 70011-044, Thermofisher). Blocking (steps 2 and 8) and washing B (steps 4 and 6) were done adding 10% fetal bovine serum (FCS) (code: F7524, Sigma Aldrich) to the washing A buffer. Primary (step 5) and secondary (step 10) Abs were diluted in blocking buffer. For both blocking and Ab solutions, 0.02% of sodium azide (code: 08591, Sigma Aldrich) was added. Finally, tissues that were not imaged on-chip were mounted in a petri-dish (step 12) using a solution containing DAPI called Fluoroshield (code: F6057, Sigma Aldrich).

Table 5:1 | Staining protocol using the MTS. Fixation with acetone at -20 °C was performed off-chip. Washing, blocking, primary Ab and secondary Ab steps were performed on-chip. The flow rate during delivery -column (i)- was set to

100 µl/s for buffers and 25 µl/s for Abs. The dispensed volume -column (ii)- was set to 1000 µl/s for all the on-chip steps. Incubation times and number of repetitions are detailed in columns (iii) and (iv), respectively.

Step	*Description*	*(i) Flush flow rate (µl/s)*	*(ii) Volume (µl/)*	*(iii) Incubation time (min)*	*(iv) Repetitions*	*On-chip*
1	Fixation: acetone (-20 °C)	N/A	N/A	5	1	N
2	Washing A: 1% Triton-X in PBS	N/A	N/A	5	3	Y
3	Blocking: 1% Triton-X + 10% FCS + 0.2%NaN_3	100	1000	30	2	Y
4	Washing B: 1%Triton-X + 10%FCS	100	1000	7.5	2	Y
5	Primary Ab: 1/100 anti-human CK, 1% Triton-X, 10% FCS, 0.02% NaN_3	25	1000	60	1	Y
6	Washing B: 1% Triton-X + 10% FCS	100	1000	5	3	Y
7	Washing A: 1% Triton-X	100	1000	7.5	2	Y
8	Blocking: 1% Triton-X + 10% FCS + 0.2% NaN_3	100	1000	60	1	Y
9	Washing A: 1% Triton-X	100	1000	7.5	2	Y
10	Secondary Ab: AF594 1/140 goat anti-mouse IgGs, 1% Triton-X, 10% FCS, 0.02% NaN_3	25	1000	60	1	Y
11	Washing A: 1%Triton-X	100	1000	10	3	Y
12	Mounting: Fluoroshield coverslipping	N/A	N/A	N/A	N/A	N

5.2.5 Fluorescence image acquisition

Off-chip imaging was done using an inverted confocal microscope (LSM 700, Zeiss) through a plastic petri-dish. A color depth of 24-bit and a resolution of 195 nm/pixel was achieved. On-chip imaging was done with an upright microscope (Axio Imager M2m, Zeiss) through the PSA window of the COC/PSA MTS. Images were taken with a depth of 12-bit per channel and a resolution of 645 nm/pixel. For both microscopes, 20x 0.75 NA objectives were used. Images were treated using ImageJ software.

5.3 Results

5.3.1 Characterization

Pictures of the Si/Pyrex MTS and the COC/PSA MTS are shown in **Figure 5:2b.i** and **Figure 5:2b.ii**, respectively. A scanning electron microscope (SEM) image of the cross-shaped pillars present in the Si/Pyrex MTS is shown in **Figure 5:2b.iii**. A picture of the assembled manifold with a COC/PSA MTS is shown in **Figure 5:2c**. Pictures of a characterization experiment showing the delivery and washing of food colorants over a breast cancer tumorectomy sample at a flow rate of 100 µl/s are shown in **Figure 5:2d**. Snapshots were taken (i) after complete filling of the chamber during 10 s with red dye, (ii) after washing during 20 s with PBS buffer and (iii) after subsequent filling after 10 s with yellow dye.

5.3.2 CK staining using the MTS

We performed CK staining experiments using the protocol described in **Table 5:1**, both using the Si/Pyrex MTS and the COC/PSA MTS. **Figure 5:3a** shows snapshot off-chip images using wide-field microscope settings for staining experiments done using the Si/Pyrex MTS, while **Figure 5:3b** shows on-chip images of the same staining protocol using the COC/PSA MTS. In both cases, a specific staining was achieved, as observed in a comparison with the corresponding negative controls. Recognition of the CK-positive structures was clear under microscope observation, though the focusing was troublesome due to the wide-field settings. We therefore repeated the staining protocol on both MTS designs and performed off-chip imaging on a petri dish using confocal microscope settings. As shown in **Figure 5:4**, the results specific to CK staining and the focusing was sharper.

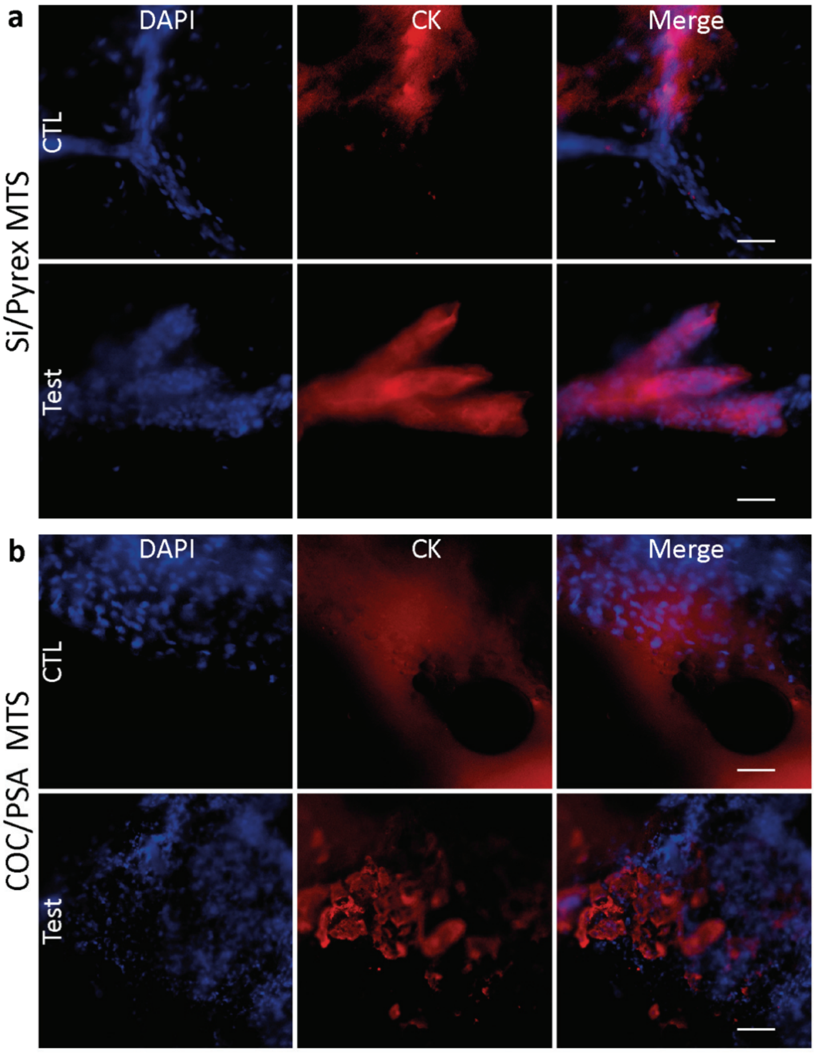

Figure 5:3 │ Images taken by a widefield fluorescence microscope. (a) Snapshot off-chip images of CK staining done using the Si/Pyrex MTS. **(b)** Snapshot on-chip images of CK staining performed with a COC/PSA MTS. (CTL: negative control in which a fluorescent secondary antibody (Ab) but no primary anti-CK Ab is applied in the staining protocol; Test: both primary and secondary antibodies are applied in the staining protocol; DAPI: counterstain for highlighting the nuclei; Merge: overlapping DAPI and CK channels. Scale bar: 50 μm)

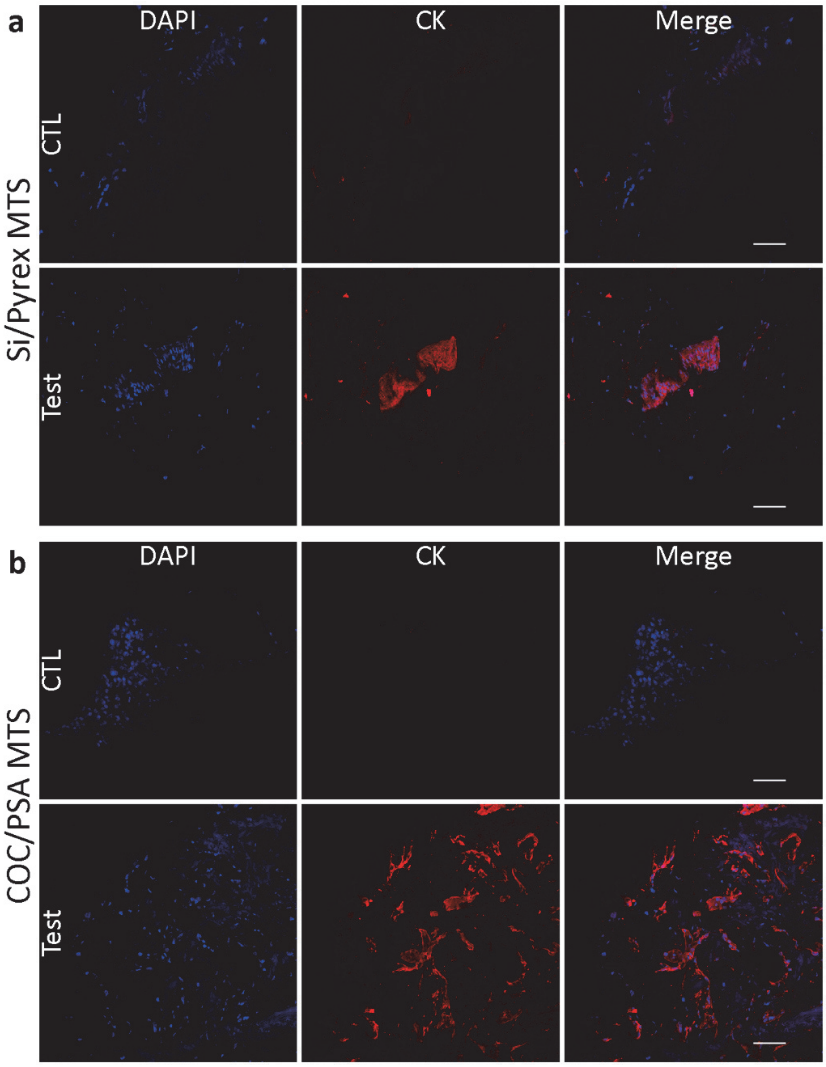

Figure 5:4 | Images taken by a confocal fluorescence microscope. (a) Snapshot off-chip images of CK staining done using the Si/Pyrex MTS. **(b)** Snapshot off-chip images of CK staining performed with a COC/PSA MTS. (CTL: negative control in which a fluorescent secondary Ab but no primary anti-CK Ab is applied in the staining protocol; Test: both primary and secondary antibodies are applied in the staining protocol; DAPI: counterstain for highlighting the nuclei; Merge: overlapping DAPI and CK channels. Scale bar: 50 μm)

5.4 Discussion

The main advantage of using silicon-based fabrication technologies for the development of microfluidic chips lies on the sub-micron resolution capabilities that can be obtained with photolithography. Moreover, deep reactive ion etching of Si allows for the microfabrication of sharp, high-aspect ratio features, such as the cross-shaped pillars, that would not be possible using polymers. Finally, the thin layer of native oxide that forms on Si makes it similar to glass, which makes it suitable for most applications due to its chemical compatibility. Fabrication of microfluidic chips in polymer is nevertheless preferred for most industrial microfluidic applications, due to the possibility to scale up the chip production by injection molding. Rapid prototyping polymer technologies, such as micromilling and hot-embossing, are available that allow for testing of microfluidic features during development. Two common disadvantages of polymers with respect to glass are the inferior chemical resistance to solvents and the spectrum of transparency to light, but COC has been recently used for fluorescence application. For our particular imaging application, COC versatility allowed us to combine a COC frame with a custom-fabricated imaging window made of a sheet of PSA. Furthermore, Si/Pyrex chips were significantly more fragile with respect to the ones in COC, rendering the latter more flexible to apply more pressure in the clamping operation without breaking.

5.5 Conclusions and outlook

We presented the development of a microfluidic tool that allows automated staining and imaging of thick tissue samples using two different microfabrication methods and materials. The two types of MTS demonstrated the advantageous use of microfluidics to stain tissue samples in an automated way, replacing cumbersome manual protocols. If coupled with fluorescence scanners, currently gaining importance in the field, we think that it would be easily possible to stain and assess several resections of fresh tumor samples during surgery with our devices, increasing the capabilities of intraoperative assessment. Moreover, having demonstrated that antibody incubation times can be significantly reduced in immunohistochemical stainings with the help of microfluidics, we anticipate that our MTS devices could be large benefit to intraoperative applications.

Chapter 6 Conclusion

6.1 Achieved results

Microfluidics have brought substantial development in many fields of *in vitro* diagnostics, with point-of-care as the leading application. Laboratory-based microfluidics has also helped push forward applications such as genomics, sequencing, high-throughput screening, and separation. The higher SVR achieved by handling reagents in the micrometer scale allows for higher sensitivity and assay turn-around-time. Surprisingly enough, only a few microfluidic devices have been designed to improve the performance of IHC assays used in the field of tissue-based diagnostics. During the course of this thesis, we explored silicon-based and polymer-based fabrication methods. We then focused our research in the development of microfluidic tools to improve precision, speed and automation in tissue-based diagnosis, when compared to what is provided by standard diagnostic tools until now.

We first characterized the fluorescence of the intermediate Parylene C bonding layer used in the fabrication of Si/Pyrex microfluidic chips and showed its programming capabilities for data storage. Industrialization of microfluidic devices possibly will bring additional automation challenges where the functionality, layout and protocol parameters will need to be stored and adjusted with changing versions of microfluidic chips. Therefore, information required for successful operation of each individual microfluidic chip, like the expiry date, optimized protocol for the specific layout and external hardware, should be communicated to automated platforms that microfluidic devices operate with. Using the programming capabilities of iPBLF, we showed data storage on Si/Pyrex microfluidic devices, where writing and erasing cycles of 5 min and 3 min, respectively, could be achieved repeatedly by alternating the exposure of Parylene C to UV and green light. This technique allowed data on a microfluidic chip to be read, written and erased using a common fluorescence microscope and could be useful to overcome automation challenges in industrial applications for which communication of information is required. In a second study, we showed how modifying iPBLF could we create an on-chip reference, which could be used to estimate concentrations down to a 7.6 $\mu g/ml$ at flow-rates of a few nl/s of fluorescent molecules in a microfluidic channel, when experimental conditions, like the intensity of the light, were tuned. A large number of lab-on-a-chip applications use fluorescence for quantifying biological entities, for which the incorporation of a stable on-chip fluorescent reference source could compensate for instrumental parameter variations, like non-constant illumination intensity over time. The major advantage of this method relies on the possibility to modify the fluorescence of an existing structural layer just by illuminating with UV light after fabrication, with no additional materials or steps. In addition, a standard mask aligner is sufficient to assure printing of fluorescent references on all devices of a wafer.

Subsequently, we focused our research on the use of the MTP to answer clinically relevant questions in the field of anatomic pathology, where microfluidic devices start to be introduced for the immunostaining of tissue sections. We proposed a microfluidic precision IF method, which proved to be very powerful in terms of quantifying Ag expression in histopathological tissue sections. Experiments on 25 breast cancer cases showed that HER2 biomarker quantification can provide molecular information that is as precise as data obtained by FISH tests, while keeping the cost and time advantage of an IF assay. FISH is used as a gold standard for *HER2* gene amplification assessment in breast cancer and for other diagnostic applications, and is replaced to some extent by conventional IHC as a surrogate marker of the genetic status. We showed that low incubation times (< 8 minutes) allowed by MTP-based staining resulted in a proportional relationship between the IF signal and the corresponding Ag concentration, and that this feature was lost when using higher incubation times, which explained the basis of the precision in the results. The linearity of the staining, combined with low-complexity image analysis, allowed us to establish a continuous scoring that linearly followed the gene copy number as assessed by FISH analysis. This method has the potential of providing automated, fast and high-quality quantitative *in situ* biomarker data using low-cost IF assays, as increasingly required in the era of individually tailored cancer therapy.

Next, we turned our interest towards the development of intraoperative solutions using microfluidics. FSs of tumor samples play an important role in the microscopic analysis of specimens during surgery for different purposes, such as the assessment of a resection margin in a tissue-conserving procedure, the determination of a metastatic condition or the identification of the possible cause of the symptoms in exploratory surgeries. Classical H&E staining methods often suffer from lack of sensitivity, which can be attributed to the absence of cancer cell-specific staining, leaving interpretation completely to the pathologist's experience. Moreover, the need for fast pathological examination during surgery makes FSs analysis one of the most challenging tasks that the pathologist performs in practice. We demonstrated that our microfluidic technology can deliver fast (< 12 min) and automated IHC stains using conventional anti-CK Abs on multiple frozen tissue types. Results showed specificity to cells of epithelial origin and low levels of background in the negative controls. The dimension of the prototype used for the staining experiments is compatible with the space constraints typically observed in intraoperative laboratories.

An increasingly common intraoperative analysis is done during BCS, which, accompanied by adjuvant radiotherapy, has become a standard method for treatment of low grade breast cancers. It has been demonstrated that survival rates after BCS are similar to those achieved after complete mastectomy, though the recurrence rates are generally higher. Therefore, accurate assessment of surgical margins has become crucial to guarantee the best treatment of breast cancer. We developed a new microfluidic tool that allows automated staining and imaging of thick (> 2 mm) tissue samples. Scalpel resections of breast mastectomies taken from the proximity of the tumor location were located in a reaction chamber and fluorescently stained for CK using the two different MTS designs. The two types of MTS demonstrated the advantageous use of microfluidics to stain tissue samples in an automated way, replacing cumbersome manual protocols. If coupled with fluorescence scanners, currently gaining importance in the field, we think that it would be easily possible to stain and assess several resections of fresh tumor samples during surgery with our devices, increasing the capabilities of intraoperative assessment.

6.2 Future development

As our understanding of carcinogenesis is increasing, quantitative and multiplexed detection of tumor biomarkers will become increasingly important to allow diagnosis, individualized medicine and follow-up of the disease as a function of treatment [143]. Indeed, the integration of several potentially significant clinical parameters into a comprehensive clinical decision-making algorithm will have an impact on individual cancer patient management and will lead towards individualized medicine [144]. The evaluation of the relative contributions of multiple levels of data, *e.g.* proteomics, genetics, genomics and IHC analysis, in the prediction of disease outcome and the response to newly developed anticancer agents, will be a great challenge. The MTP technology and its derived tools can deliver the required precision, speed and automation to open lines of research in the quantification of Ag expression, multiplexed full-section staining and even *in situ* targeting of DNA and RNA sequences.

The development and clinical validation of the MTP led to the incorporation of a startup company that I co-founded, together with Dr. Ata Tuna Ciftlik and Ms. Déborah Heintze: Lunaphore Technologies SA. I strongly believe that this company, in collaboration with LMIS2 and other research laboratories, will constitute the main vehicle for the development of the following research lines, as well as for the commercialization of the technology both in the IVD and in the Research markets. I therefore also included a brief description of some of the of the research activities that will be carried out by the company, as well as an executive summary of the business plan.

6.2.1 Quantification of Ag expression

Our « microfluidic precision IF » method (see chapter 3) could be readily used for the quantification of any biomarker in tissues. A clear example is rearranged ALK, a key oncogenic driver in NSCLC for which the resulting fusion protein is stabilized in the cytosol. Treatment decision for ALK inhibition is based on the proof of a protein overexpression by IHC or genomic translocation by break-apart FISH and real-time polymerase chain reaction. However, the semi-quantitative immunoreactivity score, which ranges from 0 to 3, is subjective for scores 1 and 2, and these two categories show non-linear correlations with FISH and PCR data. The response rate to targeted therapy (Crizotinib) remains around 58% for ALK-positive patients diagnosed this way [145]. IHC is generally considered to be performed at saturating conditions. Still, results vary heavily depending on the Ab dilution, time and temperature of Ab incubation and time of pretreatment Ag retrieval. Full saturation is often not desired, since the signal-to-noise ratio may be compromised. One immediate further validation of our microfluidic precision IF approach could therefore involve the quantitative evaluation of ALK expression in NSCLC.

6.2.2 Multiplexed staining

By far, the mostly used technique in routine biomarker diagnostics is IHC analysis, which has become an indispensable tool in diagnostic anatomical pathology, especially in protein expression profiling for detection of tumor biomarkers. However, today the state-of-the art of IHC is being challenged with the increasing need for precision in molecular subtyping of cancers. Recent trends in personalized medicine proved that a higher number of biomarker tests allows a more precise diagnosis, and eventually higher treatment success. Today, « IHC Panels » can consist of up to 20 IHC tests per patient [146], [147]. The number of different IHC biomarkers that can be observed simultaneously in a single tissue section has traditionally been limited to 2-3, and multiple markers can only be searched using multiple cuts from the same sample, resulting in loss of localization information between various biomarkers. Plus, such approach with multiple cuts overloads existing IHC workflow automation systems. On top of this, not all the samples are large enough to perform all the biomarker tests in this fashion, and there is a growing need to perform multiple IHC profiling on the same specimen. A major limitation of the multiplexing ability using immune-based approaches arises from the requirement that each primary antibody has to be derived from different animal species to ensure specific amplification and detection with secondary antibodies. Recent advances in immunostaining technologies are highly promising to overcome these limitations by applying multi-cycle *in situ* imaging [148], though, obtaining a reliable and sufficiently high throughput molecular profiling of tissue specimens becomes practically impossible. Eventually, both the multiplicity and the throughput of routine diagnostic

IHC or IF has to be increased in order to answer the growing need expected in the next years. A clear line of research for the development based on the automation capabilities of the MTP technology consists on filling the technological gaps that prevents high-throughput multi-cycle multiplexing of IHC markers on tissue sections.

6.2.3 *In situ* sequencing

Current solutions for RNA detection either lack spatial resolution or multiplicity. NGS platforms allow highly parallelized sequencing of up to billions of short reads within miniaturized flow cells. They commonly rely on either DNA-synthesis or DNA-ligation based chemistry for reading single molecule targets or clonally amplified templates with high throughput. However, for diagnostics this is disconnected from the current paradigms, where the morphology of the tissue is of central importance. For example, to understand cancer development and progression, it is essential to monitor the intricate interplay between the typically heterogeneous populations of cancer cells and the tumor microenvironment, itself containing numerous different cell types. This heterogeneous composition is reflected by highly localized, cell type-specific expression of representative biomarkers rather than average transcription profiles of the tissue and hence requires technology to map biomarkers. FISH is by virtue strong in localization of gene transcripts, however, limited in the number of biomarkers that can be distinguished in parallel. FISH methods either rely on hybridization of multiple transcript-specific probes or on branched amplification of transcripts bound to fluorescent probes to generate a discernable signal. In a proof-of-concept study Nilsson *et al.* recently demonstrated a technique that performs NGS *in situ* directly in biological specimens, combining unique specificity with currently unmatched multiplicity [149]. Combining this technique with the automation capabilities of the MTP, we possibly could demonstrate automated execution of a considerably more complex *in situ* sequencing (ISS) protocols. ISS combined with the MTP platform has the potential to replace FISH and NGS methods, since it could outperform the existing options in terms of time, automation level, assay flexibility and data generated per sample.

6.2.4 Commercial development at Lunaphore Technologies SA

The microscopic assessment of protein expression patterns on tissues and cells by IHC is the most widely used biomarker diagnosis method in anatomical pathology. Advances in personalized medicine and a growing incidence of cancer clearly indicate that millions of additional IHC tests will be required globally each year. This growing need cannot be optimally met today due to: (i) tremendous cost-cutting pressure in diagnostic labs, limited space, reduced manpower and investment resources, which create fundamental bottlenecks; (ii) the capacities of the current automated equipment cannot be increased to meet the demand due to slow core processing technology (2-8 hours) and high equipment costs (CHF 100-200K), which limits overall throughput; and (iii) the lack of precision in quantitative IHC requires additional gene profiling tests to be performed which are 10x more expensive than an IHC test.

Lunaphore’s solution is a complete tissue processing platform performing IHC which can (i) realize the same assay 20x faster, (ii) increase the processing volume up to 10x, and (iii) perform precise quantitative analysis, thereby decreasing the need for additional tests by 90%. Thanks to our fast fluidic exchange technology, based on the development of the MTP invented by Dr. Ciftlik, we can control assay times with a resolution of one-second and reduce the staining time down to 5 min. Clinical data has also shown an increase in diagnostic accuracy with our system due to precise quantitative analysis.

Routine diagnostic laboratories repeatedly perform IHC for tumor diagnosis: 2’500 laboratories in Europe and US analyze 25 million biopsies annually. Benchmarking with prices between CHF 55 – 200 /assay, yields a market potential of around CHF 2 BN/year. Our primary target market in routine diagnostics are labs performing > 25’000 IHCs annually for breast, lung, prostate and colon cancers, indicating an addressable market of around CHF 1 BN/year.

Two products are under development (see **Figure 6:1**):

- *Satellite* is a compact platform designed for diagnostic laboratories with up to 20x higher throughput/reaction-chamber than existing machines, the shortest turn-around time, and precise quantitative assays, which minimizes the need for additional tests.
- *Application chips* will address 4 high-incidence cancer markers which will allow customers to run about 50% of their daily routine diagnostic workload with our high-throughput and precise technology.

Development of the diagnostic product, *Satellite*, began in 2015 and we plan to have the first prototype ready to start clinical validation in Q2/2017. Non-certified products will be launched on the research market by Q2/2018 and certified products for diagnostic labs is planned for Q4/2018.

Competitive automated laboratory workflow equipment for IHC is supplied by main players such as Dako, Roche-Ventana and Leica. Their limitations include: duration (2-8 hours), bulky equipment that requires specially trained personnel, limited multiplexing ability (2-3 markers), low precision in quantitative assay, and no accurate reaction control. In addition, prices for IHC systems are very high ranging from CHF 100 – 200K.

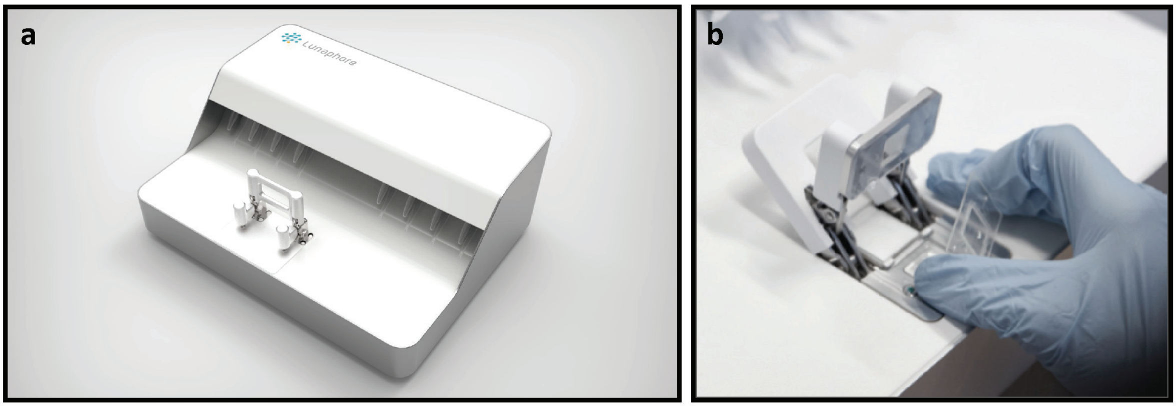

Figure 6:1 | Laboratory Satellite prototype called LABSAT 3. (a) Render view of Lunaphore’s staining prototype called LABSAT 3. **(b)** Picture of user inserting a COC MTP chip into the staining area of LABSAT 3. The MTP is clamped automatically against a tissue slide for formation of the reaction chamber and staining.

Appendix A. COMSOL simulations of the Microfluidic Tissue Processor

The MTP, developed at the Laboratory of Microsystems LMIS2 of EPFL, was described in chapter 1. Briefly, a microfluidic reaction chamber is formed at the interface between the MTP and a tissue-containing glass slide. The performance of the MTP is based on a controlled wash and delivery of reagents over the tissue surface, as well as the short diffusion distances in the vertical direction. Bioreagents need to be uniformly and rapidly distributed into a chamber through microfluidic channels and vias, and washed away after a few minutes of incubation. The MTP demonstrated to be faster and more accurate in performing immunohistochemical reactions when compared to conventional techniques. Finite element modelling (FEM) is an efficient approach to compare different designs of the MTP, since knowing the geometry and input parameters such as flow rate or concentration, it is possible to estimate the value of the parameters of interest as a function of time. Moreover, complex geometries combined with several physical phenomena (fluidics, reaction kinetics, diffusion kinetics) are frequently impossible to solve in a deterministic fashion. Finally, FEM allows for rapid parameter modification, which enables a qualitative determination of the effect of each parameter on the behavior of the system. In this appendix, we use COMSOL Multiphysics to run simulations of the MTP device, in order to understand the effect of different parameters on the pressure, velocity, concentration and reaction rate. In the first part, we show the effect of the geometry on the fluidic behavior of the MTP. We start by a 17x17 mm^2 chamber and modify it in order to boost the staining capabilities of the MTP, with the ultimate goal of staining the area corresponding to a complete glass slide. The second part deals with the reaction kinetics observed at the interface between the tissue section and the MTP chamber. By sweeping the values of unknown parameters in the reaction kinetics, such as the association constant and the surface concentration of binding sites, we observed different regimes of Ab-Ag complex formation in time.

A.1. Fluidic behavior of the MTP

In order to study the fluidic behavior of the MTP, we performed FEM simulations of a typical washing step taking place in the reaction chamber, where a solution containing Abs with an initial concentration of $3\times10^{-4}\ \mathrm{mol/m^3}$ is replaced by a buffer solution with no Abs. The washing time is defined as the time passed from the moment when the buffer starts to be flushed into the channels to the moment when the concentration inside the whole chamber is 10^{-7} times the initial concentration, as in previous simulations performed by Ciftlik *et al.* [65] and shown in chapter 1 of this thesis. These simulations return the concentration as a function of time during washing, as well as the velocity and pressure profiles. A 2D top-view geometry of the MTP was extracted from the graphic data system (GDS) files used for the fabrication of the microfluidic chips (see **Figure A:2**). Once the geometry was built, different assumptions regarding the microfluidic behavior were given to the software:

- Incompressible flow: especially applicable in microfluidics, when the flow velocities are much smaller than the velocity of pressure waves (sound) in the liquid, the liquid can be treated as being incompressible. This means that the density is constant in space and time and that the continuity equation applies, with the $\mathbf{v}$ velocity field [150].

$$\boldsymbol{\nabla}\cdot\mathbf{v}=0 \tag{A.1}$$

- Creeping flow: also called Stokes flow, it applies for limits of low flow velocities, where the nonlinear term of the Navier-Stokes equation can be neglected, leading to the Stokes equation with pressure p and dynamic viscosity η [150].

$$\mathbf{0}=-\boldsymbol{\nabla}p+\eta\nabla^2\mathbf{v} \tag{A.2}$$

- No slip boundary condition: the velocity field at the solid walls of the microfluidic system is equal to the velocity of the wall.

$$\mathbf{v}(\mathbf{r})=\mathbf{v}_{\boldsymbol{wall}}\,;\,\mathbf{r}\ \in \text{wall surface} \tag{A.3}$$

- Shallow channel approximation: the distance between the boundaries in the channels is small. A drag term is then added to the Navier-Stokes equation to account for the fluidic resistance induced by the close boundaries on the third dimension.

A.1.1 Parameters

Mesh. As the device includes a big chamber and small channels, it is necessary to define different meshes for those different geometries. Free triangular meshes were used for all geometries, but the sizes used were adjusted to the different features. In general, a « normal » mesh was selected for the chamber and a « extremely fine » mesh for the channels. Both meshes needed a final refinement to obtain a good transition at the boundary between the end of the channels and the entrance of the chamber. The size of the mesh in the channels had to be extremely fine to avoid sharp transitions of the velocity profile at every corner.

Inlets and Outlets. Inlets were defined as having constant « laminar inflow » and « flow rate ». The reason for this choice was that the experimental setup to which the simulations were confronted were flow rate-driven, corresponding to 25 $\mu l/s$ for a 17x17 mm^2 chamber. This starting flow rate was used to calculate the equivalent required flow rate for all the chamber size listed in **Table A:1** in order to obtain the same washing performance. In this calculation the chamber volume and the dead volumes were taken into consideration. The obtained flow rates for each MTP device are listed in **Table A:1**. Finally, outlets were defined by using a no pressure boundary condition.

Table A:1 | MTP device design. Four MTP designs were simulated. The name of each device is given by its reaction chamber lateral dimension and whether the liquid is flown on its longitudinal or transversal axis. The second column shows the volume for each MTP device. The third column shows the flow rate applied at the inlet, which was chosen so as to have a constant average velocity u_{av} in all designs ($u_{av} = Q/V$; Q: flow rate; V: volume)

Device	Volume $\boldsymbol{V}$ ($\boldsymbol{\mu l}$)	Flow rate $\boldsymbol{Q}$ ($\boldsymbol{\mu l/s}$)
17x17	29	25
22x22	52	45
22x50 (longitudinal)	102	88
22x50 (transversal)	107	92

Geometry. The starting geometry was imported from the GDS file used during fabrication of the MTP, corresponding to chamber of reaction with a surface of 17x17 mm^2. A snapshot of the GDS file is illustrated in **Figure A:2**. The picture shows a 4-inch wafer-level design having two MTPs. From this, subsequent geometries were built to set the simulations for all the devices listed in **Table A:1**.

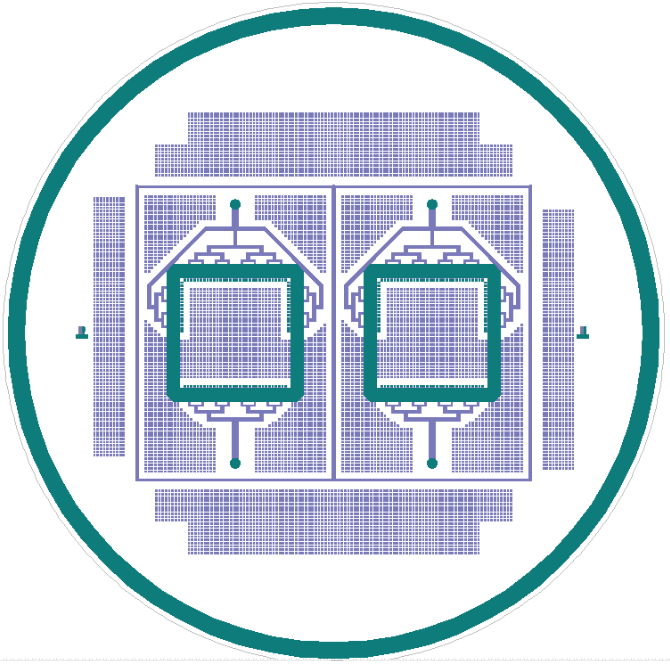

Figure A:2 | MTP 17x17 GDS. Snapshot of the GDS file used for the fabrication of the MTP 17x17 design. Three masks were used on a 4-inch wafer.

Transported molecules. Even though several different molecules are flushed into the reaction chamber of the MTP during staining, we consider Abs being the most relevant one since they are involved in the immunological recognition of the antigen. Therefore we set a diffusion coefficient $D = 9\times10^{-11}\ \mathrm{m}^2/\mathrm{s}$ for the molecules in solution, typical value for IgG antibodies grown in mouse dissolved in water.

A.1.2 Velocity profile

The velocity profiles inside the reaction chambers, obtained for the different MTP designs, are shown in **Figure A:3**. The arrows show the direction of the velocity inside the chamber. In order to assure a uniform staining of the lateral areas of the tissue with respect to the center, the velocity profile during reagent delivery should be as uniform as possible. To achieve this, the inlet and outlet microfluidic channels were designed to equally distribute the flow rate at the entry of the reaction chamber. Moreover, lateral channels at the exit were designed to reduce the fluidic resistance at the border of the channel, where due to the no-slip boundary condition, the liquid tend to flow at lower velocity than in the center. This counterbalances the formation of a parabolic profile and, thus, enables a more uniform velocity over the chamber.

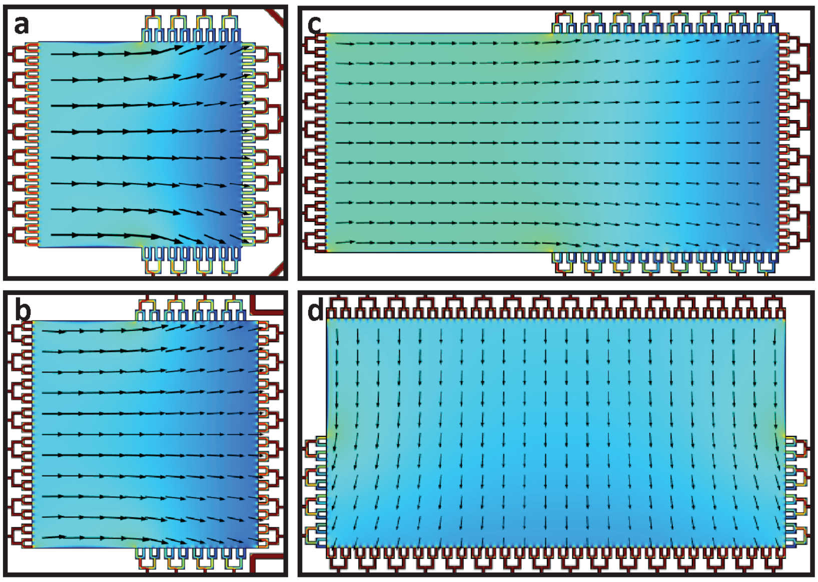

Figure A:3 | Velocity profile. (a) 17x17 (Linear color scale: Blue 0 m/s, Red 0.04 m/s.); **(b)** 22x22 (Linear color scale: Blue 0 m/s, Red 0.06 m/s.); **(c)** 22x50 (longitudinal) (Linear color scale: Blue 0 m/s, Red 0.1 m/s.); **(d)** 22x50 (transversal). (Linear color scale: Blue 0 m/s, Red 0.06 m/s.)

In order to better understand the « Shallow Channel Approximation » chosen among the assumptions described above, the simulation of the 17x17 device was run removing this feature. The effect on the velocity profile can be clearly observed in **Figure A:4**. The velocity is higher at the center of the chamber, this is typically the behavior that would be expected if the depth of the device was of the same order of magnitude as its width and length.

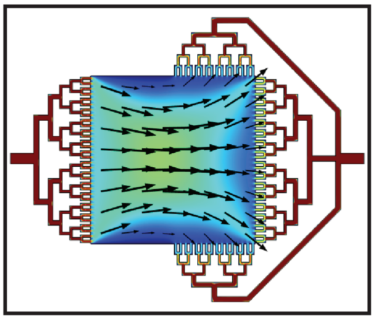

Figure A:4 | Velocity profile without "Shallow Channel Approximation". The third dimension of 2D simulation is considered of the same order of the lateral dimensions when the "Shallow Channel Approximation" is inactive. (Linear color scale: Blue 0 m/s, Red 0.04 m/s.)

A.1.3 Pressure

The fluidic simulations described above return the pressure profile at steady-state conditions. As a result, the inlet pressure required to obtain the desired flow rate can be extrapolated. For each MTP design, we estimated the inlet pressure in **Table A:2.**

Table A:2 | Inlet pressure. Inlet pressure obtained from fluidic simulations where the inlet flow rate is set as in **Table A:1** for the each MTP design.

Device	**Pressure (kPa)**
17x17	7
22x22	15
22x50 (longitudinal)	24
22x50 (transversal)	28

From the fluidic simulations of the 17x17 device, we could observe a strong increase of velocity in one of the channels located at the outlet (see **Figure A:5a**). This sudden velocity increase was avoided by increasing the width of the channel (see **Figure A:5b**). Moreover, the pressure required at the inlet in order to obtain a flow rate of 25 μl/s turned out to be reduced from 7 kPa to 6.3 kPa. In a similar modification of the outlet channels of the MTP 22X22 design, we obtained an inlet pressure reduction from 15 kPa to 14.5 kPa.

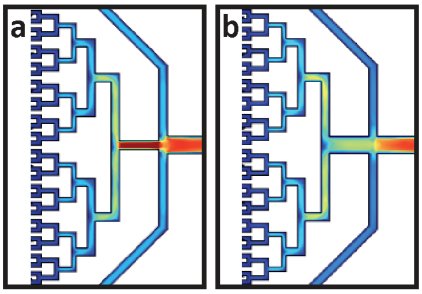

Figure A:5 | Velocity profile of MTP 17x17 design. (a) Original design. **(b)** Modified design with wider outlet channel. (Linear color scale: Blue 0 m/s, Red 0.3 m/s.)

A.1.4 Concentration

A time-dependent simulation was then added to the model to simulate the washing of the reagents present in the chamber. The concentration profile of the bioreagent inside the chamber and channels is shown in logarithmic scale for the 4 devices in **Figure A:6** at three different times from the beginning of the delivery: 0.4 s, 0.8 s and 1.4 s. The washing of the bioreagent in the chamber is done with a flat profile for all devices, which means that the whole area in the chamber is exposed to the bioreagents in during the same time and with the same same flux. The washing time, defined as the time passed from the beginning of the buffer delivery into the channels to the moment when the concentration inside the whole chamber is 10^{-7} times the initial concentration, was estimated to be 1.6 s for all the MTP devices when the flow rate from **Table A:1** was applied.

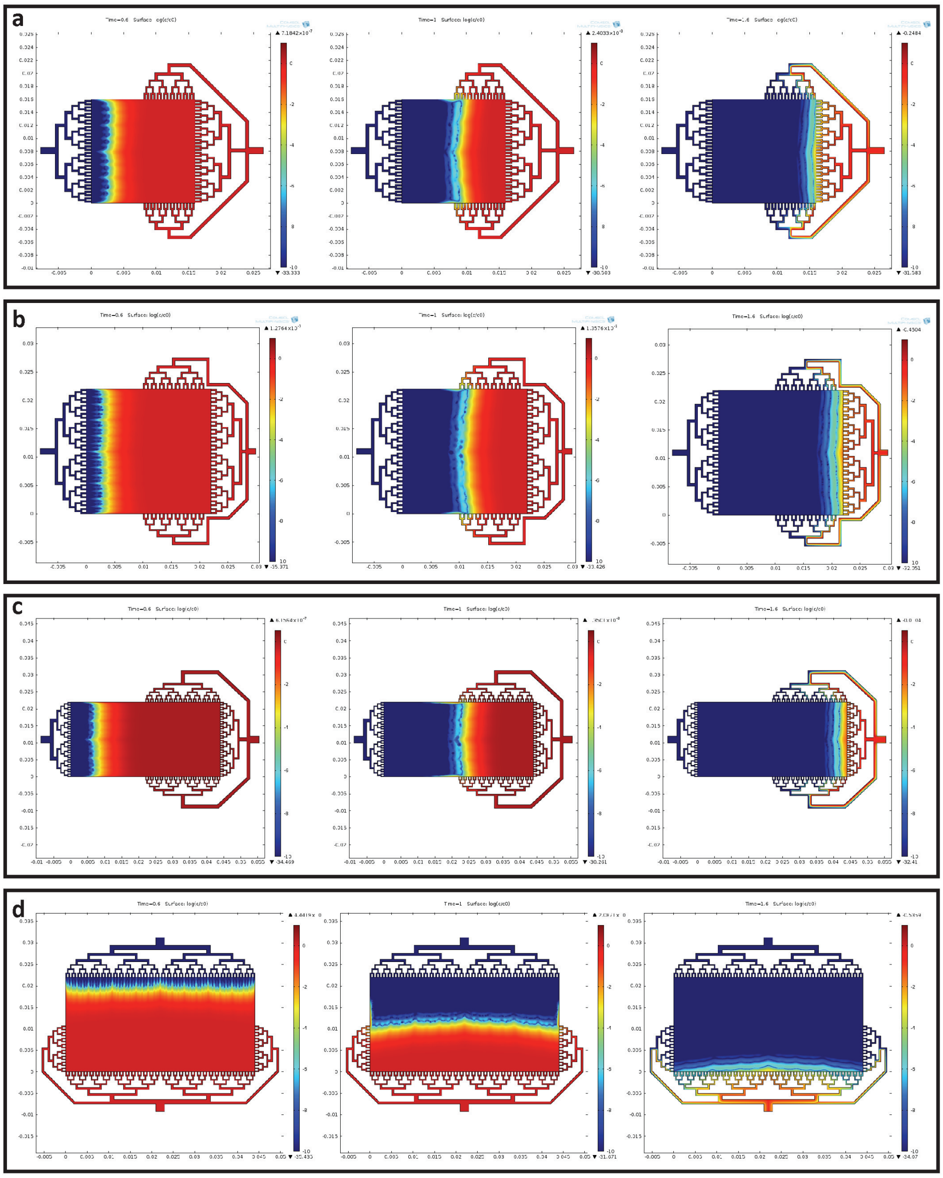

Figure A:6 |Concentration profile at washing. Logarithm of the concentration plot for **(a)** MTP 17x17, **(b)** MTP 22x22, **(c)** MTP 22x50 (longitudinal), **(d)** MTP 22x50 (transversal) devices. For each simulation the image was taken at 0.4 s (left), 0.8 s (middle) and 1.4 s (right) from the beginning of the washing. Red represents initial concentration. Blue represent 10^{-7} times the initial concentration. Washing is considered complete when the concentration in the chamber reaches 10^{-7} of the initial concentration. (Logarithmic color scale, c: concentration, c_0: initial concentration, Blue -10, Red 0.)

A.1.5 3D simulation of the velocity field

In order to verify the results obtained in the 2D simulations, and to determine the velocity profile in the z direction (direction perpendicular to the plane of the chamber), a 3D simulation was run. A Solidworks design of the MTP 17x17 was created and exported to COMSOL in order to define the geometry. A «Free Tetrahedral» mesh was used, with an aspect ratio of voxel width over voxel thickness of 10. The size of the mesh of the channels was chosen as « Extra fine », while the mesh of the chamber was set as «Fine». To visualize the velocity profiles, a slice-plot was created that was parallel to the x-y and located at middle of the chamber height in the z direction, so as to obtain the maximum velocity profile. The velocity profile on this plane is represented in **Figure A:7**. An inlet pressure of 8.8 kPa was estimated from the 3D simulation, being in 1.8 kPa higher than estimated from teh 2D model.

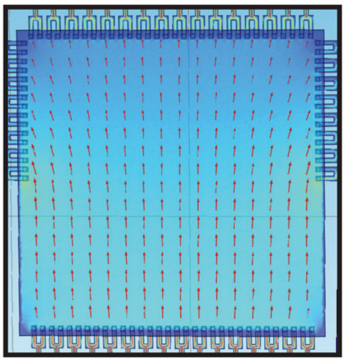

Figure A:7 | 3D fluidic simulation of MTP 17x17 device. The fluidic simulation with an applied flow rate of 25 µl/s returned a required inlet pressure of 8.8 kPa, which differes of 1.8 kPa from the pressure calculated from the analogous 2D simulation.

A.2. Reaction Kinetic analysis of the MTP

A 2D design of the MTP microfluidic chamber from the lateral viewpoint was simulated to analyze the kinetics of the antibodies in solution reacting with antigens present at different surface concentrations on the surface of a glass slide.

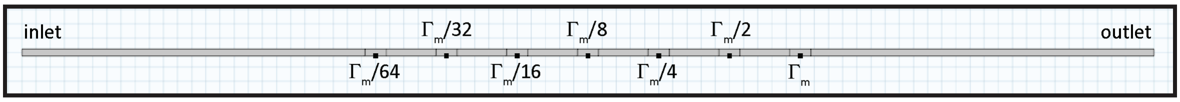

Figure A:8 | Schematic of reaction kinetic simulation. Lateral view of the reaction chamber of an MTP 17x17 design. Seven reaction points simulating regions containing Ags with an increasing concentration Γ_{max} from left to right.

Similarly, to the previous sections, a number of assumptions and parameter values were set in COMSOL. Abs in solution were once again set to a concentration of $3\times10^{-4}\ \mathrm{mol/m^3} = 3\times10^{-7}\ \mathrm{M}$. Additionally, a surface concentration of Ags was set on the bottom of the reaction chamber, simulating the presence of Ags in a tissue section or in a protein microarray. Once the geometry was built, different assumptions regarding the microfluidic behavior were given to the software. The assumptions of incompressible flow, creeping flow and no-slip boundary conditions were applied to this section. However, when we observe the reaction chamber from the side, it can be modelled as infinite parallel-plate channel, thus the shallow channel approximation was not activated. The simulation was run in 3 steps: (1) Loading, (2) Incubation and (3) Washing.

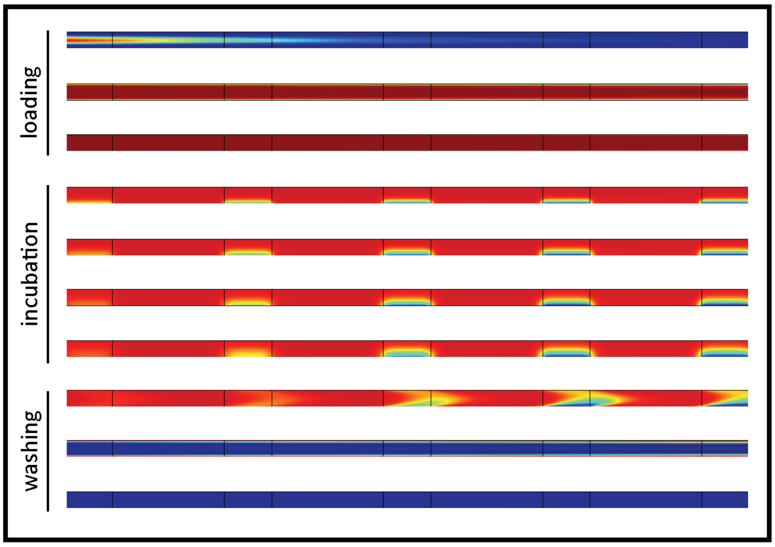

Figure A:9 | Simulation steps. Loading or reagents starts by flushing a solution with a concentration of Abs of 30 μM into a chamber with no Abs until the complete solution is exchanged. Incubation takes place for a minimum of 250 s and a maximum of 2000 s. Subsequently, washing is achieved by flusing a solution with no Abs. Color code: Blue: 0 μM, Red: 30 μM

A.2.1 Loading

As introduced in chapter 1, the theoretical steady-state depletion region δ_s can be calculated as

$$\delta_s = \left(\frac{DLH}{6u_{av}}\right)^{1/3} \tag{A.4}$$

where $D = 9\times10^{-11}\ \mathrm{m^2/s}$ is the diffusion coefficient of IgG antibodies chosen for these simulations, $L = 10\ \mathrm{mm}$ was selected as the typical size of a tissue section and $H = 100\ \mathrm{\mu m}$ is the height of the MTP chamber.

The average velocity u_{av} can be obtained from the flow rate $Q = 25\ \mathrm{\mu l/s}$ use for loading of the reagents, and the section of the chamber

$$u_{av} = \frac{Q}{W_c * H} = \frac{25\ \mathrm{\mu l/s}}{17\ \mathrm{mm} \times 100\ \mathrm{\mu m}} \approx 15\ \mathrm{mm/s} \tag{A.5}$$

Thus, during delivery of the reagents in the chamber $\delta_s \approx 10\ \mathrm{\mu m}$. The time for δ_s to develop can be calculated as

$$\tau_c = \frac{\delta_s^2}{D} \approx 1.1\ \mathrm{s} \tag{A.6}$$

A.2.2 Incubation

During incubation of the antibodies over the tissue section, the kinetics of the binding depends on the Damköhler number, given by $\mathfrak{D} = k_{on}\Gamma_{max}\delta/D$, which represents represents the ratio between the characteristic binding rate and the characteristic diffusion rate, as explained in chapter 1. If $\mathfrak{D} \ll 1$, the diffusion is not limiting the reaction and we obtain

$$\Gamma(\mathrm{t}) = k_{on}c_b\Gamma_{max}t \tag{A.7}$$

where the surface concentration of Ab-Ag complex increases proportionally to the time, being in pure reaction-limited regime. On the other hand, when $\mathfrak{D} \gg 1$ we obtain a pure diffusion-controlled reaction.

$$\Gamma(\mathrm{t}) = \frac{c_b}{2}\sqrt{2Dt} \tag{A.8}$$

In Eq.(A.7) and Eq. (A.8) $c_b = 3\times10^{-4}\ \mathrm{mol/m^3}$ represents the Ab bulk concentration, k_{on} is the association constant. In our simulated system k_{on} takes values from $10^3\ \mathrm{M^{-1}s^{-1}}$ to $10^6\ \mathrm{M^{-1}s^{-1}}$ and Γ_{max} from $10^{-11}\ \mathrm{mol/m^2}$ to $10^{-4}\ \mathrm{mol/m^2}$.

Therefore, in a system that works in a reaction-limited regime the relation between the number of reacting sites Γ and the time needs is linear. Nevertheless, when Γ approaches Γ_{max}, saturation appears and the linearity is lost.

Regarding the dissociation constant k_{off}, if we cannot assume $k_{on} \gg k_{off}$, then k_{off} will limit the number of reacted sites, and the value of Γ will saturate at a fraction of Γ_{max}.

It was possible to identify four possible behaviors for the MTP:

Rapid saturation. A reaction-limited regime is observed, thus a linear relation between Γ and t. The small number of available sites (small Γ_{max}) results in a very fast saturation. The curve $\Gamma(t)$ for this behavior is shown in **Figure A:10**.

Diffusion-limited. A diffusion-limited regime is observed, thus a non linear relation between Γ and t. The large number of available sites (large Γ_{max}) generates a fast consumption of the Abs in close vicinity to the tissue. A depletion region can be observed as in **Figure A:9** through which Abs need to diffuse before reaching the binding sites. The curve $\Gamma(t)$ for this behavior is shown in **Figure A:11**

Slow reaction. A reaction-limited regime where the association constant k_{on} is so small that the dissociation constant k_{off} starts playing a significant role even a the beginning of the reaction. This behavior is not expected where high-affinity Abs are used. The curve $\Gamma(t)$ for this behavior is shown in **Figure A:12**.

Slow saturation. The time it takes for the reaction to saturate is long enough to observe first a reaction-limited regime that lasts a few minutes, depending on Γ_{max}, and then a saturation plateau. The curve $\Gamma(t)$ for this behavior is shown in **Figure A:13**.

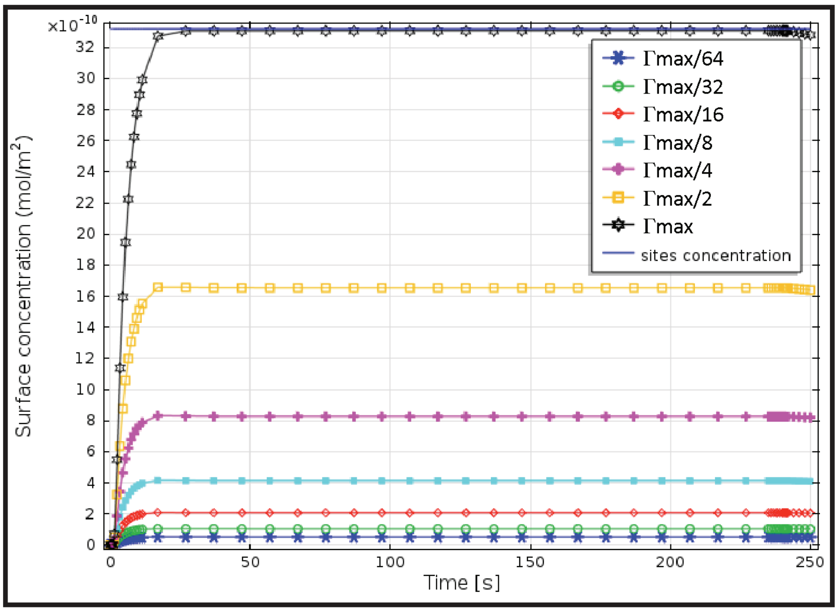

Figure A:10 | Rapid Saturation. Time-dependence of Γ for $\Gamma_{max} \sim 10^{-9}$ mol/m^2 and $k_{on} \sim 10^6$ M^{-1}s^{-1}.

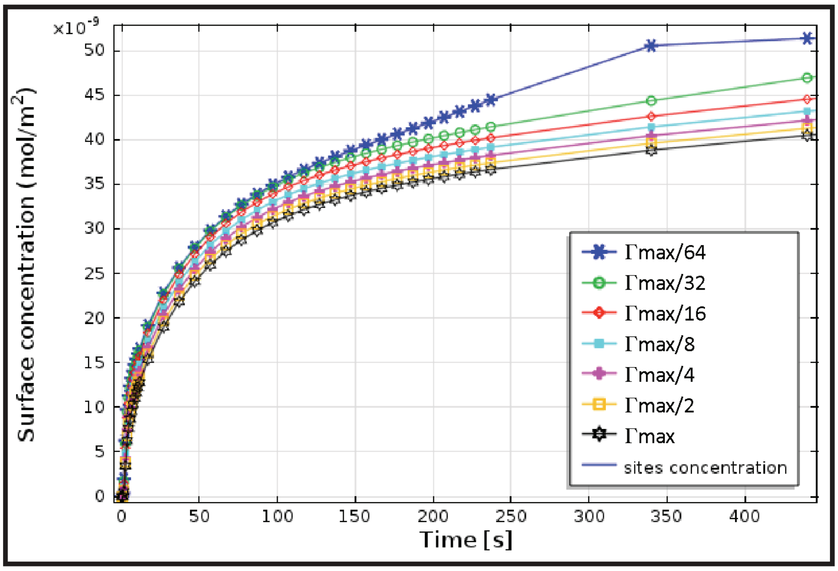

Figure A:11 | Diffusion limited. Time-dependence of Γ for $\Gamma_{max} \sim 10^{-6}$ mol/m^2 and $k_{on} \sim 10^6$ M^{-1}s^{-1}.

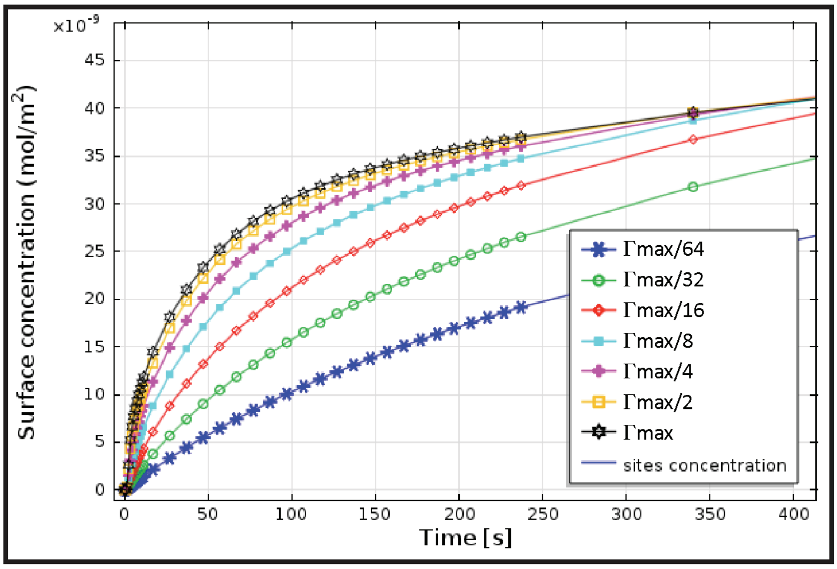

Figure A:12 | Slow reaction. Time-dependence of Γ for $\Gamma_{max} \sim 10^{-5}$ mol/m^2 and $k_{on} \sim 10^3$ M^{-1}s^{-1}.

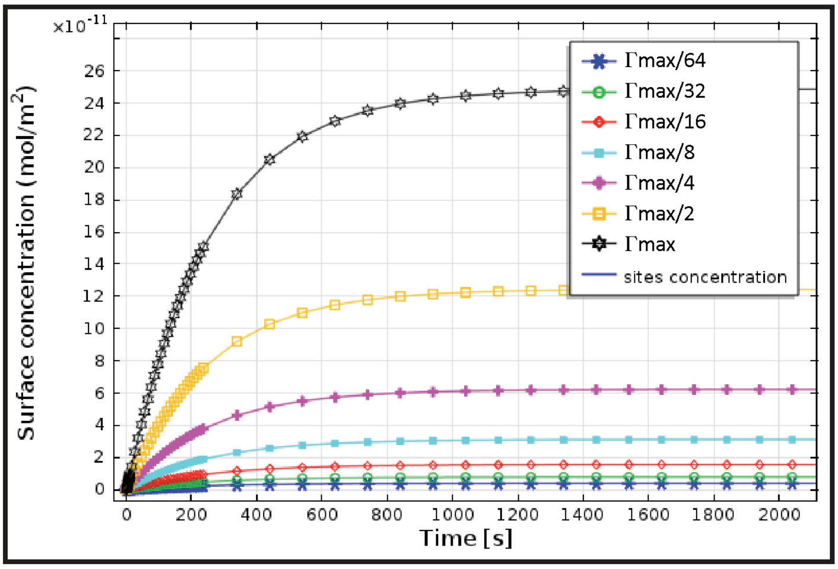

Figure A:13 | Slow saturation. Time-dependence of Γ for Γ_{max} ~ 10^{-10} mol/m^2 and k_{on} ~ 10^4 M^{-1}s^{-1}.

A.2.3 Washing

Similarly to the loading of the reagents in the chamber, the washing is done by flushing a solution containing no Abs. At the moment in which the flow rate is set to 25 µl/s to perform the washing, the depletion region generated above the binding sites is destroyed by the movement of the content of the chamber from left to right (see **Figure A:9**). This phenomenon may or not may have an effect in the final value of Γ, depending on whether saturation was already reached or not, since additional Abs are made available in close vicinity to the binding site for a short period of time. The parabolic profile generated at the entrance tubes, before the chamber, is also observed in this step.

Curriculum Vitae

Diego G. Dupouy

Chemin des Uttins 8, 1028 Préverenges, CH
diegodupouy@gmail.com
Phone: +41 78 924 88 89

Argentinean, Italian,
29 years old, married

EXPERIENCE

2013 - present

Co-founder and CTO at Lunaphore Technologies SA, Switzerland

- Company management
- Responsible for leading R&D activities
- Relationship with suppliers and subcontractors
- Relationship with research collaborators and grant writing

2011 - present

Doctoral assistant at the Laboratory of Microsystems (LMIS2), EPFL, Switzerland

- Clean Room fabrication: Photolithography, DRIE, Wet Etching, Sputtering, Wafer Bonding
- Characterization techniques: SEM, AFM
- Design and modeling of microfluidic devices
- On-chip techniques for cancer diagnosis
- Immunohistochemistry, fluorescence microscopy

2011 - 2014

Clean room practical work assistant at Center of MicroNano Technology (CMI), EPFL, Switzerland

- Practical work sessions: planning and preparation
- Teach bachelor student the basics of lithography, etching and electrical measurements
- Report correction

2008 (4 months)

Teaching assistant at the department of Mathematics III, Universidad Nacional de Entre Ríos, Argentina

2007 (3 months)

Deli Clerk, (Work and Travel experience), Breckenridge, CO, USA

EDUCATION

2011 - present

Doctoral assistant in Microsystems and Microelectronics
Swiss Federal Institute of Technology Lausanne (EPFL), Lausanne, Switzerland

Doctoral project *« Microfluidic staining technology and automated image processing for fast and accurate tissue-based diagnostics»,* Laboratory of Microsystems (LMIS2).

2008 – 2010

Master of Science in Nanotechnologies for the ICT (Joint degree)
Swiss Federal Institute of Technology Lausanne (EPFL), Lausanne, Switzerland
Politecnico di Torino (EPFL), Turin, Italy
Institute National Polytechnique de Grenoble (INPG), Grenoble, France
Graduation: September 2010. Grade: 110/110.

Mar 2010 – Aug 2010

Master thesis project *«Modeling of Ultra-Scaled PCM Devices»,* IBM Almaden Research Center, San Jose, CA.

May 2019 – Jul 2009

Summer project *«Gold Nanoparticles as Labels in Planar Waveguide-based Protein Microarrays»,* Laboratory of Biosensors and Bioelectronics, ETH, Zurich, Switzerland.

2005 – 2008 **Bioengineering**
Universidad Nacional de Entre Ríos, Oro Verde, Argentina

PERSONAL SKILLS

Language	**Spanish**	Native language
	English	Proficiency (C2), TOEFL, FCE, 1 year living experience in the USA.
	Italian	Proficiency (C2), two years of courses, one semester studies in Italy.
	French	Advanced skills (C2), courses, six years living in French-speaking countries.

Computing MATLAB, Mathemathica, C/C++, VHDL, EDA Tools, SolidWorks, COMSOL Multiphysics, ImageJ, Origin, Word, Excel, Powerpoint.

Engineering skills Mathematics, Physics, Electronics, BioMEMS, Fluid Mechanics, Optical Microscopy, Signal Processing, Image processing, Clean Room Processes, Nanotechnologies

PERSONAL INTERESTS

Scuba diving (advanced level), volleyball, basketball, hiking, backpacking.

List of Publications

Journal papers

1. **D.G. Dupouy**, A. Cavinato, M. Fiche, L. de Leval and M.A.M. Gijs, Automated microfluidic cytokeratin staining of thick resections of breast carcinomas, Lab on a Chip, in preparation
2. S. Brajkovic, **D.G. Dupouy**, L. de Leval and M.A.M. Gijs, Microfluidics for rapid cytokeratin immunohistochemical staining in frozen sections, Laboratory Investigations, in preparation
3. **D.G. Dupouy**, A.T. Ciftlik, M. Fiche, D. Heintze, B. Bisig, L. de Leval and M.A. M. Gijs, Continuous quantification of HER2 expression by microfluidic precision immunofluorescence estimates HER2 gene amplification in breast cancer, Scientific Reports 6, 20277 (2016), doi: 10.1038/srep20277
4. **D.G. Dupouy**, A.T. Ciftlik, J. Teixidor and M.A.M. Gijs, Programming and use of Parylene C fluorescence as a quantitative on-chip reference. RSC Adv. 4, 49367–49373 (2014), doi: 10.1039/C4RA08982K
5. A.T. Ciftlik, **D.G. Dupouy** and M.A.M. Gijs, Programmable Parylene-C bonding layer fluorescence for storing information on microfluidic chips. Lab on a Chip 13, 1482 (2013), doi: 10.1039/c3lc41280f
6. A. Padilla, G.W. Burr, C.T. Rettner, T. Topuria, P.M. Rice, B. Jackson, K. Virwani, A.J. Kellock, **D.G. Dupouy**, A. Debunne, R.M. Shelby, K. Gopalakrishnan, R.S. Shenoy, B.N. Kurdi, 2011. Voltage polarity effects in Ge2Sb2Te5-based phase change memory devices. Journal of Applied Physics 110, 054501, doi: 10.1063/1.3626047
7. G.W. Burr, A. Padilla, M. Franceschini, B. Jackson, **D. G. Dupouy**, C.T. Rettner, K. Gopalakrishnan, R. Shenoy, J. Karidis, 2010. The inner workings of phase change memory: Lessons from prototype PCM devices. IEEE, pp. 1890–1894, doi: 10.1109/GLOCOMW.2010.5700271

Conference contributions

1. **D.G. Dupouy**, A.T. Ciftlik, M. Fiche, D. Heintze, B. Bisig, L. de Leval and M. A. M. Gijs, Continuous quantification of HER2 expression by microfluidic precision immunofluorescence estimates HER2 gene amplification in breast cancer, XXXI International Congress of the International Academy of Pathology and 28th Congress of the European Society of Pathology, September 2016, Cologne, Germany.

2. S. Brajkovic, G. Repond, **D.G. Dupouy**, A. Soltermann, Rapid and accurate ALK detection in lung adenocarcinoma using a microfluidic tissue processor, p. S153, Der Pathologie Suppl 1, May 2016, Berlin, Germany
3. **D.G. Dupouy**, S. Ghiasikhou, A.T. Ciftlik, M. Fiche, L. de Leval, and M.A.M. Gijs, Rapid immunohistochemistry microfluidic protocol allows the detection of cancer cells at the margins of surgical cuts, Proc. of 19th Int. Conference on Miniaturized Systems for Chemistry and Life Sciences (microTAS '15), October 2015, Gyeongju, Korea
4. **D.G. Dupouy**, A.T. Ciftlik, J. Teixidor, M.A.M. Gijs, Fluorescence-based on-chip analyte concentration sensor using parylene-C bonding layer fluorescence, Biosensors 2014, Melbourne, Australia
5. **D.G. Dupouy**, A.T. Ciftlik., M.A.M. Gijs, Use of a Parylene-C bonding layer fluorescence as reference for on-chip imaging and detection applications, Proc. of 17th International Conference on Miniaturized Systems for Chemistry and Life Sciences (microTAS '13), October 2013, Freiburg, Germany

Patents pending

1. A.T. Ciftlik, **D.G. Dupouy**, P. Joris, M.D. Herrmann, L. Pelkmans, M.A.M. Gijs, Methods of sample cycle multiplexing and in situ imaging, European Patent Application (provisional) n° EP16154746.8
2. **D.G. Dupouy**, A.T. Ciftlik, D. Heintze, M.A.M. Gijs, Method for quantitative measurement of a biomarker by in situ immunofluorescence and uses of thereof, European Patent Application (provisional) n° EP16154745.0
3. A.T. Ciftlik, P. Joris, **D.G. Dupouy**, A.T. Ciftlik, M.A.M. Gijs, Microfluidic network device, European Patent Application (provisional) n° EP16162091.9

References

[1] A. Manz, N. Graber, and H. M. Widmer, “Miniaturized total chemical analysis systems: A novel concept for chemical sensing,” *Sens. Actuators B Chem.*, vol. 1, no. 1–6, pp. 244–248, Jan. 1990.

[2] R. Mukhopadhyay, “Microfluidics: On the Slope of Enlightenment,” *Anal. Chem.*, vol. 81, no. 11, pp. 4169–4173, Jun. 2009.

[3] C. D. Chin, V. Linder, and S. K. Sia, “Commercialization of microfluidic point-of-care diagnostic devices,” *Lab. Chip*, vol. 12, no. 12, p. 2118, 2012.

[4] P. Li, “Microfluidics For IVD: In Pursuit Of The Holy Grail,” *J. Bioeng. Biomed. Sci.*, vol. 03, no. 03, 2013.

[5] D. Mark, S. Haeberle, G. Roth, F. von Stetten, and R. Zengerle, “Microfluidic lab-on-a-chip platforms: requirements, characteristics and applications,” *Chem. Soc. Rev.*, vol. 39, no. 3, p. 1153, 2010.

[6] A. Manz *et al.*, “Planar chips technology for miniaturization and integration of separation techniques into monitoring systems,” *J. Chromatogr. A*, vol. 593, no. 1–2, pp. 253–258, Feb. 1992.

[7] D. J. Harrison, A. Manz, Z. Fan, H. Luedi, and H. M. Widmer, “Capillary electrophoresis and sample injection systems integrated on a planar glass chip,” *Anal. Chem.*, vol. 64, no. 17, pp. 1926–1932, Sep. 1992.

[8] S. C. Terry, J. H. Jerman, and J. B. Angell, “A gas chromatographic air analyzer fabricated on a silicon wafer,” *IEEE Trans. Electron Devices*, vol. 26, no. 12, pp. 1880–1886, Dec. 1979.

[9] G. Fiorini and D. Chiu, “Disposable microfluidic devices: fabrication, function, and application,” *BioTechniques*, vol. 38, no. 3, pp. 429–446, Mar. 2005.

[10] L. Martynova, L. E. Locascio, M. Gaitan, G. W. Kramer, R. G. Christensen, and W. A. MacCrehan, “Fabrication of Plastic Microfluid Channels by Imprinting Methods,” *Anal. Chem.*, vol. 69, no. 23, pp. 4783–4789, Dec. 1997.

[11] G. M. Whitesides, E. Ostuni, S. Takayama, X. Jiang, and D. E. Ingber, “Soft Lithography in Biology and Biochemistry,” *Annu. Rev. Biomed. Eng.*, vol. 3, no. 1, pp. 335–373, Aug. 2001.

[12] R. Mukhopadhyay, “When PDMS isn’t the best,” *Anal. Chem.*, vol. 79, no. 9, pp. 3248–3253, May 2007.

[13] H. Becker, “Polymer microfluidic devices,” *Talanta*, vol. 56, no. 2, pp. 267–287, Feb. 2002.

[14] A. T. Ciftlik, D. G. Dupouy, and M. A. M. Gijs, “Programmable parylene-C bonding layer fluorescence for storing information on microfluidic chips,” *Lab. Chip*, vol. 13, no. 8, p. 1482, 2013.

[15] D. G. Dupouy, A. T. Ciftlik, J. Teixidor, and M. A. M. Gijs, “Programming and use of Parylene C fluorescence as a quantitative on-chip reference,” *RSC Adv*, vol. 4, no. 90, pp. 49367–49373, Sep. 2014.

[16] A. T. Ciftlik and M. A. M. Gijs, “A low-temperature parylene-to-silicon dioxide bonding technique for high-pressure microfluidics,” *J. Micromechanics Microengineering*, vol. 21, no. 3, p. 035011, Mar. 2011.

[17] A. T. Ciftlik and M. A. M. Gijs, “Parylene to silicon nitride bonding for post-integration of high pressure microfluidics to CMOS devices,” *Lab. Chip*, vol. 12, no. 2, p. 396, 2012.

[18] J. Steigert *et al.*, “Rapid prototyping of microfluidic chips in COC,” *J. Micromechanics Microengineering*, vol. 17, no. 2, pp. 333–341, Feb. 2007.

[19] D. J. Guckenberger, T. E. de Groot, A. M. D. Wan, D. J. Beebe, and E. W. K. Young, “Micromilling: a method for ultra-rapid prototyping of plastic microfluidic devices,” *Lab Chip*, vol. 15, no. 11, pp. 2364–2378, 2015.

[20] A. Waldbaur, H. Rapp, K. Länge, and B. E. Rapp, “Let there be chip—towards rapid prototyping of microfluidic devices: one-step manufacturing processes,” *Anal. Methods*, vol. 3, no. 12, p. 2681, 2011.

[21] A. K. Au, W. Lee, and A. Folch, “Mail-order microfluidics: evaluation of stereolithography for the production of microfluidic devices,” *Lab Chip*, vol. 14, no. 7, pp. 1294–1301, 2014.

[22] R. M. McCormick, R. J. Nelson, M. G. Alonso-Amigo, D. J. Benvegnu, and H. H. Hooper, “Microchannel Electrophoretic Separations of DNA in Injection-Molded Plastic Substrates,” *Anal. Chem.*, vol. 69, no. 14, pp. 2626–2630, Jul. 1997.

[23] J. Giboz, T. Copponnex, and P. Mélé, “Microinjection molding of thermoplastic polymers: a review,” *J. Micromechanics Microengineering*, vol. 17, no. 6, pp. R96–R109, Jun. 2007.

[24] S. Cesaro-Tadic *et al.*, “High-sensitivity miniaturized immunoassays for tumor necrosis factor ? using microfluidic systems,” *Lab. Chip*, vol. 4, no. 6, p. 563, 2004.

[25] M. Zimmermann, E. Delamarche, M. Wolf, and P. Hunziker, “Modeling and optimization of high-sensitivity, low-volume microfluidic-based surface immunoassays,” *Biomed. Microdevices*, vol. 7, no. 2, pp. 99–110, Jun. 2005.

[26] H. C. Tekin, M. Cornaglia, and M. A. M. Gijs, “Attomolar protein detection using a magnetic bead surface coverage assay,” *Lab. Chip*, vol. 13, no. 6, p. 1053, 2013.

[27] A. H. C. Ng, U. Uddayasankar, and A. R. Wheeler, “Immunoassays in microfluidic systems,” *Anal. Bioanal. Chem.*, vol. 397, no. 3, pp. 991–1007, Jun. 2010.

[28] K. N. Han, C. A. Li, and G. H. Seong, “Microfluidic Chips for Immunoassays,” *Annu. Rev. Anal. Chem.*, vol. 6, no. 1, pp. 119–141, Jun. 2013.

[29] G. MacBeath, “Protein Arrays: Labeling the Protein and Probing the Array for Protein-Protein Interactions,” *Cold Spring Harb. Protoc.*, vol. 2007, no. 6, p. pdb.prot4630–pdb.prot4630, Mar. 2007.

[30] M. Herrmann, T. Veres, and M. Tabrizian, “Enzymatically-generated fluorescent detection in micro-channels with internal magnetic mixing for the development of parallel microfluidic ELISA,” *Lab. Chip*, vol. 6, no. 4, pp. 555–560, Apr. 2006.

[31] M. Herrmann, T. Veres, and M. Tabrizian, “Quantification of low-picomolar concentrations of TNF-alpha in serum using the dual-network microfluidic ELISA platform,” *Anal. Chem.*, vol. 80, no. 13, pp. 5160–5167, Jul. 2008.

[32] N. Yanagisawa and D. Dutta, “Kinetic ELISA in Microfluidic Channels,” *Biosensors*, vol. 1, no. 4, pp. 58–69, Jun. 2011.

[33] D. Berdat, A. Marin, F. Herrera, and M. A. M. Gijs, “DNA biosensor using fluorescence microscopy and impedance spectroscopy,” *Sens. Actuators B Chem.*, vol. 118, no. 1–2, pp. 53–59, Oct. 2006.

[34] D. Berdat, A. C. Martin Rodríguez, F. Herrera, and M. A. M. Gijs, “Label-free detection of DNA with interdigitated micro-electrodes in a fluidic cell,” *Lab. Chip*, vol. 8, no. 2, pp. 302–308, Feb. 2008.

[35] L. Wang and P. C. H. Li, “Microfluidic DNA microarray analysis: a review,” *Anal. Chim. Acta*, vol. 687, no. 1, pp. 12–27, Feb. 2011.

[36] T. M. Squires, R. J. Messinger, and S. R. Manalis, “Making it stick: convection, reaction and diffusion in surface-based biosensors,” *Nat. Biotechnol.*, vol. 26, no. 4, pp. 417–426, Apr. 2008.

[37] D. Janasek, J. Franzke, and A. Manz, “Scaling and the design of miniaturized chemical-analysis systems,” *Nature*, vol. 442, no. 7101, pp. 374–380, Jul. 2006.

[38] I. Langmuir, “THE ADSORPTION OF GASES ON PLANE SURFACES OF GLASS, MICA AND PLATINUM.,” *J. Am. Chem. Soc.*, vol. 40, no. 9, pp. 1361–1403, Sep. 1918.

[39] L. Brewer, “The Determination of Stability Constants and Other Equilibrium Constants in Solution. Francis J. C. Rossotti and Hazel Rossotti. McGraw-Hill, New York, 1961. xiv + 425 pp. $12.50,” *Science*, vol. 136, no. 3516, pp. 643–644, May 1962.

[40] A. Kovacs and L. Kaiser, “Supernatant in, kinetics out,” *Nat. Methods*, vol. 5, no. 9, 2008.

[41] J. W. Prichard, “Overview of Automated Immunohistochemistry,” *Arch. Pathol. Lab. Med.*, vol. 138, no. 12, pp. 1578–1582, Dec. 2014.

[42] “Maximizing capacity and throughput with continuous flow,” Ventana Medical Systems, Inc., 2014.

[43] M. Pekmezci, A. Szpaderska, C. Osipo, and Ç. Erşahin, “The Effect of Cold Ischemia Time and/or Formalin Fixation on Estrogen Receptor, Progesterone Receptor, and Human Epidermal Growth Factor Receptor-2 Results in Breast Carcinoma,” *Pathol. Res. Int.*, vol. 2012, pp. 1–7, 2012.

[44] G. H. Lyman, “American Society of Clinical Oncology Guideline Recommendations for Sentinel Lymph Node Biopsy in Early-Stage Breast Cancer,” *J. Clin. Oncol.*, vol. 23, no. 30, pp. 7703–7720, Sep. 2005.

[45] J. A. Ramos-Vara, “Technical Aspects of Immunohistochemistry,” *Vet. Pathol.*, vol. 42, no. 4, pp. 405–426, Jul. 2005.

[46] D. L. Rimm, “What brown cannot do for you,” *Nat. Biotechnol.*, vol. 24, no. 8, pp. 914–916, Aug. 2006.

[47] D. E. Carvajal-Hausdorf, K. A. Schalper, V. M. Neumeister, and D. L. Rimm, “Quantitative measurement of cancer tissue biomarkers in the lab and in the clinic,” *Lab. Invest.*, vol. 95, no. 4, pp. 385–396, Apr. 2015.

[48] C. Taylor *et al.*, “Immunohistochemical Staining Methods,” *IHC Guideb. 6th Ed. Den. Dako Den. Agil. Technol. Co.*, 2013.

[49] A. G. Rivenbark, S. M. O’Connor, and W. B. Coleman, “Molecular and Cellular Heterogeneity in Breast Cancer,” *Am. J. Pathol.*, vol. 183, no. 4, pp. 1113–1124, Oct. 2013.

[50] D. C. Allred, J. M. Harvey, M. Berardo, and G. M. Clark, “Prognostic and predictive factors in breast cancer by immunohistochemical analysis,” *Mod. Pathol. Off. J. U. S. Can. Acad. Pathol. Inc*, vol. 11, no. 2, pp. 155–168, Feb. 1998.

[51] K. Horowitz and W. McGuire, “Predicting response to endocrine therapy in human breast cancer: a hypothesis,” *Science*, vol. 189, no. 4204, pp. 726–727, Aug. 1975.

[52] D. Slamon, G. Clark, S. Wong, W. Levin, A. Ullrich, and W. McGuire, “Human breast cancer: correlation of relapse and survival with amplification of the HER-2/neu oncogene,” *Science*, vol. 235, no. 4785, pp. 177–182, Jan. 1987.

[53] J. P. Baak, D. Chin, P. J. van Diest, R. Ortiz, P. Matze-Cok, and S. S. Bacus, “Comparative long-term prognostic value of quantitative HER-2/neu protein expression, DNA ploidy, and morphometric and clinical features in paraffin-embedded invasive breast cancer,” *Lab. Investig. J. Tech. Methods Pathol.*, vol. 64, no. 2, pp. 215–223, Feb. 1991.

[54] D. J. Slamon *et al.*, “Use of Chemotherapy plus a Monoclonal Antibody against HER2 for Metastatic Breast Cancer That Over-expresses HER2,” *N. Engl. J. Med.*, vol. 344, no. 11, pp. 783–792, Mar. 2001.

[55] C. L. Vogel *et al.*, “Efficacy and safety of trastuzumab as a single agent in first-line treatment of HER2-overexpressing metastatic breast cancer,” *J. Clin. Oncol. Off. J. Am. Soc. Clin. Oncol.*, vol. 20, no. 3, pp. 719–726, Feb. 2002.

[56] A. C. Wolff *et al.*, “American Society of Clinical Oncology/College of American Pathologists Guideline Recommendations for Human Epidermal Growth Factor Receptor 2 Testing in Breast Cancer,” *J. Clin. Oncol.*, vol. 25, no. 1, pp. 118–145, Jul. 2006.

[57] A. C. Wolff *et al.*, “Recommendations for Human Epidermal Growth Factor Receptor 2 Testing in Breast Cancer: American Society of Clinical Oncology/College of American Pathologists Clinical Practice Guideline Update,” *J. Clin. Oncol.*, vol. 31, no. 31, pp. 3997–4013, Nov. 2013.

[58] J. Schweizer *et al.*, “New consensus nomenclature for mammalian keratins,” *J. Cell Biol.*, vol. 174, no. 2, pp. 169–174, Jul. 2006.

[59] R. R. Turner, D. W. Ollila, D. L. Krasne, and A. E. Giuliano, “Histopathologic validation of the sentinel lymph node hypothesis for breast carcinoma,” *Ann. Surg.*, vol. 226, no. 3, pp. 271–276; discussion 276–278, Sep. 1997.

[60] P. R. Langer-Safer, M. Levine, and D. C. Ward, “Immunological method for mapping genes on Drosophila polytene chromosomes,” *Proc. Natl. Acad. Sci. U. S. A.*, vol. 79, no. 14, pp. 4381–4385, Jul. 1982.

[61] O. P. Kallioniemi *et al.*, “ERBB2 amplification in breast cancer analyzed by fluorescence in situ hybridization.,” *Proc. Natl. Acad. Sci.*, vol. 89, no. 12, pp. 5321–5325, Jun. 1992.

[62] M. S. Kim *et al.*, “Breast Cancer Diagnosis Using a Microfluidic Multiplexed Immunohistochemistry Platform,” *PLoS ONE*, vol. 5, no. 5, p. e10441, May 2010.

[63] D. Juncker, H. Schmid, and E. Delamarche, “Multipurpose microfluidic probe,” *Nat. Mater.*, vol. 4, no. 8, pp. 622–628, Jul. 2005.

[64] R. D. Lovchik, G. V. Kaigala, M. Georgiadis, and E. Delamarche, “Micro-immunohistochemistry using a microfluidic probe,” *Lab. Chip*, vol. 12, no. 6, p. 1040, 2012.

[65] A. T. Ciftlik, H.-A. Lehr, and M. A. M. Gijs, “Microfluidic processor allows rapid HER2 immunohistochemistry of breast carcinomas and significantly reduces ambiguous (2+) read-outs,” *Proc. Natl. Acad. Sci.*, vol. 110, no. 14, pp. 5363–5368, Mar. 2013.

[66] K. R. Hawkins and P. Yager, “Nonlinear decrease of background fluorescence in polymer thin-films ? a survey of materials and how they can complicate fluorescence detection in MICROTAS,” *Lab. Chip*, vol. 3, no. 4, p. 248, 2003.

[67] A. Piruska *et al.*, “The autofluorescence of plastic materials and chips measured under laser irradiation,” *Lab. Chip*, vol. 5, no. 12, p. 1348, 2005.

[68] B. Lu, S. Zheng, B. Q. Quach, and Y.-C. Tai, “A study of the autofluorescence of parylene materials for μTAS applications,” *Lab. Chip*, vol. 10, no. 14, p. 1826, 2010.

[69] W. F. Beach, T. M. Austin, and B. J. Humphrey, *Process for the creation of selective fluorescent sites or regions in parylene films and coatings*. Google Patents, 1991.

[70] M. Bera, A. Rivaton, C. Gandon, and J. . Gardette, “Comparison of the photodegradation of parylene C and parylene N,” *Eur. Polym. J.*, vol. 36, no. 9, pp. 1765–1777, Sep. 2000.

[71] S. J. Remington, “Fluorescent proteins: maturation, photochemistry and photophysics,” *Curr. Opin. Struct. Biol.*, vol. 16, no. 6, pp. 714–721, Dec. 2006.

[72] S. Han *et al.*, “Lithographically Encoded Polymer Microtaggant Using High-Capacity and Error-Correctable QR Code for Anti-Counterfeiting of Drugs,” *Adv. Mater.*, vol. 24, no. 44, pp. 5924–5929, Nov. 2012.

[73] T. Yang, S. Jung, H. Mao, and P. S. Cremer, “Fabrication of Phospholipid Bilayer-Coated Microchannels for On-Chip Immunoassays,” *Anal. Chem.*, vol. 73, no. 2, pp. 165–169, Jan. 2001.

[74] I. Caelen, A. Bernard, D. Juncker, B. Michel, H. Heinzelmann, and E. Delamarche, “Formation of Gradients of Proteins on Surfaces with Microfluidic Networks,” *Langmuir*, vol. 16, no. 24, pp. 9125–9130, Nov. 2000.

[75] S. Ghaemmaghami *et al.*, “Global analysis of protein expression in yeast,” *Nature*, vol. 425, no. 6959, pp. 737–741, Oct. 2003.

[76] W. David E., “Fundamentals of Fluorescence and Fluorescence Microscopy,” in *Methods in Cell Biology*, pp. 63 – 91.

[77] M. A. Model and K. E. Healy, “Quantification of the surface density of a fluorescent label with the optical microscope,” *J. Biomed. Mater. Res.*, vol. 50, no. 1, pp. 90–96, 2000.

[78] J. C. Waters, “Accuracy and precision in quantitative fluorescence microscopy,” *J. Cell Biol.*, vol. 185, no. 7, pp. 1135–1148, Jun. 2009.

[79] K. M. Kedziora, J. H. M. Prehn, J. Dobrucki, and T. Bernas, “Method of calibration of a fluorescence microscope for quantitative studies,” *J. Microsc.*, vol. 244, no. 1, pp. 101–111, Oct. 2011.

[80] J. R. Swedlow, “Quantitative Fluorescence Microscopy and Image Deconvolution,” in *Methods in Cell Biology*, vol. 114, Elsevier, 2013, pp. 407–426.

[81] L. Song, E. J. Hennink, I. T. Young, and H. J. Tanke, “Photobleaching kinetics of fluorescein in quantitative fluorescence microscopy,” *Biophys. J.*, vol. 68, no. 6, pp. 2588–2600, Jun. 1995.

[82] M. Talhavini and T. D. Z. Atvars, “Dye-polymer interactions controlling the kinetics of fluorescein photobleaching reactions in poly(vinyl alcohol),” *J. Photochem. Photobiol. Chem.*, vol. 114, no. 1, pp. 65–73, Mar. 1998.

[83] J. M. Zwier, G. J. Van Rooij, J. W. Hofstraat, and G. J. Brakenhoff, “Image calibration in fluorescence microscopy,” *J. Microsc.*, vol. 216, no. 1, pp. 15–24, Oct. 2004.

[84] J. M. Zwier, L. Oomen, L. Brocks, K. Jalink, and G. J. Brakenhoff, “Absolute and relative quantification and calibration for sectioning fluorescence microscopy using standardized uniform fluorescent layers and SIPchart-based correction procedures</title>,” 2007, p. 64430C–64430C–11.

[85] J. M. Zwier, L. Oomen, L. Brocks, K. Jalink, and G. J. Brakenhoff, “Quantitative image correction and calibration for confocal fluorescence microscopy using thin reference layers and SIPchart-based calibration procedures,” *J. Microsc.*, vol. 231, no. 1, pp. 59–69, Jul. 2008.

[86] D. S. Baskin, M. A. Widmayer, and M. A. Sharpe, “Quantification and calibration of images in fluorescence microscopy,” *Anal. Biochem.*, vol. 404, no. 2, pp. 118–126, Sep. 2010.

[87] S.-K. Hoi, X. Chen, V. S. Kumar, S. Homhuan, C.-H. Sow, and A. A. Bettiol, “A Microfluidic Chip with Integrated Colloidal Crystal for Online Optical Analysis,” *Adv. Funct. Mater.*, vol. 21, no. 15, pp. 2847–2853, Aug. 2011.

[88] D. Gonzalez de Castro, P. A. Clarke, B. Al-Lazikani, and P. Workman, “Personalized Cancer Medicine: Molecular Diagnostics, Predictive biomarkers, and Drug Resistance,” *Clin. Pharmacol. Ther.*, vol. 93, no. 3, pp. 252–259, Mar. 2013.

[89] A.-M. Tsimberidou *et al.*, “Personalized Medicine in a Phase I Clinical Trials Program: The MD Anderson Cancer Center Initiative,” *Clin. Cancer Res.*, vol. 18, no. 22, pp. 6373–6383, Nov. 2012.

[90] K.-F. Becker *et al.*, “Quantitative protein analysis from formalin-fixed tissues: implications for translational clinical research and nanoscale molecular diagnosis,” *J. Pathol.*, vol. 211, no. 3, pp. 370–378, Feb. 2007.

[91] J. Koh, H. Go, M.-Y. Kim, Y. K. Jeon, J.-H. Chung, and D. H. Chung, “A comprehensive immunohistochemistry algorithm for the histological subtyping of small biopsies obtained from non-small cell lung cancers,” *Histopathology*, vol. 65, no. 6, pp. 868–878, Dec. 2014.

[92] G. Pauletti, “Assessment of Methods for Tissue-Based Detection of the HER-2/neu Alteration in Human Breast Cancer: A Direct Comparison of Fluorescence In Situ Hybridization and Immunohistochemistry.”

[93] M. A. Owens, B. C. Horten, and M. M. Da Silva, “HER2 Amplification Ratios by Fluorescence In Situ Hybridization and Correlation with Immunohistochemistry in a Cohort of 6556 Breast Cancer Tissues,” *Clin. Breast Cancer*, vol. 5, no. 1, pp. 63–69, Apr. 2004.

[94] J. R. Brown, M. P. DiGiovanna, B. Killelea, D. R. Lannin, and D. L. Rimm, “Quantitative assessment Ki-67 score for prediction of response to neoadjuvant chemotherapy in breast cancer,” *Lab. Invest.*, vol. 94, no. 1, pp. 98–106, Jan. 2014.

[95] A. McCabe, M. Dolled-Filhart, R. L. Camp, and D. L. Rimm, “Automated Quantitative Analysis (AQUA) of In Situ Protein Expression, Antibody Concentration, and Prognosis,” *JNCI J. Natl. Cancer Inst.*, vol. 97, no. 24, pp. 1808–1815, Dec. 2005.

[96] M. G. Rojo, G. Bueno, and J. Slodkowska, “Review of imaging solutions for integrated quantitative immunohistochemistry in the Pathology daily practice.,” *Folia Histochem. Cytobiol.*, vol. 47, no. 3, Feb. 2010.

[97] J. Janin, “The kinetics of protein-protein recognition,” *Proteins Struct. Funct. Genet.*, vol. 28, no. 2, pp. 153–161, Jun. 1997.

[98] P. Bongrand, “Ligand-receptor interactions,” *Rep. Prog. Phys.*, vol. 62, no. 6, pp. 921–968, Jun. 1999.

[99] S. P. Kent, K. H. Ryan, and A. L. Siegel, “Steric hindrance as a factor in the reaction of labeled antibody with cell surface antigenic determinants.,” *J. Histochem. Cytochem.*, vol. 26, no. 8, pp. 618–621, Aug. 1978.

[100] C. M. Van der Loos, P. K. Das, J. J. Van den Oord, and H. J. Houthoff, “Multiple immunoenzyme staining techniques use of fluoresceinated, biotinylated and unlabelled monoclonal antibodies,” *J. Immunol. Methods*, vol. 117, no. 1, pp. 45–52, Feb. 1989.

[101] C. M. van der Loos, “Multiple Immunoenzyme Staining: Methods and Visualizations for the Observation With Spectral Imaging,” *J. Histochem. Cytochem.*, vol. 56, no. 4, pp. 313–328, Dec. 2007.

[102] E. B. Lane and C. M. Alexander, “Use of keratin antibodies in tumor diagnosis,” *Semin. Cancer Biol.*, vol. 1, no. 3, pp. 165–179, Jun. 1990.

[103] V. Barak, H. Goike, K. W. Panaretakis, and R. Einarsson, “Clinical utility of cytokeratins as tumor markers,” *Clin. Biochem.*, vol. 37, no. 7, pp. 529–540, Jul. 2004.

[104] M. D. Gustavson *et al.*, “Standardization of HER2 Immunohistochemistry in Breast Cancer by Automated Quantitative Analysis,” *Arch. Pathol. Lab. Med.*, vol. 133, no. 9, pp. 1413–1419, Sep. 2009.

[105] S. Kwon, C. H. Cho, E. S. Lee, and J.-K. Park, “Automated Measurement of Multiple Cancer Biomarkers Using Quantum-Dot-Based Microfluidic Immunohistochemistry,” *Anal. Chem.*, vol. 87, no. 8, pp. 4177–4183, Apr. 2015.

[106] W. M. Hanna *et al.*, “HER2 in situ hybridization in breast cancer: clinical implications of polysomy 17 and genetic heterogeneity,” *Mod. Pathol.*, vol. 27, no. 1, pp. 4–18, Jan. 2014.

[107] A. J. Weickhardt, D. L. Aisner, W. A. Franklin, M. Varella-Garcia, R. C. Doebele, and D. R. Camidge, “Diagnostic assays for identification of anaplastic lymphoma kinase-positive non-small cell lung cancer: Diagnostic Assays for *ALK* in NSCLC,” *Cancer*, vol. 119, no. 8, pp. 1467–1477, Apr. 2013.

[108] A. T. Shaw *et al.*, “Ceritinib in *ALK* -Rearranged Non–Small-Cell Lung Cancer,” *N. Engl. J. Med.*, vol. 370, no. 13, pp. 1189–1197, Mar. 2014.

[109] J. M. Boland *et al.*, “Anaplastic lymphoma kinase immunoreactivity correlates with ALK gene rearrangement and transcriptional up-regulation in non–small cell lung carcinomas,” *Hum. Pathol.*, vol. 40, no. 8, pp. 1152–1158, Aug. 2009.

[110] C. I. Selinger *et al.*, “Testing for ALK rearrangement in lung adenocarcinoma: a multicenter comparison of immunohistochemistry and fluorescent in situ hybridization,” *Mod. Pathol.*, vol. 26, no. 12, pp. 1545–1553, Dec. 2013.

[111] J. Lechago, “The Frozen Section: Pathology in the Trenches,” *Arch. Pathol. Lab. Med.*, vol. 129, no. 12, pp. 1529–1531, 2005.

[112] J. B. Osborn, G. L. Keeney, J. W. Jakub, A. C. Degnim, and J. C. Boughey, “Cost-Effectiveness Analysis of Routine Frozen-Section Analysis of Breast Margins Compared with Reoperation for Positive Margins,” *Ann. Surg. Oncol.*, vol. 18, no. 11, pp. 3204–3209, Oct. 2011.

[113] M. Holm, B. Paaschburg, E. Balslev, C. K. Axelsson, G. L. Willemoe, and H. L. Flyger, “Intraoperative immunohistochemistry staining of sentinel nodes in breast cancer: Clinical and economical implications,” *The Breast*, vol. 17, no. 4, pp. 372–375, Aug. 2008.

[114] R. Emmadi and E. L. Wiley, “Evaluation of Resection Margins in Breast Conservation Therapy: The Pathology Perspective—Past, Present, and Future,” *Int. J. Surg. Oncol.*, vol. 2012, pp. 1–9, 2012.

[115] J. M. Jorns *et al.*, “Intraoperative Frozen Section Analysis of Margins in Breast Conserving Surgery Significantly Decreases Reoperative Rates: One-Year Experience at an Ambulatory Surgical Center,” *Am. J. Clin. Pathol.*, vol. 138, no. 5, pp. 657–669, Nov. 2012.

[116] J. C. Boughey *et al.*, “Impact of analysis of frozen-section margin on reoperation rates in women undergoing lumpectomy for breast cancer: Evaluation of the National Surgical Quality Improvement Program data,” *Surgery*, vol. 156, no. 1, pp. 190–197, Jul. 2014.

[117] E. S. Stovgaard, T. F. Tvedskov, A. V. Lænkholm, and E. Balslev, “Cytokeratin on Frozen Sections of Sentinel Node May Spare Breast Cancer Patients Secondary Axillary Surgery,” *Pathol. Res. Int.*, vol. 2012, pp. 1–5, 2012.

[118] J. M. Nahrig *et al.*, “Intraoperative Examination of Sentinel Lymph Nodes by Ultrarapid Immunohistochemistry,” *Breast J.*, vol. 9, no. 4, pp. 277–281, Jul. 2003.

[119] J. P. Leikola, T. S. Toivonen, L. A. Krogerus, K. A. J. von Smitten, and M. H. K. Leidenius, “Rapid immunohistochemistry enhances the intraoperative diagnosis of sentinel lymph node metastases in invasive lobular breast carcinoma,” *Cancer*, vol. 104, no. 1, pp. 14–19, Jul. 2005.

[120] E. I. Johnston, R. A. Beach, S. M. Waldrop, D. Lawson, and C. Cohen, “Rapid Intraoperative Immunohistochemical Evaluation of Sentinel Lymph Nodes for Metastatic Breast Carcinoma:,” *Appl. Immunohistochem. Mol. Morphol.*, vol. 14, no. 1, pp. 57–62, Mar. 2006.

[121] I.-K. Lee *et al.*, “Intraoperative examination of sentinel lymph nodes by immunohistochemical staining in patients with breast cancer,” *Eur. J. Surg. Oncol. EJSO*, vol. 32, no. 4, pp. 405–409, May 2006.

[122] G. M. Bricca, D. G. Brodland, and J. A. Zitelli, “Immunostaining Melanoma Frozen Sections: The 1-Hour Protocol,” *Dermatol. Surg.*, vol. 30, no. 3, pp. 403–408, Mar. 2004.

[123] A. Kimyai-Asadi, G. B. Ayala, L. H. Goldberg, J. Vujevich, and M. H. Jih, “The 20-Minute Rapid MART-1 Immunostain for Malignant Melanoma Frozen Sections,” *Dermatol. Surg.*, vol. 34, no. 4, pp. 498–500, Apr. 2008.

[124] L. F. Glass *et al.*, “Rapid Frozen Section Immunostaining of Melanocytes by Microphthalmia-Associated Transcription Factor:,” *Am. J. Dermatopathol.*, p. 1, Mar. 2010.

[125] K. H. Chang, D. T. Finn, D. Lee, J. Bhawan, G. E. Dallal, and G. S. Rogers, “Novel 16-minute technique for evaluating melanoma resection margins during Mohs surgery,” *J. Am. Acad. Dermatol.*, vol. 64, no. 1, pp. 107–112, Jan. 2011.

[126] J. Haapasalo, “Ultrarapid Ki-67 immunostaining in frozen section interpretation of gliomas,” *J. Clin. Pathol.*, vol. 58, no. 3, pp. 263–268, Mar. 2005.

[127] O. F. Rasmussen, T. Binzer, and L. Rudbeck, “Dynamic Gap Staining A New IHC Staining Technology,” Dako, 2014.

[128] “Dako Denmark A/S. Dako Omnis Data Sheet. http://www.dako.com/ch/29067_dako-omnis-data-sheet.pdf (accessed 22.08.16).”

[129] H. Toda *et al.*, “A Novel Immunohistochemical Staining Method Allows Ultrarapid Detection of Lymph Node Micrometastases While Conserving Antibody,” *ACTA Histochem. Cytochem.*, vol. 44, no. 3, pp. 133–139, 2011.

[130] R-IHC Study Group *et al.*, “Rapid immunohistochemistry based on alternating current electric field for intraoperative diagnosis of brain tumors,” *Brain Tumor Pathol.*, vol. 32, no. 1, pp. 12–19, Jan. 2015.

[131] D. G. Dupouy *et al.*, “Continuous quantification of HER2 expression by microfluidic precision immunofluorescence estimates HER2 gene amplification in breast cancer,” *Sci. Rep.*, vol. 6, p. 20277, Feb. 2016.

[132] U. Veronesi *et al.*, “Twenty-Year Follow-up of a Randomized Study Comparing Breast-Conserving Surgery with Radical Mastectomy for Early Breast Cancer,” *N. Engl. J. Med.*, vol. 347, no. 16, pp. 1227–1232, Oct. 2002.

[133] M. C. Smitt, K. Nowels, R. W. Carlson, and S. S. Jeffrey, “Predictors of reexcision findings and recurrence after breast conservation,” *Int. J. Radiat. Oncol. Biol. Phys.*, vol. 57, no. 4, pp. 979–985, Nov. 2003.

[134] D. E. Wazer *et al.*, “Factors influencing cosmetic outcome and complication risk after conservative surgery and radiotherapy for early-stage breast carcinoma,” *J. Clin. Oncol. Off. J. Am. Soc. Clin. Oncol.*, vol. 10, no. 3, pp. 356–363, Mar. 1992.

[135] N. Cabioglu *et al.*, “Role for Intraoperative Margin Assessment in Patients Undergoing Breast-Conserving Surgery,” *Ann. Surg. Oncol.*, vol. 14, no. 4, pp. 1458–1471, Mar. 2007.

[136] M. S. Moran *et al.*, “Society of Surgical Oncology–American Society for Radiation Oncology Consensus Guideline on Margins for Breast-Conserving Surgery With Whole-Breast Irradiation in Stages I and II Invasive Breast Cancer,” *Ann. Surg. Oncol.*, vol. 21, no. 3, pp. 704–716, Mar. 2014.

[137] K. C. Suen, W. S. Wood, A. A. Syed, N. F. Quenville, and P. B. Clement, “Role of imprint cytology in intraoperative diagnosis: value and limitations.,” *J. Clin. Pathol.*, vol. 31, no. 4, pp. 328–337, Apr. 1978.

[138] A. J. Creager, J. A. Shaw, P. R. Young, and K. R. Geisinger, “Intraoperative evaluation of lumpectomy margins by imprint cytology with histologic correlation: a community hospital experience,” *Arch. Pathol. Lab. Med.*, vol. 126, no. 7, pp. 846–848, Jul. 2002.

[139] E. R. Camp *et al.*, “Minimizing Local Recurrence after Breast Conserving Therapy Using Intraoperative Shaved Margins to Determine Pathologic Tumor Clearance,” *J. Am. Coll. Surg.*, vol. 201, no. 6, pp. 855–861, Dec. 2005.

[140] J. M. K. Mislow, A. J. Golby, and P. M. Black, “Origins of Intraoperative MRI,” *Neurosurg. Clin. N. Am.*, vol. 20, no. 2, pp. 137–146, Apr. 2009.

[141] R. M. Comeau, A. F. Sadikot, A. Fenster, and T. M. Peters, “Intraoperative ultrasound for guidance and tissue shift correction in image-guided neurosurgery,” *Med. Phys.*, vol. 27, no. 4, pp. 787–800, Apr. 2000.

[142] R. J. Halter *et al.*, “The correlation of in vivo and ex vivo tissue dielectric properties to validate electromagnetic breast imaging: initial clinical experience,” *Physiol. Meas.*, vol. 30, no. 6, pp. S121–136, Jun. 2009.

[143] M. Ferrari, “Cancer nanotechnology: opportunities and challenges,” *Nat. Rev. Cancer*, vol. 5, no. 3, pp. 161–171, Mar. 2005.

[144] C. Sotiriou and M. J. Piccart, “Taking gene-expression profiling to the clinic: when will molecular signatures become relevant to patient care?,” *Nat. Rev. Cancer*, vol. 7, no. 7, pp. 545–553, Jul. 2007.

[145] K. J. Shaw *et al.*, “Rapid PCR amplification using a microfluidic device with integrated microwave heating and air impingement cooling,” *Lab. Chip*, vol. 10, no. 13, p. 1725, 2010.

[146] D. G. Hicks and P. Tang, “Molecular Classifications of Breast Carcinoma: Is Immunohistochemistry a Viable Alternative to Other Molecular Methodologies?,” *Connection*, vol. 13, pp. 31–34, 2009.

[147] D. Tan and D. S. Zander, “Immunohistochemistry for Assessment of Pulmonary and Pleural Neoplasms: A Review and Update,” *Int. J. Clin. Exp. Pathol.*, vol. 1, no. 1, pp. 19–31, 2008.

[148] M. J. Gerdes *et al.*, “Highly multiplexed single-cell analysis of formalin-fixed, paraffin-embedded cancer tissue,” *Proc. Natl. Acad. Sci.*, vol. 110, no. 29, pp. 11982–11987, Jul. 2013.

[149] R. Ke *et al.*, “In situ sequencing for RNA analysis in preserved tissue and cells,” *Nat. Methods*, Jul. 2013.

[150] H. Bruus, *Theoretical microfluidics*. Oxford ; New York: Oxford University Press, 2008.